Drone Platform for Automated Pest Control

Final Report

AE3200: Design Synthesis

Project Group 9

Delft University of Technology

TU Delft

This page is intentionally left blank.

Drone Platform for Automated Pest Control

Final Report

by

Project Group 9

Student Name	Student Number
Bram Baarda	5957788
Martin Georgiev	5905850
Tim Jacobs	6019331
Meine Scheltema	5976782
Max Schuurkes	5497515
Lucas van der Klugt	5271177
Jens Dijk	5996139
Stanislav Pashkulev	5954347
Dennis Spelt	5998719
Jonathan van Boven	5583276

Course:	AE3200 Design Synthesis
Tutor and coaches:	Frits de Prenter, Reinier Vos, Shantha Kilambi
Responsible instructor:	Ir. J.A. Melkert
Faculty:	Faculty of Aerospace Engineering, Delft

Cover:	AI enhanced by Gemini (prompt in logbook)
Style:	TU Delft Report Style, with modifications by Daan Zwaneveld

TU Delft

Preface

This report presents the outcomes of the work conducted by 10 students over 10 weeks during the Design Synthesis Exercise. The project was provided by PATS, a high-tech company based in Delft, whose goal is to develop an autonomous drone system that intercepts moths mid-air using the drone's propellers, reducing the need for harmful pesticides. The goal of the team was therefore to design a highly agile drone that integrates with PATS' existing control system. This report presents the full design process and final design, along with all analyses performed to validate that the design meets the requirements.

This outcome would not have been possible without the guidance and assistance provided by the tutor, coaches, and external experts throughout the project. In particular, the team would like to thank:

Frits de Prenter
Tutor, TU Delft Faculty of Aerospace Engineering

Reinier Vos
Coach, TU Delft Faculty of Aerospace Engineering

Shantha Kilambi
Coach, TU Delft Faculty of Aerospace Engineering

Daniël Eikelenboom
External Expert, PATS

Raoul Mink
External Expert, PATS

Sjoerd Tijmons
External Expert, PATS

The team hopes that this report provides an insightful and engaging account of the design journey, and that the reader finds both the process and the resulting design as compelling as we did.

DSE Group 09 - Drone Platform for Automated Pest Control

B. Baarda, M. Georgiev, T. Jacobs, M. Scheltema, M. Schuurkes,
L. van der Klugt, J. Dijk, S. Pashkulev, D. Spelt, J. van Boven

Delft, June 2026

Executive Overview

This overview summarises the detailed design phase of this project and provides a stand-alone view into the context of the design assignment. It covers the market opportunity and sustainability strategy driving the project, the system requirements and design methodology used to develop the final design, the general design layout of the final design and its compliance with mission requirements, as well as the risks taken into consideration and the financial viability and return on investment of the project.

Project setting

This project is part of the Aerospace Engineering bachelor's program at TU Delft. In the third and last year, bachelor students perform a Design Synthesis Exercise (DSE), where they are given the opportunity to obtain design experience and are encouraged to explore new and innovative design concepts. The DSE is a full-time project and lasts 10 weeks, in which the students undergo a full design cycle from initial research to a detailed design. The DSE team consists of 10 students and is guided and graded by two coaches and one tutor. For this project specifically, the team also has access to two outside experts who are working for the company providing the project: PATS.

Pest control is a crucial part of greenhouse operations. Moths fall in a gap where common methods like pesticides and biological solutions are less effective and expensive. PATS hopes to fill this gap by trying to intercept these moths using a drone, and using the propellers of the drone as a moth interception and elimination mechanism. This leads to the mission objective:

"Design an autonomous drone platform for mechanical pest control in greenhouses"

The goal is to design a highly agile drone that integrates with PATS' existing control system to intercept moths mid-flight, eliminate them via propeller impact, and autonomously return to a docking station to recharge. As PATS has already made significant advancements in the control algorithm, and due to its complexity, this is considered to be outside of the scope of this project. However, significant improvements can be made in braking, reliability, modularity, sustainability and manufacturing.

Sustainable Development Strategy

The drone system is designed as a sustainable alternative to chemical pest control, addressing both the environmental harm caused by pesticides and the lifecycle impact of the drone itself. Pesticide use in greenhouse agriculture drives biodiversity loss, aquatic toxicity, human health risks, and the emergence of pest resistance-problems that persist even in closed greenhouse systems. To minimise the drone's own environmental footprint, a three-phase design philosophy is applied:

- **Manufacturing:** Commercially available components are prioritised for their economies-of-scale benefits, with non-standard parts produced via additive manufacturing to reduce material waste by up to 80%.
- **Operation:** Component lifetime is extended through failure analysis and modular design, ensuring individual parts can be replaced without discarding the full system.
- **End-of-Life:** Permanent joining methods are avoided in favour of screws and snap-fit connections, enabling non-destructive disassembly and enabling the reuse and recycling of high-impact components.

These principles are formalised into six Sustainable Design Philosophy guidelines:

SDP-1: Commercially available components shall be used whenever possible.

SDP-2: Non-standard components shall be manufactured using additive manufacturing methods.

SDP-3: Component lifetime shall be compatible with the intended operational lifetime of the drone.

SDP-4: Components expected to fail prematurely shall be designed for easy replacement.

SDP-5: Permanent joining methods, such as adhesives, shall be avoided where possible.

SDP-6: High environmental impact components shall have suitable end-of-life recycling strategies.

Market Analysis

The *Chrysodeixis chalcites* moth is a persistent pest in European high-tech greenhouses, and current control methods are failing to address it adequately. Chemical pesticides achieve less than 50% control efficiency, cost growers an estimated EUR 15,000 per hectare per year, and are increasingly restricted by EU regulation. Biological alternatives remain commercially unviable for short-cycle crops and cannot keep damage below needed levels. This creates a critical market gap that PATS addresses with an autonomous, mechanical interception drone, the only active moth control solution in the greenhouse sector.

The commercial opportunity is substantial:

- **Total Addressable Market (TAM):** 33,637 ha of European high-tech greenhouse area, representing approximately EUR 504.6 million annually.
- **Serviceable Addressable Market (SAM):** 4,500 ha in the Dutch Westland region, representing EUR 67.5 million annually.
- **Target Market Share:** An active fleet is projected to cover 410 ha by Year 5, capturing 9.11% of the Westland market.

The system is offered under a subscription model at EUR 10,000/ha/year, significantly undercutting pesticide expenditure, covering an active fleet of ten drones per hectare including all maintenance and replacements. To sustain this pricing, drone unit cost is EUR 239, achieved through off-the-shelf components and 3D printing. Future scalability is supported by a forecasted smart agriculture CAGR of 16.1% and incoming EU pesticide reduction legislation, which will further accelerate grower adoption.

System Constraints and Design Methodology

The design is governed by a hierarchical requirements structure, flowing from high-level user requirements down to system and subsystem specifications. The user requirements establish the most critical operational and commercial constraints on the drone platform, the most demanding of which are listed below:

DPAPC-USER-01: The drone shall intercept the pest without sustaining damage that results in loss of flight capability or requires manual repair.

DPAPC-USER-03: The drone shall be capable of executing 80 sorties per day.

DPAPC-USER-04: The drone shall have a maximum recharge time of 5 minutes between flights.

DPAPC-USER-06: The drone shall weigh less than 200 grams.

DPAPC-USER-16: The cost per drone shall be below EUR 250.

Due to the highly interdependent nature of the drone subsystems, a concurrent systems engineering approach is employed rather than a sequential design process. The methodology is structured around four iteration loops, each targeting a specific subsystem interaction such as propeller-motor matching, mass-power budgeting, structural optimisation, aerodynamic layout, and flight profile validation. These loops operate in parallel, with subsystem parameters exchanged through daily integration meetings to resolve conflicts and maintain system-level consistency. The overarching loop ensures all technical requirements are satisfied, with further optimisation performed where the project timeline permits.

Final Design Overview

An extensive trade-off identified a tethered flying duct to be the optimal concept for the required mission. Afterwards, the above-mentioned design methodology was applied while taking into account the sustainability guidelines, together with the specified user requirements. This led to the creation of *The Chameleon*, a name inspired by the hunting behaviour of a chameleon, which strikes insect prey with its tongue within a fraction of a second.

The Chameleon consists of a cylinder-shaped frame with two counter-rotating propellers in the middle and batteries located on the outside. It is steered by veins located at the outlet of the duct, driven by micro-servos. For better visualisation, CAD renders of the drone are shown in Figure 1.

(a) Internal layout render

(b) External Render

Figure 1: CAD Renders of *the Chameleon* showing (a) the internal components and (b) the outer chassis layout.

Furthermore, the main characteristics of *the Chameleon* are presented in Table 1

Table 1: *Chameleon* Final Design Overview

Category	Parameter	Value
Performance	Total system mass	143 g
	Max Thrust-to-weight ratio	5.3
	Braking distance from 9.6 m/s	0.4 m
Power & Ops	Battery capacity	320 mAh
	Recharge time (nominal)	$\leq$5 min
	Daily sorties capability	$\geq$ 80
Cost	Unit cost per drone	EUR 239
	Total development cost	EUR 103k

Requirements Compliance

The final design is compliant with all mission requirements except **MIS-15**, which required the drone to be fully integratable with the existing PATS infrastructure. The tethered system required the integration of a spool in the docking station. Not meeting the requirement was accepted, and the redesign of the docking station is included in the development costs. A full verification and validation plan has been established, with most requirements verifiable through analysis or inspection, and physical testing reserved for post-DSE prototype phases.

Life Cycle Analysis

A Life Cycle Analysis was performed using the IDEMAT eco-cost framework, which quantifies environmental burden across resource depletion, eco-toxicity, human health, and carbon footprint. The assessment accounts for full drone manufacturing, three battery replacements over the operational lifetime, and end-of-life processing, including a conservative 25% safety margin for material and energy uncertainties.

The resulting eco-cost of *the Chameleon* is **EUR 68.00** per hectare over its operational lifetime, compared to **EUR 15,840** for the equivalent Deltamethrin pesticide treatment of a hectare over the same period: a reduction of **>99%**. This confirms *the Chameleon* as a substantially more sustainable alternative to chemical pest control, even under conservative assumptions.

Risk Assessment

A technical risk assessment identified the tether, propulsion, and control subsystems as the highest risk areas, with development budget overrun, tether failure, and control delay being the most significant risks to mitigate. Targeted mitigations, including a 4.5 safety factor on the tether, a predictive control algorithm, and a dedicated contingency budget, substantially reduced most risks. Remaining high-impact risks, such as control delay failure, are accepted at this stage but flagged for future monitoring.

Finances & Return on Investment

A bottom-up cost analysis confirms *the Chameleon* is financially viable at every level. All estimated costs satisfy their respective requirements, with key figures summarised below:

Unit Cost: EUR 239 per drone, comfortably below the EUR 250 cap.

Development Cost: EUR 103k nominal / EUR 212k pessimistic, both above EUR 100k budget cap. However, profit margins remain high.

Contingency Budget: EUR 109k, derived from a scenario-based schedule variance analysis rather than an arbitrary percentage.

Annual Operating Cost: EUR 561k, scaling with a flat 30% every year.

A five-year discounted cash flow model, applying a conservative 35% discount rate appropriate for early-stage ventures, projects revenues growing from EUR 50k in Year 1 to EUR 1,640k by Year 5, yielding a net present value of **EUR 1.5 million**.

Nomenclature

Symbol	Definition	Unit	Symbol	Definition	Unit
Abbreviations and Acronyms					
BEMT	Blade Element Momentum Theory	[-]	LQR-I	LQR with Integrator	[-]
BOM	Bill of Materials	[-]	LTI	Linear Time Invariant	[-]
BR	Baseline Report	[-]	MAI	Manufacturing, Assembly & Integration	[-]
CAD	Computer-Aided Design	[-]	MCU	Micro Controller Unit	[-]
CAGR	Compound Annual Growth Rate	[-]	MDOF	Multiple Degree of Freedom	[-]
CBS	Cost Breakdown Structure	[-]	MTBF	Mean Time Before Failure	[-]
CFD	Computational Fluid Dynamics	[-]	MuJoCo	Multi-Joint dynamics with Contact	[-]
CoM	Center of Mass	[-]	NPV	Net Present Value	[-]
COTS	Commercial Off-The-Shelf	[-]	NRC	Non-Recurring Costs	[-]
CTGB	Board for Authorisation of Pesticides	[-]	OL	Optimisation Loop	[-]
DFMA	Design for Manufacturing and Assembly	[-]	PATS	PATS Indoor Drone Solutions	[-]
DFN	Doyle-Fuller-Newman	[-]	PC FR	Fire-Retardant Polycarbonate	[-]
DoF	Degrees of Freedom	[-]	PCB	Printed Circuit Board	[-]
DSE	Design Synthesis Exercise	[-]	PWM	Pulse Width Modulation	[-]
EASA	EU Aviation Safety Agency	[-]	RAMS	Reliability, Availability, Maintainability, Safety	[-]
EEA	European Environment Agency	[-]	RK4	Runge-Kutta 4th Order	[-]
EOL	End-Of-Life	[-]	ROI	Return on Investment	[-]
ESC	Electronic Speed Controller	[-]	RPM	Rotations Per Minute	[-]
EU	European Union	[-]	RX	Receiver	[-]
FBS	Functional Breakdown Structure	[-]	SAM	Serviceable Addressable Market	[-]
FDM	Fused Deposition Modelling	[-]	SDOF	Single Degree of Freedom	[-]
FFD	Functional Flow Diagram	[-]	SDP	Sustainable Design Philosophy	[-]
IMU	Inertial Measurement Unit	[-]	SOC	State of Charge	[-]
IPM	Integrated Pest Management	[-]	STEP	Standard for the Exchange of Product Data	[-]
IRR	Internal Rate of Return	[-]	SWOT	Strengths, Weaknesses, Opportunities, Threats	[-]

Symbol	Definition	Unit	Symbol	Definition	Unit
LCA	Life Cycle Analysis	[-]	TAM	Total Addressable Market	[-]
Li-ion	Lithium-Ion	[-]	T/W	Thrust-to-Weight Ratio	[-]
LiHV	Lithium Polymer High Voltage	[-]	TBD	To Be Determined	[-]
LiPo	Lithium-Polymer	[-]	VLM	Vortex Lattice Method	[-]
LQR	Linear-Quadratic Regulator	[-]	VTOL	Vertical Take-Off and Landing	[-]
Roman Symbols					
A	Reference area	$[m^2]$	m	Mass of the body	[kg]
$\mathbf{A}, \mathbf{B}, \mathbf{C}, \mathbf{D}$	State-space matrices	[-]	N_{cells}	Number of cells in series	[-]
a	Acceleration	$[m/s^2]$	P	Power	[W]
a	Launch angle	[rad]	P_{avg}	Average motor power	[W]
C_0	Initial investment	[€]	P_{max}	Peak motor power	[W]
$[C]$	Damping matrix	$[N \cdot s/m]$	$p, \mathbf{p}$	Position in launch frame	[m]
C_D, C_d	Drag coefficient	[-]	Q_{nom}	Nominal pack capacity	[Ah]
CF_t	Annual cash flow	[€]	q	Dynamic pressure	[Pa]
C_{ij}	Aerodynamic derivatives	[rad^{-1}]	R	Radius	[m]
C_P	Power coefficient	[-]	R_d	Dynamic amplification factor	[-]
C_T	Thrust coefficient	[-]	R_i	Internal resistance per cell	[Ω]
c_{ref}	Reference chord	[m]	$R(t)$	Reliability after t hours	[-]
D	Drag force	[N]	r	Discount rate	[-]
D	Tether diameter	[mm]	S_{ref}	Reference surface	$[m^2]$
d	Braking distance	[m]	T	System thrust	[N]
d	Propeller distance	[m]	T_p	Propeller torque	[Nm]
E	Tether modulus	[GPa]	t	Time	[s]
E	Young's modulus	[GPa]	t	Year	[-]
F	External force	[N]	t_{flight}	Target flight duration	[s]
F_{brake}	Tether brake force	[N]	t_{p_max}	Duration spent at peak power	[s]
f	State eq. vector	[-]	t_{ramp}	Brake ramp-up time	[s]
$\mathbf{f_0}$	Residual term	[-]	u	Displacement	[m]
I	Current	[A]	**u**	Input vector	[-]
I	Moment of Inertia	$[kg \cdot m^2]$	V	Flight velocity	[m/s]
$I_{xx,yy,zz}$	Diagonal inertia matrix entries	$[g \cdot mm^2]$	V_{in}	Effective throttled voltage	[V]
J	Inertia matrix	$[kg \cdot m^2]$	V_{max}	Max voltage	[V]
J	Moment of inertia about CoM	$[kg \cdot m^2]$	V_{ocv}	Open Circuit Voltage	[V]
K	Gain vector	[-]	$\mathbf{v_b}$	Velocity in the body frame	[m/s]
$[K]$	Stiffness matrix	$[N/m]$	$v_{x,y,z}$	Velocity components in body frame	[m/s]
K_V	Motor velocity constant	[RPM/V]	$\mathbf{W}_\eta$	Tait-Bryan transformation matrix	[-]
k	Tether stiffness	[N/m]	**x**	State vector	[-]
L	Length	[m]	x, y, z	Position coordinates	[m]

Symbol	Definition	Unit	Symbol	Definition	Unit
$M, \mathbf{M}$	External moment	[Nm]	$\mathbf{y}$	Output vector	[-]
$[M]$	Mass matrix	[kg]			
Greek Symbols					
α	Angle of attack	[rad]	θ	Pitch angle	[rad]
β	Pitch offset	[°]	ξ	Damping ratio	[-]
β	Sideslip angle	[rad]	ρ	Air density	$[kg/m^3]$
Δt	Time step	[s]	τ	Time constant	[s]
δ	Control surface deflection	[rad]	ϕ	Roll angle	[rad]
δ_t	Throttle setting	[-]	ψ	Yaw angle	[rad]
ε, ϵ	Launch angle	[rad]	Ω	Rotations per minute	[RPM]
η	Tait-Bryan angles	[rad]	ω_{max}	Highest natural frequency	[rad/s]
η^*	Motor efficiency	[%]	$\omega_{x,y,z}$	Body angular velocities	[rad/s]

Contents

1 Introduction

Ensuring global food security while minimising ecological damage is a defining challenge of modern agriculture. Within the environment of greenhouse crop cultivation, controlling moths remains a critical challenge. The traditional reliance on pesticides is becoming increasingly unsustainable due to moths rapidly developing resistance [1], alongside the severe negative impacts these chemicals have on both human health and the broader ecosystem [2]. To drive the transition towards a more sustainable agricultural industry, a fundamental shift in pest management is required. Therefore, this Design Synthesis Exercise (DSE) project, in collaboration with PATS Indoor Drone Solutions, aims to transform crop cultivation by proposing a purely mechanical, zero-chemical alternative: intercepting moths mid-air using an autonomous drone's propellers.

The objective of this DSE is to design specialised hardware for an autonomous, agile, and lightweight moth-intercepting drone. To succeed in this objective, project boundaries have been defined. The main control algorithms, the camera detection system (PATS-C), the communication and controller hardware, and the charging infrastructure are provided by the client (PATS). The scope of the project is therefore strictly limited to designing the physical drone platform and ensuring seamless integration with the existing PATS infrastructure. However, the hardware itself poses its own design challenges, as it should satisfy conflicting requirements such as combining a crash-resistant structure with a very low maximum mass, or combining high-speed interception with quick deceleration. The design challenge is therefore to balance these requirements and present an optimised final design, with the secondary ambition of presenting a competitive entry at the final symposium.

Achieving this goal requires the team to transition from theoretical concepts to an actual design. During the Project Plan and Baseline phases, the team defined the problem space, established the governing requirements, and generated five initial drone concepts: the Cyclocopter, the Flying Squirrel, the Tether, Variable Pitch, and the Flying Duct. The concepts were then traded off in the Midterm report, based on four criteria: Interceptability, durability, cost and sustainability, weighted at 45%, 30%, 15% and 10%, respectively. Following the trade off, it was chosen to further develop a combination of the Tether and Flying Duct concepts. A preliminary design of the combination was presented as *the Chameleon*. The purpose of this Final report is to design *the Chameleon* in detail and deliver a manufacturable system to PATS. Each subsystem is designed in coherence with the others to converge to a final system design, from which the performance is analysed. The design also considers reliability, risks and costs of system implementation, to ensure PATS can accurately assess this revised Autonomous Drone Platform and conclude its use for their operation.

This report is structured to document the detailed design of *the Chameleon* drone. It begins by situating the project within its sustainability and market context (Chapter 2, Chapter 3), before establishing the system requirements and constraints (Chapter 4). The core of the report then presents work done on the detailed design by each department: the propulsion (Chapter 6), power and electronics (Chapter 7), structure (Chapter 8), aerodynamics (Chapter 9), control (Chapter 10) and flight profile (Chapter 11). Following the detailed subsystem designs, the final design is reviewed holistically (Chapter 12), and its environmental impact and risks are rigorously analysed through life cycle assessment (Chapter 13) and a risk and reliability evaluation (Chapter 14). The report then proceeds by discussing future development planning and manufacturing (Chapter 15) and addresses project finances (Chapter 16), requirements compliance and verification methods (Chapter 17), and finally concludes with recommendations (Chapter 18). Equipping PATS with the information necessary to evaluate the manufacturability, feasibility, and operational readiness of the product.

2
Sustainable Development Strategy

The goal behind this project is to provide a sustainable alternative to pesticides for moth pest control by using drones. To achieve this goal, sustainability is highly relevant to the design in two ways. The environmental impact of the design should be minimised to provide a serious alternative to chemical and biological pest control methods. This has been taken into account by making the drone design sustainable over three phases, namely: Manufacturing, Operation, and End-Of-Life (EOL). The second way, the reason this project exists is to eliminate the harmful effects of pesticides on humans and the entire ecosystem by removing the need to use them. This chapter shows the effects of pesticides on the environment and demonstrates how the sustainable design philosophy is present during the three phases previously mentioned. The environmental impact will be further discussed and quantified in Chapter 13.

2.1. Environmental Impact of Pesticides

Spraying pesticides is currently one of the most used methods for pest control in greenhouse agriculture [3]. Although pesticides are effective in reducing insect populations, pesticide usage is associated with significant environmental and health impacts. The European Environment Agency (EEA) states that pesticide pollution drives the biodiversity loss in Europe as it causes significant declines in insect population, threatening the critical role they play in food production [4]. Pesticide use has been linked to a 50% reduction in wild plant diversity within 500 meters of fields where they are used [5]. Furthermore, pesticides that enter nearby water systems through run-off and drainage can become toxic to aquatic organisms [6].

Historically, greenhouses were considered closed systems, meaning that there is almost no mass exchange with the outside environment. However, recent studies have shown that pesticides still escape into the surrounding environment through drainage water, ventilation systems and soil dumping [7]. A study in Norway concluded that (water) pollution caused by greenhouses is worse than the pollution from open crop fields, with their pollution exceeding environmental risk levels [8].

Besides the environmental concerns, there are also human health risks associated with pesticide exposure. Greenhouse workers are particularly vulnerable. Exposure mainly occurs during fumigation, mixture preparation and/or application in indoor environments [9]. Long-term exposure has been associated with an increase in cardiovascular diseases, skeletal muscle system diseases and digestive diseases [10].

Finally, another major drawback of pesticide usage is the development of resistance in the pest population. Insects evolve to become resistant to the effects of pesticides. This creates a perpetuating cycle of pesticide dependence where the potency and dosage of the pesticides need to be increased [11].

2.2. Sustainable Design Philosophy

In order to minimize the environmental impact of our drone system it is required to establish a clear design philosophy that will be incorporated by all subsystems during all design phases. This approach has been split into three different phases, namely: Manufacturing, Operation and End-Of-Life.

Manufacturing

The manufacturing phase focuses on the environmental impact of the components and production process. To mitigate the impact of our drone during this phase the parts used for the production of the drone will be either commercially available or manufactured using 3D printing. The use of commercially available components decreases the environmental impact per component due to efficiency gains made in economies of scale [12]. Components that cannot be bought off the shelf are produced using additive manufacturing methods (e.g. 3D printing). A study has shown that the use of additive manufacturing reduced the material usage by 35% to 80% [13]. In Chapter 13 the impact of all the materials used is discussed and quantified.

Operation

The operation phase focuses decreasing environmental impact by extending the product lifetime. The dominant factors to increase the operational life time are: Reducing component failure and designing for repair. For high-wear, high-impact subsystems such as the battery system, extra analysis has been done to evaluate the impact of the wear on the expected lifetime. This ensures that component failure is reduced, reducing the need for premature replacement and thereby lowering the environmental impact of the system. Furthermore, components that are expected to fail before the EOL of the drone system have been designed for easy replacement, ensuring that only the failed component needs to be replaced instead of the whole system.

End-Of-Life

The End-Of-Life phase focuses on minimizing environmental impact by enabling efficient disassembly, reuse and recycling of the drone and its components. Given the system consists of multiple materials and parts, design choices must ensure that these can be separated an processed with minimal effort.

To increase the ease of disassembly, permanent joints such as adhesives are avoided. Instead screws or snap-fit connections will be used. This enables non-destructive disassembly and increases the likelihood that components can be reused or recycled. Furthermore, high environmental impact components should be recycled at the end of life. This will be incorporated into the cost-breakdown in Chapter 16.

2.3. Sustainability Guidelines

In order to ensure that sustainability is considered throughout the entire design process a list of sustainability guidelines have been created (Table 2.1). These guidelines will be integrated throughout the design of the subsystems.

Table 2.1: Sustainability guidelines

Identifier	Explanation
SDP-1	Commercially available components shall be used whenever possible.
SDP-2	Components that cannot be obtained off-the-shelf shall be manufactured using additive manufacturing methods.
SDP-3	Components shall be optimized such that their expected lifetime is compatible with the intended operational lifetime of the drone where possible.
SDP-4	Components expected to fail during the operational lifetime of the system shall be designed for easy replacement.
SDP-5	Permanent joining methods, such as adhesives, shall be avoided where possible.
SDP-6	Components with a high environmental impact shall be identified and suitable end-Of-life recycling strategies shall be considered.

3 Market Analysis

Lepidopteran pests, specifically the Golden Twin-spot moth (*Chrysodeixis Chalcites*), are a persistent integrated pest control (IPM) challenge in European greenhouses [14, 15]. Current IPM strategies rely on chemical pesticides or biological control, both of which exhibit significant limitations (Figure 3.1). PATS proposes a mechanical interception drone to address these shortcomings. This chapter evaluates the commercial viability of this system by quantifying the financial shortcomings of current methods, defining the serviceable market volume, and deriving a target system cost.

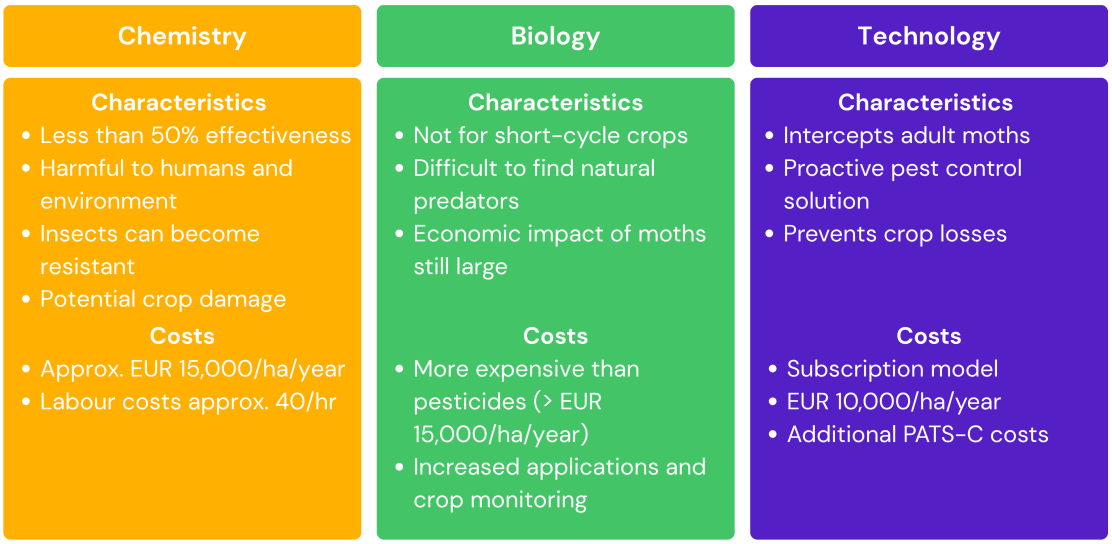

Figure 3.1: Synthesis of current pest management methods and the advantages of mechanical pest control (compiled from data detailed in Section 3.3 and Appendix C, follows translated motto from PATS: ”Chemie, Biologie, Technologie”).

3.1. Stakeholder Analysis

A stakeholder analysis was performed to establish the system’s commercial constraints. Figure 3.2 presents a Mendelow Matrix classifying stakeholders by their relative influence and operational interest.

Primary Active Stakeholders

The clients (PATS and the tutor) and greenhouse growers (end-users) drive the core market requirements and prioritise interception efficacy, system reliability, and economic Return on Investment (ROI). Investors[1] and insurance providers can exert indirect influence by imposing constraints on expenses and liability (e.g., fail-safes against crop or infrastructure damage).

[1] `https://www.pats-drones.com/post/pats-raises-2-7m-to-accelerate-smarter-more-sustainable-pest-control` – Accessed: 27.05.2026

Regulatory and Passive stakeholders

European regulatory bodies (e.g., EASA, agricultural authorities) act as key stakeholders by dictating the system's legal and operational constraints. Environmental interests, such as the decrease in chemical run-off, are formally represented by regulatory stakeholders such as the CTGB[2] and the European Green Deal (Farm-to-Fork strategy [16]). These bodies enforce sustainability constraints and force the market away from chemical methods [16].

Operational & Community Stakeholders

Greenhouse employees and maintenance technicians have low purchasing power but dictate critical constraints regarding occupational safety and system modularity. Similarly, residents living near greenhouses hold minimal direct influence over the design, but maintain a high interest in the mitigation of localised chemical run-off. Finally, currently, retail-end consumers hold negligible influence but maintain an interest in the availability of pesticide-free produce [17].

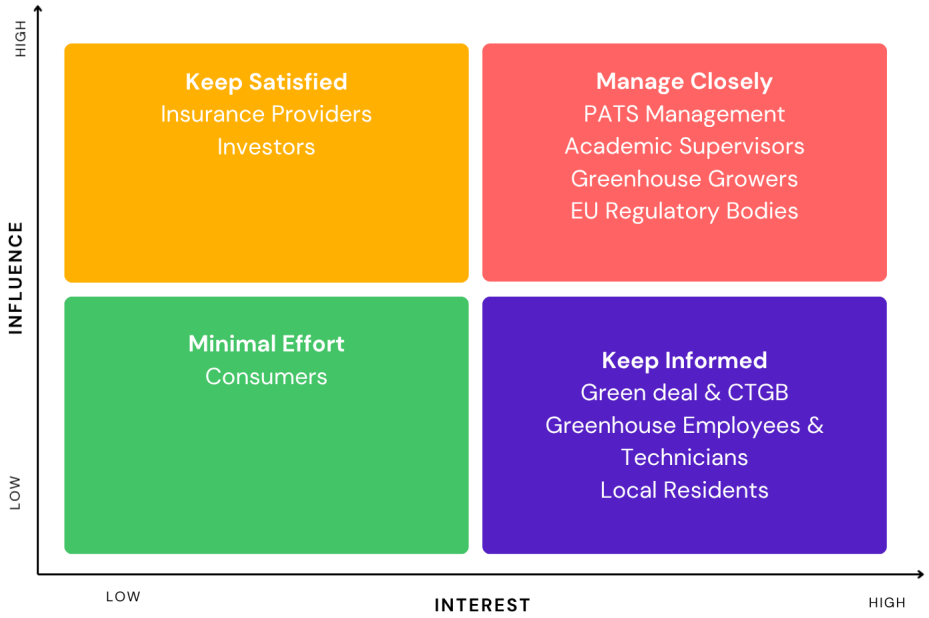

Figure 3.2: Mendelow Matrix

3.2. Current IPM market

Current IPM strategies for *C. Chalcites* rely on either chemical pesticides or biological control. Pesticides are extremely harmful to humans and the environment [18, 19], cause phytotoxic damage that reduces crop yield [20], and disrupt biological pest control methods [21]. Most importantly, their effectiveness is poor for controlling *C. Chalcites* (demonstrating less than 50% control) [22]. The financial burden of this inefficiency is significant; growers currently spend a conservatively estimated EUR 15,000 per hectare per year on pest control of moths (see Appendix C), yet will still face recurring infestations as moths quickly develop resistance due to their short lifecycles [1].

Biological control methods represent the other primary market segment, but leave a portion of the greenhouse market unserved. They are not economically viable for crops with short cycle times [21], and commercial natural predators of *C. Chalcites* fail to keep damage below economic injury levels [23, 24]. Emerging biological solutions, like the Baculovirus, remain commercially unavailable and only target the caterpillar stage [25]. Typically, biological control methods cost more than chemical methods, mainly because of the need of multiple applications and additional crop monitoring [26], and effficacy highly varies per plant type [23]. When these interventions fail, uncontrolled *C. Chalcites* populations cause direct aesthetic damage to crops, which can render up to 7% of a harvest unmarketable and represent a severe revenue loss [27].

[2] `https://english.ctgb.nl/about-ctgb` – Accessed: 27.05.2026

3.3. Market, Competition & Future outlook

The long-term commercial scalability relies on expanding its target pest portfolio and the growth of the high-tech agriculture market, forecasted at a CAGR of 16.1% over 2026–2034[3]. Because detection is done by the PATS-C cameras, adapting the drone for new pests primarily requires the detection algorithm to be updated rather than hardware redesigns. Two moth species are identified for possible market expansion:

- **European Pepper Moth:** A primary focus of the "Masterplan Rups" [25]. Though smaller and more hidden, expansion into this market is possible with an updated control algorithm.
- **Cabbage Looper:** Shares strong morphological similarities to *C. Chalcites*[4] and targets the same crops such as tomatoes[5], making it an ideal alternative pest to control.

While competitors such as Corvus Drones[6] operate micro-drones within greenhouse environments, their systems are strictly designed for crop monitoring, leaving PATS as the only specialised, active, mechanical moth control solution. Competition therefore comes only from chemical and biological methods, imposing a pricing ceiling of EUR 15,000/ha/year. Future EU pesticide reduction regulations[7] will act as a strong market catalyst [16]: the EU typically bans chemical methods when an alternative of similar efficacy is available (EU Regulation (EC) No 1107/2009, Article 50 [28]), which would eliminate pesticide competition entirely. The TAM spans the European high-tech greenhouse sector at 33,637 ha [29], representing EUR 504.6 million annually, while the SAM covers the Dutch Westland region (4,500 ha [30]), translating to EUR 67.5 million, as visualised in Figure 3.3.

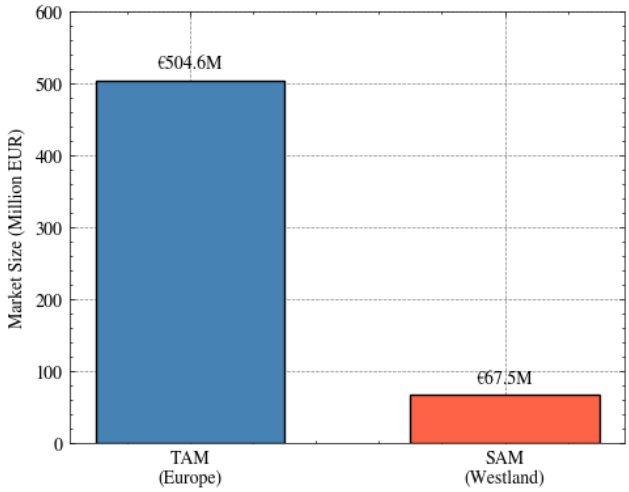

Figure 3.3: Total Addressable Market and Serviceable Addressable Market sizes

3.4. SWOT analysis & Market Share

A SWOT analysis from the business perspective is visualised in Figure 3.4. To realistically project the target market share, a bottom-up calculation is utilised (detailed in Appendix C). Assuming a production rate of 1,000 drones per year, no production growth to allow for market adaptation, and a conservative 10% total-loss hardware failure rate, the active fleet is projected to cover 410 hectares of the Westland market by year 5, capturing 9.11% of the serviceable area close to the PATS headquarters. To account for operational and manufacturing variance, a two-variable sensitivity analysis evaluating this Year 5 market penetration against varying production growth and hardware failure rates is provided in Appendix C.

[3] `https://www.intelmarketresearch.com/europe-smart-agriculture-market-market-45398` – Accessed: 27.05.2026

[4] `https://vlinderstichting.nl/vlinder/turkse-uil/` – Accessed: 30.04.2026

[5] `https://www.koppert.nl/plagen/rupsen/ni-uil/` – Accessed: 30.04.2026

[6] `https://www.corvusdrones.com/drone-voordelen-hulp-in-de-kas/` – Accessed: 27.05.2026

[7] `https://www.pan-europe.info/blog/eu-court-rulings-should-lead-better-regulation-pesticides` – Accessed: 27.05.2026

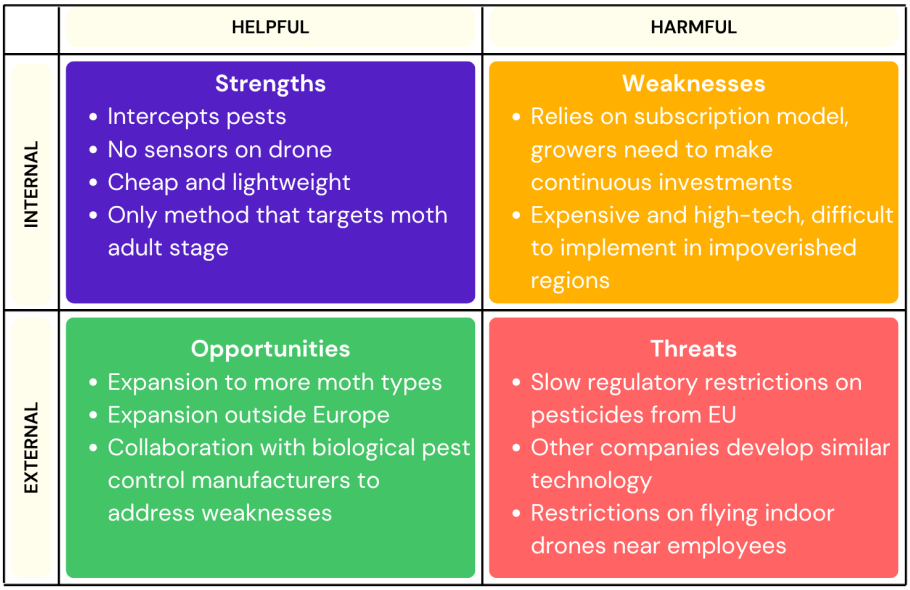

Figure 3.4: SWOT analysis for the market analysis

3.5. Target Price, Conclusion & Requirements

The baseline infrastructure, utilising the external PATS-C camera network, requires a one-time installation fee of EUR 500 alongside an annual software licensing cost of EUR 534 per hectare. To ensure an attractive price, the system will utilise a subscription model priced at EUR 10,000 per hectare, per year, excluding the PATS-C system fees. This fee covers an active fleet of 10 drones per hectare and includes all maintenance, repairs, and total-loss replacements. This is significantly cheaper than the EUR 15,000 pesticide costs per hectare, per year.

In conclusion, the persistent threat of *C. chalcites*, combined with failing chemical effectiveness and incoming EU regulations, creates a critical market gap. An autonomous, mechanical interception system not only provides better pest control but also presents an attractive business case for high-tech greenhouse growers. To maintain the profit margins of this EUR 10,000/ha subscription model, the drone's expenses must be strictly controlled. The commercial, operational, and safety constraints identified throughout this market analysis translate directly into hard engineering specifications. The requirements that were derived or validated from the market analysis are tabulated in Table 3.1.

Table 3.1: Validated Existing Requirements based on Market Analysis

Identifier	Requirement Description	Market Analysis Validation
SYS-27	The drone shall have a minimum of 1000 mission cycles.	High reliability is necessary to ensure profitability and minimize replacement costs.
SYS-28	Drone shall consist of modular parts.	Ensures fast, local maintenance by technicians.
SYS-29	The cost per drone shall be below 250 euros.	Essential to undercut pesticide costs while remaining profitable.
SYS-32	Drone shall be made fully of off-the-shelf or 3D-printed components.	Avoids high tooling costs, which aligns with manufacturing strategy.
SYS-34	The communication system shall interface with the existing external moth tracking system.	Validated by the architecture constraint to do computer tasks externally.
SYS-44 (New)	The drone system shall be priced at EUR 10,000/ha/year	For commercial viability and to provide a competitive alternative to chemical and biological IPM methods.

4

System Constraints and Review of Selected Concept

This chapter provides a brief description of the status of the design before the detailed design phase commenced. It shows a short recap of the trade-off conducted and presents the constraints which the final design has to meet together with the Functional Flow Diagram and Functional Breakdown Structure of the system.

4.1. Review of Concept

After a detailed trade-off between four options was conducted, a concept was chosen to be detailed further. It consists of a ducted fan which is tethered to a charging station and is dubbed *the Chameleon*. It can be better visualized in Figure 4.1 The mission profile followed by this design consists of three parts: first, *the Chameleon* spools up its propellers while docked to the charging station, then it uses its high T/W to intercept its target at a high speed, and finally it gets decelerated and reeled back in towards the charging station by the attached tether.

The Chameleon is controlled by four vanes at the exit of the duct's fuselage. These vanes are mounted on spokes and moved by micro-servos positioned in the centre of the fuselage. Thrust is generated by two counter-rotating propellers positioned as close to the entrance of the duct as possible. These are mounted on the top and bottom of a central hub, which is connected to the fuselage through eight circular hollow struts. The fuselage itself is hollow as well, and its top and bottom lips have a circular cross section. Four battery casings are positioned symmetrically around the roll axis on the outside of the fuselage. Four single-cell LiPo batteries slide into these casings from the bottom, which is then closed off by a removable lid. The drone is autonomously recharged via pogo-pin contacts located on the frame at the outlet of the duct.

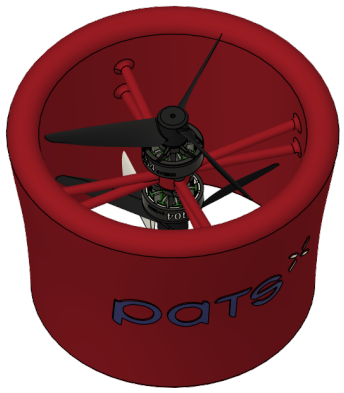

Figure 4.1: Preliminary Simplified Frame Design of *the Chameleon*.

4.2. User requirements

In Table 4.1, the user requirements are presented. These are the highest-level requirements on which the whole design process is built. From these user requirements, the system and later the sub-system requirements were derived.

Table 4.1: User Requirements

Identifier	User Requirement
DPAPC-USER-01	The drone shall intercept the pest without sustaining damage that results in a loss of flight capability or requires manual repair.
DPAPC-USER-02	The drone hardware shall integrate electronically and physically with the existing PATS docking and detection infrastructure.
DPAPC-USER-03	The drone shall be capable of executing a mission profile of 80 sorties per day.
DPAPC-USER-04	The drone shall have a maximum recharge time of 5 minutes between flights.
DPAPC-USER-05	The drone shall operate without the use of chemical pesticides.
DPAPC-USER-06	The drone shall have a weight smaller than 200 grams.
DPAPC-USER-07	The drone shall be able to withstand crashes of up to two meters high with a forward velocity of 5 m/s.
DPAPC-USER-08	The drone shall be able to decelerate at a minimum of $15.6\,\mathrm{m/s^2}$ to avoid collisions with walls.
DPAPC-USER-09	The drone shall be able to operate in a greenhouse environment with a relative humidity of 85%.
DPAPC-USER-10	The drone shall be able to operate in a greenhouse environment with a temperature range of 10–35°C.
DPAPC-USER-14	All components shall be either off the shelf or be able to be 3D-printed.
DPAPC-USER-15	The design must be scalable to a production rate of 1000 drones per year.
DPAPC-USER-16	The cost per drone shall be below 250 EUR, assuming a maximum of 10% allocated to assembly labour.
DPAPC-USER-17	Total development cost, including prototypes and field tests, shall be less than 100 000 EUR.

Requirements DPAPC-USER-11 & 12 were requirements with regard to the aeroacoustic capabilities of the drone. During the preliminary design phase, all requirements regarding aeroacoustics were identified as killer requirements and removed in correspondence with the client. The system requirements are listed in Chapter 17, where the compliance of the design with the requirements is evaluated. The subsystem requirements, which were derived from the system requirements and will be the constraints of each subsystem's design, are presented at the beginning of each chapter presenting the tools used to design the respective subsystem.

4.3. Functional Flow Diagram

In Figure 4.2, the Functional Flow Diagram of *the Chameleon* is presented. It includes all functions to be performed during its lifetime from manufacturing until End of Life. The diagram is structured with the highest-level diagram showing the entire lifecycle of the drone in the top-left corner. Afterwards, each of the functions F1, F2, F3 and F4 are presented in more detail. Finally, because it shows the entire operation process, each sub-function of F2 also has many sub-sub-functions. For this reason, each sub-function of F2 is also included in a separate window.

4.4. Functional Breakdown Structure

In Figure 4.3 the functional breakdown structure is presented. For compactness, the sub-sub-functions are presented as bullet points. The function F5: Global Functionality is present in the Figure 4.3 but not in the Figure 4.2. This is due to the fact that it includes general functions which have to be performed mostly in parallel with the rest of the functions throughout the lifetime of the drone. In addition, each function has one or more subsystems assigned, which are responsible for its successful completion.

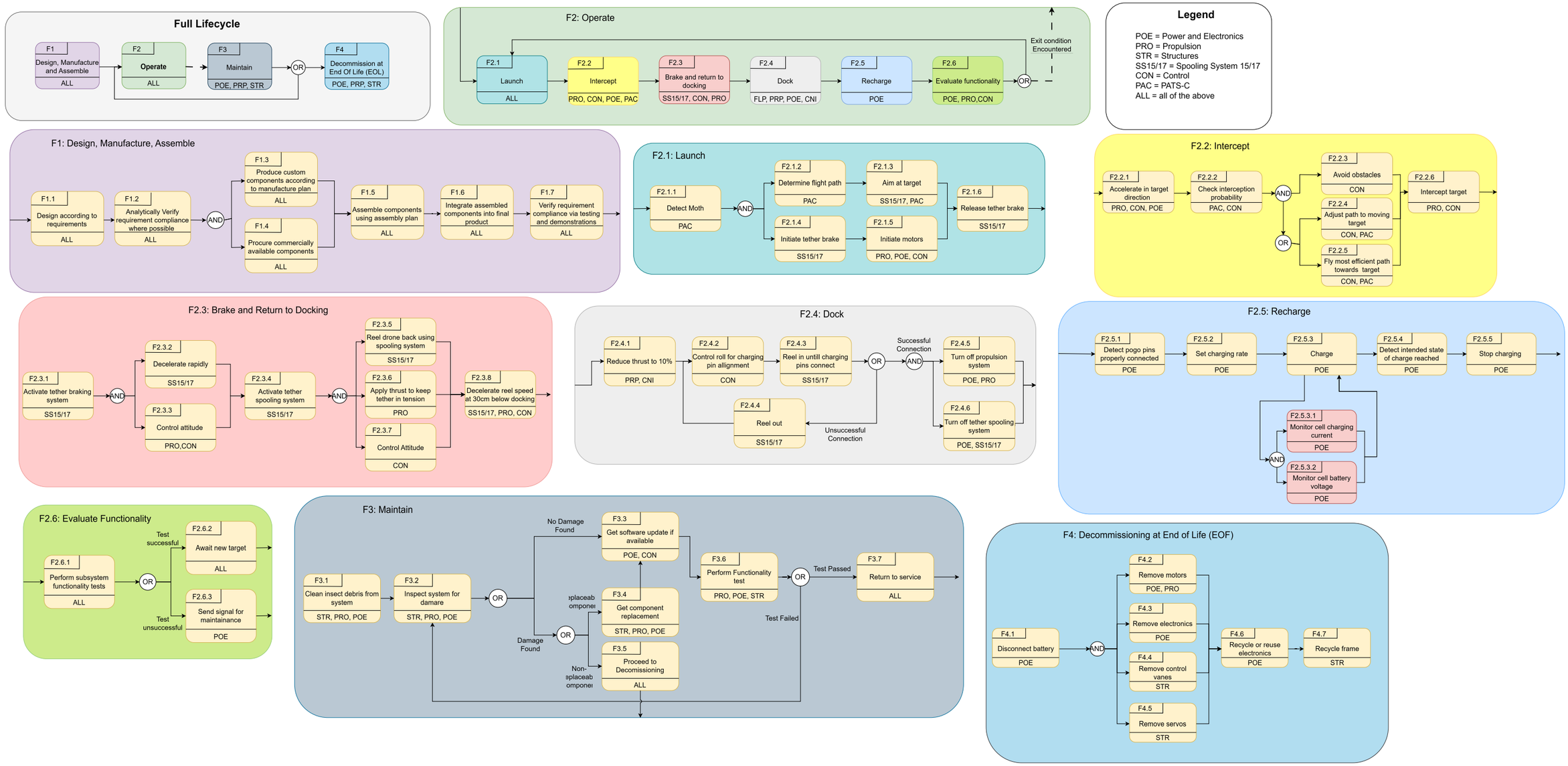

Figure 4.2: Functional Flow Diagram

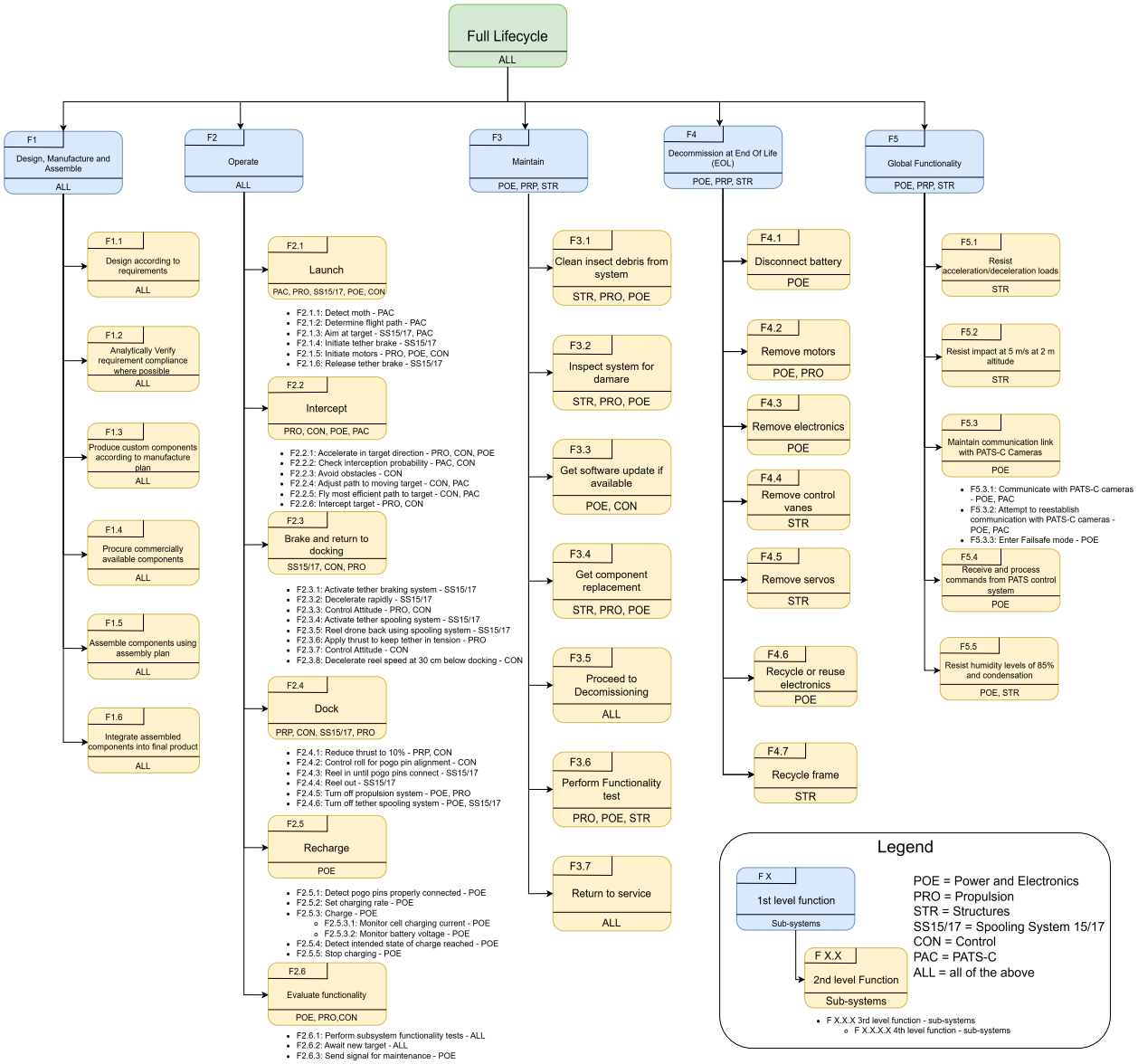

Figure 4.3: Functional Breakdown Structure

5
Concurrent Engineering Framework

The detailed design of *the Chameleon* necessitates a structured, concurrent systems engineering approach. Due to the highly interdependent nature of the subsystems, the unconventional layout (see Chapter 8), and the lack of an existing control algorithm (see Chapter 10), a traditional sequential design process is inadequate. To achieve a feasible, manufacturable platform, the design process utilises a concurrent framework comprising four primary iteration loops.

This framework groups the interrelated subsystems and captures engineering snowball effects. The process begins with initial constraints and cascades through sizing, stability, and final mission performance. System integration was maintained through daily reviews, ensuring any mass or aerodynamic penalties were immediately propagated through the loops. The high-level framework is visualized in Figure 5.1. The detailed explanation for all of these loops is presented in Section 5.1

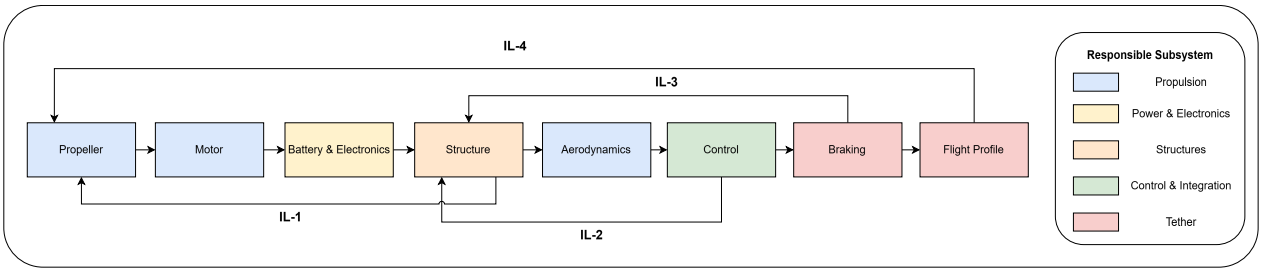

Figure 5.1: Overview of the primary iteration loops within the Concurrent Engineering Framework. IL-4 is the overall iteration loop, where a full design is optimised.

5.1. System Sizing & Iteration Loops

The design methodology is governed by the following four overarching iteration loops:

IL-1: Powertrain & Structure

This primary sizing loop balances propulsion capabilities against the structural mass penalty. The sequence begins with the propeller, initially sized at 75 mm diameter (To adhere to Class 1 and Class 2 propeller sizes, as defined in the Baseline report: Class 1 has 90 mm propellers, Class 2 has 75 mm). Subsequently, the motor and battery are selected to sustain the required aerodynamic torque and electrical current without severe voltage sag. Finally, the structural frame is sized to house these components.

- Trigger: If the total integrated mass results in a Thrust-to-Weight (T/W) ratio below the required threshold, the loop restarts. A larger propeller or motor must be selected, which inherently increases mass. This triggers the weight snowball effect. This snowball effect is reduced by taking a conservative initial weight estimate (160 g).

IL-2: Aerodynamics & Control

With the baseline structure established, the external aerodynamic surfaces and control vanes are sized. Because the specific geometry of *the Chameleon* is difficult to control (see Chapter 10), this loop is critical to

ensure the control surfaces have sufficient authority to stabilise the drone.

- Internal Trigger: If the platform is uncontrollable, the aerodynamic shape, vane placement, or vane size must be altered.
- Cascade Trigger: If achieving control authority requires structural additions that violate the T/W requirement, it triggers a return to IL-1 to resize the powertrain.

IL-3: Braking Dynamics

This loop evaluates the dynamic loading during operation. The platform is simulated undergoing severe deceleration g-forces during a tether braking manoeuvre. This loop is required to evaluate whether the drone structure can withstand the experienced g-forces.

- Internal Trigger: If the simulated g-forces exceed the material limits at the tether attachment nodes, the structural frame must be reinforced.
- Cascade Trigger: If this reinforcement significantly increases the total inertia and mass, it cascades back to IL-1.

IL-4: Global Mission

The final system-level loop ensures that the converged design from IL-1 through IL-3 can successfully execute the operational mission.

- Trigger: The full mission is simulated. If the battery capacity is not sufficient or other problems arise, a global iteration is required. In addition, when all requirements are met, this loop can be utilised to optimise the design.

5.2. Methods & Software Integration

The computational methods and specific software tools employed to execute the iterations and verify convergence are detailed in Table 5.1. In this table, the purpose and

Table 5.1: System Sizing and Optimisation Operation Loops

Loop	Purpose & Convergence Criteria	Methods & Software
IL-1: Sizing & Structure	To ensure the powertrain can provide the required thrust within mass limits. Converges when the T/W ratio requirement is met.	Propeller-Motor Matching (Python) Battery Simulation (Python) CROTOR QPROP CAD (Fusion)
IL-2: Aero & Control	To iterate vane placement and size for sufficient authority. Converges when the LQR-I controller can reliably stabilize the drone.	CFD (OpenVSP) LQR-I Controller (MatLAB) CAD (Fusion)
IL-3: Braking Dynamics	To ensure structural integrity during braking. Converges when the structure withstands simulated maximum deceleration g-loads.	Multibody Dynamics (MuJoCo) FEM (Fusion) 3D Print Prep (Bambu Studio)
IL-4: Full Mission	To verify operational capability. Converges when all previous loops converge, and the batteries sustain the mission profile.	Battery Simulation (Python) Multibody Dynamics (MuJoCo)

6
Propeller and Motor Selection

This chapter outlines the design process of the Propulsion Subsystem and details the requirements, simulation tools, and resulting performance parameters that interface with the Battery & Electronics and Aerodynamics subsystems. The verification and validation of this final propeller and motor selection can be found in Appendix A.

6.1. Core Subsystem Requirements

These requirements represent the core design constraints imposed on the Propulsion Subsystem.

- SYS-16-PRO-01: The propulsion system shall achieve a net T/W ≥ 5
- SYS-22-PRO-01: Each motor mass shall not exceed 10 g
- SYS-29-PRO-01: The total cost of the propulsion components shall remain within the allocated propulsion cost budget of EUR 20
- PRO-01: The propulsion system shall be ducted
- PRO-02: The propulsion system shall employ counter-rotating rotors
- PRO-04: Both counter-rotating rotors shall operate at matched RPM at all times

Due to *the Chameleon*'s mission profile, the drone is optimised for a single intercept attempt per mission. Assuming near-instant braking and inherently low agility, the time to intercept is to be minimised, and the area of interception maximised. Thus, the rotor geometries are optimised for size and static thrust within the mass and power budget. Static thrust is designed for maximum initial acceleration.

6.2. Tools and Motivation

To achieve the optimised rotor geometries, CROTOR in combination with QPROP has been used within a custom Python script. CROTOR is used to iterate different rotor geometry configurations over a grid of design points. Subsequently, the outputs are matched against a FPV drone motor database using QPROP to find an ideal combination. The Python script operates the tools and translates them into visualised results. The tools are elaborated upon below, and Section 6.3 discusses the simulation structure, procedure and outcomes in detail. If the physics behind the tools is not of interest, continue to Section 6.3.

CROTOR

CROTOR is an extension of XROTOR developed by M. Drela[1]. The tool is verified by peers using high-fidelity CFD tools and validated using wind tunnel test data. Bergmann et al. determine a 3%-6% relative error against static thrust results[31]. This is relevant, since the propeller is optimised for static thrust. XROTOR is an interactive propeller design program. It can be used to analyse ducted and free-tip propellers and windmills. The program optimises propeller design to minimise induced velocity losses. It includes two different evaluation methods: Graded Momentum Formulation and Potential Formulation. Both methods treat the rotor blades as lifting lines, and both assume that disk loading is relatively low and hence the wake contrac-

[1] https://web.mit.edu/drela/Public/web/xrotor/

tion and the wake self-deformation are small. The software makes use of the Potential Formulation method. It is an extension of Goldstein's 2 and 4-blade solutions to all blade numbers and arbitrary radial load. In 'On the Vortex Theory of Screw Propellers', Goldstein solves the helicoidal vortex wake of a lightly loaded propeller with finite blades. He replaces the vortex sheet with a rigid helicoidal surface and solves the resulting Laplace equation to formulate the Goldstein Circulation Function. The output of this is a radially varying factor that gives the optimal loading for minimum induced loss with a specific number of blades [32]. CROTOR is an extension of XROTOR specifically developed for counter-rotating propellers. XROTOR analyses an isolated propeller at certain flight conditions. CROTOR automatically determines the slipstreams generated by the forward rotor and loads them onto the aft rotor. It analyses the forward and aft rotor alternately, updating the slipstream each iteration. The iteration stops when the thrust of both rotors converges, yielding the converged dual-rotor system.

QPROP

QPROP uses a specified propeller geometry to evaluate the performance of a propeller/motor combination. It takes the KV (RPM per volt), Internal resistance and the no-load current of the motor to calculate the performance in combination with the propeller across a range of operating conditions. It uses the classical blade element/vortex formulation developed by Betz [33], Goldstein [32], Theodorsen [34], and Larrabee [35][36]. QPROP calculates the thrust, torque, power and overall efficiency over a range of airspeeds and RPM's [36]. Figure 6.1 shows the equivalent circuit for a DC electric motor used by QPROP.

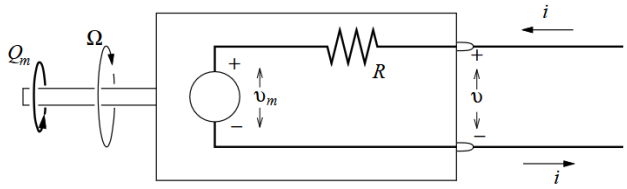

Figure 6.1: Equivalent circuit for a DC electric motor used by QPROP [36].

One limitation of the simple electric motor model used by QPROP is that it fails to account for throttle settings. To account for the risks of battery voltage sag and degradation, capped throttle configurations are also considered. While not natively supported by QPROP, the effective throttled voltage V_{in} can be ideally modelled as follows [37]:

$$V_{\text{in}} = V_{\text{max}}\delta_t \tag{6.1}$$

where the throttle $0<\delta_t\leq 1$.

6.3. Simulations

The goal of the simulation is to find operating parameters and system characteristics regarding the propulsion system that are needed in other subsystems for iteration. The input and output parameters are listed in Table 6.1 and Table 6.2, respectively. A rotor/motor combination should be designed for a specific operating condition, yielding its optimal RPM and the associated power requirement. In the specific counter-rotating configuration, another dimension is added. The aft rotor experiences swirled airflow due to it operating in the forward rotor's wake. The rotors are operating in the low advance ratio regime (high RPM), meaning that the swirled flow velocity is mostly tangential and the aft rotor experiences a significant increase in angle of attack. This can cause the aft rotor to stall and prevent the counter-rotating system from converging. To avoid this, the aft rotor requires less aggressive pitch. The simulation finds a converged configuration for each design point, matches it with a motor, and maps the results.

Table 6.1: Input parameters

Name	Symbol	Unit
Flight Condition Parameters		
Flight velocity	V	m/s
Ducted	-	-
Propeller Parameters		
Chord distribution	c/R	-
Twist distribution	β^0	$^\circ$
Radius	R	m
Motor Parameters		
Max power	P_{max}	W
Motor efficiencies	η^*	%
Max rotations per minute	Ω_{max}	RPM

Table 6.2: Output parameters

Name	Symbol	Unit
Propeller Parameters		
System thrust	T	N
Thrust coefficient	c_T	-
Power coefficient	c_P	-
Torque	T_p	Nm
Pitch offset	β	$^\circ$
Motor Parameters		
Operating power	P	W
Motor efficiency	η	%
Rotations per minute	Ω	RPM

Simulation Architecture

Due to its similar nature, the simulation takes a commercially available ducted cinewhoop propeller[2] as a starting point, adopting its hub and tip radius, and chord and twist distribution. It loads the rotor as both the forward and aft rotors in CROTOR, realising the counter-rotating configuration required by PRO-02, and adds a straight duct ($\frac{A_{inlet}}{A_{exit}} = 1$) in accordance with PRO-01. Using the 'INPU' command, the flight velocity is set to 0.001 m/s to approximate static thrust conditions and thereby determine the maximum achievable initial acceleration. Subsequently, using the same command, the counter-rotating system is operated over the RPM–power grid shown below.

$$\mathbf{G} = \begin{array}{c|cccc} \Omega \setminus P & 200\,\text{W} & 207\,\text{W} & \cdots & 400\,\text{W} \\ \hline 25{,}000\,\text{RPM} & \bullet & \bullet & \cdots & \bullet \\ 26{,}207\,\text{RPM} & \bullet & \bullet & \cdots & \bullet \\ \vdots & \vdots & \vdots & \ddots & \vdots \\ 60{,}000\,\text{RPM} & \bullet & \bullet & \cdots & \bullet \end{array}$$

Where each • represents one evaluated design point, with uniform step sizes:

$$\Delta\Omega = \frac{35{,}000}{29} \approx 1{,}207\ \text{RPM}, \qquad \Delta P = \frac{200}{29} \approx 6.9\ \text{W}$$

giving a total of $30 \times 30 = 900$ design points. If a configuration initially doesn't converge due to stalling of the aft prop, the simulation triggers the 'AUTO' command to sweep the aft rotor pitch till the system converges. Once a configuration is converged, it triggers the 'FIX' command to fix the system geometry and run it over a range of RPM and plots the associated thrust and power against it, to display the configuration's performance. After the performance of each configuration is plotted, the simulation evaluates each resulting performance profile against the FPV drone motor database and records the motor match that achieves optimal thrust-to-weight within the power budget. Subsequently, it generates a heat map that represents the maximum achievable thrust for a specified throttle setting. Then, the configuration performance is further analysed over the entire operating range.

Simulation Assumptions

For the CROTOR and QPROP simulations, the following assuptions are made:

- The flow is assumed to have only axial and tangential velocity components, implying zero flow in the

[2] `https://droneshop.nl/hqprop-t76mmx3-v2-propellers-cinewhoop` – Accessed: 16.06.2026

radial direction.

- Compressibility correction is done via the Prandtl-Glauert factor[38]. Assuming the rotor speeds do not exceed Mach 0.7, this approximation is valid.
- The flow is assumed to be steady and uniform. This causes the simulation to be unable to capture transient effects.
- The 2D airfoil characteristics of the blades are uniform and determined from the default XROTOR settings to ensure convergence[3]. This is an optimistic profile to ensure convergence and stability of the XROTOR simulation. While information on exact FPV propeller airfoils is proprietary, low Reynolds number airfoils operate in highly non-linear regimes where laminar separation bubbles significantly affect performance.
- Both rotors are assumed to have perfect RPM matching at all times during operation (PRO-04). This ensures the induced torque from the rotors is approximately cancelled out and the drone does not spin during operation.
- The wake between the rotors is assumed to be rigid, meaning that the flow is identical after the forward rotor and before the aft rotor. Realistically, wakes will deform downstream, causing inflow angles to change at the aft rotor[38].
- The rotors are assumed to have zero tip clearance with the duct. This ensures the tip losses are zero and the duct is augmenting the thrust optimally. Practically, manufacturing limits and crash resistance requirements necessitate a clearance, causing flow leakage and inducing tip vortices[39].
- Only the motor resistance contributes to the total resistance of the circuit and is constant. This implies thermal resistance is neglected. Given operating temperatures reaching upwards of 80 degrees Celsius during demanding manoeuvres and assuming copper wire with a heating resistivity coefficient of 0.393% per degrees Celsius, the resistance can increase by 31.4%.
- The mass of the complete system excluding motors is assumed to be 130 gram. This value follows approximately from the preliminary mass budget.
- The mass of the individual motors is at most 10 gram (SYS-22-PRO-01). Heavier configurations are assumed to result in structural failure of the motor mounting structure.

Simulation Results

The RPM-power grid heatmap is shown in Figure 6.2 with the gradient representing the maximum achievable thrust-to-weight for each design point and blank points representing unconverged designs. The optimal design is marked by the red box. This point corresponds to a design RPM and power of 40419 and 267 W, resulting in an estimated thrust-to-weight of 5.4 at static conditions, thereby satisfying SYS-16-PRO-01. It should be noted, however, that the model assumptions could lead to the actual thrust-to-weight being lower than predicted. As such, higher fidelity models and experimental data are needed to get a more accurate metric. The propeller is matched to a 4500 KV, 0.1385 Ohm, 8.7 gram motor[4], which lies within the 10 g limit of SYS-22-PRO-01. Notably, the optimal design is a throttle-limited one, namely at 68.9% duty cycle before the electrical power curve exceeds the predefined budget.

The performance of the propeller and motor selection over the full operating range is shown in Figure 6.3. Regions of infeasibility are denoted by dashed faded lines. Though the results show minor numerical noise, the model is able to capture the trends well. From the thrust curves (Figure 6.3a) it can be seen that the highest thrust is achieved at static conditions, before shifting down for higher flight speeds. In total, the thrust varies between 6-8 N over the entire flight profile. A similar shift happens for the power curves (Figure 6.3c), which allows for a higher maximum throttle setting (69-75% from highest to lowest flight speeds) within the electrical power limit, indicated by the horizontal red dashed line. This effect can also be seen in the

[3] `https://web.mit.edu/drela/Public/web/xrotor/xrotor_doc.txt` - Accessed: 17-06-2026

[4] `https://www.drone-fpv-racer.com/en/c145-4500kv-motor-by-axisflying-10466.html` - Accessed: 17.06.2026

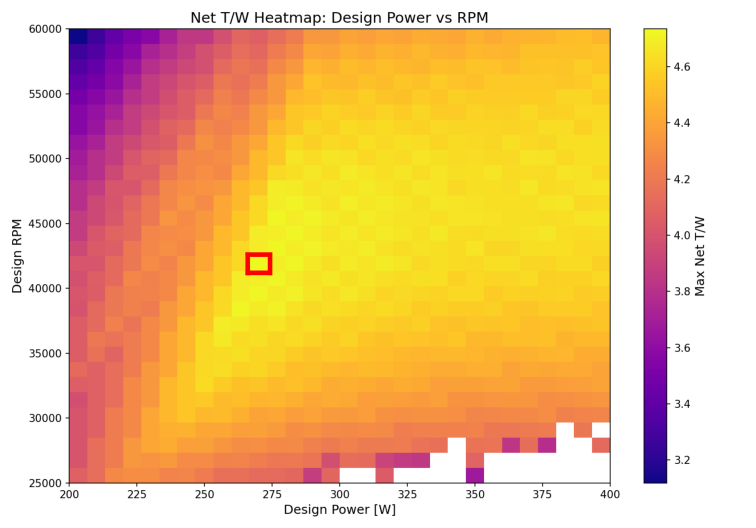

Figure 6.2: RPM-power grid heatmap with the maximum achievable thrust-to-weight as gradient. Blank points correspond to design points that failed to converge. The optimal design is marked in red.

system efficiency curves (Figure 6.3d), where higher flight speeds correspond to generally higher efficiencies. The efficiency curves themselves additionally reflect the effect of propeller efficiency approaching zero and dictating the total efficiency at low advance ratios.

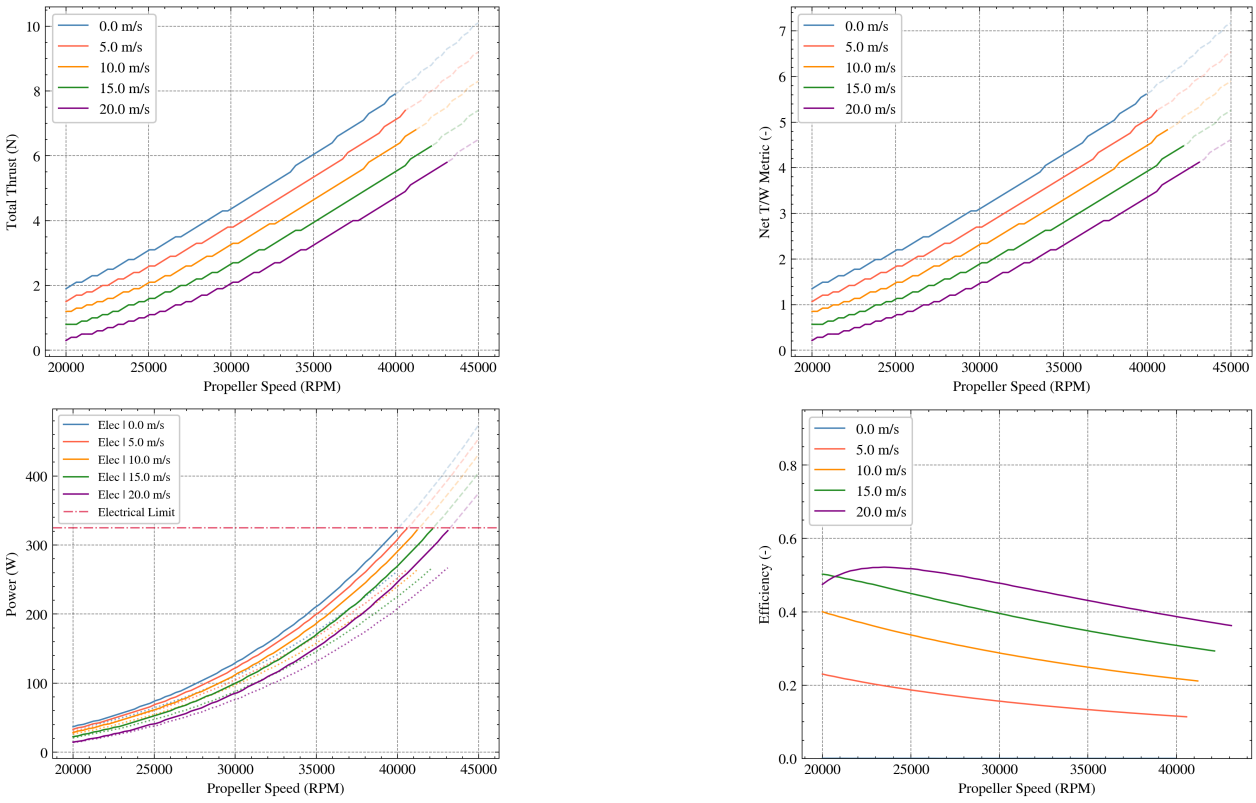

(c) System Power Matrix

(d) Combined System Efficiency

Figure 6.3: 2D performance sweep results as a function of propeller speed (RPM) across discrete flight velocities. Dashed faded lines indicate unfeasible regions violating the predefined power budget.

The pitch distributions of the forward and aft rotors of the optimal design are shown in Figure 6.4a and Figure 6.4b, alongside the velocity vector inflow angles over a range of advance ratios. The difference between

these two angles denotes the effective angle of attack distribution, additionally displayed in Figure 6.4c and Figure 6.4d. Here, the stall limit of the assumed 2D airfoil is also denoted by a horizontal red dashed line at 17 degrees. The optimizer finds the optimal distribution at a higher pitch offset from the baseline for the forward rotor (+3.55 degrees) than for the aft rotor (+2.48 degrees). This is a direct consequence of the inflow angles, which are generally higher for the forward rotor than for the aft rotor. The advance ratio dictates a great part of the inflow angle close to the hub, where tangential velocity is lower than closer to the tip. This discrepancy causes the hub to stall prematurely, first at the aft rotor at an advance ratio J of 0.0637 (Figure 6.4d), followed by the front rotor at a J of 0.0955 (Figure 6.4c). While suboptimal, it is to be noted that the range of inflow angle at the hub for different J has a variance great enough (33 and 20 degrees for front and aft rotors respectively) such that parts of the operating range will always operate suboptimally for a fixed pitch rotor. Given that the propulsion system is optimised for static thrust, the design ensures that during the launch sequence the blades are operating as close to their maximum thrust as possible.

The selected propeller–motor configuration satisfies all subsystem requirements specified in Section 6.1, except requirement SYS-29-PRO-01. The propeller requires a custom design, which results in an overran budget. Given the critical role of the propulsion system in overall system performance, this overrun is considered acceptable. A full breakdown of the unit costs and budget margins is outlined in Chapter 16. If, in a later stage, this proves unacceptable, iteration is required.

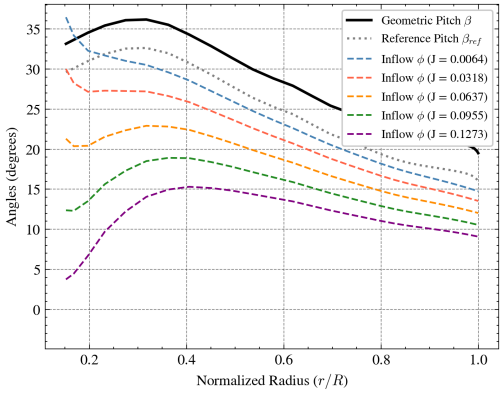

(a) Forward rotor: pitch (black), reference pitch (grey) and inflow angle (colored)

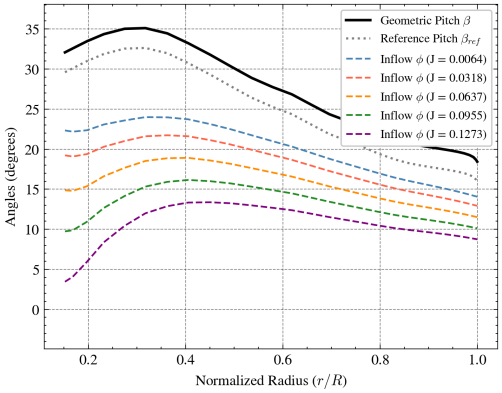

(b) Aft rotor: pitch (black), reference pitch (grey) and inflow angle (colored)

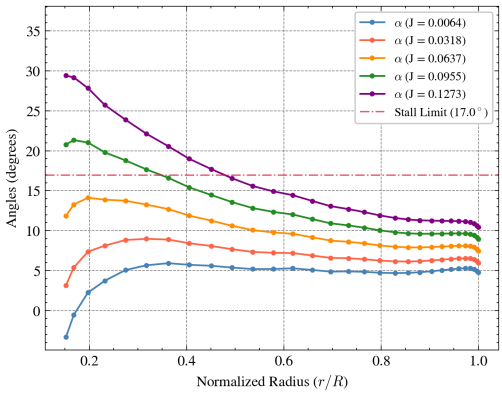

(c) Forward rotor: operating α with stall limit of 17 degrees (horizontal red dashed line)

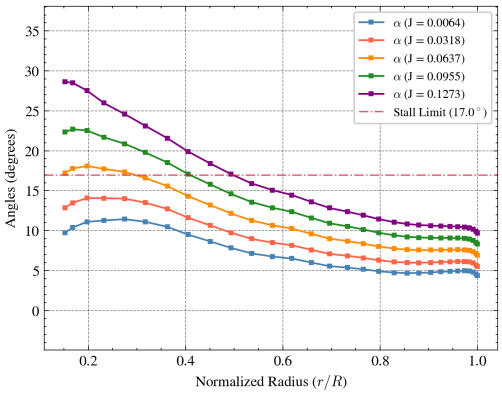

(d) Aft rotor: operating α with stall limit of 17 degrees (horizontal red dashed line)

Figure 6.4: Pitch (black) and inflow angles (colored) across normalized radius (r/R) for the counter-rotating rotor assembly (a and b). The inflow angle contour is determined over a sweep of advance ratios. The angle of attack distribution is shown over this sweep with the stall limit denoted by a horizontal red dashed line at 17 degrees (c and d).

7
Power and Electronics

This chapter presents the design process of the Power and Electronics subsystem. It is divided into two main parts: the selection of the battery and the identification of the required electrical components. The tools used and the simulations performed for the battery selection are also described. Their verification and validation can be found in Appendix A.

7.1. Core Subsystem Requirements

The requirements below represent the design constraints imposed on the Power and Electronics Subsystem and are traceable to higher-level system requirements and allocated engineering budgets.

- SYS-03-POE-01: The battery shall be able to withstand deceleration loads of 40 g
- SYS-07-POE-01: After a flight, the battery shall be recharged to its pre-flight level in $\leq$ 5 min
- SYS-22-POE-01: The electronic components excluding motors and servos shall weigh $\leq$ 15 g
- SYS-22-POE-02: The battery shall weigh $\leq$ 37 g
- SYS-24-POE-01: The battery and electronics shall operate nominally in temperature range of 10-35 °C
- SYS-28-POE-01: The battery shall be replaceable.
- SYS-32-POE-01: The battery and all electrical components shall be commercially off-the-shelf available.

In addition, the following requirement was received from other departments:

- TET-POW-01: The battery shall be able to sustain a flight of 0.5s at peak power and 1.5s at average power

Those requirements give the constraints of the subsystem. In addition, the Power and Electronics Department works closely with the Propulsion Department to ensure that the power which the batteries deliver is sufficient. The Power and Electronics department attempts to find a solution which delivers sufficient power while also adhering to the subsystem requirements derived above. If this is not possible, iteration loop 1 (IL-1) is then triggered as described in Section 5.1 such that a working solution can be found. In addition to satisfying the requirements listed above, possible batteries are assessed based on their expected operational lifetime. Since battery replacement contributes to both operating cost and environmental impact, the expected cycle life is used as a secondary selection criterion (SDP-3, (SDP-4). The Power and Electronics department then gives as an output the weight and size of the battery as well as the weight of the electrical components.

7.2. Tools and Motivation

The design of the power and electrical subsystem encompasses two distinctive processes. The first one is the selection of all electrical components needed for the drone to fly and recharge, and determining the connections between them. The second is the selection of the battery, which should provide sufficient electrical power during flight.

Electrical Components

Regarding the electrical components, a few things should be noted. Generally, all components have to be commercial off-the-shelf (SDP-1). This means that if a certain component is deemed necessary, but it is not found to be available, it cannot be used and a workaround has to be found. It is assumed that if needed, a custom Printed Circuit Board (PCB) can be designed by PATS, provided the required additional components on it are listed, and it is found through research that integrating them in a PCB is viable. While simulations are not performed for general electrical component selection, the process is strictly driven by specific subsystem requirements and analytical verification derived from literature and market research.

Battery Selection

Regarding the battery selection, the chosen design approach is different. A simulation is made to model the battery during flight. The simulation can be used in two general ways. Firstly, through iteration, the exact optimal properties (Capacity, Discharge Rate, etc.) of the battery that enable it to sustain the required flight can be found. The alternative is to choose an existing battery, input its parameters into the simulation and see if and how well it fits with the requirements. At the current stage of the design, some general characteristics of the battery are already known (weight budget, required voltage for motors, etc.). This means that, since the battery has to be an existing off-the-shelf one, the possible options are already narrowed down to just a handful. Consequently, if the simulation outputs a theoretically optimal parameter, such as the exact capacity required to complete the mission, finding a commercial battery that matches this value while satisfying all other predefined constraints is highly improbable due to the discrete nature of market availability. For these reasons, it was determined that the better approach would be to build the simulation such that existing batteries' specifications can be input, and afterwards the flight is simulated, and the battery performance is analysed.

7.3. Simulations

While numerous tools to simulate Lithium-ion (Li-ion) batteries are available ([40], Pybamm Library, etc.), no existing tools to simulate Lithium-Polymer (LiPo) batteries were found. Additionally, all Li-ion simulators found were focused on simulating the electrochemical reactions inside cells using sophisticated models, like the Doyle-Fuller-Newman (DFN) model, which comprises several tightly coupled non-linear PDEs [41]. As a result, for correct simulations, there are more than 50 electrochemical cell parameters that need to be input. While datasets with those parameters exist for Li-ion cells, no such ones for a LiPo cell were found. It was determined that it would not be feasible within the time constraints to try to determine these values for a LiPo cell. Thus, it was concluded that the more beneficial approach would be to create a simulation in Python based on real LiPo battery experiments, rather than utilise one of these tools.

Simulation Construction

The goal of the simulation is to simulate the work of the battery during flight. Firstly, this involves taking into account numerous details about the battery itself:

- Open Circuit Voltage (V_{ocv}) of the battery decreases with the State of Charge (SOC)
- Internal Resistance of the battery changes both with battery degradation and with SOC
- Capacity of the battery decreases with battery degradation

To simulate these using physical formulas, a cell would need to be simulated down to the nanoscopic or even atomic level. A workaround is to use data from a LiPo battery experiment, train regression models on the data and use them as a way to approximate the working of the LiPo battery. An extensive dataset with results from experiments performed on five LiPo batteries was utilised [42]. While not perfectly accurate, this would be a sufficiently precise way to take these factors into account, since the experiments are performed on batteries that have the same chemistry (LiPo). This was concluded by observing the differences in the data between the 5 batteries tested. For example, the V_{ocv} and the Ohmic Resistance for a given SOC varied by less than 0.5% across the five batteries. The following models were fitted:

- A fourth-order polynomial regression used to create a model for $V_{ocv}(SOC)$. The order was selected

by training on data from one battery and using the data from the other ones as a validation set and minimising the RMSE. The final model was trained on the dataset that minimised the total RMSE over the four remaining sets.

- A linear regression used to create a model for the fractional increase in internal resistance with a decrease in SOC. The data was observed to be nearly linear, hence, a simple linear model was selected.
- A linear regression used to estimate the growth factor in internal resistance with battery cycle degradation.
- An exponential decay model used to simulate battery capacity degradation over cycling, which is subsequently integrated in a Monte Carlo simulation to take into account the big variances in cell degradation.

It should be noted that battery degradation is virtually random across cells [43]. While driven by physics fundamentally, in practice, uncontrollable cell imperfections make it essentially random on the consumer level. It was seen that the five batteries which were tested under the exact same conditions survived a completely different number of cycles, ranging from 200 to 500. To capture this, capacity degradation was modelled using a Monte Carlo simulation, which will be discussed in further detail.

These empirical models were subsequently integrated with governing physical equations to construct a comprehensive simulation framework detailed in the following section.

Simulation Assumptions

Numerous assumptions have been made in order to create the model. Most assumptions are made out of necessity, due to a lack of data and inability to fully correctly determine and calculate. All assumptions are listed below:

- Motors are assumed to consume 95% of the total power during maximum-power manoeuvres and 80% during average flight conditions. This assumption is based on an analysis of the power requirements of all non-propulsive subsystems, which account for approximately 4% and 11% of total power consumption, respectively.
- Effective internal resistance per cell R_i = 12 mΩ. The effective internal resistance encompasses all factors which lead to voltage sag when using a battery. So $IR_i = V_{polarization} + V_{activation} + V_{ohmic}$. The Python library Pybamm (which has been verified to correctly solve and utilise the DFN model [44]), a library specifically used to simulate electrochemical reactions inside cells [45], was used to simulate a Li-ion cell operating under the same conditions using the Chen2020 Li-ion parameter set [46]. The simulation gave a maximum R_i of 12 mΩ. Since Li-ion cells generally have a higher effective resistance than LiPo cells [42, 47], it was determined that setting $R_i = 12\text{m}\Omega$ would be an acceptable and safe assumption.
- Charging is assumed to happen at a rate of 2C. This is the current rate PATS charges its batteries at.
- R_i is assumed to be constant with temperature. Although R_i varies with temperature, literature indicates that within the expected operating temperature range of 10-35 C$^\circ$ the variation remains below approximately 20% [48]. The resulting effect on mission performance is considered small relative to other modelling uncertainties and is therefore neglected.
- The effect on degradation due to high discharge rates is not explicitly modelled. Even though those high rates are only reached for up to 3 seconds, there is still a possibility that the battery will degrade faster for the same cycle count compared to a battery which is operated at low discharge rates. To take it into account, each cycle the battery performs is counted as 3 equivalent cycles, thus making the battery age faster. The accuracy of this assumption is unknown, and no corresponding literature was found for LiPo cells. The assumption was thus made in order to take this into account in some way, however, for more accuracy, tests will need to be performed.
- Average power required outside of maximum-power manoeuvres is assumed to be $P_{\text{avg}} = 0.4P_{\text{max}}$.

This assumption is based on reported power consumption data for drone systems [1]. Since the battery sizing is governed primarily by peak power requirements, this assumption has a negligible influence on the overall system design and results.

- V_{ocv} is assumed to be constant with battery state of health. While V_{ocv} does vary significantly with state of charge, it was observed from LiPo experimental data [42] that it shows no significant dependence on state of health over the range considered in this study.
- All cells in the 4-cell pack are assumed to remain perfectly balanced at all times, with identical SOC, voltage, and internal resistance. Whilst this is not completely correct in practice, it was not possible to construct a simulation for a 4-cell battery in the given timeframe without making this assumption.
- Electrical dynamics of the battery are neglected, and the battery is assumed to respond instantaneously to current demand.
- Monte Carlo uncertainty is limited to uncertainty in the degradation exponent parameter due to lack of available statistical data.
- Losses in voltage and power that occur between the battery and motors due to wire losses and ESC efficiency are considered to be 5%. This is a typical value for ESC efficiency [49]. Regarding wire losses, typical values for the resistivity of copper wires are around 9Ω per km. The wires connecting the battery and the ESC are expected to be less than 10 cm, which leads to a maximal resistance of 0.9 mΩ, which can be neglected.
- The battery is assumed to be able to perform as specified in its listing specifications. For example if the battery is advertised as a 50C battery, it is assumed that it, can discharge at up to 50C.

Simulation Architecture

Inputs

The simulation models the electrical behaviour of the battery pack over a sequence of charge-discharge cycles, using the empirical models described above with a physically consistent battery representation. The inputs required to run the simulation and their values according to the assumptions made stated above are shown in Table 7.1. The outputs of the simulation, while directly showing battery performance, indirectly and more importantly result in the weight and size of the battery, those are shown in Table 7.2

Table 7.1: Battery input parameters

Name	Symbol	Unit
Mission and Power Profile Parameters		
Average motor electrical power demand	P_{avg}	W
Peak motor electrical power demand	P_{max}	W
Total target flight duration	t_{flight}	s
Duration spent at peak power	$t_{\text{p\_max}}$	s
Peak power onset time	$t_{\text{t\_p\_max\_frac}}$	-
Battery Parameters		
Number of cells in series	N_{cells}	-
Nominal pack capacity	Q_{nominal}	Ah
Maximum peak discharge rate	-	C
Initial State of Charge	$\text{SOC}_{\text{initial}}$	-
Standard battery recharging rate	-	C

Table 7.2: Battery output parameters

Name	Symbol	Unit
Battery Design Outputs		
Battery mass	m_{batt}	kg
Battery size	$-$	m x m x m
Recharge time after mission	t_{recharge}	s
Time-Dependent Profiles (Graphs)		
Voltage profile	$V(t)$	V
Current profile	$I(t)$	A
C-rate profile	C-rate(t)	C
State of Charge profile	SOC(t)	-

[1] `https://www.batterydesign.net/drone-power-and-energy-estimation/`. Accessed: 06.06.2026

Logic

The developed model simulates both the instantaneous performance of the battery during a flight and the gradual degradation of the battery over its operational lifetime. Once the parameters stated above are input, the simulation starts simulating the flight.

In-flight Simulation: The state of charge of the battery starts at the value to which it is charged. Based on this, the model described above is used to calculate open-circuit voltage $V_{ocv}(SOC)$ and effective internal resistance $R_i(SOC)$. The required power demand (P(t)) is defined as a function of elapsed flight time in order to represent different flight phases (e.g. cruise and maximum-power manoeuvres). To avoid discontinuities between these phases, a smooth transition function is introduced:

A smooth step function is used to interpolate between the average and maximum power regimes:

$$\mathrm{T}(t) = \text{smoothstep}\left(\frac{t - t_{\text{max,1}}}{t_r}\right) - \text{smoothstep}\left(\frac{t - t_{\text{max,2}}}{t_r}\right)$$

where $t_{\text{max,1}}$ and $t_{\text{max,2}}$ define the start and end of the high-power manoeuvre window, and t_r is a characteristic ramp time controlling the smoothness of the transition.

The target power is then defined as:

$$P_{\text{target}} = P_{\text{avg}} + (P_{\text{max}} - P_{\text{avg}})\,\mathrm{T}(t)$$

To avoid unrealistic instantaneous changes in power demand, the delivered power is smoothed using a first-order response to P_{target}:

$$P_{\text{actual}}(t) = P_{\text{actual}}(t - \Delta t) + \frac{\Delta t}{\tau}\left(P_{\text{target}} - P_{\text{actual}}\right)$$

where τ is a time constant that depends on whether the system is ramping up or down in power demand (τ_{up} or τ_{down}). It should be noted that the selected values of τ are not intended to represent the physical response characteristics of the system. Thus, they are not considered as specific input parameters. Rather, they are introduced solely to smooth the power profile and prevent unrealistic instantaneous changes in power demand. A sensitivity analysis showed that including this smoothing changes the predicted energy consumption by less than 0.1 % compared to a model without response lag.

Finally, the delivered power P_{actual} is used as the instantaneous power demand in the battery model. Afterwards, using:

$$V_{\text{delivered}} = V_{\text{ocv}} - I_{drawn}R_i \qquad \text{and} \qquad P = I_{drawn}V_{\text{delivered}}$$

an equation for the current that needs to be drawn from the battery is constructed:

$$I_{drawn}^2 R - V_{\text{ocv}} I_{drawn} + P = 0$$

The equation is then solved to obtain the current being drawn I_{drawn}. The total charge removed from the battery is obtained by integrating the current draw over time:

$$Q_{\text{used}} = \int I(t)\,\mathrm{d}t$$

Since the simulation is evaluated using discrete timesteps, this integral is approximated numerically. For a timestep Δt, the charge removed during that timestep is given by

$$\Delta Q_{\text{used}} = I_{\text{drawn}}\,\Delta t$$

The total charge consumed is then obtained by summing the charge removed over all timesteps.

and the used charge for the whole flight is updated. Then, the simulation moves over to the next timestep, updates SOC using the charge used for the whole flight, and everything is repeated. At any instant, the following parameters are recorded: $V_{delivered}$, I_{drawn}, SOC, Discharge Rate. In the end, the total charge used is also calculated, from which the recharge time needed to reach the preflight initial SOC is determined.

Cycle Degradation and Failure Detection: Each cycle the battery goes through is regarded as independent from all previous cycles. Naturally, the initial conditions for certain parameters ($R_i, Q_{initial}$) at the start of each cycle are different and are calculated with the regression models concerning battery degradation discussed above.

As capacity drops with each cycle, the peak discharge rate needed, as well as the minimum V_{ocv} reached during flight, increase and decrease, respectively. Failure of the battery is considered to happen when the required discharge rate exceeds 95% of the rate specified on the battery datasheet, when V_{ocv} drops below 2.75 V per cell or when the battery's capacity drops to below 80 % of the initial capacity. The first cycle when either of these happens is then considered to be the cycle at which the battery can no longer perform the specified mission and fails. It should of course be said that in reality the battery might not be replaced instantly and would be safe to operate more (in case the failure is due to the first reason mentioned), however, it would not be able to provide the needed performance. Then the choice of when the battery needs to be replaced lies fully with the user, and can happen at any point until the battery's complete failure. For this reason, it was considered to be of most use to calculate and report the number of cycles after which it would not be able to perform the specific mission required.

As stated previously, however, battery capacity degradation from a customer point of view is essentially random. Thus, creating a single decay model with fixed parameters would not give any useful information about the expected cycles the battery can operate for. For this reason, a Monte Carlo simulation was performed. To do so, an exponential decay model of the type $a - be^{cN}$, where N is the number of cycles, was fitted to the results of Capacity vs Cycle Number for each of the five batteries tested, with a and b being kept constant and c being calculated such that the RMSE of the fit is the smallest. Afterwards, the values of c which gave the most and the least cycles were chosen, and c was set to be a random variable following a normal distribution with mean the average of the two and a standard deviation such that both are located within approximately one standard deviation of the mean. The simulation is then run 5000 times, keeping track of the failure cycle for each run.

Iterations and Final Parameters

Battery

Selection Process: The battery selection is based on an initial power budget estimate, indicating a peak power requirement of approximately 320 W. In combination with the flight profile provided by the flight profile department, this forms the basis for the battery simulation model.

The flight profile provided by the flight profile department is extended for the purpose of this analysis to a 10-second mission with 3 seconds at maximum power. This is done to include additional margins and account for modelling uncertainties.

After a discussion with the control department, it was indicated that a symmetric configuration is preferred, resulting in a requirement for either two or four batteries. In combination with the propulsion requirement for a higher-voltage system, a four-cell architecture was selected. The option of two 2-cell batteries was considered but rejected after consultation with the structures department due to packaging constraints, leading to a final configuration of four 1-cell batteries.

Final Selection: Several commercially available battery options were evaluated using the simulation model

(280 mAh, 320 mAh, 480 mAh). Based on this analysis, it was found that the 280 mAh battery could not deliver the required power, while the 480 mAh battery was working very far from its maximum capability, thus a 1S (4.35 V Lithium Polymer High Voltage-LiHV) 320 mAh[2] battery with a discharge rating of 95C was found to be the most optimal solution as it could provide the required power at a weight of 4 x 8.2 = 32.8 g. This battery fit very well within the mass budget and, in addition, fit perfectly within the structure. It was thus decided that the power budget and battery will be kept the same, and motors will have this peak power available. The key results from the simulation of the selected battery are presented below:

- Weight = 32.8 g
- Size = 64 x 10 x 6 mm
- Highest recharge time when charging at 2C = 4 minutes and 16 seconds. This refers to the charging time needed in the cycle just before failure, which is the one in which the battery gets drained the most and thus requires the longest charging time. This results in the longest out of all Monte Carlo runs. All other cycles have an equal or lower charging time.
- Absolute minimum voltage delivered during a flight = 13.48 V. This follows the exact same logic as the recharge time and is measured during the flight just before failure, again taking the lowest of all Monte Carlo runs.
- The cycle life distribution follows a $N(308, 30.4^2)$ distribution. This means that a single battery has a 99.5 % chance of lasting more than 230 cycles, while the four batteries consequently have a 98 % chance of doing so. It should again be noted that this number represents the number of cycles after which the battery is not able to perform the specific mission described above, however, it could still be operational afterwards and can be used until the user is dissatisfied with its performance or its end of life is reached.
- The battery can be charged to 80 % SOC after each cycle in order to maximise battery life. Even though it is not simulated what impact charging to more than 80 % will have, the simulations are performed with the battery charged to 80 %.

It should be said that there is a trade-off between the number of cycles the battery can perform and its size and thus weight. Had the result for this battery been that the cycles it can perform are very few and insufficient to adhere to the sustainability guidelines, a different option would have been considered. In addition, it was verified that the battery complies with the deceleration loads requirement (SYS-03-POE-01) since tests of LiPo batteries were found which successfully sustained a load of more than 20 000 g [50].

As a final note for better visualisation, presented below in Figure 7.1 and Figure 7.2 are graphs showing the performance of the battery during the first cycle and the last cycle of a randomly selected Monte Carlo instance. It can be seen that initially the battery does not operate extremely close to its discharge rate limit, reaching a peak discharge rate during the first flight of around 83 C. In addition, it is observed that the voltage and current stay within safe limits during the whole flight. In the second figure, showing the last flight before failure, it can be seen that the discharge rate reaches a peak of almost 95 C, while the voltage does not drop below 13 V. This is a clear indication that the battery fails because of exceeding the C-rate limit, which supports the conclusion made before that even after the battery stops being able to perform the mission, it is still safe to operate and could still be used further depending on performance.

[2] `https://betafpv.com/collections/batteries/products/lava-ii-1s-battery-` Accessed 14.06.2026

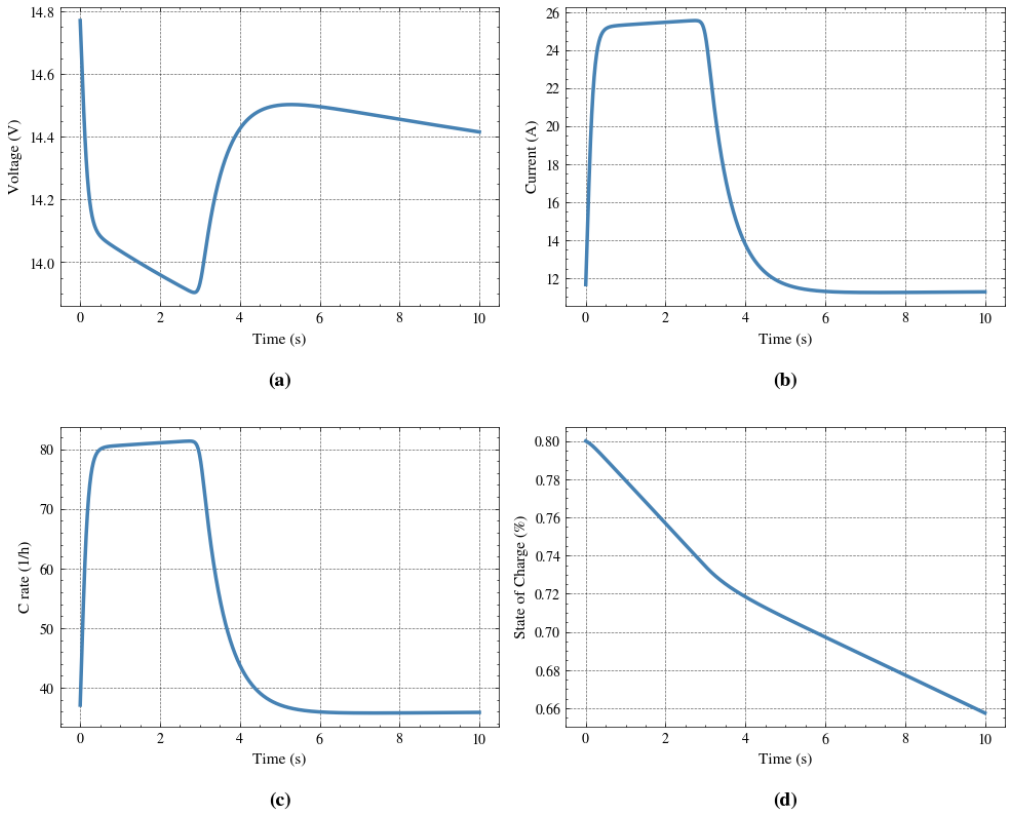

Figure 7.1: Graphs showing Voltage Curve (a), Current Curve (b), Discharge Rate Curve (c), SOC Curve (d) during the first cycle for a randomly selected Monte Carlo instance

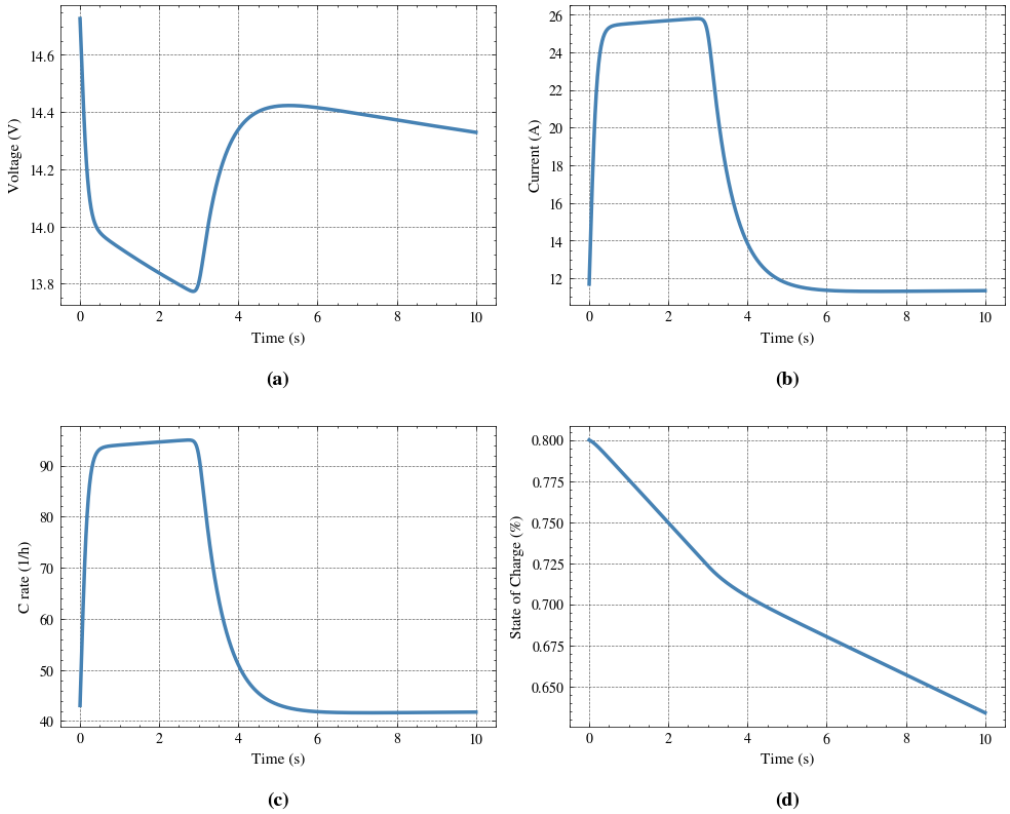

Figure 7.2: Graphs showing Voltage Curve (a), Current Curve (b), Discharge Rate Curve (c), SOC Curve (d) during the last cycle before failure for a randomly selected Monte Carlo instance

Electrical Components

The electrical architecture (the diagram of which is presented in full detail later in Chapter 12) is based on a standard multicopter-type drone electronics layout. Although PATS develops its own custom flight controller PCB, a full redesign of the electrical system was not considered necessary for this project. The reason for this is that the core electrical architecture of the vehicle remains largely unchanged compared to a conventional quadcopter configuration, with the primary functions of flight control, motor control, communication, and power management already being present in the existing design. Nevertheless, components which are typically found on a drone PCB are still shown in the diagram; however, it is assumed for the scope of the project that PATS already has a working PCB with all typical components (voltage regulators, ESCs, RX receiver, IMU, and MCU) present.

The focus is placed on identifying the limited set of modifications and additions required to support the updated vehicle design. This approach is justified by the fact that the underlying electrical architecture remains fundamentally compatible with a standard drone configuration.

The most relevant addition to the baseline system is the integration of aerodynamic vane actuation servos. These require additional control outputs and power delivery from the flight controller. It is assumed that the existing PCB architecture provides sufficient available PWM outputs for this purpose, although this assumption should be verified during detailed implementation. If required, minor extensions to the PCB would be sufficient to accommodate any additional signal lines.

A second modification concerns the battery and charging system. The drone continues to use a pogo-pin-based charging interface, consistent with the existing PATS platform. However, the transition to four LiPo batteries instead of one introduces the need for cell balancing functionality during charging. This requires changes to the PCB to accommodate the balancing wires to be soldered onto it, such that they can then be connected to five additional pogo pins, which will need to be placed so that the drone can be plugged into the balancing connector of a smart LiPo charger, although the overall charging concept remains unchanged. In addition, a small capacitor with a capacitance of 470 μF and a voltage rating of 35 V is added in order to absorb voltage spikes. The capacitor has to be soldered to the connection point of the battery power lines with the PCB.

Since the detailed PCB design is not available, the electrical subsystem mass was estimated using representative values. The contributions are summarised in Table 7.3.

Table 7.3: Electrical subsystem mass breakdown.

Component	**Mass [g]**
AIO flight controller (assumed PCB weight)	7.0 [3]
Safety capacitor: 35V, 470 μF	1.8 [4]
Pogo-pin contacts (7 pins, 0.3 g each)	2.1 [5]
Wiring (approx. 15 cm AWG14)	5.2 [6]
Total	**16.1**

These assumptions ensure that the electrical subsystem is represented realistically within the overall mass budget without requiring detailed low-level hardware design. It can be seen that the weight is 1 g over the required weight however, this was determined to be acceptable.

Overall, the electrical system is treated as an extension of a conventional multicopter architecture rather than a redesigned subsystem. This reflects the fact that the proposed vehicle modifications do not fundamentally alter the core electrical requirements, allowing the existing architecture to be retained with only targeted additions.

8

Structure and Layout

This chapter aims to optimize the structure of the drone and ensure that it is in compliance with its subsystem requirements. The design of the structure subsystem encompasses two areas: the design of the frame, from now on referred to as the fuselage, and the selection of a material. In Section 8.1 subsystem requirements for the structure are detailed. Section 8.2 explains which approach is used in the design of the subsystem and which outputs and inputs the subsystem uses. Then, Section 8.3 presents the simulations that have been performed to check compliance with the requirements after design iterations. The final parameters for the structure subsystem can be found in Table 8.4.

8.1. Core Subsystem Requirements

The integrated system for the drone has to comply with the system requirements detailed in Chapter 17. The subsystem requirements for the structure that were used in the design phase are listed below:

- SYS-02-STR-01: The structure shall absorb an impact energy of 2.806 J
- SYS-03-STR-01: The structure shall not deform plastically due to loads from maximum acceleration and deceleration
- SYS-28-STR-01: The structure shall allow for the components to be secured using reversible methods
- SYS-31-STR-01: The structure should be 3D printable in less than 24 hours
- SYS-31-STR-02: The structure shall be able to be assembled in $\leq$ 2 hours
- SYS-32-STR-01: The structure shall be fully 3D printable
- SYS-32-STR-02: The structure shall use off-the-shelf fasteners exclusively

8.2. Tools and Motivation

In order to achieve optimized values for the outputs defined in Table 8.1b and simultaneously ensure compliance with the subsystem requirements listed in Section 8.1, the structure's design is iterated using the methods described in this chapter. The layout of the preliminary design developed in the preliminary design is taken as a starting point for this iteration, as to provide a foundation on which subsequent improvements can be made. Shortly summarized, this layout consisted of a motor hub centralized within the hollow cylindrical duct, connected to the rest of the structure using four hollow circular struts. Below the motor hub, a servo assembly was positioned to control the vanes. The tether is connected to the drone through four connection points positioned symmetrically around the fuselage. Using this layout as a basis in combination with the iteration inputs received from other subsystems, presented in Table 8.1a, the structure will converge towards an optimum for the integrated design.

Design Tools

To determine the outputs specified above, a tool capable of Finite Element Analysis (FEM) and Computer-Aided Design (CAD) is needed. Using CAD, models of the structures and of the complete assembly of *the Chameleon* can be created. These models can then be used to show the layout of *the Chameleon*, creating assembly and manufacturing instructions, and blender animations. Additionally, the models can be simplified

and then used in FEM simulations, which are necessary for determining crash resistance and the response to thrust and braking loads.

The tool decided on for these purposes is Autodesk Fusion, from now on referred to as simply Fusion, as it provides free access to basic CAD and FEM for students through its education license. The reason FEM and impact simulations are performed, despite their relative complexity, is that there is extensive documentation and numerous tutorials available online detailing how to do it in Fusion. LS-Dyna and Ansys were considered as well, but on recommendation of Frits de Prenter and seeing that documentation and tutorials for these programs are limited, it was decided that their learning curves were too steep, and using them would be unfeasible within the time constraints of the DSE.

A limitation of Fusion and FEM software in general is that the weight they estimate is not accurate for 3D printed parts. They assume perfectly solid bodies, while 3D printed parts do not have perfectly smooth walls and can contain complex infill patterns. Therefore, to complement Fusion, a second tool is used as well: Bambu Studios. It measures the total amount of filament deposited, and thus takes infill and more accurate wall thicknesses into account. Furthermore, this software prepares the CAD models designed in Fusion for 3D printing and gives control over parameters such as the diameter of the depositing nozzle, the layer height, and the type of infill. For more details on Bambu Studios capabilities and settings, please refer to Section 15.2.

(a) Structures subsystem inputs

Component	Parameter	Symbol	Unit
Propeller	Quantity	—	–
	Diameter	D_p	mm
	Mass	m_p	g
Battery	Quantity	—	–
	Size	l_{bat}	mm
	Weight	m_{bat}	g
Motor	Quantity	—	–
	Size	D_m	mm
	Mass	m_m	g
Duct	Aerodynamic shape	—	–

(b) Structures subsystem outputs

Output	Symbol	Unit
Structural mass	m_{struc}	g
Total integrated system mass	m_{tot}	g
Layout	–	–
Structural wall thickness	t_{wall}	mm

8.3. Simulations

The objective of performing simulations using FEM is to determine the structure's behaviour during a crash and to find if the braking loads induced by the tether can be withstood. The two types of simulations performed are dynamic event simulations and static stress simulations. This section contains two subsections, both explaining which values are found using that particular simulation type and why that simulation type is chosen. That explanation is then followed by the simulation architecture, which assumptions are made, which settings are selected, and which simplifications are made.

As mentioned earlier, the simulations make use of FEM. In FEM, a body is discretized into a finite number of elements which are connected at shared nodes. The nodes have three translational degrees of freedom and ensure displacement compatibility between elements. Fusion automatically generates a mesh consisting of tetrahedral elements, which are 3-dimensional shapes capable of approximating complex geometry. All simulations have in common that they are performed on a simplified version of *the Chameleon* or fuselage.

Dynamic Event Simulation

A dynamic event simulation is used to determine the stresses and strains experienced by the fuselage due to a crash. During a crash deformations can be large, stresses far above yield strength can occur, and yielding

and plastic deformation takes place. Inertia, velocity, accelerations, and contact interactions influence the structural response [1]. A dynamic event simulation accounts for these time-dependent effects and can therefore accurately predict stresses, deformations, and plastic strains during an impact.

Fusion's dynamic event simulations use an explicit solver, where Hooke's Law, Newton's second law, and the damping equation are combined and integrated using a central difference method. For more details on the solver and its architecture, please refer to the Autodesk Explicit 2022 User's Manual [51].

Two types of crash situations are considered in this report. The first of these is a direct impact in which the fuselage crashes into a wall sideways. This impact is meant to determine how the fuselage would behave if it crashed to the ground and landed on its side. The second is a frontal crash into a wall, meant to simulate how the fuselage behaves in the event of a tether failure.

Dynamic Event Simulations are conducted according to the settings and simplifications found in Table 8.2.

Table 8.2: Dynamic event simulations simplifications & settings

Simplification / Simulation setting	**Purpose / Note**
Initial Conditions	
• Drone starts with an initial relative velocity of 6.26 m/s w.r.t. the impact surface.	Impact energy from requirement
• Simulations include gravity.	
• The drone starts 0.5 mm away from the impact surface.	Saves computational time
Bodies	
• The impact surface is modelled as a flat steel plate.	Non-linear material properties and friction coefficient available
• The impact surface is a rigid body constrained in space.	Saves computational time
• The drone frame has no constraints and is fully free to move in space.	
• The drone frames are modelled from Polycarbonate.	See Figure 8.3 for material properties and reasoning.
• The frame is modelled as a solid	See notes
Placeholder Masses	
• Placeholder bodies are used to simulate the weight of the Power and Electronics Subsystem and the Propulsion and Interception Subsystem.	
• The placeholder masses are treated as rigid steel bodies.	Saves computational time
• No contacts are modelled between the placeholder mass bodies and the impact surface. These bodies are free to phase through the impact surface.	See notes for reasoning
• No contacts are modelled between the placeholder masses themselves in case they are, for some reason, to collide.	Not interested in placeholder interaction + rigid bodies
Contact Definitions	
• The contacts between the placeholder mass bodies and the frame are modelled as bonded (as if the two bodies are welded together). This introduces "ghost stresses" in the order of 10^{-6} MPa, which can safely be ignored.	See notes for details on why point masses were not used
• The contact between the frame and the impact surface is modelled as a separation contact with a friction coefficient of 0.31.	See notes for detailed explanation

Continued on next page

[1] `https://help.autodesk.com/view/fusion360/ENU/?guid=SIM-EVENT-SIM-STUDY-CONCEPT` - Accessed 17.06.2026

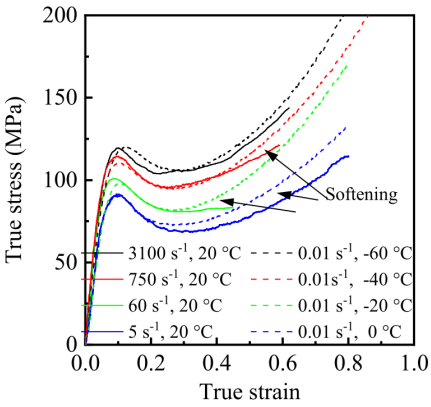

(a) Polycarbonate true stress-strain curves at low temperatures and high strain rates, University of Oxford and the Dutch Polymer Institute [52]. The curve at 3100 s^{-1} and 20°C is used.

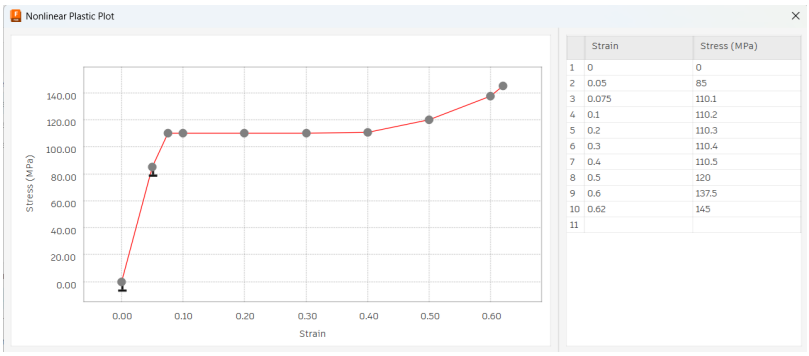

(b) Averaged 3100 s^{-1} and 20°C true stress-strain curve such that there are no points with negative slope. This is the input into the Autodesk Fusion simulations.

Figure 8.1: Polycarbonate material properties used in the simulation

Table 8.2 – continued from previous page

Simplification / Simulation setting	Purpose / Note
Meshing	
• Autodesk Fusion's smart meshing options are used for generating the model meshes — the option to locally scale mesh size based on feature size is selected. The average mesh size is set as a percentage of the model size. • Local mesh control is used to increase the mesh element size for the rigid bodies. • Local mesh refinement is used near the impact zone to get more accurate results, as coarser meshes tend to lead to singularities at the point of impact. • An element deletion criterion is added to the simulation based on equivalent strain. If a mesh element reaches the failure strain of the material, it is deleted to simulate the material failing.	Saves computational time

Notes on simulation settings

Dynamic impact simulations require non-linear materials to account for yielding. Additionally, during impact, very high strain rates occur locally. Fusion has mostly metals in its non-linear library, as their properties aren't very strain-rate dependent, and their simulations are more accurate. Since the mechanical properties of plastics are highly strain-rate dependent, a custom polycarbonate material needs to be defined. Strain rates vary during a crash meaning that a viscoplastic material model would normally be required, which Fusion unfortunately does not support. Therefore, a plastic material model was used based on the true stress-strain curve instead [2]. Experimental data from Oxford University and the Dutch Polymer Institute [52] is utilised, specifically the true stress-strain curve at 3100 s^{-1} strain and 20°C from Fig. 15 in the article [52]. Polycarbonate exhibits points with a negative slope on its true stress-strain curve [52]. Because the simulation solver does not accept such negative slopes [3], the post-yield behaviour was averaged into a straight-line segment, as suggested by Fusion's documentation [2]. This adaptation provides a conservative estimate, as the ultimate failure strain decreases at high strain rates.

When modelling the fuselage as a hollow body Fusion automatically generates a high number of elements, making simulations get stuck or go over the solving time limit of twelve hours. Furthermore, Fusion does not

[2] `https://help.autodesk.com/view/fusion360/ENU/?guid=SIM-NL-MATERIAL-PROPS-CONCEPT` – Accessed 12.05.2026

[3] `https://help.autodesk.com/view/fusion360/ENU/?guid=SIM-DEF-PLASTIC-NL-MATERIAL` – Accessed 12.05.2026

support shell elements in their simulations, meaning solid elements always have to be used [4]. This limitation of Fusion means that infill cannot be accurately simulated, and means that the simulation outputs are mainly useful in a quantitive way to see where the design should be reinforced. Rigorous testing in the post-DSE phase is recommended to ensure the structural integrity.

The impact surface was modelled as a rigid body. Steel was selected for it, as friction coefficients are most often reported against it or the material itself. Additionally, greenhouse frames are commonly constructed from materials like galvanised steel or aluminium [5]. The kinetic friction coefficient for plastics depends heavily on surface finish and applied pressure [53]. Manufacturers report static friction coefficients for polycarbonate against steel ranging from 0.31 [6] to 0.39 [7]. Because kinetic friction is generally lower than static friction, and no exact kinetic value was found, the conservative value of 0.31 was selected. Sensitivity testing confirmed that minor variations on the order of ± 0.05 do not significantly influence the deformation mechanics.

Placeholder rigid bodies (density of steel) are used to simulate the mass and inertia of the motors, battery and electronics. Through experimentation, it was found that using meshed bodies is more prudent than using point masses, as they can cause singularities. These placeholder rigid bodies are connected to the frame with bonded contacts (as if welded). This introduces simulation inaccuracies by making the local stiffness at the attachment surface infinite. However, in real life, where rigid metal motors are bolted to the plastic frame, rigidity is also greatly increased locally, just not to infinity. The bonded contact creates "ghost" stresses on the order of 10^{-6} MPa prior to impact, which can safely be neglected. During impact, the maximum stresses also do not appear directly next to these attachment zones. Thus, these "ghost" stresses do not detract from the quality of the simulation. Overall, this approach produced much better results than using point masses.

Because contacts between the placeholder masses and the impact surface are not modelled, it is possible that the placeholder masses phase through the impact surface. The kinetic energy that would otherwise be absorbed by the placeholder mass and structure around it is instead absorbed elsewhere in the structure, thus locally violating conservation of momentum. However, as the frame itself cannot phase through and the placeholder is connected to it, all of its momentum will get transferred and global momentum conservation is not violated. The resulting inaccuracy should thus be small. If a significant phase through is observed, the CAD models will be designed, and the simulation reevaluated.

Simulation Outputs
As explained earlier in this section, the goal of performing a dynamic event simulation is to determine stresses and strains in crash situations, as these show if the design is crash-worthy and thus compliant with SYS-02-STR-01, or if it should be improved. Figure 8.2 shows what simulation results after an impact against a vertical wall look like, while Figure 8.3 shows the simulation results after impact against a horizontal wall. The low amount of yielded elements shows that the impact can be comfortably withstood in the case of a solid body. As recommended earlier, physical testing has to be performed to see how the 3D printed part would perform in real life, however these values are promising.

Static Stress Simulation

To determine the structure's response to the loads induced by braking, static stress simulations are conducted. The goal of these simulations is to determine the von Mises stress and the strain in the connection points after a braking force, which is derived from the flight path, is applied to them. From these stresses and strains, events such as yielding, fatigue, and creep can be determined.

As they change over a short period of time, braking loads are generally dynamic in nature. There are, however,

[4] `https://www.autodesk.com/support/technical/article/caas/sfdcarticles/sfdcarticles/Comparison-of-simulation-capabilities-in-Fusion-360-and-Inventor-Nastran.html` - Accessed: 18-06-2026

[5] `https://grandiogreenhouses.com/blogs/news/choose-the-best-frame-type-for-your-greenhouse` – Accessed 19.05.2026

[6] `https://www.polymerplastics.com/images/dataSheets/DSPolycarbonate.pdf` – Accessed 12.05.2026

[7] `https://www.redwoodplastics.com/wp-content/uploads/2010/08/Redco-Metric-POLYCARBONATE.pdf` – Accessed 12.05.2026

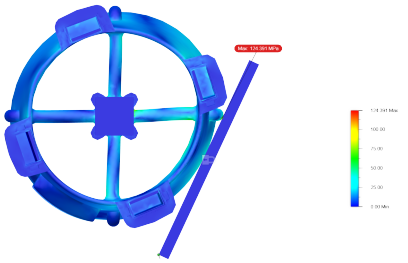

(a) Maximum stress of $\sigma = 124.391$ MPa at t = 0.56 ms (step 14/25) - bottom view.

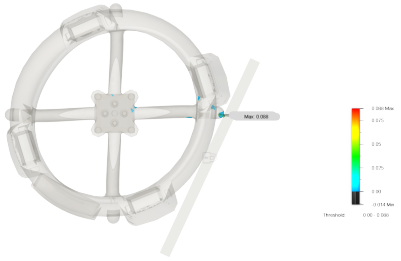

(b) Plastic strain at t = 1 ms (step 25/25). The mean plastic strain equals 0.001463, and 111/76914 (0.144%) elements have yielded.

Figure 8.2: Result of a dynamic event simulation showing the stress and strain distributions over the body after an impact against a vertical wall.

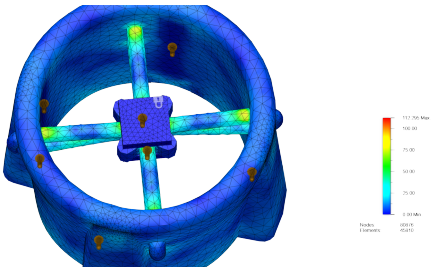

(a) Maximum stress of $\sigma = 112.295$ MPa at t = 0.36 ms (step 9/25) - bottom view.

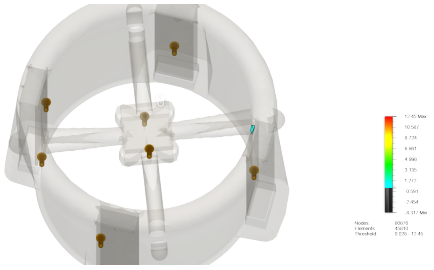

(b) Plastic strain at t = 1 ms (step 25/25). The mean plastic strain equals 0.001801, and 474/42018 (1.128%) elements have yielded. Four unphysical outliers (plastic strains up to around 12) cause the graph to be skewed.

Figure 8.3: Result of a dynamic event simulation showing the stress and strain distributions over the body after an impact against a horizontal wall.

two main reasons why dynamic event simulations are not employed. Firstly, Fusion does not support wire or rope objects, meaning that it is not possible to accurately model the tether [8]. Secondly, braking is estimated to take around 0.1 seconds. Dynamic event simulations are meant for events lasting in the order of milliseconds, making their use for this purpose unfeasible.

In addition to the infeasibility of dynamic event simulations, there are certain benefits to using static stress simulations. The three main advantages are that they are relatively quick to compute, that a mesh convergence study can be automatically performed, and that they provide safety factors for the von Mises equivalent stress in the structure compared to the yield strength of the material [9].

For the results of a static stress simulation to be valid, the conditions below have to be met [10]:

- The loading causes only small deflections or rotations. For deformations to be small, the following individual conditions have to be satisfied:
  - The deformation does not have a significant effect on the load direction, load magnitude, or the surface area of faces to which loads are applied.
  - The deformation does not alter the boundary conditions (that is, where, and in what manner, the parts are constrained).
- The materials behave linearly and remain within the elastic region of the material's stress-strain curve. In other words, the stiffness and strength of the material does not change.

[8] `https://www.autodesk.com/support/technical/article/caas/sfdcarticles/sfdcarticles/How-to-create-Flexible-Joints-in-Fusion-360.html` - Accessed 18-06-2026

[9] `https://help.autodesk.com/view/fusion360/ENU/?guid=SIM-SAFETY-FACTOR-CALC-CONCEPT` - Accessed 19.06.2026

[10] `https://help.autodesk.com/view/fusion360/ENU/?guid=SIM-STATIC-STRESS-ANALYSIS` - Accessed: 19.06.2026

- Dynamic effects from the loading conditions are not significant. Static stress analysis does not consider inertial effects.

By seeing how close the material comes to yielding, it can be determined whether the first two conditions are satisfied. Large strains and stresses would indicate that the deflections are high enough that the load direction has changed or the surface area of the ear has decreased. They would also indicate that the material might have reached the inelastic region of the stress-strain curve. The final condition cannot be satisfied, as braking is dynamic (see Chapter 11). However, Fusion's documentation states that a static force can be multiplied with an amplification factor to account for transient or inertial effects [10]. This multiplication factor is called the dynamic amplification factor (DAF).

The magnitude of the DAF is dependent on factors such as the structure's degree of freedom, the force's shape (e.g. pulse, step, half sinusoid), and the structure's natural frequency. Here, a structure's degree of freedom refers to the number of independent displacements required to define the displaced positions of all the masses relative to their original position [54]. Using a modal analysis, which is not described here in detail due to the time constraints of the DSE, it was determined that the structure has at least 50 degrees of freedom (maximum amount of modes simulated to limit computational time). For multiple-degree-of-freedom (MDOF) systems, the DAF can exceed values of 2.0 [55], and Mozos and Aparicio [56] even present a value of 3.24 for the case where a MDOF system is subjected to a rectangular pulse load. As it was determined from the braking analysis that the shape was approximately rectangular, this value was used in the simulations.

In addition, 3D printed materials are weaker than their solid counterparts. This is particularly relevant for the braking force as this is applied perpendicular to the printing direction, meaning that the material strength there depends on the strength between layers. In Section 15.2 it is explained how the strength of the structure is improved by printing at low layer heights, very high temperatures, and 100% infill in the connection points. De Vries et al. [57] presents a tensile strength for polycarbonate in the direction which is perpendicular to the printing direction of 61.4 MPa, when a layer height of 0.2 mm is used. The component of the stress experienced by the connection points perpendicular to the printing direction will be compared to this tensile strength to determine whether the braking forces can be withstood.

Fusion uses the Autodesk NASTRAN solver for their static stress simulations[11], which is a modified version of the original developed by NASA. For more information on its applications and capabilities, please reference the user's guide [58]. NASTRAN itself has been extensively verified [59], making use of Fusion for static stress simulations justified.

Static Stress Simulations are conducted according to the settings and simplifications found in Table 8.3.

Table 8.3: Static Stress Simulations simplifications & settings

Simplification / Simulation setting	Purpose / Note
Initial Conditions	
• The braking force is distributed over the inner surface of the four connection points	See notes for reasoning
• Simulations do not include gravity.	
• Remove rigid body modes is selected	Enables inertial relief, putting body in equilibrium
Bodies	
• The drone frame has no constraints and is fully free to move in space.	Normal state of drone
• No other bodies are modelled except for the fuselage	Their inertia is taken into account in the braking force

Continued on next page

[11] https://forums.autodesk.com/t5/fusion-design-validate-document/fusion-360-simulation-fea-solver-compared-to-inventor/td-p/7833208 - Accessed: 22.06.2026

Table 8.3 – continued from previous page

Simplification / Simulation setting	Purpose / Note
• The drone frames are modelled from Polycarbonate.	Same reason and definition as for dynamic event simulations
Meshing	
• Autodesk Fusion's smart meshing options are used for generating the model meshes. The average mesh size is set as 2% of the model size, resulting in 416428 nodes and 260280 elements	
• A custom adaptive mesh refinement is performed.	See notes for reasoning

Notes on simulation settings

The total braking force is found by multiplying the deceleration by the total integrated mass. The ears are placed symmetrically around the fuselage and internal load paths from them to the struts are designed, ensuring that the force is distributed through the entire structure. Due to the tether being positioned directly behind the drone, it is assumed that braking occurs in the axial direction. Therefore, the braking force is distributed equally over the four ears. This makes each of the connection points carry a quarter of the total force.

A mesh convergence study is performed to reduce mathematical artifacts and increases the accuracy of results, while minimizing computation time. Through a mesh convergence study the minimal fidelity of the mesh can be determined, optimizing for the solving time of simulations. Fusion offers an automatic adaptive mesh refinement tool which performs this convergence study, where after the initial solve finishes the regions which contain the highest stresses are remeshed using finer elements, until the change in the convergence criteria falls below the convergence tolerance[12]. In the custom settings selected, a maximum of ten refinements are done, each refining at most 40% of elements, up until the Von Mises stress changes less than 1% compared to the previous refinement. The Von Mises stress is used as a convergence criteria as it is indicative of how close the material came to yielding.

Simulation Outputs

As mentioned earlier in this section, this simulation is conducted to test whether the structure can withstand the braking forces, and ensure compliance with SYS-03-STR-01. To check this, the von Mises stress and the strain in the ears are analyzed. If they are sufficiently low such that the conditions for a static stress simulation are met, the design for the connection points will be used in the iterations. Figure 8.4 presents the output of the simulation, while Figure 8.5 shows what a convergence plot looks like. The maximum von Mises stress is 5.36 MPa which is well below the yield strength of polycarbonate. The maximum strain is 0.005, which is small enough that the loading direction will not have changed significantly. These results show that the use of a static stress simulation is justified. This maximum stress in the connection point can be compared to the S-N curve in Figure 8.6 to determine how many cycles the connection point can be loaded before failure. A maximum stress of 5.36 MPa corresponds to a lifetime of $10^{4.5}$ cycles, which exceeds the minimum of 1000 cycles demanded by SYS-27.

Furthermore, the maximum stress in the direction perpendicular to the printing direction is , which is less than 10% of the tensile strength mentioned earlier in this section. This means that the 3D printed structure will not fail during braking. Should testing during the post-DSE phase show that the connections points cannot withstand the load despite this large safety margin, it can be considered to print the structure at an angle instead of in a perfectly flat plane. This would put the braking force more parallel with the direction of the filament, improving strength.

[12] `https://help.autodesk.com/view/fusion360/ENU/?guid=SIM-ADAPTIVE-REFINEMENT-CONCEPT` - Accessed: 21-06-2026

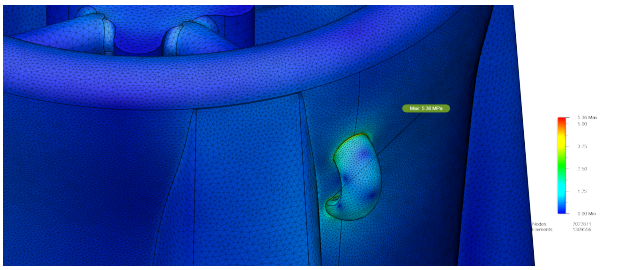

(a) Maximum von Mises stress resulting from the applied braking loads. The probe indicates a maximum stress of 5.36 MPa.

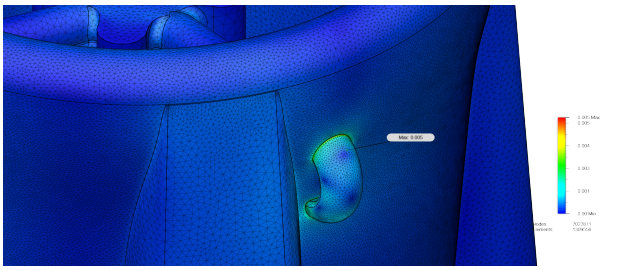

(b) Maximum equivalent strain resulting from the applied braking loads. The probe indicates a maximum strain of 0.005.

Figure 8.4: Results of the static analysis of the fuselage under the braking loads derived from the flight path. Figure 8.4a presents the von Mises stress distribution, while Figure 8.4b presents the equivalent strain distribution.

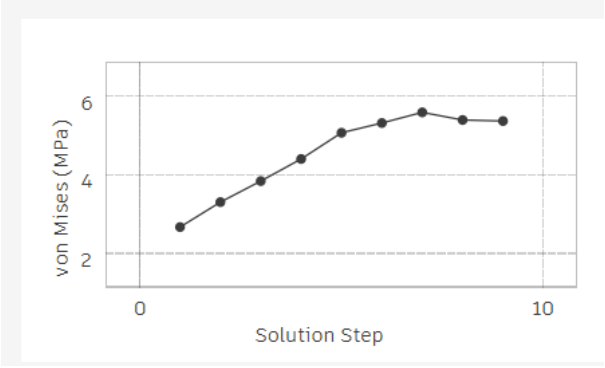

Figure 8.5: Convergence plot resulting from the adaptive mesh refinement performed by Fusion. The actual convergence rate is (0.496%) the difference in percentage between the previous refinement and the current one, while the target convergence (1&) is the maximum difference they can have.

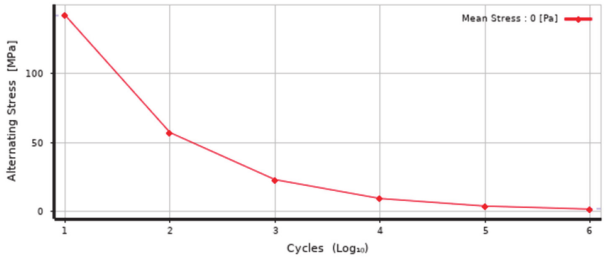

Figure 8.6: S-N curve for FDM polycarbonate [60]. The y-axis shows the amplitude of the stress while the x-axis shows the number of cycles until failure at that amplitude.

Material Selection

Previously in the Midterm report the material choice was narrowed down to four promising candidates, namely polycarbonate, ASA, PETG and TPU. The client currently uses the Bambu Lab ecosystem of 3D printers and materials [61], so for their comparison the Bambu Lab commercially avaliable versions of these materials were considered.

height**Property**	**PC-FR**	**PC**	**ASA**	**PETG HF**	**TPU 95A HF**
Density (g/cm^3)	1.18	1.20	1.05	1.28	1.22
Vicat Softening Temp. (°C)	114	119	106	70	N/A
Tensile Strength (MPa)	60 ± 4	55 ± 4	37 ± 3	34 ± 4	27.3 ± 0.8
Elongation at Break (%)	2.4 ± 0.3	3.8 ± 0.3	9.2 ± 1.4	8.6 ± 1.2	>650
Impact Strength (kJ/m^2)	8.4 ± 2.1	34.8 ± 2.1	41.0 ± 2.3	31.5 ± 2.2	N/A
Flexural Strength (MPa)	90 ± 4	108 ± 4	65 ± 5	64 ± 3	N/A
Flame Retardant	V-0	No	No	No	No
Price per spool (€ / kg)	59.99	42.99	24.99	22.99	34.99

Considering the materials and the properties outlined in Figure 8.3, regular polycarbonate (PC) is the best choice for a crash-resistant 3D-printed drone, as it combines high toughness, strength, and heat resistance. The fire-retardant version of this filament, PC FR, is much too brittle for a crash-resistant design. PETG, on the other hand, is too heavy, while its mechanical properties like tensile strength and impact strength are poorer. TPU is very soft, which will lead to a compliant and energy-absorbing structure. However, this softness means that during a crash, the propellers will rub on the inside of the structure and shred it. ASA is a compelling option because it is very light. However, PC still offers a better balance of tensile strength,

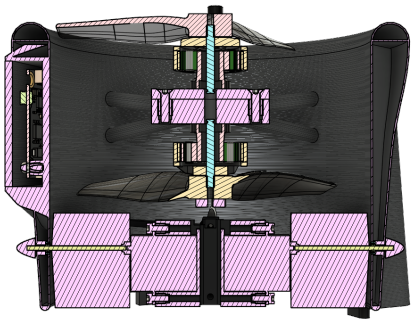

Figure 8.7: Cross section showing the internal layout of the drone.

stiffness, toughness, and heat resistance, while ASA lacks in tensile strength. Additionally, polycarbonate is used for making fighter jet canopies [13], proving its excellent impact resistance. Lastly, unlike most other plastics, regular polycarbonate has moderate flame resistance [14], which is very important for a drone carrying lithium polymer batteries.

Iterations

The structure played a role in IL-1 to keep the total mass low. It was also the subsystem responsible for improving crash resistance by changing the thickness of the wall of the fuselage, the number of struts and their diameter, and changing the motor hub size to accommodate different motors. Its layout provided the input in IL-2, where the Aerodynamic subsystem is linked to it and later provides aerodynamic coefficients to control. Lastly, IL-3 was iterated until the load induced by braking could be withstood comfortably.

The resulting layout can be found in Figure 8.7 and a short summary is included in Table 8.4. As this chapter is focused on the iteration process and how outputs were determined, it does not aim to give a detailed overview of how exactly this layout is structured and which considerations were made when deciding on component placement. This is done in Section 15.3. SYS-28-STR-01 demanded that components are secured using reversible methods to ensure that the design is modular. This modularity is shown in Section 15.2.

Table 8.4: Optimal structure parameters derived from simulation iterations and constraints.

Parameter	**Optimal Value (sideways/frontal)**
Fuselage	
Structural mass	55.14 g
Fuselage wall thickness	0.4 mm
Layout	
Nr. of struts	8
Nr. of vanes	4
Attachment node width	5 mm
Attachment node thickness	3.6 mm
Crash Resistance Characteristics	
Mean plastic strain after crash	0.001463/0.001801
Plastic strain volume (% of total elements)	0.144%/1.128%
Braking Characteristics	
Braking stress	5.36 MPa
Braking strain	0.005

[13] `https://www.curbellplastics.com/resource-library/articles/plastic-materials-proving-to-be-good-fit-for-aerospace-parts/` - Accessed 17.06.2026

[14] `https://polymaker.com/product/polymax-pc-fr/` - Accessed 17.06.2026

9
Aerodynamic Performance

In this chapter, an aerodynamic analysis of the design is performed using OpenVSP. The selection process and underlying principle of this software is discussed in Section 9.2, followed by an explanation of the setup of the grid and geometry used in the simulation in Section 9.3. Finally, the inputs and outputs of the analysis are summarized in Table 9.1 and Table 9.2 respectively.

9.1. Core Subsystem Requirements

The aerodynamic analysis outputs the drag coefficients and aerodynamic derivatives. While the aerodynamic shapes of the duct and flaps are evaluated and determined, these design considerations lead to marginal performance improvements and are thus considered to not affect compliance of the actual design significantly. As such, no direct requirements can be assigned to the subsystem given its passive role.

9.2. Tools and Motivation

To determine the aerodynamic characteristics, a software needs to be selected. This section explains the working of different softwares and choice of software. The theory behind the selected software, OpenVSP, can be found in Appendix A.

Simulation tools

During the preliminary design phase, the performance of the propulsion system was analysed using blade element momentum theory (BEMT). While efficient, such methods fail to account for complex wake interactions [62]. Given the needed determination of aerodynamic characteristics and stability derivatives of the integrated system, the previously used tools will not suffice. For a more detailed approach, two tools and their corresponding methods are identified: OpenVSP (Vortex Lattice Method and Panel Method combined with actuator disk theory) and FLOWUnsteady (reformulated Vortex Particle Method). Note that full-fidelity Reynolds-Averaged-Navier-Stokes (RANS) simulations were previously determined during the design orientation phase to be unfit given the allocated resources(estimated compute time $\approx$ 3 days [63]).

OpenVSP makes use of Vortex Lattice Method (VLM) and Panel Method. The assumptions and explanation of the VLM and panel method applied in VSPAERO is based on the explanation given by [64] and can be found in Appendix A. In contrast to other frequently used VLM and Panel Method tools, OpenVSP supports the modelling of actuator disks and rotors. As such, an actuator disk model is used to model the propeller, for which the underlying theory is also explained in Appendix A. As unsteady rotor simulations induce high frequency oscillations due to blade passage, they are unfit for OpenVSP stability analyses where derivatives are derived from the system response under small perturbations, leading to low signal-to-noise ratios.

FLOWUnsteady uses particles to discretize the Navier-Stokes equations, which provides several advantages over conventional mesh-based CFD, such as avoiding the process of mesh generation and faster compute times [65]. Although unsteady simulations can provide more accurate propeller performance parameters than VLM [66], these still require too much compute within the given timeframe. Sheridan et al. report that VSPAERO runs with an actuator disk require 98% less time than a run with unsteady rotating blades for wing propeller configurations. They report an average runtime of approximately 370 minutes for a wing propeller combination, making iterations for the more complex simulated geometry analysed in this report too lengthy.

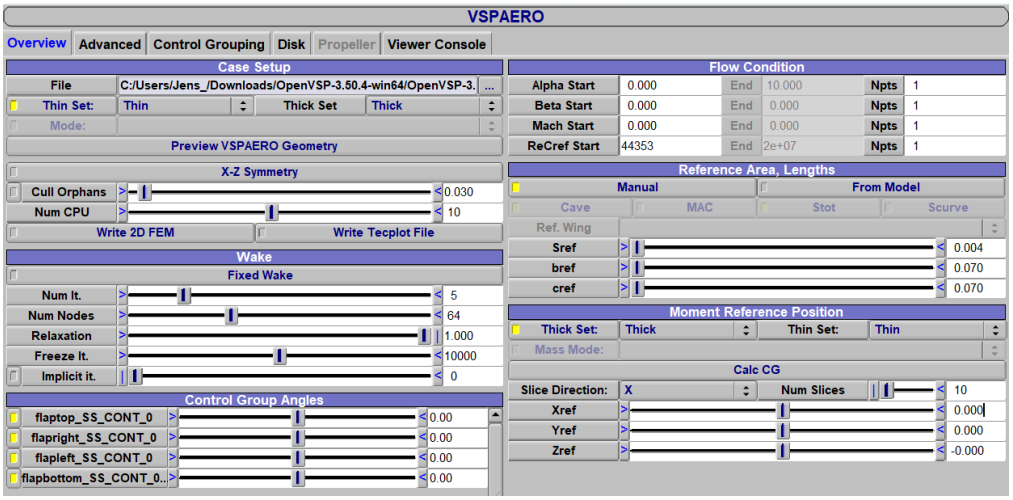

Figure 9.1: VSPAERO simulation settings.

As such, the use of FLOWUnsteady is reserved for verification and validation of the design at a later stage.

9.3. Simulations

To obtain accurate results, the geometry, grid and settings of the simulation have to be set. The accuracy of the results is highly dependent on the selected grid. The selected grid should be as coarse as possible to reduce the computational effort but needs to be fine enough to ensure accurate results. This section explains the exact geometry and grid settings used in the simulation. Validation of simulation results can be found in Appendix A. An overview of all inputs used to setup the simulation, and outputs computed by the simulation is presented in Table 9.1 and Table 9.2.

Table 9.1: Input parameters

Name	Symbol	Unit
Propeller Parameters		
Thrust coefficient	C_T	-
Power coefficient	C_P	-
Motor Parameters		
Rotations per minute	Ω	RPM
Structure Parameters		
Duct geometry	-	-
Flaps geometry	-	-

Table 9.2: Output parameters

Name	Symbol	Unit
Aerodynamic Parameters		
Drag coefficient	C_D	-
Aerodynamic derivatives	C_{ij}	rad^{-1}
Structure Parameters		
Duct aerodynamic shape	-	-
Flaps aerodynamic shape	-	-

Simulation settings

In VSPAERO, the number of nodes, flow conditions and reference values have to be set. The setting interface is shown in Figure 9.1. Five iterations using 64 wake nodes are found to yield accurate and converged results[67]. The number of iterations and number of nodes setting can be seen in the lower left of Figure 9.1. Reference area and lengths are based on flap geometry and used to calculate the Reynolds number at $V = 9$ m/s. This velocity is used as it is the average of the operating velocities used in the control simulation. Reynolds numbers, reference area and lengths are defined on the right in Figure 9.1. All other settings were left at their default values.

Duct and control flap geometry

To analyse the design in OpenVSP, the exact shape of the duct and airfoil of the control surfaces have to be defined.

A NACA 0010 airfoil is used for simulating the control surfaces. Symmetric airfoils are commonly used for control surfaces because they have similar aerodynamic characteristics at positive and negative angles of attack and generate zero lift at zero angle of attack [68]. The NACA 0010 airfoil, sitting between the NACA 0006 and NACA 0015 presented in [68], was selected to provide a baseline estimate of properties of the thrust vectoring surfaces. The properties of the NACA 0010 airfoil are well documented, making it easier to validate results.

The shape of the duct has been designed based on the optimal shape for electric ducted fans suggested by Yacoubi et al.[69]. The leading edge of the duct has a toroidal shape with a torus radius of $\frac{r_{tip}}{D_r} = 0.06$, where D_r corresponds to the diameter of the propeller with clearance. The rest of the duct is made cylindrical on the inside and follows an airfoil-like shape on the outside. The cylindrical inner surface is easy to manufacturing while the outside shape helps to maintain attached flow. The shape thus provides a balance between manufacturing simplicity and aerodynamic performance. The inner and outer surface converge to thickness of 2.34 mm at the outlet, as an infinitely thin shape would be impossible to manufacture.

Geometry in OpenVSP

This subsection describes the model used in OpenVSP to obtain the aerodynamic and stability coefficients of the design. The model consists of two counter rotating actuator disks, four flaps and a duct. The grid and placement of all components are shown in Table 9.3. The accuracy of the results is highly dependent on the selected grid. The selected grid should be as coarse as possible to reduce the computational effort but needs to be fine enough to ensure accurate results. Size and placement in the model are based on the geometry defined in structure design. Small components like servos are left out as they increase computational effort significantly without much accuracy improvement due to the limited fidelity of the simulation method.

Table 9.3: Tessellation and location of the components used in the VSPAERO simulation.

Component	Longitudinal Tessellation(U)	Transverse Tessellation(W)	X (m)	Y (m)	Z (m)
Duct	25	49	0	0	0
Fwd propeller	32	8	-0.015	0	0
Aft propeller	32	8	0.024	0	0
Left flap	61	61	0.034	0	-0.036
Right flap	61	61	0.034	0	0.013
Top flap	61	61	0.034	0.013	0
Bottom flap	61	61	0.034	-0.036	0

The selected duct, flap and propeller tessellation is based on a convergence study conducted in [67] and [66]. These tessellations are found to provide a good balance between accuracy and computational effort. The assembled geometry using the tessellation specified in Table 9.3 is shown in Figure 9.2a.

Simulation Output

Running the simulation using the previously described settings at different velocities and rotational speeds yields the aerodynamic characteristics. An example of the resulting pressure distribution is shown in Figure 9.2b. OpenVSP then computes the aerodynamic coefficient based on this pressure distribution. The steady stability run mode is used to obtain stability coefficients. An example at $V = 12m/s$ of both outputs can be found in Figure A.3 and Table A.4. Figure 9.3 outlines the $\log_{10}(L_2)$ between iterations. This value steadily decreases between iterations, reaching a low value of -3.3 at the fifth wake iteration, suggesting convergence. A final summary of the output values is shown in Table 9.5.

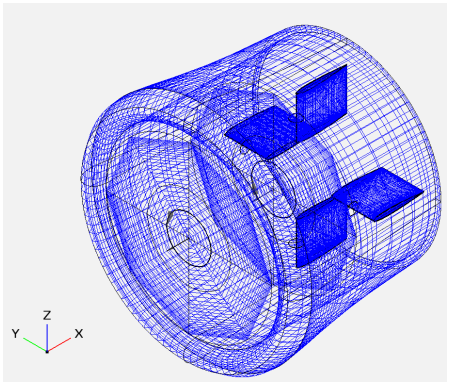

(a) Assembly used in OpenVSP simulation.

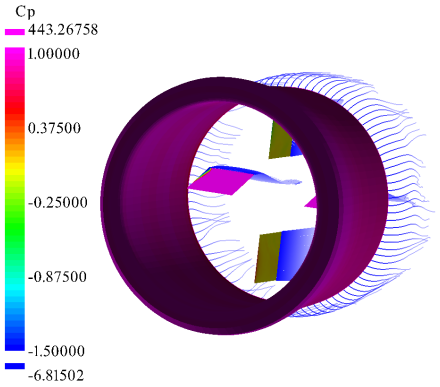

(b) Pressure distribution of *the Chameleon* design at $V = 9m/s$ and n = 40419 RPM with an illustrative7 horizontal flap deflection of 18 °. Note that the propellers are not shown as these are modelled as actuator disks.

Figure 9.2: OpenVSP figures of the Duct

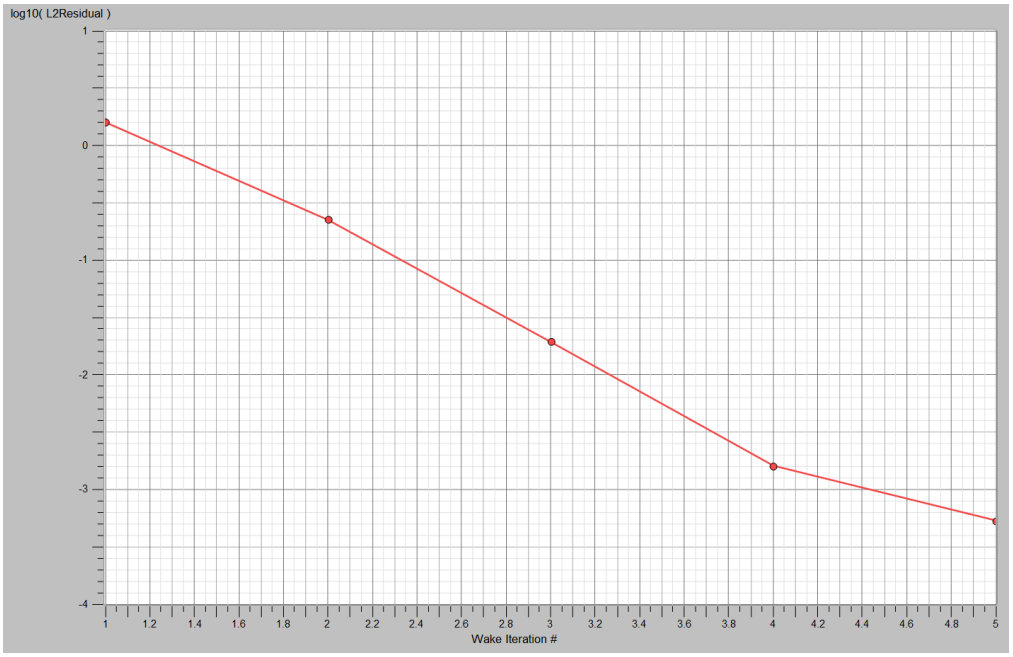

Figure 9.3: OpenVSP $\log_{10}(L_2)$ vs wake iterations output at $V = 9m/s$ and n = 40419 RPM with a horizontal flap deflection of 18 °.

Table 9.5: Aerodynamic analysis results

Parameter	**Value**
C_D	Depends on operating point. Example at $V = 12m/s$ shown in appendix(Figure A.3)
Stability derivatives	Depends on operating point. Example shown at $V = 12m/s$ in appendix(Table A.4)
Duct aerodynamic shape	see Section 9.3
Flaps aerodynamic shape	NACA 0010 airfoil

10 Control

This chapter aims to confirm controllability of the system. It sequentially builds up from defining the approach, forces and equations of motion to setting up a linear state model and the simulation step. The simulation aims to show *the Chameleon*'s ability to follow a straight line trajectory under disturbances, including actuator and input delay.

10.1. Core Subsystem Requirements

Due to *the Chameleon* design being unconventional and unproven regarding control strategy, the goal of this subsystem is to verify that stabilising the inherently unstable Chameleon design is possible within reasonable assumptions on the system. In the design process that means this subsystem is a test that the design needs to pass in order for it to be feasible. This goal is met once *the Chameleon* can reject step and oscillating disturbances similar to moth velocity jumps and resonant frequencies, while following a straight line trajectory within one *Chameleon* diameter $\sim 0.8\ m$.

10.2. Inputs and Outputs

The approach for controlling *the Chameleon* is built up from several steps. First the inputs and outputs of the system are stated. Next is a description of the modelling approach. Then the coordinate system, system states and modelling principle are briefly defined, followed by the Equations of Motion (EOM). The EOM are linearised, and used for a simulation of the states given a reference state.

The inputs required for this simulation are given in Table 10.1:

Table 10.1: All parameters used as input for the controller.

Parameter	Value	Unit	Justification
Total mass m	143.4	g	Structures
Diagonals Inertia matrix (I_{xx}, I_{yy}, I_{zz})	$[128358, 121242, 116419]$	$g{\cdot}mm^2$	Structures
Density ρ	1.225	kg/m^3	Aerodynamic Performance
Aerodynamic derivatives	depends on operating point see Table A.4 for an example	-	Aerodynamic Performance
Reference surface S_{ref}	0.004	m^2	Aerodynamic Performance
Reference chord c_{ref}	0.07	m	Aerodynamic Performance
Launch angle ε	Angle at which turret aims	rad	Tether
Time constant servo τ	0.032	s	Structures

These values are used to simulate the stability and control characteristics of *the Chameleon*. The output it produces functions as a measure of feasibility of the design given its parameters. This simulation will mainly

be used to confirm that the vane placement and size will allow *the Chameleon* to follow a target trajectory.

10.3. Modelling approach

Since *the Chameleon* does not operate in an equilibrium point, the states can not be linearised around one point. Besides this, the dynamics of the system are derived from computationally expensive VSPAERO simulations ($\sim$ 2 hours) done by the propulsion department. The combination of these two make a non-linear forward simulation computationally infeasible. To solve this a grid of three forward velocities (1, 6 and 12 m/s) and two motor rotation speeds (30000 and 41807 rpm) have been defined as operating points, based on a typical flight envelope velocities and rpm at 50% and 100% thrust. As the non-equilibrium operating points are linearised, a residual term is included stemming from the first term $\mathbf{f}(\mathbf{x_0}, \mathbf{u_0})$ of the Taylor series which would drop out in equilibrium. This term is included as a constant forcing term in the state-space model. These points are then interpolated to get a state-pace model based on the current velocity and rpm, for which gains are then obtained using a LQR-I controller. This approach can be compared to already well-established gain scheduling method [70, 71], however in this case the gains are based on the interpolated A and B matrices instead of interpolating the gains themselves. The LQR controller alone would not suffice, due to the constant term being impossible to reduce with just linear quadratic control [72]. This allows the LQR-I gains to be used to update the system state in a simulation, compared to just obtaining gains for a given grid point.

In these operating points the body is bilaterally symmetric and undergoes small disturbances, meaning lateral and longitudinal forces can be decoupled, and coupling terms can be neglected [73, 74]. Roll control can be actively stabilised in the current configuration as has been well established according to cited research by Theodoulis et all [75] and patents for roll damping controllers [76, 77]. Active roll stabilisation is necessary for the body to stay in the symmetrical and small disturbance regime keeping the decoupled forces simplification valid. Roll control will not be treated in this report due to aforementioned established methods, as well as integration of active roll control and pitch/yaw control being common practice [78, 79]. This means that when deriving and linearising the EOM roll angle and rate $\phi, \dot{\phi}$ and angular velocity and acceleration around the x_b axis, $\omega_x, \dot{\omega}_x$ are set to 0 as they are actively stabilised by the roll controller. This approach is verified in Table A by comparing the interpolated state-space matrices to a VSPAERO simulation at that exact point, as well as confirming that the LQR controller and simulation methods have been implemented correctly.

10.4. Model preliminaries

Three coordinate frames are defined in the context of the simulation, all of which are depicted in Figure 10.1.

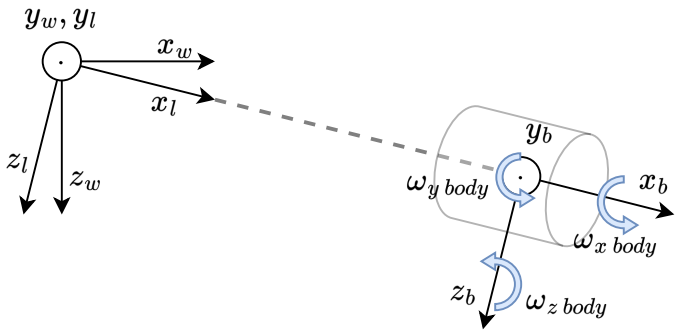

Figure 10.1: The world (inertial), launch and body coordinate frames depicted. The corresponding axis are labelled, with the y-axis pointing out of the page for each coordinate system. The launch coordinate system does not rotate when the mission starts.

The world frame is the static frame the moths are detected in, with the z_w axis pointing towards the centre of the Earth, and has its origin in the docking station. The launch frame has the same origin, however it is rotated by an angle ε about the y_w axis and by an angle δ about the z_w axis. These angles are determined by

the attitude of the docking station at launch (see Figure 12.2), and this frame is static once the mission starts. The body frame has its origin in the Centre of Mass (CoM) of *the Chameleon*, with the x_b axis being in line with the thrust force, the y_b axis being in line with the horizontal control vanes and the z_b axis being in line with the vertical control vanes.

To express the dynamic behaviour of *the Chameleon*, kinematic equations need to be expressed. From now on $\mathbf{p}$ refers to the position of *the Chameleon* expressed in the launch frame, $\mathbf{v_b}$ refers to the velocity of *the Chameleon* expressed in the body frame, $\boldsymbol{\eta}$ refers to the Tait-Bryan angles between the launch and the body frame, and $\boldsymbol{\omega_b}$ refers to the angular velocities in the body frame. Lastly, $\mathbf{a}$ indicates the angle between the world and the launch frame. The docking station will not rotate about the x_l axis, so this angle is left out.

$$\mathbf{p} = \begin{bmatrix} x \\ y \\ z \end{bmatrix}, \qquad \mathbf{v_b} = \begin{bmatrix} v_x \\ v_y \\ v_z \end{bmatrix}, \qquad \boldsymbol{\eta} = \begin{bmatrix} \phi \\ \theta \\ \psi \end{bmatrix}, \qquad \boldsymbol{\omega_b} = \begin{bmatrix} \omega_x \\ \omega_y \\ \omega_z \end{bmatrix}, \qquad \mathbf{a} = \begin{bmatrix} \varepsilon \\ \delta \end{bmatrix} \tag{10.1}$$

A typical trajectory of *the Chameleon* is aligned with the x_l axis due to disturbances being kept small, allowing the launch frame to be treated as an inertial frame [73]. A rotation matrix is needed to transform coordinates from the body to the launch frame and vice versa [80]. Since the roll controller keeps $\phi \approx 0$, assuming small angles means it can be left out of the rotation matrix. This simplifies the rotation matrix to Equation 10.3 which can transform a vector expressed in the body frame to the launch frame. For these equations to be valid, *the Chameleon* is assumed to be a rigid body [81].

$$\mathbf{R}_b^l(\psi, \theta) = \mathbf{R}_z(\psi) \cdot \mathbf{R}_y(\theta) \tag{10.2}$$

$$\mathbf{R}_b^l(\psi, \theta) = \begin{bmatrix} \cos\theta\cos\psi & -\sin\psi & \sin\theta\cos\psi \\ \cos\theta\sin\psi & \cos\psi & \sin\theta\sin\psi \\ -\sin\theta & 0 & \cos\theta \end{bmatrix} \tag{10.3}$$

Since Tait-Bryan rotation describe rotations about an independent reference frame their angular rates do not directly represent the angular velocities $\omega_\mathbf{b}$ [80]. To transform from $\omega_\mathbf{b}$ to $\dot{\eta}$, the rotational matrix W_η is needed [80, 81]. Again taking $\phi \approx 0$.

$$\boldsymbol{\omega_b} = \mathbf{W}_\eta \, \dot{\boldsymbol{\eta}} \quad \Rightarrow \quad \dot{\boldsymbol{\eta}} = \mathbf{W}_\eta^{-1} \, \boldsymbol{\omega_b} \tag{10.4}$$

$$\mathbf{W}_\eta = \begin{bmatrix} 1 & 0 & -\sin\theta \\ 0 & \cos\phi & \cos\theta\sin\phi \\ 0 & -\sin\phi & \cos\theta\cos\phi \end{bmatrix} = \begin{bmatrix} 1 & 0 & -\sin\theta \\ 0 & 1 & 0 \\ 0 & 0 & \cos\theta \end{bmatrix} \tag{10.5}$$

The inverse of this transformation matrix has singularities at $\pm 90°$ causing the transformation to fail [80]. This can be solved using quaternions, which add an additional variable to express an attitude [82]. Because the goal of this chapter is to show controllability and not provide the final controller of *the Chameleon*, quaternions will be left out of the scope. This means that the singularity-affected zone is excluded from the operating volume. Assuming a cone of 10° from ceiling to plant bed ($V \approx 0.88\ m^3$), reduces the operating volume ($V = 6 \cdot 6 \cdot 3 = 108\ m^3$) by 0.81% , making it safe to leave quaternions out of scope.

The Chameleon can translate and rotate in 3 different directions and around 3 different axes, making it a 6 Degrees of Freedom (DoF) system. To analyse the dynamics of the system in these six degrees, the Newton-Euler equations can be used under the assumption that the body is rigid and at a constant mass [80]. *the Chameleon* is considered rigid, as structure simulations confirm a maximum strain of 0.005 during braking. These loads are significantly higher than the loads during flight, thus, the strain is negligible and the body can be considered rigid. Mass is constant since *the Chameleon* does not consume or release anything during flight. The equations describe the forces and moments acting on a body's CoM as a function its translational

and rotational accelerations, and are given in Equation 10.6 [80, 83].

$$\begin{bmatrix} \mathbf{F} \\ \mathbf{M} \end{bmatrix} = \begin{bmatrix} m\mathbf{I}_3 & \mathbf{0} \\ \mathbf{0} & \mathbf{J} \end{bmatrix} \begin{bmatrix} \dot{\mathbf{v}}_b \\ \dot{\boldsymbol{\omega}}_b \end{bmatrix} + \begin{bmatrix} \mathbf{0} \\ \boldsymbol{\omega_b} \times \mathbf{J}\boldsymbol{\omega_b} \end{bmatrix} \tag{10.6}$$

$\mathbf{F}$	: $\mathbb{R}^3$ - External force acting on the CoM	[N]
$\mathbf{M}$	: $\mathbb{R}^3$ - External moment acting about the CoM	[N·m]
m	: $\mathbb{R}^1$ - Mass of the body	[kg]
$\mathbf{J}$	: $\mathbb{R}^{3\times3}$ - Moment of inertia about the CoM	$[kg \cdot m^2]$
$\dot{\boldsymbol{v}}_{\boldsymbol{b}}$	: $\mathbb{R}^3$ - Linear acceleration	$[m/s^2]$
$\dot{\boldsymbol{\omega}}_{\boldsymbol{b}}$	: $\mathbb{R}^3$ - Angular acceleration	$[rad/s^2]$

The Chameleon is assumed to be cylindrically symmetric about the x_b axis making the inertia matrix $\mathbf{J}$ only keep its diagonal entries as visible in Equation 10.7.

$$\mathbf{J} = \begin{bmatrix} J_{xx} & 0 & 0 \\ 0 & J_{yy} & 0 \\ 0 & 0 & J_{zz} \end{bmatrix} \tag{10.7}$$

This is validated by the CAD model made by the structures department, which showed the off diagonal inertias being two orders of magnitude lower.

10.5. Equations of Motion

To solve the Newton-Euler equations mentioned in the previous section. The forces and moments acting on the body need to be determined. A sketch of the forces acting on *the Chameleon* is shown in Figure 10.2.

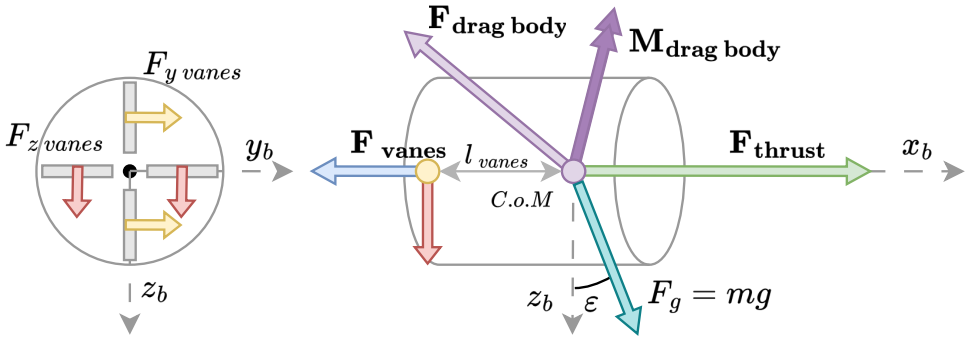

Figure 10.2: Side and back view showing vane, body, gravity and thrust forces and moments. Coloured circles indicate forces coming out of the page. The moments created by the vanes are not shown, but can be derived from the acting point of the vane forces.

Since the roll controller keeps $\phi \approx 0$, the four vane forces will be grouped into a horizontal (vanes at$\pm y$) and a vertical (vanes at $\pm z$) mode where these vanes act together to influence the remaining pitch and yaw angles. They create control forces in pure y_b and z_b directions and drag in the negative x_b direction. These control forces acting at the vane locations result in control moments acting about the CoM. The thrust force acts along the x_b axis and does not produce a moment. Asymmetric vane deflections are not treated here and are left for the roll controller. The aerodynamic forces and moments on the body are modelled as unknown 3-dimensional vectors acting in the CoM. They will depend on the angle of attack $\alpha = \arctan(\frac{v_z}{v_x})$, sideslip angle $\beta = \arcsin(\frac{v_y}{|\mathbf{v}|})$, ω_y and ω_z. The gravity force acts under the angle ε determined at launch. Due to the way these forces will be determined, they are all modelled as positive forces expressed in pure x_b, y_b and z_b directions and are elaborated upon in linearisation. The roll controller keeps the moment around x_b in

equilibrium, meaning M_x is set to 0 for this controller, and gravity will only be considered in the x_b and z_b directions. A summary of all forces and moments is given in Equation 10.8:

$$\mathbf{F_b} = \begin{bmatrix} F_{x\ body} + F_{x\ vanes} + F_{thrust} + F_{x\ grav} \\ F_{y\ body} + F_{y\ vanes} \\ F_{z\ body} + F_{z\ vanes} + F_{z\ grav} \end{bmatrix},\ \mathbf{M_b} = \begin{bmatrix} 0 \\ M_{y\ body} + M_{y\ vanes} \\ M_{z\ body} + M_{z\ vanes} \end{bmatrix} \tag{10.8}$$

To describe the translational and rotational dynamics of *the Chameleon*, firstly the derivative of the velocity and angular velocity needs to be expressed in terms of forces and moments [84]. Secondly, the derivatives of position $\dot{\mathbf{p}}$ and attitude $\dot{\boldsymbol{\eta}}$ need to be connected to the translational and angular velocity by a kinematic relation [84]. For the translational dynamics Equation 10.6 can be used, however, this equation only holds in an inertial frame, meaning the Coriolis rotation needs to be included [73]:

$$\dot{\mathbf{v}}_b = \frac{\mathbf{F_b}}{m} - \boldsymbol{\omega_b} \times \mathbf{v_b} \tag{10.9}$$

Due to the roll controller stabilising ω_x, it is taken to be zero resulting in:

$$\begin{bmatrix} \dot{v}_x \\ \dot{v}_y \\ \dot{v}_z \end{bmatrix} = \frac{1}{m} \begin{bmatrix} F_{x\ body} + F_{x\ vanes} + F_{thrust} + F_{x\ grav} \\ F_{y\ body} + F_{y\ vanes} \\ F_{z\ body} + F_{z\ vanes} + F_{z\ grav} \end{bmatrix} + \begin{bmatrix} \omega_z \cdot v_y - \omega_y \cdot v_z \\ -\omega_z \cdot v_x \\ \omega_y \cdot v_x \end{bmatrix} \tag{10.10}$$

The derivative of position is the velocity of the body expressed in the launch frame. To connect this to the velocity in the body frame, the transformation matrix $\mathbf{R}_b^l$ in Equation 10.3 can be used resulting in:

$$\dot{\mathbf{p}} = \mathbf{R}_b^l\ \mathbf{v_b} \tag{10.11}$$

Writing out this multiplication and adding Equation 10.10 gives us the following set of equations to describe the translational dynamics:

$$\mathbf{f_T}(\mathbf{x}, \mathbf{u}) \begin{cases} \dot{x} = v_x \cos\theta \cos\psi - v_y \sin\psi + v_z \sin\theta \cos\psi \\ \dot{y} = v_x \cos\theta \sin\psi + v_y \cos\psi + v_z \sin\theta \sin\psi \\ \dot{z} = -v_x \sin\theta + v_z \cos\theta \\ \dot{v}_x = \frac{1}{m}(F_{x\ body} + F_{x\ vanes} + F_{thrust} + F_{x\ grav}) + \omega_z \cdot v_y - \omega_y \cdot v_z \\ \dot{v}_y = \frac{1}{m}(F_{y\ body} + F_{y\ vanes}) + \omega_z \cdot v_x \\ \dot{v}_z = \frac{1}{m}(F_{z\ body} + F_{z\ vanes} + F_{z\ grav}) + \omega_y \cdot v_x \end{cases} \tag{10.12}$$

The rotational acceleration in the body frame can be solved from Equation 10.6.

$$\dot{\boldsymbol{\omega}}_{\boldsymbol{b}} = \mathbf{J}^{-1}(\mathbf{M_b} - \boldsymbol{\omega_b} \times \mathbf{J}\boldsymbol{\omega_b}) \tag{10.13}$$

Since ω_x and $\dot{\omega}_b$ are treated separately by the roll controller they are taken to be zero, causing the cross product $\boldsymbol{\omega_b} \times \mathbf{J}\boldsymbol{\omega_b}$ to reduce to zero and giving:

$$\begin{bmatrix} \dot{\omega}_x \\ \dot{\omega}_y \\ \dot{\omega}_z \end{bmatrix} = \begin{bmatrix} 0 \\ \frac{1}{J_{yy}}(M_{y\ body} + M_{y\ vanes}) \\ \frac{1}{J_{zz}}(M_{z\ body} + M_{z\ vanes}) \end{bmatrix} \tag{10.14}$$

Now to transform from the angular velocities in the body frame to the derivatives of the Tait-Bryan angles the inverse of Equation 10.5 can be used. Similarly to $\dot{\omega}_x$ the roll rate $\dot{\phi}$ is also taken to be zero, as it is treated by the roll controller.

$$\dot{\boldsymbol{\eta}} = \mathbf{W}_\eta^{-1} \boldsymbol{\omega_b} \tag{10.15}$$

Writing out this multiplication and adding Equation 10.14 gives the following set of equations to describe the rotational dynamics:

$$\mathbf{f_R}(\mathbf{x},\mathbf{u}) \begin{cases} \dot{\phi} = 0 \\ \dot{\theta} = \omega_y \\ \dot{\psi} = \frac{1}{\cos\theta}\omega_z \\ \dot{\omega}_x = 0 \\ \dot{\omega}_y = \frac{1}{J_{yy}}(M_{y\ body} + M_{y\ vanes}) \\ \dot{\omega}_z = \frac{1}{J_{zz}}(M_{z\ body} + M_{z\ vanes}) \end{cases} \tag{10.16}$$

10.6. Linearisation

The non-linear translational and rotational dynamic equations can be split into state and output equations [84].

$$\dot{\mathbf{x}} = \mathbf{f}(\mathbf{x},\mathbf{u}) \tag{10.17}$$

$$\mathbf{y} = \mathbf{h}(\mathbf{x},\mathbf{u}) \tag{10.18}$$

Where **x** and **u** are the state- and input-vector, **f** is the state equation-vector and **y** and **h** are the output-vector and output equations-vector, respectively. As mentioned during the modelling approach, six grid points with varying forward $+x_b$ velocity (1, 6 and 12 m/s) and rpm (30000 and 41807 rpm) are defined as operating points to approximate the non-linear characteristics. The characteristics of *the Chameleon*, will vary at each of these points meaning each force and moment is a function of velocity and rpm. Besides that, these forces and moments also depend on states and inputs, requiring derivatives with respect to these states and inputs to perform linearisation. Due to the small disturbances in these operating points, many of the forces and moments can be decoupled, and coupling forces can be neglected. It was found that linearising around $\theta \approx 0$, limits how much thrust can be used to sustain *the Chameleon*'s weight. Linearising around the angle required to sustain its weight $\theta = \arcsin(\frac{1}{TtW})$ resulted in a moment about the y_b axis too large to counteract. As a solution, an angle between these two was chosen to linearise around, which gives, $\theta_0 = \arcsin(\frac{1}{TtW})/2$. This angle can be calculated from the thrust coefficient C_{thr} and rpm at each grid point, and the VSPAERO simulations are also set at this angle. Following are the definitions of a few (linearised) terms starting with the dynamic pressure:

$$V = \sqrt{v_x^2 + v_y^2 + v_z^2}, \quad q = \frac{1}{2}\rho V^2, \quad v_{x0} = \cos(\theta_0)V, \quad v_{z0} = \sin(\theta_0)V \tag{10.19}$$

$$\frac{\partial q}{\partial x}\Big|_{\mathbf{x_0},\mathbf{u_0}} = \rho v_{x0} = q_x, \quad \frac{\partial q}{\partial y}\Big|_{\mathbf{x_0},\mathbf{u_0}} = 0, \quad \frac{\partial q}{\partial z}\Big|_{\mathbf{x_0},\mathbf{u_0}} = \rho v_{z0} = q_z, \quad q_0 = \frac{1}{2}\rho(v_{x0}^2 + v_{z0}^2) \tag{10.20}$$

The angle of attack α and sideslip angle β become:

$$\frac{\partial \alpha}{\partial v_x}\Big|_{\mathbf{x_0},\mathbf{u_0}} = \frac{-v_{z0}}{v_{x0}^2 + v_{z0}^2} = \alpha_x, \quad \frac{\partial \alpha}{\partial v_y}\Big|_{\mathbf{x_0},\mathbf{u_0}} = 0, \quad \frac{\partial \alpha}{\partial v_z}\Big|_{\mathbf{x_0},\mathbf{u_0}} = \frac{v_{x0}}{v_{x0}^2 + v_{z0}^2} = \alpha_z \tag{10.21}$$

$$\frac{\partial \beta}{\partial v_x}\Big|_{\mathbf{x_0},\mathbf{u_0}} = 0, \quad \frac{\partial \beta}{\partial v_y}\Big|_{\mathbf{x_0},\mathbf{u_0}} = \frac{1}{\sqrt{v_{x0}^2 + v_{z0}^2}} = \beta_y, \quad \frac{\partial \beta}{\partial v_z}\Big|_{\mathbf{x_0},\mathbf{u_0}} = 0 \tag{10.22}$$

Lastly the gravity terms are linearised:

$$\dot{v}_{x\ grav} = g\sin(\varepsilon - \theta)\Big|_{\mathbf{x_0},\mathbf{u_0}} \approx g\sin(\varepsilon - \theta_0) - g\cos(\varepsilon - \theta_0)\cdot\theta \tag{10.23}$$

$$\dot{v}_{z\ grav} = g\cos(\varepsilon - \theta)\Big|_{\mathbf{x_0},\mathbf{u_0}} \approx g\cos(\varepsilon - \theta_0) + g\sin(\varepsilon - \theta_0)\cdot\theta \tag{10.24}$$

Combining all these terms, and linearising the forces with respect to their corresponding derivatives results in the following linearised EOM:

$$\mathbf{f}(\mathbf{x},\mathbf{u}) \begin{cases} \dot{x} \approx v_{x0}\cos(\theta_0) + v_{z0}\sin(\theta_0) + v_x \cdot \cos(\theta_0) + v_z \cdot \sin(\theta_0) + \theta \cdot (v_{z0}\cos(\theta_0) - v_{x0}\sin(\theta_0)) \\ \dot{y} \approx v_y \cdot \cos(\theta_0) + \psi \cdot (v_{x0}\cos(\theta_0) + v_{z0}\sin(\theta_0)) \\ \dot{z} \approx -v_{x0}\sin(\theta_0) + v_{z0}\cos(\theta_0) - v_x \cdot \sin(\theta_0) + v_z \cdot \cos(\theta_0) - \theta \cdot (v_{x0}\cos(\theta_0) + v_{z0}\sin(\theta_0)) \\ \dot{v}_x \approx \frac{1}{m}C_{X0}S_{ref}(q_0 + v_x \cdot q_x + v_z \cdot q_z) + \frac{1}{m}C_{thr}\rho d^4((\frac{rpm_0}{60})^2 + 2 \cdot \frac{rpm}{3600}) \\ +g\sin(\varepsilon - \theta_0) - \theta \cdot g\cos(\varepsilon - \theta_0) - \omega_y \cdot v_{z0} \\ \dot{v}_y \approx \frac{1}{m}C_{Y_\beta}q_0 S_{ref}(v_y \cdot \beta_y) + \frac{1}{m}C_{Y\delta_{ver}}q_0 S_{ref} \cdot \delta_{ver} - \omega_z \cdot v_{x0} \\ \dot{v}_z \approx \frac{1}{m}C_{Z0}S_{ref}(q_0 + v_x \cdot q_x + v_z \cdot q_z) + \frac{1}{m}C_{Z_\alpha}q_0 S_{ref}(v_x \cdot \alpha_x + v_z \cdot \alpha_z) + \frac{1}{m}C_{Z\delta_{hor}}q_0 S_{ref} \cdot \delta_{hor} \\ +g\cos(\varepsilon - \theta_0) + \theta \cdot g\sin(\varepsilon - \theta_0) + \omega_y \cdot v_{x0} \\ \dot{\phi} = 0 \\ \dot{\theta} \approx \omega_y \\ \dot{\psi} \approx \frac{1}{\cos(\theta_0)} \cdot \omega_z \\ \dot{\omega}_x = 0 \\ \dot{\omega}_y \approx \frac{1}{J_{yy}}C_{MY0}S_{ref}c_{ref}(q_0 + v_x \cdot q_x + v_z \cdot q_z) + \frac{1}{J_{yy}}C_{MY_\alpha}q_0 S_{ref}c_{ref}(v_x \cdot \alpha_x + v_z \cdot \alpha_z) \\ +\frac{1}{J_{yy}}q_0 S_{ref}c_{ref}(C_{MY\omega_y} \cdot \omega_y + C_{MY\delta_{hor}} \cdot \delta_{hor}) \\ \dot{\omega}_z \approx \frac{1}{J_{zz}}q_0 S_{ref}c_{ref}(C_{MZ_\beta} \cdot v_y \cdot \beta_y + C_{MZ\omega_z} \cdot \omega_z + C_{MY\delta_{ver}} \cdot \delta_{ver}) \end{cases} \tag{10.25}$$

Here all coefficients except the thrust coefficient are normalised with dynamic pressure $q = \frac{1}{2}\rho V^2$ and a reference surface S_{ref}. The thrust coefficient is normalised with $rps^2\rho d^4$ where RPS stands for revolutions per second and d is the propeller diameter which is the usual convention for VSPAERO [63]. Moments are normalised with an extra reference chord c_{ref}. All coefficients mentioned will be approximated using VSPAERO simulations done by the propulsion department (see Chapter 9). These simulations change one state or input variable ($\alpha, \beta, \omega_y, \omega_z, \delta_{hor}$ or δ_{ver}) by 0.1 deg, measure resultant forces and moments and subtract them from a non-disturbed simulation to then calculate the slope to linearise the corresponding variable [85]. Because of this, the typical drag behaviour (parabolic drag curve) can not be modelled. The drag terms will remain small around the linearisation point (α and β deviate $\pm 5°$), and are therefore not included. The basic drag C_{X0} is included as it only depends on velocity. The non-zero force C_{Z0} in z_b and moment C_{MY0} about y_b caused by the tilt angle θ_0 are also included.

The VSPAERO derivatives provide a first-order approximation of the aerodynamic characteristics of *the Chameleon*. Meaning the simulation method imposes limitations on the accuracy and the types of derivatives that can be obtained. Linearised potential flow-based solvers used by VSPAERO can not accurately simulate flow separation and underestimate total drag due to inviscid flow assumptions [86]. Besides this, VSPAERO can not estimate second-order derivatives [85]. These limitations introduce error in the derivatives as shown in Appendix A. In the context of this controller, there are no real alternatives to using results from this simulation as motivated in Section 9.2.

10.7. State-space system

With most terms being or ready to be linearised, the modelling method can be established. Linear Time Invariant (LTI) systems are traditionally represented with a state-space model [84], however due to the non-zero equilibrium a residual term $\mathbf{f}(\mathbf{x_0}, \mathbf{u_0})$ must be included making it an affine system [87]. This term can be modelled as a constant disturbance for which the controller then must correct for [88, 87]. This results in the following set of equations:

$$\dot{\mathbf{x}} = \mathbf{A}\mathbf{x} + \mathbf{B}\mathbf{u} + \mathbf{f_0} \tag{10.26}$$

$$\mathbf{y} = \mathbf{C}\mathbf{x} + \mathbf{D}\mathbf{u} \tag{10.27}$$

Where **A** is the state matrix, **B** is the input matrix, **C** is the output matrix and **D** is the feedthrough matrix. The state and input vector can be defined based on the simplified equations in Equation 10.25.

$$\mathbf{x} = \begin{bmatrix} x & y & z & v_x & v_y & v_z & \theta & \psi & \omega_y & \omega_z \end{bmatrix}^T \tag{10.28}$$

$$\mathbf{u} = \begin{bmatrix} rpm & \delta_{hor} & \delta_{ver} \end{bmatrix}^T \tag{10.29}$$

Each entry of matrix A and B is then defined as the derivative of $f(\mathbf{x}, \mathbf{u})_i$ with respect to each state x_j and input u_j respectively, linearised at the operating point:

$$\mathbf{A}_{i,j} = \frac{\delta f(\mathbf{x}, \mathbf{u})_i}{\delta x_j}\Big|_{\mathbf{x_0}, \mathbf{u_0}} \qquad \mathbf{B}_{i,j} = \frac{\delta f(\mathbf{x}, \mathbf{u})_i}{\delta u_j}\Big|_{\mathbf{x_0}, \mathbf{u_0}} \tag{10.30}$$

This then results in the state matrix, input matrix and residual term for *the Chameleon*, which are all linearised about their corresponding grid point velocity $\mathbf{x_0}$ and rpm $\mathbf{u_0}$.

$$\text{A=}\begin{bmatrix} \mathbf{0}_3 & \begin{bmatrix} \cos(\theta_0) & 0 & \sin(\theta_0) \\ 0 & \cos(\theta_0) & 0 \\ -\sin(\theta_0) & 0 & \cos(\theta_0) \end{bmatrix} & \begin{bmatrix} v_{z0}\cos(\theta_0) - v_{x0}\sin(\theta_0) & 0 \\ 0 & v_{x0}\cos(\theta_0) + v_{z0}\sin(\theta_0) \\ -v_{x0}\cos(\theta_0) - v_{z0}\sin(\theta_0) & 0 \end{bmatrix} & \mathbf{0}_{3\times 2} \\ \mathbf{0}_3 & \begin{bmatrix} \frac{1}{m}C_{X0}q_xS_{ref} & 0 & \frac{1}{m}C_{X0}q_zS_{ref} \\ 0 & \frac{1}{m}C_{Y_\beta}k_f\beta_y & 0 \\ \frac{1}{m}C_{Z0}q_xS_{ref} + \frac{1}{m}C_{Z_\alpha}k_f\alpha_x & 0 & \frac{1}{m}C_{Z0}q_xS_{ref} + \frac{1}{m}C_{Z_\alpha}k_f\alpha_z \end{bmatrix} & \begin{bmatrix} -g\cos(\varepsilon-\theta_0) & 0 \\ 0 & 0 \\ g\sin(\varepsilon-\theta_0) & 0 \end{bmatrix} & \begin{bmatrix} -v_{z0} & 0 \\ 0 & -v_{x0} \\ v_{x0} & 0 \end{bmatrix} \\ \mathbf{0}_{2\times 3} & \mathbf{0}_{2\times 3} & \mathbf{0}_{2\times 2} & \begin{bmatrix} 1 & 0 \\ 0 & \frac{1}{\cos(\theta_0)} \end{bmatrix} \\ \mathbf{0}_{2\times 3} & \begin{bmatrix} \frac{1}{J_{yy}}C_{MY0}q_xS_{ref}c_{ref} & 0 & \frac{1}{J_{yy}}C_{MY0}q_zS_{ref}c_{ref} \\ +\frac{1}{J_{yy}}C_{MY_\alpha}k_m\alpha_x & & +\frac{1}{J_{yy}}C_{MY_\alpha}k_m\alpha_z \\ 0 & \frac{1}{J_{zz}}C_{MZ_\beta}k_m\beta_y & 0 \end{bmatrix} & \mathbf{0}_{2\times 2} & \begin{bmatrix} \frac{1}{J_{yy}}C_{MY_{\omega_y}}k_m & 0 \\ 0 & \frac{1}{J_{zz}}C_{MZ_{\omega_z}}k_m \end{bmatrix} \end{bmatrix} \in \mathbb{R}^{10\times 10} \tag{10.31}$$

$$\mathbf{B} = \begin{bmatrix} \mathbf{0}_3 \\ \begin{bmatrix} \frac{2}{m}C_{thr}(\frac{rpm}{3600})\rho d^4 & 0 & 0 \\ 0 & 0 & \frac{1}{m}C_{Y\delta_{ver}}k_f \\ 0 & \frac{1}{m}C_{Z\delta_{hor}}k_f & 0 \end{bmatrix} \\ \mathbf{0}_{3\times 2} \\ \begin{bmatrix} 0 & \frac{1}{J_{yy}}C_{MY\delta_{hor}}k_m & 0 \\ 0 & 0 & \frac{1}{J_{zz}}C_{MZ\delta_{ver}}k_m \end{bmatrix} \end{bmatrix} \in \mathbb{R}^{10\times 3} \tag{10.32}$$

$$\mathbf{f}_0 = \begin{bmatrix} v_{x0}\cos(\theta_0) + v_{z0}\sin(\theta_0) \\ 0 \\ -v_{x0}\sin(\theta_0) + v_{z0}\cos(\theta_0) \\ \frac{1}{m}\left(C_{X0}k_f + C_{thr}\left(\frac{rpm_0}{60}\right)^2\rho d^4\right) + g\sin(\varepsilon - \theta_0) \\ 0 \\ \frac{1}{m}C_{Z0}k_f + g\cos(\varepsilon - \theta_0) \\ \mathbf{0}_{2\times 1} \\ \frac{1}{J_{yy}}C_{MY0}k_m \\ 0 \end{bmatrix} \in \mathbb{R}^{10\times 1} \tag{10.33}$$

With coefficients $k_f = q_0 S_{ref}$ and $k_m = q_0 S_{ref} c_{ref}$ the **C** matrix is an identity matrix $[\mathbf{I_{10}}]$ as position can be measured by the PATS-C camera system from which velocity can be estimated. Angular rate can be measured by the IMU (will be presented in Figure 12.9a), and in combination with accelerometer data it can be used to estimate attitude [89]. The **D** matrix is $[\mathbf{0_{10\times 3}}]$, since the input does not affect the output state directly [88].

10.8. Interpolation and simulation

The interpolation and simulation methods used will be sequentially explained based on when they happen in the time step. First the current velocity and rpm are extracted from the state and input vector. The A

and B matrix and residual term are set up at the 3x2 velocity-, rpm-grid. These are interpolated by calling the MATLAB `interpn()` function for each matrix entry and linearly interpolating on the 3x2 grid at the current velocity and rpm [90]. This results in an interpolated matrix $\mathbf{A_i}$, $\mathbf{B_i}$ and $\mathbf{f_{0i}}$. Then a LQR-I controller is implemented. A LQR-I controller finds gains $\mathbf{K}$ that minimise the cost function [72].

$$\mathbf{J} = \int_0^\infty [\mathbf{x^T Q x} + \mathbf{u^T R u}]dt \tag{10.34}$$

Where $\mathbf{Q}$ and $\mathbf{R}$ are the state weighting matrix and input weighting matrix respectively [72]. These are tuning parameters that are to be experimentally found by the control designer. This cost function can be automatically reduced by the `lqr(A, B, Q, R)` function in MATLAB [91]. An integrator is required to reduce the steady state error introduced by the residual term to zero. To implement the integral controller A, B, Q and R matrix in this function are augmented analogous to the method described by Srivastava et all [92]. This results in a gain vector $\mathbf{K}$ which is based on the interpolated matrices $\mathbf{A_i}$, $\mathbf{B_i}$ and $\mathbf{f_{0i}}$ the experimentally determined $\mathbf{Q}$ (including weights for the integrator terms $\mathbf{K_r}$) and $\mathbf{R}$ matrices and the tracking matrix $\mathbf{C_{track}}$ which selects the terms the integrator should reduce (in this case p_y and p_z these terms cause deviation from the reference path). These gains can then be used to calculate the optimal inputs for the next time step based on the reference state and input [72].

$$\mathbf{u_{n+1}} = \mathbf{u_0} - \mathbf{K_x}(\mathbf{x} - \mathbf{x_0}) - \mathbf{K_r z} \tag{10.35}$$

Here $\mathbf{u_0}$ is the reference input which is full throttle (41807 rpm), $\mathbf{x_0}$ is the reference state which has p_x unregulated, tries to let the v_x and v_z follow the linearisation about the tilt angle and keeps the remaining terms zero. Steady state error is given by $\mathbf{z}$. The input gains $\mathbf{K_x}$ are by the LQR function in MATLAB, $\mathbf{K_r}$ are the integrator gains. With the updated inputs per step calculated, the states can be updated using RK4, which is has better cost vs error characteristics $\mathcal{O}(h^4)$ compared to other first-order methods [93].

$$\dot{\mathbf{x}}_n = \mathbf{A_i x_n} + \mathbf{B_i u_{n+1}} + \mathbf{f_{0i}} = \mathbf{f}(\mathbf{x_n}) \tag{10.36}$$
$$k_1 = \mathbf{f}(\mathbf{x_n}) \tag{10.37}$$
$$k_2 = \mathbf{f}(\mathbf{x_n} + \frac{k_1}{2}) \tag{10.38}$$
$$k_3 = \mathbf{f}(\mathbf{x_n} + \frac{k_2}{2}) \tag{10.39}$$
$$k_4 = \mathbf{f}(\mathbf{x_n} + k_3) \tag{10.40}$$
$$\mathbf{x}_{n+1} = \mathbf{x_n} + \frac{1}{6}(k_1 + 2k_2 + 2k_3 + k_4) + \mathcal{O}(h^4) \tag{10.41}$$

This loop can be repeated at every time step for a specified amount of running time, given the time step is small enough to stay in the stability region. The stability condition is given in Equation 10.42 [94].

$$|R(z)| \leq 1, \qquad R(z) = 1 + z + \frac{z^2}{2} + \frac{z^3}{6} + \frac{z^4}{24}, \quad with\ z = \lambda dt \tag{10.42}$$

Here lambda represents the largest eigenvalue in the matrix. The largest eigenvalue is -2371.5 and can be found in Table 10.2. A timestep of $dt = 1e^{-4}$ then results in $z = -0.237$ meaning $|R(z)| = 0.808$ giving a margin of 0.192.

10.9. Delay and disturbances

The current simulation does not implement delays or disturbances, which is not realistic. The gap between reality and simulation is an active area of research for UAV's [95]. In the context of this controller, servo time delay, input delay and external velocity disturbances were expected to have the highest impact [96, 97]. Motor settling time is not included since an average mission flies at max throttle only. Methods used for implementing these effects are well established, and will only be referred to for this section. The time constant is implemented as a first-order process explained in the Aircraft Control and Simulation textbook by Stevens

[84] and demonstrated by Spencer et al. [96]. Actuator delay is explained and demonstrated by Shampine et all [98]. Disturbance inputs are explained and demonstrated by Franklin et all [72]. The actuator delay is derived from the servo selected by the Structures department ($60°/0.15s \rightarrow 20°/0.05s,\ 0.632 \cdot 0.05 = 0.032s$). The delay is taken to be 5 ms based on an estimation provided by PATS and ExpressLRS packet rate frequencies (protocol used by pats) [99]. Disturbance inputs are based on oscillations at the propeller frequency as well as longitudinal and lateral rectangular pulses based on moth velocity jumps.

10.10. Confirming stability

To confirm that assumptions are not violated (linearisation, small angles) two disturbance scenarios are given. These scenarios are given as a worst case trajectory (launch angle $\varepsilon = 10°$ and mission duration 0.7 s). Accuracy numbers are not presented here and will be treated in Chapter 12. The first scenario is the response of the Chameleon to a sudden change in moth velocity. From provided data by PATS, the normalised velocity and it's slope (acceleration) were plotted, from which a rectangular pulse of 20 m/s in v_y and v_z at a pulse width of 0.05 s was modelled as an external disturbance.

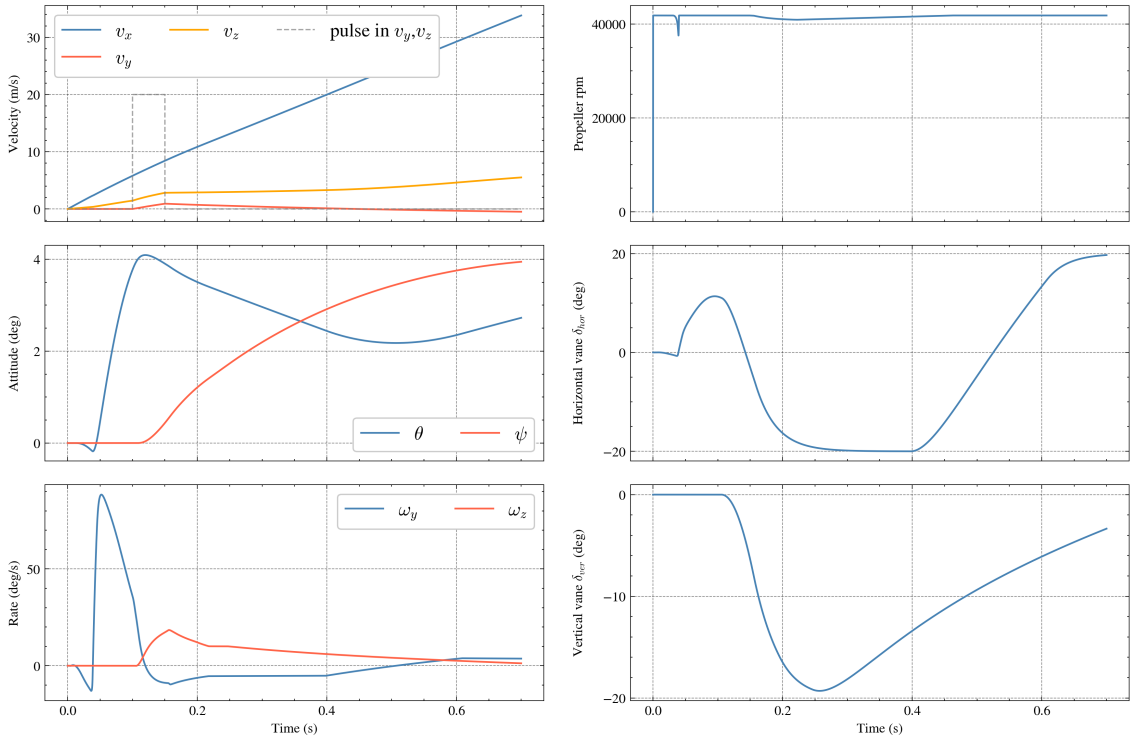

Figure 10.3: States and Inputs of Chameleon responding to rectangular pulse at t=0.1 s. Pulse has magnitude 20 m/s and pulse width 0.05 s. Launch angle $\varepsilon = 10°$ and mission duration 0.7 s (worst case scenario).

The second scenario is based on oscillations at the maximum propeller frequency ($41807/60 = 696\ Hz$) and using a balancing grade of G6.3 from the ISO standard [100]. Then using $e = \frac{G}{\omega} =$ this gives a vibration force of $F_0 = me\omega^2 = 0.055N$ giving an acceleration of $a_0 = \frac{0.055}{0.143} = 0.38m/s^2$ [101]. Assuming a harmonic cosine wave of amplitude a_0, a velocity disturbance is approximated by assuming the velocity jump is equal to the area underneath the oscillation in one wave which results in $v_{dist} \approx 2 \cdot 0.38 = 0.76\ m/s \approx 1$. This results in the following graph.

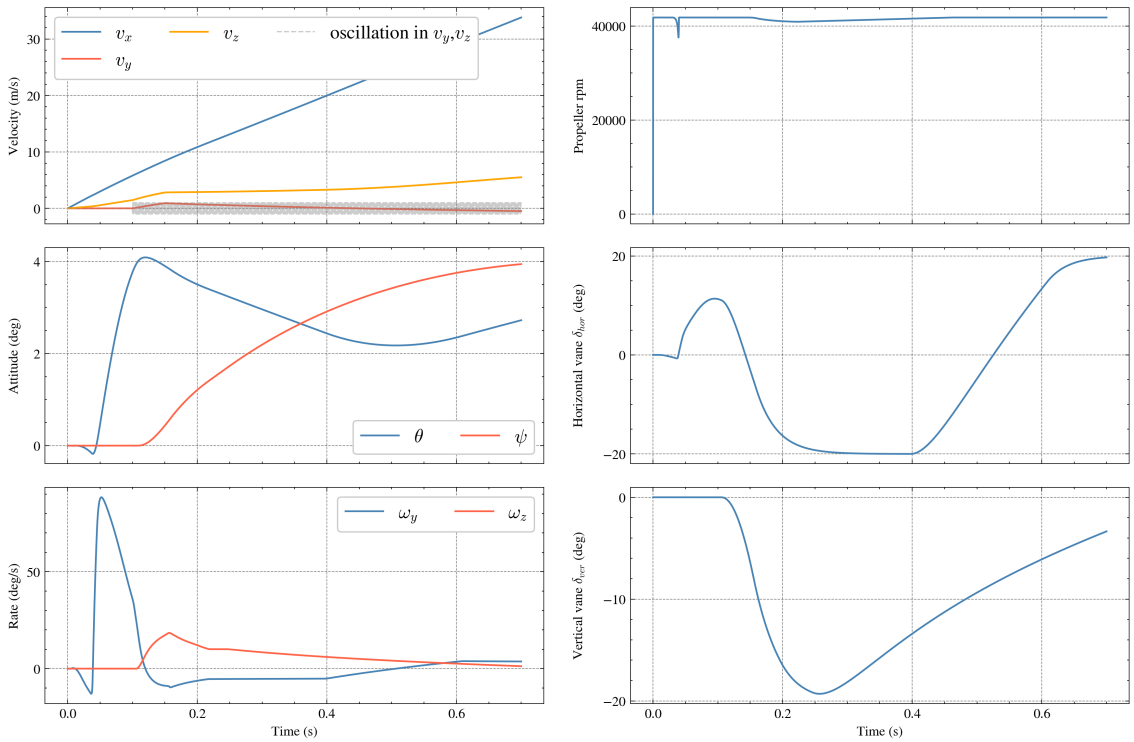

Figure 10.4: States and Inputs of Chameleon responding to an oscillation at t=0.1 s. Oscillation has magnitude 1 m/s and frequency of 696 Hz. Launch angle $\varepsilon = 10°$ and mission duration 0.7 s (worst case scenario).

As can be seen in both Figure 10.3 and Figure 10.4, the pitch and yaw angles stay under 5° meaning small angle error stays below $(1 - \cos(5°) \cdot 100\% \approx 0.38\%,\ \sin(5°) \cdot 100\% \approx 8.71\%)$. Error in VSPAERO parameters depends on the parameter itself, however typically error remains small for $\alpha, \beta < 10 - 20°$ which is generally true for both disturbance scenarios ($v_y, v_z < \frac{1}{3} v_x$.
To confirm that the controller stabilises the Chameleon, the open- and closed-loop eigenvalues are given in Table 10.2.

Table 10.2: Eigenvalues of open- and closed-loop state-space matrix at t=0.7 s.

Mode	Open loop eigenvalue	Closed loop eigenvalue
1	0	-971.6
2	0	-2137.5
3	0	-31.3
4	0	-31.3
5	2.1	-2.2
6	-971.5	-1.1 + 1.2i
7	-2137.4	-1.1 - 1.2i
8	0	-2.7
9	-0.1	-0.8 + 0.9i
10	-2.7	-0.8 - 0.9i
11	-31.2	-0.1
12	-31.2	-0.7

The open-loop eigenvalues have one positive unstable entry. The closed-loop eigenvalues are all negative, meaning the controller does effectively stabilise the Chameleon.

10.11. Iterations

The Control subsystem is included in IL-2 aiming to confirm stability, IL-3 aiming to balance loads on structure, and IL-4 aiming to confirm compliance with requirements. For each iteration loop, the convergence for control follows the same procedures. First, new aerodynamic derivatives, mass and inertia figures are provided by other subsystems. Then the Q and R matrices for the LQR-I controller are tuned, and finally the simulation is run to see the accuracy of the new model. The output is either a confirmation of the trajectory error being acceptable, or the trajectory error being too big, meaning the loop gets retriggered. The simulation also allows for troubleshooting, giving insight in what property of the design limits *the Chameleon*'s performance.

11
Flight Profile

In this final iteration chapter, mission and operational requirements are considered and iterated. With the values mentioned throughout the previous iteration chapters, the general performance of the system can be determined.

11.1. Core Subsystem Requirements

The following core subsystem requirements were derived. These first-listed requirements are only the core requirements that were derived from the system requirements and were actively used in the design phase. The second-listed requirements are requirements that the tether department received from other subsystems.

- SYS-01-TET-01: The tether shall be used as the braking mechanism.
- SYS-01-TET-02: The tether shall enable a stopping distance $\leq$ 0.8 m from 5 m/s.
- SYS-03-TET-01: The tether shall withstand a force of at least 5 kg.
- SYS-22-TET-01: The tether subsystem mass shall be below 3 grams.
- SYS-32-TET-01: The tether subsystem shall be made of off-the-shelf or 3D-printed components.
- SYS-38-TET-01: The subsystem shall be able to reel back the drone without hitting the ground.

The only constraint that was received from other subsystems was the following:

- STR-TET-01: The g-loading during braking shall not exceed 40 g

11.2. Tools and Motivation

The primary objective of the tether analysis is to validate that the tethered drone can execute its target mission profile within the defined constraints of Section 11.1. This section outlines the analytical framework and subsystem interfaces used to evaluate the platform.

Simulation tools

To assess the kinematic and dynamic performance of *the Chameleon*, a continuous-time multibody dynamics approach is employed using the MuJoCo (Multi-Joint dynamics with Contact) engine [102, 103]. MuJoCo's use of generalised coordinates allows for the evaluation of the continuous flight envelope, specifically, the spooling dynamics, tether tension spikes, and multibody interactions during the mission.

The simulation quantifies the feasible operating area, maximum g-forces, braking distance, interception speed, and drone behaviour during and after braking. The selection of MuJoCo over structural solvers (such as ANSYS) was driven by its native Python bindings, which facilitate the integration of a custom aerodynamic algorithm within a familiar programming environment for the team.

Because MuJoCo lacks a native aerodynamic drag model [104], a standard quadratic drag formula is implemented. The aerodynamic drag is relevant in modelling the thrust and velocity during the interception phase; however, during the braking phase, it is negligible. Instead, the braking dynamics and g-forces are governed by the tether tension and spool brake. Therefore, the simulation's fidelity relies heavily on MuJoCo's

continuous-time contact and tension models during braking.

To verify that the engine accurately captures these sudden tension spikes, a quantitative verification and validation procedure was performed. The thrust, drag, and tether dynamics models were verified were verified against analytical calculations. In addition, the tether stretch and peak forces were validated against standard climbing rope drop tests, which resulted in an average relative error of 7.2% for the elongation and 8.5% for the peak force, confirming the validity of the model for this application. A detailed breakdown of the verification and validation is provided in Appendix A.

11.3. Simulations

This section outlines the simulation that is used to determine the performance characteristics of *the Chameleon*. Before the simulation architecture and iterations are discussed, the interfaces of this simulation are presented in Table 11.1 and Table 11.2. The list of assumptions, verification, and validation of this appendix are all located in Appendix A.

Table 11.1: Input parameters

Name	Symbol	Unit
Structural Parameters		
Maximum g-forces	-	-
Total system mass	m	kg
Inertia	I	kgm^2
Drone Dimensions	-	m
Aerodynamic Paramaters		
Thrust over Weight	T/W	-
Drag coefficients	C_D	-

Table 11.2: Output parameters

Name	Symbol	Unit
Braking Parameters		
Braking distance	d	m
Tether modulus	E	GPa
Tether diameter	D	mm
Spooling-system architecture	-	-
Tether brake force	F_{brake}	N
Brake ramp-up time	t_{ramp}	s
G-forces during braking	-	-
Flight Profile Parameters		
Total flight time	t_{flight}	s
Thrust during flight phases	T	N

Simulation Architecture

The tether simulation is composed of four independent modules feeding in to the main simulation of the tether. Each of these modules is responsible for a distinct aspect of the system:

- **MuJoCo scene model** (`chameleon.xml`): defines the space of the simulation, including: bodies, joints, tether and actuators.
- **Aerodynamic engine** (`aero.py`): Computes the body velocity and drag forces
- **Flight controller** (`controller.py`): Rotates the drone thrust towards a target direction and manages the spool rotation.
- **Moth trajectory** (`moth.py`): Loads the moth location data from pats.
- **Main simulation script** (`main.py`): Combines the four modules and runs the main simulation loop

MuJoCo scene model

The MuJoCo module models the simulation's physical space. The drone body is modelled as a hollow cylinder with the physical dimensions and moment of inertia of the drone, as given in Chapter 8. The drone is modelled by a free joint giving it six degrees of freedom. The ceiling dock is a body at the coordinate origin. Below the dock, a spool drum is defined that can rotate freely around its z-axis, preventing torsional tether loads. The spool itself rotates about a joint aligned with the body y-axis, enabling it to rotate for releasing and reeling in the tether. Finally the ground is modelled as a flat surface at a z-axis of -3.

The tether is modelled as a spatial tendon connected at the outer edge of the spool and at the centre of gravity of the drone. The actual tether will split into four tethers and be mounted symmetrically around the center of gravity of the drone, which makes this representation of the tether in the center of gravity accurate. A spatial tendon is chosen because it has several properties required for an accurate simulation, namely: stiffness, spring length, damping and range limit. This allows MuJoCo to model the elasticity of the tether. All the contact simulations are handled by the MuJoCo software. However, the unwinding of the spool is not simulated by MuJoCo, as this led to unstable simulations, and is handled by the Python script. The solver used in MuJoCo is Runge-Kutta.

Aerodynamic engine

MuJoCo does not natively simulate the drag forces on the drone; a module was needed to compute the drag at each time step. The `aero.py` has two functions that are used, namely: `body_velocity()` and `compute_drag()`. `body_velocity()` fetches a six-dimensional vector that contains the angular and linear velocity of the drone. `compute_drag()` takes the velocity of the drone and returns the drag force using the formula:

$$D = C_d \frac{1}{2} \rho v^2 A$$

The drag coefficient (C_d) is dependent on angle of attack and is retrieved from the aerodynamic analysis performed using OpenVSP, see Chapter 9. A is the reference area, which was set by the Propulsion subsystem to be 0.004 m^2.

Moth trajectory

The moth trajectory module loads in a moth tracking file received from PATS. PATS records three-dimensional insect positions and velocities relative to the camera frame. The camera is mounted at approximately 3 meters above the floor. The `MothTrajectory` class has two functions defined, namely: `position()` and `velocity()`. These functions load the position or velocity data and interpolates it between time intervals to make sure that time can be continuous in the MuJoCo simulation.

Main simulation

The main simulation script `main.py` is responsible for combining the four modules described above and running the logic behind the simulation. At the start, the MuJoCo model and moth trajectory is loaded from `chameleon.xml` and `moth.py` respectively. The core of this script is the simulation loop `step_logic()` it advances the model by one time step $\Delta t = 0.002$ s per iteration. A convergence check was performed by decreasing the time step to 0.0002 s, which yielded a difference in peak g-force of less than 1%, which confirms time-step independence while maintaining computational efficiency. For the tether extension logic, the program measures the length from the drone to the spool and extends the tether with this length. The tether stiffness is calculated dynamically in each time step using the Young's modulus of the material:

$$k = \frac{EA}{L}$$

For the damping of the tether, a constant damping ratio of 0.02 is applied to the tether [105]. Initially, a dynamic damping coefficient was evaluated, but this yielded significant deviations during physical drop-test validation; the constant ratio proved more accurate (see Appendix A for the detailed reasoning). The rotation of the spool is matched to this tether extension for realistic visuals. The program flowchart, which presents a visual overview of the simulation logic, is shown in Figure 11.1.

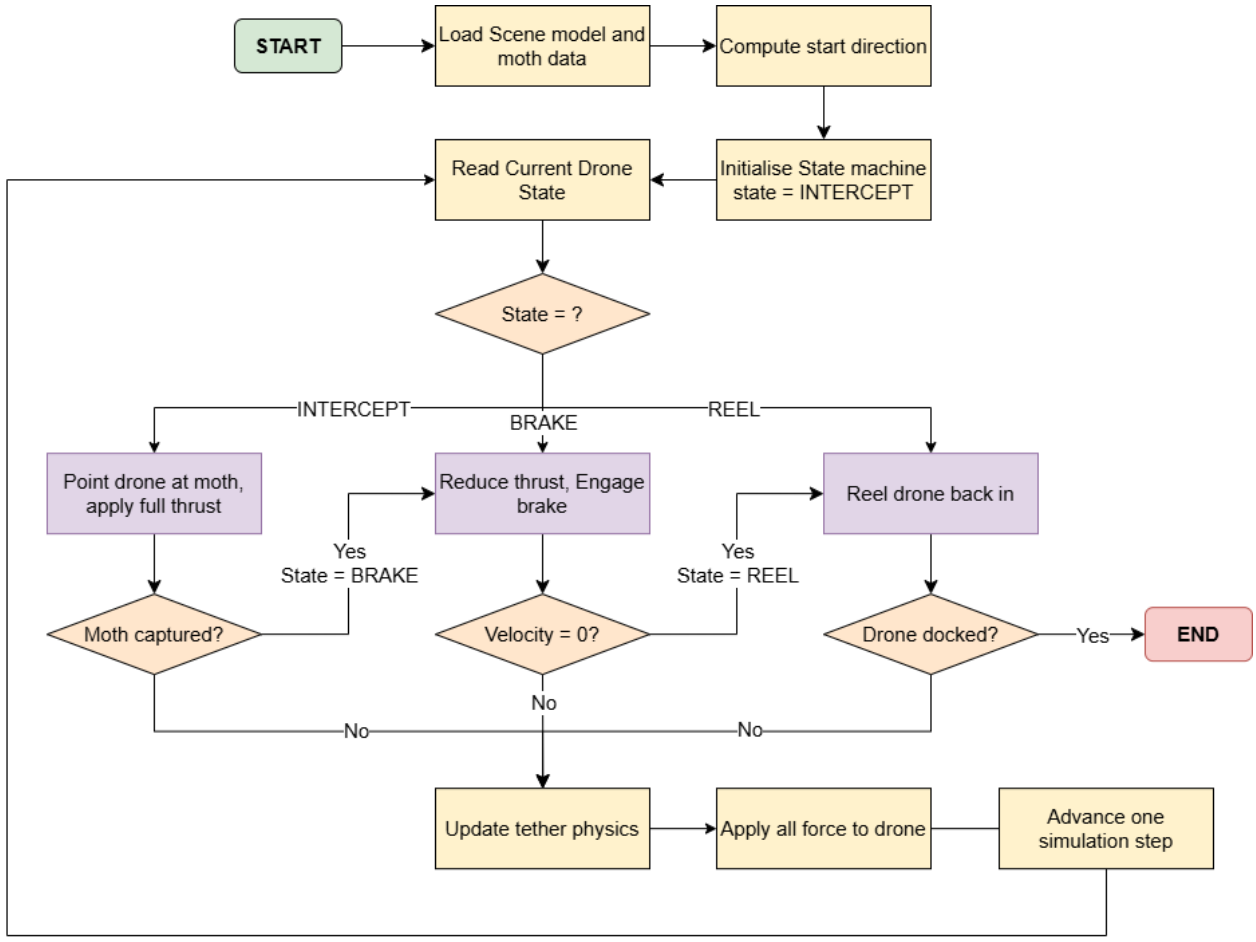

Figure 11.1: Simulation program flowchart

Simulation settings

The mission profile of *the Chameleon* platform is modelled as a state machine comprising three sequential operational phases: Intercept, Brake, and Reel. The simulation evaluates the dynamics of the tethered system across these phases to ensure operational constraints are met.

- Intercept Phase: The drone navigates towards the moth using a guidance vector. The propulsion subsystem operates at a maximum T/W of 5.3, as mentioned in Chapter 9. This produces approximately 7.5 N for the 143.4 g drone. During this phase, the tether is slightly slack so as not to decelerate the drone. This phase terminates when either the moth is hit, the drone overshoots the moth, or the drone approaches the ground closer than 0.5 m.
- Brake phase: During this phase, the drone keeps thrusting but at 30% of the maximum thrust, to reduce rebound effects. This value is selected as it was observed that thrust levels above 40% yielded negligible improvements in rebound damping, while unnecessarily increasing power consumption. Therefore, 30% was selected as an effective baseline to maintain tether tension and flight stability without heavily impacting the total battery budget.The spool brake engages and rapidly ramps up the brake force to the limit. The brake phase is finished when the drone's velocity reaches zero.
- Reel phase: Since the drone is still subject to rebound effects, it also keeps thrusting at 30% power during this phase to dampen these effects; this thrust value is also chosen for the previously stated reason. A motor that only controls the spool during this phase starts reeling back the drone at a specified speed that is determined by the selected motor. The reel phase is concluded when the drone is docked (within 0.3 m of the spool).

To clarify the various distance boundaries applied throughout the different simulation phases and constraints,

an overview of the critical thresholds is provided in Table 11.3.

Table 11.3: Overview of critical distance thresholds applied in the simulation.

Distance Parameter	Threshold	Context / Phase
Requirement stopping distance	≤ 0.80 m	Absolute limit from 5 m/s(SYS-01-TET-02)
Minimum ground clearance	0.50 m	Intercept phase termination trigger
Docking completion distance	≤ 0.30 m	Reel phase termination trigger

Iterations

To find a configuration that meets the braking distance requirement (the objective function) while maintaining peak g-forces below the 40 g structural limit (the primary constraint), an automated grid search was performed. The parameter space was discretised and evaluated with the following resolutions:

- Material modulus: 0.5 to 3 GPa; step size 0.5 GPa (stiffer tethers lead to unrealistically high G-forces).
- Tether Diameter: 0.2 to 2.0 mm; step size 0.3 mm.
- Braking force: 80 to 240 N; step size 20 N.
- Brake Ramp up time: 0.01 s, 0.1 s, and 1 s.

These simulations were executed at the standard Δt. In addition, when the following constraints were exceeded, the configuration was discarded as unfeasible:

- Peak deceleration: ≤ 40 g (as per STR-TET-01)
- Stopping distance: ≤ 0.8 m (as per SYS-01-TET-02)

Since IL-3 is linked to structures, the g-force limit of 40 g was set after iterating several structural layouts, with large safety margins. This means that even if 40 g is reached, the structural safety margin is still sufficient.

Coverage Area Trade-Off

During the simulation, a noticeable performance drop for far flight is visible. When the reel-back speed is insufficient, the drone strikes the ground with a pendulum-like motion. For this reason, it was decided to reduce the coverage area of a single drone. However, this makes the system more expensive for PATS, and possibly for the growers. PATS mentioned this coverage area reduction as a possibility in earlier meetings, if and only if the platform would be cheaper than the requirement. Since this is indeed the case (see Chapter 16), the choice is therefore made to reduce the drone coverage area from 8x5 m to 6x6 m. PATS stated that they use 8 drone systems per hectare now (which means that about 3% of a hectare is covered). With this reduction in area, an additional system is employed to cover the same area per hectare, with one more drone system extra to account for possible issues with layout (square area instead of rectangles), giving a total of 10 systems per hectare.

This reduction in coverage area deviates from the previously established coverage. However, due to the lack of standardisation in greenhouse architecture, with layouts varying significantly for different crops[106], this coverage area change will not pose significant drawbacks concerning the layout changes that are included in the coverage area changes. The new square layout is even slightly more adaptable to different greenhouse configurations. However, the drone is still at risk of hitting the ground (see Chapter 14), to mitigate this, a minimum reelback speed is established, along with other optimal parameters, in the next subsection.

Optimal parameters

Following Optimisation Loop 3, the area coverage trade-off, and multibody simulations, an optimal set of parameters was established to balance stopping distance with the 40 g structural deceleration limit (Table 11.4). These parameters will guide the COTS component selection in Chapter 12. To finalise this configuration, two practical constraints prevented the team from optimising further. First, a sensitivity study for tether

dimensions was omitted due to limited commercial options (typically nylon, $\approx$ 2.0 GPa [107]). Because the system already comfortably meets the $\leq$ 0.8 m requirement from 5 m/s, stiffer tethers were avoided to prioritize structural integrity over negligible (< 5 cm) stopping improvements. Second, maximum braking force is capped at 140 N to stay within budget, as stronger brakes significantly increase costs for minimal performance gains. Ultimately, with these parameters, the resulting mission time of maximally 2 seconds (< 0.5 seconds at full power) remains fully compatible with the battery.

Table 11.4: Tether and braking parameters derived from simulation iterations and hardware constraints.

Parameter	**Value**	**Parameter**	**Value**
Tether Material Modulus	2.0 GPa	Maximum Braking Force	140 N
Tether Diameter	0.5 mm	Brake Ramp-up Time	0.03 s
Target Reel-back Speed	3.0 m/s	Avg. Braking Distance (over 46 sorties)	0.4 m
Avg. G-force (over 46 sorties)	30 g		

Flight Dynamics

To provide an intuitive understanding of the system's scale and dynamics, the simulation telemetry and images are shown in Figure 11.2 and Figure 11.3, alongside a human reference model (1.80 m). A full recording of the simulated flight envelope, demonstrating the visual trajectory alongside the mathematical outputs, can be viewed via the provided QR code.

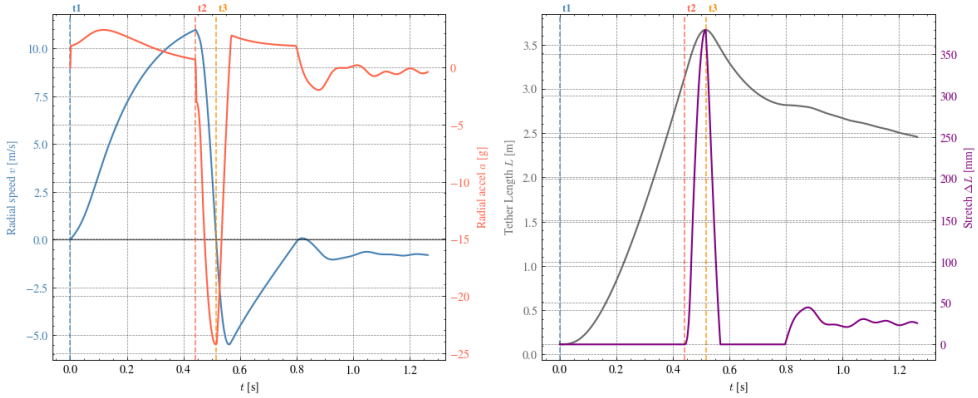

(a) Detailed telemetry of the drone velocity, acceleration, and tether elongation.

(b) QR code for the video

Figure 11.2: A flight profile, including telemetry, with a non-moving target at location (2,-2, 1); Video of the flight: QR-code; **Equivalent link:** `https://youtu.be/4zLE6-95Abw`, or **Alternative link:** `https://doi.org/10.5281/zenodo.20814282`

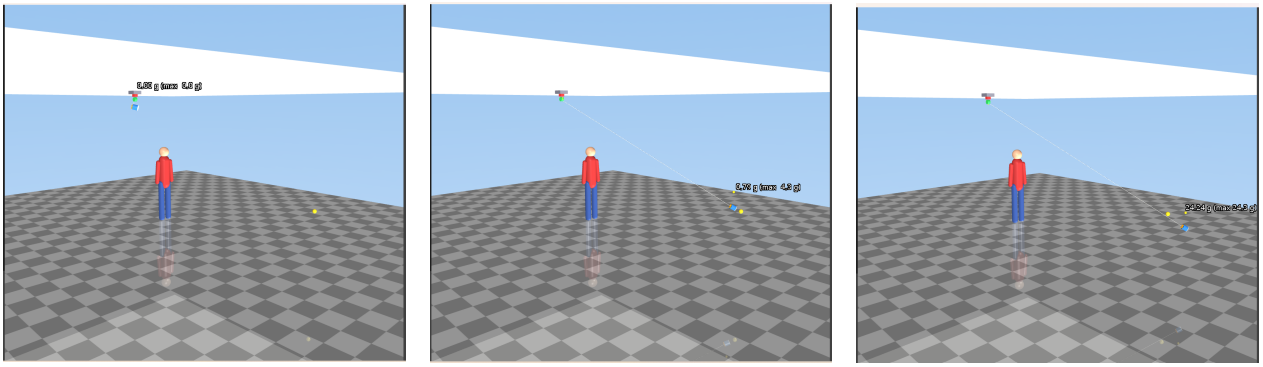

a) Start of interception phase (no spool-up time) (t_1)

b) Start of braking phase, brake engages, thrust is reduced to 30% (no delay) (t_2)

c) Start of reel-back phase, brake disengages, motor starts (t_3)

Figure 11.3: Visualisation of the simulation environment with a human scale reference.

12
Integrated System

In the previous chapters, the iterations and optimal design parameters were outlined. To achieve these parameters, corresponding hardware is selected in this chapter. After this, the hardware is selected, and a final design evaluation is performed, along with several Fusion renders of the system. Finally, this chapter details the electrical, data handling, communications, operations, and logistics flow diagrams.

12.1. Hardware Architecture: COTS components

In this section, the hardware is selected. First, the hardware selection for the drone is detailed; afterwards, the tether and spool platform hardware selection is performed.

Drone

Throughout Chapter 6 to Chapter 11, target parameters for the drone were established. In this subsection, using these target parameters, the drone architecture is determined. The separate masses of all the components are found in Appendix D. The key drone components are shown in Table 12.1

Table 12.1: Key component selection and engineering justification for the Drone Platform.

Subsystem	Component	Specifications & Justification
Frame Material	Bambu Lab polycarbonate (PC)	Req: Withstand crash loads and 34g max deceleration loads. Spec: High impact strength (34.8 kJ/m^2), density 1.20 g/cm^3, flame retardant.
Propulsion	2 x custom counter-rotating, 75 mm, 3 bladed propellers, and 2 x Axisflying C145 1404.5, 4500KV	Req: T/W of over 5. Spec: Delivers target static T/W (throttle limited to 69%), counter-rotating to maximise efficiency.
Power	4 x BetaFPV Lava II 1S, 320 mAh, 95C LiHV	Req: Sustain full mission profile. Spec: Delivers 16.5 V, and 13.4 V under load, with capacity of 320 mAh.

Tether and Spool Platform

Section 11.3 established the target parameters for the tether and spool platform. Table 12.3 summarises the most important components selected to meet the simulated parameters. A complete Bill of Materials (BOM), including standard hardware, is located in Appendix D.

Table 12.3: Key component selection and engineering justification for the Tether and Spool Platform.

Subsystem	Component	Specifications & Justification
Tether	Nylon Fishing Wire (0.5 mm)	Req: E = 2GPa, withstand peak load of 56.6 N. Spec: 21 kg (206 N) yield provides a SF of 3.5 against the 56.6 N peak simulated load (assuming 95% efficient Palomar knot).

Continued on next page

Table 12.3 – continued from previous page

Subsystem	Component	Specifications & Justification
Brake	DZD5-5A Electromagnetic	Req: 140 N braking force. Spec: 5 Nm holding torque achieves 142.9 N on a 7 cm spool (SF = 1.43). Fixed 30 ms ramp-up [108]. G-forces remain below 40 g structural limit.
Motor	960 RPM DC Motor (JGB37)	Req: 2.5 m/s reelback Spec: Achieves 3.52 m/s at the full 7 cm spool radius.
Drivetrain	One-way bearing & Coupler	Req: Decouple high-speed intercept. Spec: Prevents motor overspeeding. Coupler adapts 10 mm standard bearing outer diameter to 15 mm spool shaft.
Power & Control	Voltage regulators	Req: Interface 230 V to 24 V/9 V. Spec: Steps down grid supply for standard components (see Figure 12.5).

12.2. Design Renders & General Overview

With the hardware selection, designs for both the drone and the spool station were made in Fusion. These designs are presented in this section. Additionally, a general system characteristics overview is presented.

Drone Renders

In Figure 12.1, the visual of *the Chameleon* is presented.

Figure 12.1: Fusion render of *the Chameleon*, more detailed renders are located in Section 15.3

Spool station renders

For the spool station, the render of the general layout is visible in Figure 12.2. In the fusion model, for several off-the-shelf (SDP-1) parts, a model from GrabCAD was used. When necessary, the constraints and joints were altered to make the parts compliant with the assembly. This was the case for the motor[1], the motor mount[2], the coupling [3], and the bearings[4]. The passive yaw swivel is mounted on top, as specified in Chapter 11.

[1] `https://grabcad.com/library/jgb37-520-1` – Accessed: 13.06.2026

[2] `https://grabcad.com/library/bracket-for-jgb37-520-motor-and-tslot-2020-1` – Accessed: 13.06.2026

[3] `https://grabcad.com/library/jlcmc-shaft-couplings-jaw-coupling-spider-type-elastomer-coupling-1` – Accessed: 20.6.2026

[4] `https://grabcad.com/library/kp002-bore-15mm-1` – Accessed: 13.06.2026

(a) Side view demonstrating the motor, custom coupler, and one-way bearing integration

(b) Side view detailing the DZD5-5A electromagnetic brake assembly and mounting

Figure 12.2: Fusion renders of the spool platform assembly. Note: The passive yaw swivel acts as the required rotation point; a motorized gimbal has been excluded from the design to reduce complexity.

Aerodynamic and Performance Overview

In this subsection, the general performance metrics of *the Chameleon* are presented in Table 12.4

Table 12.4: Performance, operational, and aerodynamic overview of the Drone Platform. Performance and aerodynamic values are averaged over 46 flights.

Category	**Parameter**	**Value & Notes**
Performance	Total system mass	143.4 g
	Thrust-to-weight ratio	5.4
	Average intercept speed	9.6 m/s
	Maximum intercept speed	11.8 m/s
	Average brake distance	0.4 m
	Average G-loads	30.38 g
	Average mission time	1.156 s
	Average interception phase time	0.267 s
	Average braking phase time	0.057 s
	Average reelback phase time	0.832 s
Power & Operations	Battery capacity	320 mAh
	Recharge time after nominal mission	$\leq$ 5 min
	Daily sorties capability	$\geq$ 80
	Operational area	36 m^2
Environment	Operating temperature	10–35 °C
	Operating humidity	$\leq$85%
	Crash resistance	2 m drop, 5 m/s forward
Aerodynamics	Drag area ($C_D A$)	0.09811 m^2

The averaged braking distance, mission time, and g-force loading are also visualised in the box plots of Figure 12.3. No unexplainable outliers were found. A total of 79 sorties were simulated. Before producing

the plots, 30 cases where the moth spawned above the roof or flew through the ceiling were removed; these indicate the moth is outside the operating range, meaning a mission would not be initiated in practice.

Of the 49 valid interception attempts, 3 non-successful flights were removed from the performance averages: in 2 cases, the drone could not brake in time, and in 1 case, the drone hit the ground during reel-back. This yields a system survival rate of 93.8% (46 successful intercepts out of 49 valid attempts). Most importantly, the maximum g-force experienced (34 g) remains well below the 40 g structural limit.

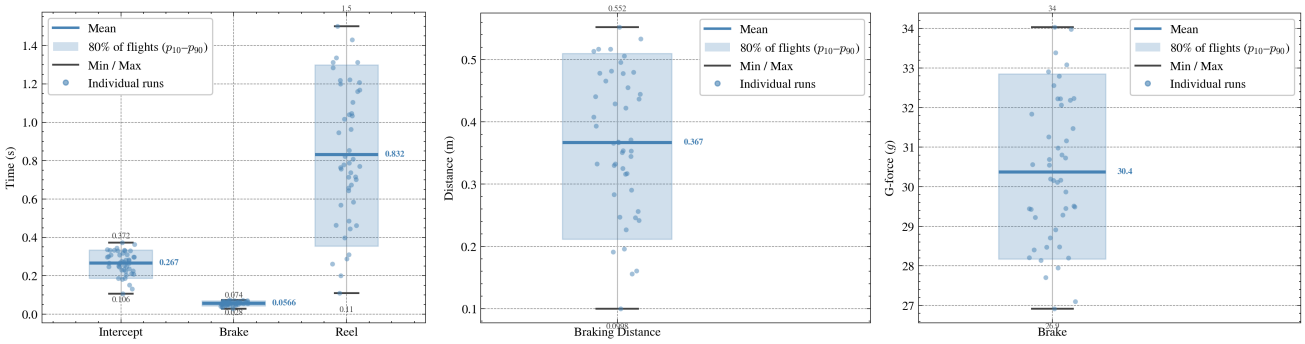

(a) Box plot: Phase Durations **(b)** Box plot: Braking Distances **(c)** Box plot: G-forces

Figure 12.3: Box plots of flight parameters conditional on successful intercept (averaged over 46 successful sorties).

Material characteristics

Bambu Lab's black polycarbonate PC [5] was chosen as the material for all custom 3d printed parts. It can be bought in bulk and is part of the same ecosystem the client currently uses [61]. Polycarbonate has such excellent impact strength and formability that it's used for fighter jet canopies [6], making it a good choice. The important mechanical properties are presented below in Figure 12.5.

Table 12.5: Bambu Lab PC Filament key properties[a]

Property	Value	Unit
Density	1.20	g/cm^3
Vicat Softening Temp.	119	°C
Tensile Strength	55 ± 4	MPa
Elongation at Break	3.8 ± 0.3	%
Impact Strength	34.8 ± 2.1	kJ/m^2
Flexural Strength	108 ± 4	MPa
Flame Retardant	Moderate flame resistance	

[a] `https://eu.store.bambulab.com/collections/bambu-lab-3d-printer-filament` - Accessed 17.06.2026

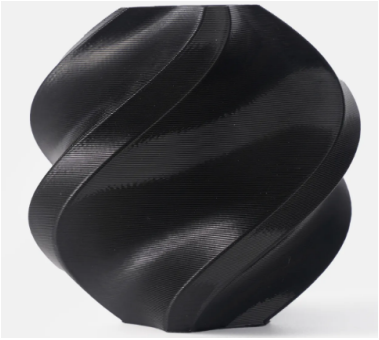

Figure 12.4: Bambu Lab PC Filament key mechanical properties[a]

[a] `https://eu.store.bambulab.com/collections/bambu-lab-3d-printer-filament` - Accessed 17.06.2026

Electrical Diagram of Drone

Explanations behind the construction of the drone's electrical system have been presented in Section 7.3. Here, only the final electrical diagram is shown in Figure 12.5. It should be noted that the electrical diagram only shows the power flow of the drone. Data and Signal flows are shown in the communication and data flow diagrams in the subsequent sections.

[5] `https://eu.store.bambulab.com/nl/products/pc-fr` - Accessed 17.06.2026

[6] `https://eu.store.bambulab.com/nl/products/pc-filament?variant=593613033543643140` - Accessed 17.06.2026

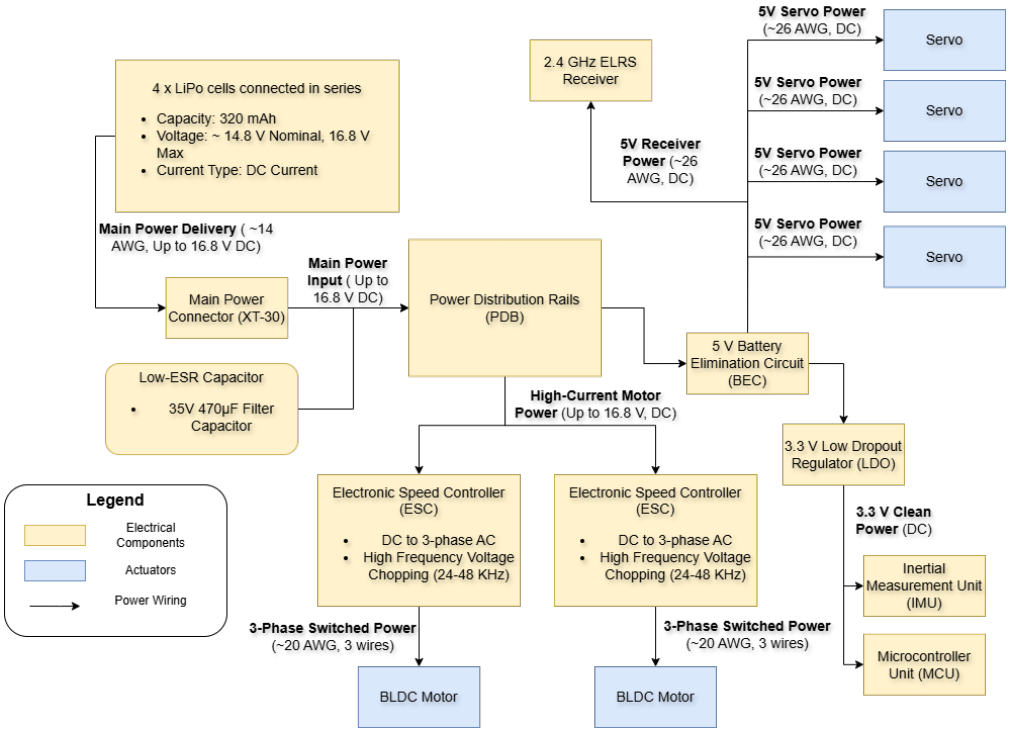

Figure 12.5: Electrical block diagram

Electrical Diagram of Spool Platform

For the spool platform, a control and power logic diagram is devised. This diagram is visualised in Figure 12.6.

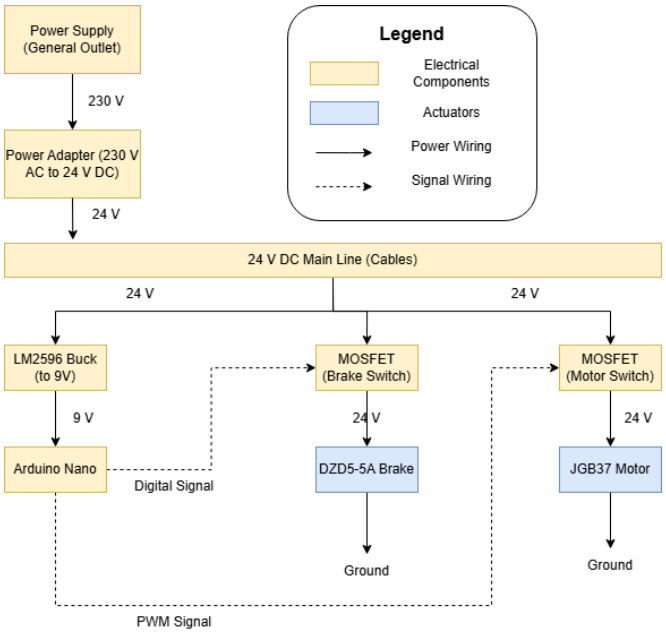

Figure 12.6: Electrical and Control Logic flow diagram for the spool platform.

Stability and Control characteristics

Results with a launch angle of $\varepsilon = 10°$ and mission duration of 0.7 s are discussed which is the worst case scenario. As can be seen in Figure 12.7, the current undisturbed design of *the Chameleon* drifts downwards (+z) slightly resulting in a maximum deviation of 0.22 m at the end of the mission.

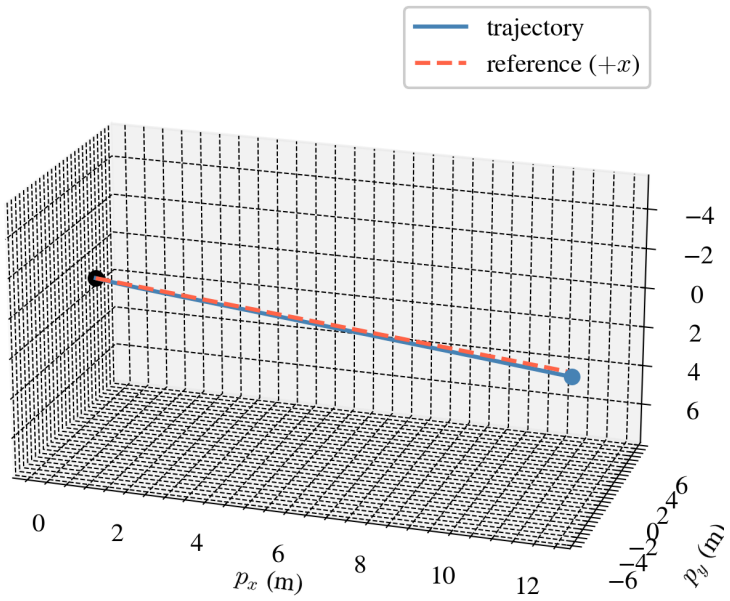

Figure 12.7: Trajectory of *the Chameleon* with respect to a straight line reference trajectory. The maximum deviation at the end of the trajectory is 0.22 m.

This drift has several causes and can be solved. There are two main challenges causing the drift. The first challenge is that the vanes try to control attitude and position simultaneously, while they can only control one. Theoretically a tilt angle at which the position error is also zero should exist, however determining this angle was deemed ineffective because of the second challenge. As can be seen in the middle-,right-plot in Figure 12.8, the horizontal vane deflection is capped at 20 degrees (maximum value at which linear approximation is valid). This maximum deflection, is not enough to change the attitude towards the reference tilt angle and the position error to zero.

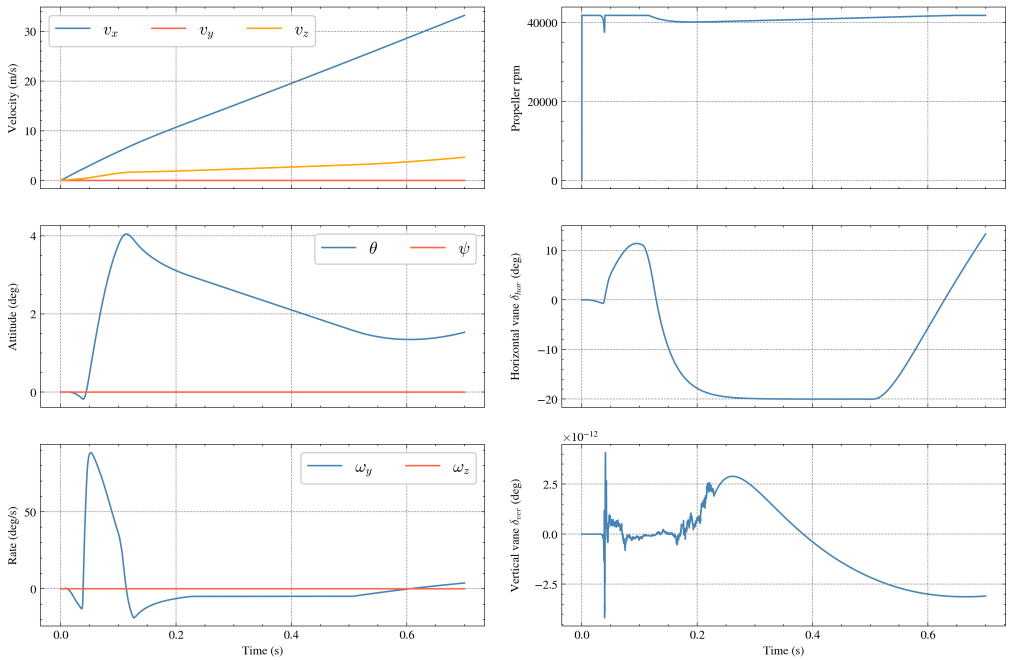

Figure 12.8: States and Inputs of *Chameleon* with respect to a straight line reference trajectory. The launch angle is ε 10° and mission time is 0.7 s.

The trajectory under a disturbance (plots shown in Chapter 10) has an error of 0.60 m for the rectangular pulse and 0.23 m for the oscillating disturbance. Overall, an error of up to 0.60 m is not acceptable when trying to hit a moth within a drone radius of ≈ 0.08 m, which is why three improvements are given as future research.

The downward drifting trajectory can be taken into account when the controller does not try to keep flying straight. Knowing that the controller will at some point in its development need to deviate from a straight line to aim at the moth, it is recommended to look at non-straight trajectories and adjustable trajectories in the future. Besides this, a larger control surface could prove beneficial as it gives the vane more authority over *the Chameleon*'s attitude and position. Lastly, it is recommended to either obtain the simulated OpenVSP derivatives experimentally, or to run a higher fidelity denser grid simulation resulting in a more accurate model of *the Chameleon*.

Drone Data Handling & Communication Block Diagrams

The communication architecture between the ground segment and the drone is shown in Figure 12.9b. Because the internal configuration of the PATS-C system is unknown, the ground segment is modeled using a typical communication setup. An RF link handles the bidirectional data transfer: the ground station transmits control commands to the onboard MCU, while the drone returns system status and link telemetry. Figure 12.9a shows the onboard data flow. The MCU acts as the central processor, combining pilot inputs from the RC receiver with motion data from the IMU to generate commands for the ESCs and servos. In parallel, an independent watchdog monitors the MCU to intervene in the event of a processor fault. The two diagrams, therefore, illustrate how sensor data and user commands are combined and processed to produce the actuator commands required for stable flight.

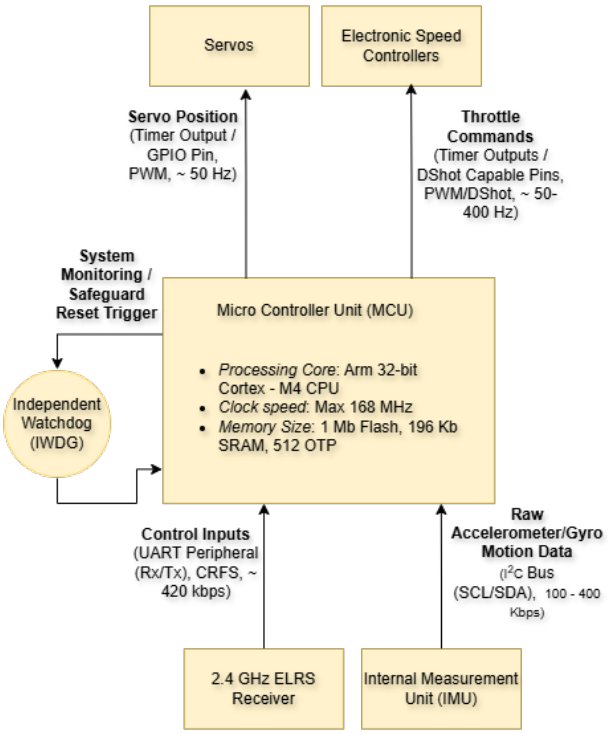

(a) Data handling block diagram

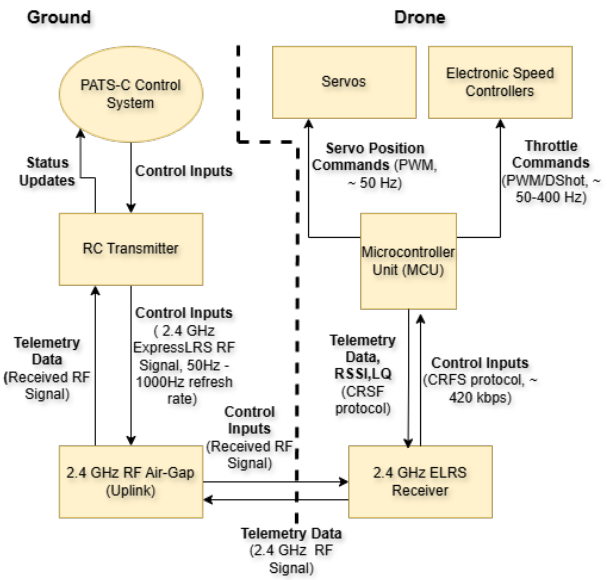

(b) Communication flow block diagram

12.3. Operations and Logistic Concept Definitions

After the development of *the Chameleon*, three operation-cycle phases are defined: installation, operation, and end of life. The phases are shown in Figure 12.10. Together, they summarise the complete operation cycle of *the Chameleon* from start to end.

During operations, there will be 10 *Chameleon* systems per hectare. They will operate in the PATS-C cameras' fields of view, in a volume of 6 x 6 x 3 m (width x length x height), as explained in the subsection Coverage

Area Trade-Off in Section 11.3. Each *Chameleon* is required to perform at least 1000 missions over its operational life (SYS-27, Table 17.1), where one mission is one moth interception attempt. This figure applies to the system as a whole over its full lifetime and is met through multiple battery replacements.

The relevant battery characteristics follow from the battery selection in Section 7.3. The cycle life of a single battery follows $N(308, 30.4^2)$, giving a 99.5% probability that an individual battery exceeds 230 cycles and a 98% probability that all four batteries in a set do so. With one charge cycle corresponding to one mission, a single battery set therefore reliably covers on the order of 250 missions. Four battery sets are consequently sufficient to reach the 1000-mission requirement, corresponding to a conservative maximum of three battery swaps over the system life.

The nominal mission frequency, as provided by PATS, is approximately 2 missions per operating period, with one operating period assumed to be a 10-hour night. At this frequency, the 1000-mission life corresponds to roughly 500 operating nights, that is, a system lifetime of about 500 days, with a battery swap required approximately every 125 days (SDP-4). This nominal load is well within the system's maximum sortie capability of at least 80 sorties per operating period (MIS-05, Table 17.2), which in turn ensures that the maximum downtime requirement of 5 min is comfortably met (SYS-07, Table 17.1).

Considering logistics, a note should be made. Upon delivery of the entire system, the spare drones and batteries are delivered in designated containers and with them a set of empty containers. Following operations, the user can collect the used drones and batteries after replacing them with spare ones (SDP-6). Once the containers fill up, they can be sent to PATS for repair, and the user will receive new containers with spares.

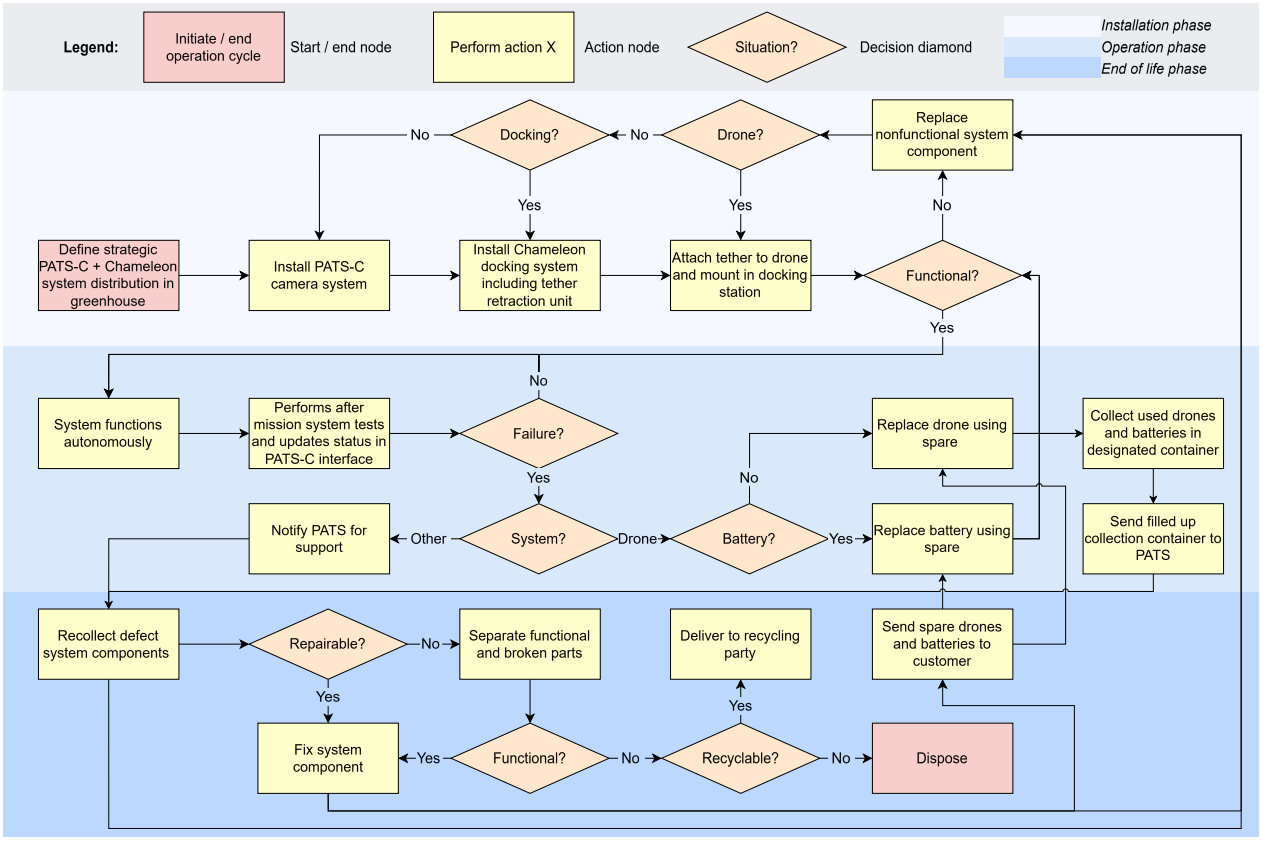

Figure 12.10: Operational flow diagram structured in three phases: installation, operation, and end of life.

13
Life Cycle Analysis

A Life Cycle Analysis (LCA) is performed to quantify the environmental impact of *the Chameleon* drone and to evaluate it as an alternative to conventional pesticide-based pest control. The assessment compares the complete life cycle of the drone with the environmental impact associated with the use of chemical pesticides over an equivalent greenhouse area and operating period. The effects of pesticide usage and the Sustainable Design Philosophy are discussed in Chapter 2.

13.1. Method

The analysis is performed using the IDEMAT [1] framework developed at TU Delft. IDEMAT estimates the environmental burden of products with eco-costs. This method is particularly suitable because it has eco-cost values for both pesticides and all materials used in the drone [109]. The eco-cost of a product is based on the combination of four sustainability aspects: Resource depletion, Eco-toxicity, Human health and Carbon footprint.

- **Resource depletion** refers to the consumption of finite natural resources such as metals, minerals and fossil fuels. Products that require scarce or energy-intensive raw materials will have a higher resource depletion score.
- **Eco-toxicity** describes the effects of a material on ecosystems and living organisms. This includes pollution of soil, air and water by the substance.
- **Human health** considers the effect that the substance has on human well-being. This includes carcinogenic and non-carcinogenic effects.
- **Carbon footprint** describes the greenhouse gas emission associated with a material through its lifecycle.

The eco-cost, calculated from these categories, represents the estimated cost required to prevent or compensate for the environmental damage caused by the product. Using the IDEMAT system, the impact of the drone is assessed Cradle-To-Grave. This means that the full life cycle is taken into account, from manufacturing to End-Of-Life processing and everything in between.

13.2. Results

The LCA of *the Chameleon* starts by setting up a list of materials used for production. The electricity consumption required for the production of the subsystems is then added. Using the IDEMAT database, eco-cost values are assigned to each material and electricity input.

The life cycle assessment considers two different End-Of-Life scenarios: landfill and closed-loop recycling. Since the environmental impact of a product depends not only on its material composition but also on replacement and disposal during its operational life, component lifetimes are incorporated into the analysis. As discussed in Section 12.3, the service life of the drone exceeds that of the battery pack, requiring approximately two to three battery replacements over the lifetime of a single drone. To account for this, the environmental impact associated with battery production is included three times in the inventory.

[1] The database versions: ecocosts 2017 V1.8 and Ecoinvent V3.6 are used

At the end of its useful life, the drone can either be disposed of through landfill or undergo material recovery. In the latter case, several high-impact subsystems: the batteries, electric motors, and polycarbonate structure, are assumed to be processed through closed-loop recycling. Consistent with the cost breakdown presented in Appendix C, part of the project budget is allocated to this End-Of-Life processing. Recovering these materials reduces the eco-cost associated with virgin material production and therefore lowers the overall environmental impact compared with the landfill scenario.

All input materials and electricity consumption are summarised in Table 13.1. To account for uncertainties in material composition and electricity usage, a conservative correction factor of 25% was added to the final eco-cost value. The final eco-cost of the drone will consist of the Closed-loop eco-cost of the: Battery, Structure and Motor and the Landfill eco-cost of the: Propeller, Fasteners, Wiring, PCB and Tether System. Afterwards the eco-cost related to the manufacturing energy will be added and finally the safety margin of 25% is applied. Using ten drones per hectare this leads to a final eco-cost of **€68.00** per hectare. The eco-cost of the drone is calculated as follows (with CL and LF being closed loop and landfill respectively)

$$\begin{aligned} \text{CL} &= 0.198 + 0.040 + 0.009 = €0.247 \\ \text{LF} &= 0.005 + 0.013 + 0.021 + 0.035 + 2.870 = €2.944 \\ \text{Total} &= (0.247 + 2.944) + 2.251 = €5.44 \\ &\Rightarrow 5.44 \times 1.25 = €6.80 \end{aligned}$$

Table 13.1: Life Cycle Analysis material inventory and eco-cost scenarios.

Material	**Percentage (%)**	**Weight (g)**	**Eco-cost scenario**	
			Landfill	**Closed-loop**
Battery, 3x[23] [110]				
Steel	9.0	9.0	0.015	0.003
Polycarbonate	11.0	10.8	0.015	0.009
Aluminium	34.5	33.9	0.069	0.009
Nickel	3.1	3.0	0.093	0.000
Lithium	1.0	0.9	0.030	0.024
Cobalt	2.8	2.7	0.153	0.102
Copper	9.2	9.0	0.048	0.003
Graphite	29.1	28.8	0.048	0.048
Battery subtotal (×3)		*98.1*	*0.471*	*0.198*
Propeller				
Nylon 6	100.0	3.3	0.005	0.003
Structure				
Polycarbonate	100.0	56.5	0.071	0.040
Fasteners, Bearings, Shafts				
Steel	100.0	7.3	0.013	0.004
Wiring				
Copper	60.0	3.1	0.017	0.001
Silicone	40.0	2.1	0.004	0.004
Motor[24]				
Iron	50.0	8.7	0.003	0.003
Copper	30.0	5.2	0.028	0.001
Aluminium	15.0	2.6	0.005	0.001
Neodymium	5.0	0.9	0.073	0.004

Continued on next page.

[2]Low-impact, low-concentration materials were aggregated into other low-impact materials.

[3]Weight and eco-cost values in this block are for all three batteries.

[4]`https://www.ligpower.com/blog/drone-motor-components-and-structure.html` Accessed 10.06.2026

Continued from previous page.

Material	Percentage (%)	Weight (g)	Eco-cost scenario	
			Landfill	Closed-loop
PCB[2]				
Polycarbonate	74.0	8.2	0.010	0.006
Copper	14.2	1.7	0.009	0.000
Lead	2.5	0.3	0.001	0.000
Iron	3.1	0.4	0.000	0.000
Tin	4.8	0.6	0.015	0.004
Tether System[2]				
Polycarbonate	49.0	731	1.16	0.48
Steel	40.6	605	1.08	0.21
Copper	6.4	95	0.51	0.01
Aluminium	4.0	60	0.12	0.01
Other				
Unspecified materials	–	9.4	–	–
Total Weight Eco-Cost		**1699.4**	**€3.595**	**€0.979**
Manufacturing				
Electricity (Battery, ×3) [111][112]		24.6 kWh	1.530	1.530
Electricity (Structure) [113]		0.4 kWh	0.025	0.025
Electricity (Wiring) [112]		0.3 kWh	0.0188	0.0188
Electricity (Motor) [112]		0.4 kWh	0.025	0.025
Electricity (PCB) [112]		9.2 kWh	0.576	0.576
Electricity (Operation) [112]		1.2 kWh	0.076	0.076
Total Electricity Eco-Cost		**36.1 kWh**	**€2.251**	**€2.251**
Total Eco-Cost (materials + electricity)				**€5.44**
Total Eco-Cost (incl. recycling & safety margin)				**€6.80**

For the pesticide system, the LCA is based on the quantity of pesticides to protect one hectare of greenhouse area during the operational lifetime of the drone fleet. One drone covers an area of 6 x 6 m (36 m^2), see Chapter 11 and operates for approximately 16 months, based upon the 1000 mission requirement and estimation of 2 missions on average per night (Section 12.3). For effective pest control, 10 *Chameleon* systems are used per hectare. The pesticide selected for the analysis is Deltamethrin, an approved and widely used insecticide for moth control in greenhouses [5]. The recommended application dose of Deltamethrin is 200 mL/ha per 3 months (non diluted) [114], which corresponds to 1066.67 mL/ha per 16 months. Using a density of 1.5 g/cm^3[115], this volume corresponds to 1.600 kg of Deltamethrin per hectare. Based on the eco-cost value of 9900 €/kg obtained from the eco-costs Value database[6] this includes the manufacturing, usage and end-of-life of the Deltamethrin, the resulting eco-cost is calculated as

$$1.600 \times 9900 = \textbf{€15,840}$$

The results show that the drone system has a substantially lower environmental impact than the pesticide-based alternative, with an estimated eco-cost of €68.00 for ten Chameleon drones per hectare compared to €15,840 for Deltamethrin use over the same area and operational period. This is a **>99% reduction** in eco-cost when comparing the two systems over one hectare.

It should be noted that this comparison represents a conservative upper estimate of the drone impact. The drone eco-cost includes a 25% safety factor to account for uncertainties in material composition and manufacturing energy. From this analysis, it can be concluded that *the Chameleon* drone is a highly sustainable alternative to chemical pest control.

[5] `https://www.niab.com/chemical-control-codling-moth` – Accessed: 22.05.2026

[6] `https://www.ecocostsvalue.com/social/internalities/` – Accessed: 22.05.2026

14
Risk and Reliability

14.1. RAMS characteristics

In this section the RAMS characteristics of *the Chameleon* are discussed. RAMS stands for: Reliability, Availability, Maintainability and Safety.

Reliability

To analyse the reliability of *the Chameleon*, the reliability of all the separate components is evaluated first. Of all components the Mean Time Before Failure (MTBF) is displayed in Table 14.1. These values have been attained from literature or calculated using the following expression:

$$MTBF = -\frac{t}{ln(R(t))} \tag{14.1}$$

Here $R(t)$ is the reliability of a system after t hours.

Table 14.1: Mean Time Before Failure (MTBF) for Drone Subsystems

Subsystem	**MTBF (Hours)**
Flight Control System	463,691 [116]
Electronics system	199,601 [117]
Motors	77,000 [118]

These values are based upon average drones. A great difference between *the Chameleon* and the average drone are the loads that are sustained during the deceleration. Even with a safety factor of 1000, to take into account the high loads, the most critical system is the motors, with a MTBF of 77 hours. This corresponds to 92400 missions, assuming a worst case mission duration of 3 seconds, way above the 1000 missions requirement.

Failure is much more likely to occur from battery degradation. Instead of MTBF, these are expressed in mission cycles. With a 98% chance of all 4 batteries still working after just 230 cycles, this is the least reliable component of *the Chameleon*. Regarding the structure, the braking loads are sufficiently low that the structure is not likely to fail due to fatigue build up.

Availability

Like mentioned in Chapter 12, the expected lifetime of a drone is 500 days. This is based on the 1000 mission requirement and an average of two missions per day. When a drone malfunctions, a request for a new one can be sent to PATS. Because the market is primarily concentrated in the Westland area, a maximum delivery time of two working days can be assumed.
During its lifetime, 3 battery swaps will be performed by the grower. Changing the battery of *the Chameleon* takes around 10 minutes. Taking into account the availability of the grower, a downtime of 1 day is assumed for a battery swap. This means that *the Chameleon* is active for 500/505 days, achieving an availability of 99%

Maintainability

The Chameleon has been designed with modularity in mind. To negate the relatively low battery lifetime, the battery placement was designed for maximum modularity. Changing the batteries is very simple because they are placed on the outside. Replacing them is just a matter of taking the old ones out and sliding the new batteries in. This repair can be done by the client themselves in about 10 minutes. Extra batteries are delivered when the system is installed.
In other cases, faulty drones are repaired at PATS. When the request for a new drone is sent, an employee of PATS will deliver the drone within two days and take the faulty drone back to PATS for repairs. In Section 15.2 the assembly process is described in detail. It can be concluded that the design is not hard to assemble; thus, replacing components is not difficult either.

Safety

Safety in this context entails: If it fails, what are the consequences? Due to the tether, *the Chameleon* scores great in this category as well. The tether essentially guarantees the safety of the surroundings. In the case of tether failure, *the Chameleon* has been designed according to EASA regulations. Because its weight is under 250 grams, it can be safely operated around people. Another safety concern is the battery catching fire after it has degraded. To mitigate, a fireproof polycarbonate has been selected as the material for the frame. [1]

14.2. Technical Risk Assessment

Before *the Chameleon* can be deployed at large scale, technical risks still pose a threat to further development. In this section, risks identified during design and stakeholder meetings are analysed, mitigated and incorporated in recommendations for future design and operations.

Risk analysis

Even though risk was an important factor in the trade-off (taken into account for durability and cost, which were trade-off criteria), a risk analysis for the future of the Chameleon has to be performed. To accomplish this, risks have been divided in subsystem and system risks. In Table 14.4, the two biggest risk for each subsystem are listed, followed by the five biggest system risks. Although there are more risks to future development, this analysis is focussed on identifying the biggest pitfalls to provide an indication of which risks need to be managed most closely. The risks receive a score for severity of consequence and likelihood based on the definition provided in Table 14.2.

Table 14.2: Impact and probability score descriptions

Impact Levels		**Probability Levels**	
Level	**Description**	**Level**	**Description**
Negligible (1)	Minimal impact on cost or operations	**Very Unlikely (1)**	Not expected to occur during operation or design(<1%)
Marginal (2)	Limited manageable impact requiring minor redesign and possible budget increase.	**Improbable (2)**	Small chance of happening during design or operation(1-10 %)
Moderate (3)	Noticeable impact on operations and economic viability of project	**Uncertain (3)**	Might happen during future design stages or operations(10% -30%)
Critical (4)	Significant impact on required development budget and operations. Could lead to reconsideration of concept or project	**Likely (4)**	Likely occurs in later design stage or during operations(30%-50%)
Catastrophic (5)	Huge impact on expected development cost making the design no longer economically viable in any way. Project cancelled or restarted	**Expected (5)**	Expected to happen multiple times during operations or be a recurring design obstacle(>50%)

[1] `https://www.easa.europa.eu/en/the-agency/faqs/open-category`

With the impact and probability levels defined, a score for the severity of consequence and chance of occurrence can be given, and the risk level can be calculated.

Table 14.4: Concept risk analysis table

ID	Risk	Consequence (Severity of Consequence)	Chance	Risk Level
Propulsion				
PR-01	Moth debris gets stuck in propulsion system	Can cause RPM-degradation resulting in torque asymmetry generated by the motors and loss of control (**4**)	4	16
PR-02	Provided thrust turns out to be insufficient to get to moth quick enough	*The Chameleon* fails to intercept the moth (**5**)	3	15
Power and Electronics				
PE-01	Unpredictable battery degradation [43]	Battery delivers insufficient power (**3**)	4	12
PE-02	Battery or circuit catches fire	A fire breaks out and the greenhouse burns down (**5**)	3	15
Structures and Layout				
SL-01	Struts connecting the motor to the duct build up strain due to heavy loads during acceleration and high-g braking manoeuvres.	Struts break and *the Chameleon* does not function any more (**4**)	3	12
SL-02	Tether connection points break from shear stress due to high deceleration loads	*Chameleon* crashes into environment (**4**)	3	12
Aerodynamics				
AE-01	Low fidelity simulations gave unreliable coefficients	*The Chameleon* needs a redesign or justification that some requirements are not met (**5**)	3	15
AE-02	Kill zone due to suction from duct effect is smaller than expected	*Chameleon* is not able to intercept moths (**4**)	3	12
Control				
CO-01	Control surfaces deflect too late due to delay in moth tracking to control input	Drone might be uncontrollable or chance of catching moths decreases and higher crash rate (**5**)	3	15
CO-02	Assumptions (e.g. linearization) made in control design fail	Control algorithm is no longer valid possibly resulting in unsuitable control inputs and crashes (**4**)	4	16
Tether				
TE-01	Tether gets entangled in propulsion/control surfaces	Operations disrupted and propulsion system likely damaged (**4**)	4	16
TE-02	Tether snaps during high-g braking manoeuvre	Drone is lost and damages environment (**4**)	4	16
System Risks				
SYS-01	Structural defaults arise during additive manufacturing process	Structure strength is reduced resulting in increased chance of premature failure of the structure (**4**)	3	12
SYS-02	Development budget cost overrun	Project might be cancelled. Severity of consequence depends on severity of overrun (**5**)	5	25
SYS-03	Return to docking sequence is uncontrollable	Drone and/or environments gets damaged due to crash into the ground or spring-back into the greenhouse (**4**)	4	16
SYS-04	Area coverage is not sufficient	Too many drones are needed per hectare rendering the project economically unviable (**5**)	4	20

Continued on next page

ID	Risk	Consequence (Severity of Consequence)	Chance	Risk Level
SYS-05	High system complexity increases maintenance	Increased operational cost and longer downtime (**4**)	3	12

Visualizing the scores of these risks results in the risk map shown in Figure 14.1. Many risks score very high on both severity of consequence and likelihood, which is expected of the biggest risks of a novel design without mitigation measures.

Subsystem risk level scores are shown in Figure 14.5 and provide an indication of which subsystems face the most risk during future development and operation. For example, the tether subsystem received the highest score (32), suggesting the tether system development will likely require the most resources.

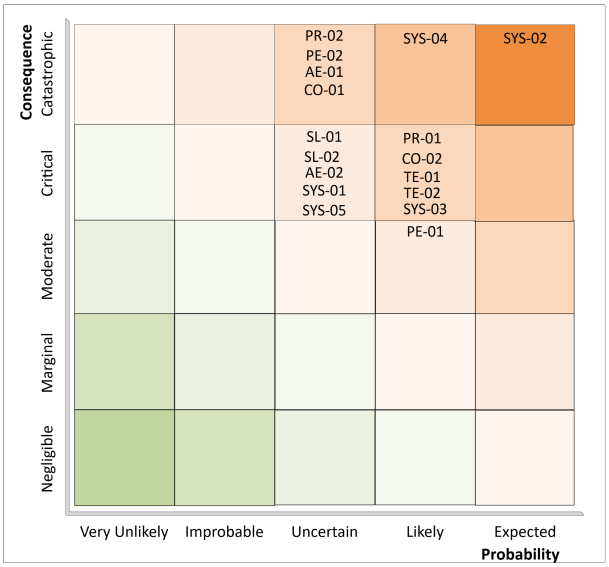

Figure 14.1: Pre-mitigation risk map

Table 14.5: Subsystem risk levels

Concept	Total risk level
Propulsion (PR)	31
Power and Electronics (PE)	27
Structures and Layout (SL)	24
Aerodynamics (AE)	27
Control (CO)	31
Tether (TE)	32

Mitigation measures

From the risk analysis in Table 14.4, it was found that many risks have a high risk level. To improve the likelihood of project success, these risks are mitigated.

The risks shown in Figure 14.1 are ranked in Table 14.6 based on their position in the risk map. The upper right corner is called the 1st diagonal, showing the biggest risk. Next, the diagonals left of the first diagonal are treated and are called the second, third and fourth diagonal. Since all risks are in the upper right triangle, all risks are mitigated. Table 14.6 shows the mitigation strategy, effect on impact and probability and suggested responsible roles.

Table 14.6: Mitigation strategy for high ranking risks

ID	Mitigation plan	Impact	Probability	Suggested responsible members
First diagonal				
SYS-02	Large contingency budget (see Chapter 16) helps keeping track of costs and provides budget margin. Reduces chance and severity of budget overrun.	$5 \rightarrow 3$	$5 \rightarrow 2$	Chief Financial Officer & Project Manager
Second Diagonal				
SYS-04	Operating range is closely discussed with stakeholders. Economic viability is monitored using the analysis in Section 3.3.	$4 \rightarrow 4$	$4 \rightarrow 2$	Chief Financial Officer & Chief Engineer
Third Diagonal				

Continued on next page

ID	Mitigation plan	Impact	Probability	Suggested responsible roles
PR-01	Include motor inspections in maintenance plan	$4 \rightarrow 2$	$4 \rightarrow 3$	Maintenance personnel
PR-02	Battery power deliver capabilities include a margin resulting in a thrust capability margin (see assumptions in Section 7.3)	$5 \rightarrow 4$	$3 \rightarrow 2$	Chief Engineer
PE-02	Make the structure out of fire resistant material[2]	$5 \rightarrow 2$	$3 \rightarrow 3$	
AE-01	Aerodynamic coefficients from the simulations are validated in Appendix A to ensure reasonable results	$5 \rightarrow 4$	$3 \rightarrow 2$	Aerodynamics Engineer
CO-01	Use a predictive algorithm in the controller or tune using model including time delay	$5 \rightarrow 5$	$3 \rightarrow 1$	Control Engineer
CO-02	Integrator term is included in controller to stay closer to operating points in order to increase controller validity	$4 \rightarrow 3$	$4 \rightarrow 3$	Control Engineer
TE-01	Tether connection points are connected in the outer wall of the duct keeping them away from the propeller (Figure 15.14)	$4 \rightarrow 4$	$4 \rightarrow 2$	System engineer
TE-02	Include a high safety factor in the design of the tether. In *the Chameleon* tether, a safety factor of 3.5 has been included, as can be read in Table 12.1	$4 \rightarrow 4$	$4 \rightarrow 1$	System Engineer
SYS-03	Tether is designed to reduce spring-back (see Brake phase in Figure 11.3). $\frac{m}{s}$.	$3 \rightarrow 2$	$5 \rightarrow 4$	Project Manager & Business Manager
Fourth Diagonal				
PE-01	Battery design includes contingency margin to reduce degradation and battery replacement is included in operations.	$3 \rightarrow 2$	$4 \rightarrow 2$	Chief Engineer
SL-01	Struts are reinforced by making them solid instead of hollow to reduce stress.	$4 \rightarrow 4$	$3 \rightarrow 2$	Chief Engineer
SL-02	Tether connections are reinforced and braking sequence is optimized to reduce maximum g-force	$4 \rightarrow 3$	$3 \rightarrow 2$	Chief Engineer
AE-02	Catch rate is increased by improving the control algorithm or redesigning to achieve a higher top speed	$4 \rightarrow 3$	$3 \rightarrow 3$	Chief Engineer
SYS-01	Reduce printing speed, adjust advanced printing settings and/or use more advanced 3D printers from same ecosystem	$4 \rightarrow 4$	$3 \rightarrow 1$	Chief Engineer
SYS-05	Design is made highly modular to decrease maintenance time and cost (see Figure 15.9 for modularity approach).	$4 \rightarrow 3$	$3 \rightarrow 2$	Chief Engineer

These mitigation measures result in the post-mitigation risk map presented in Figure 14.2. Although the map shows that the likelihood or impact of all risks can be reduced, risks like CO-01 still pose a large risk to the project. Such high-impact risks are accepted at this stage of the design but should be closely monitored and/or researched in the future design.

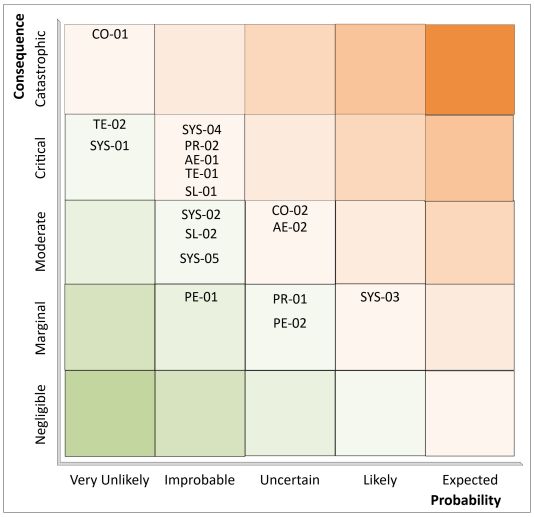

Figure 14.2: Post mitigation risk map

[2]https://biologyinsights.com/is-polycarbonate-fire-resistant/ - Accessed on 16.06.2026

15 Future Project Operations

15.1. Project Design & Development Logic

Figure 15.1 maps the primary post-DSE tasks required to transition the drone from prototyping to the operation and end-of-life phases. The flowchart assumes that the DSE delivers a complete, detailed subsystem design, leaving only the integration with the PATS-C network as a post-DSE design task.

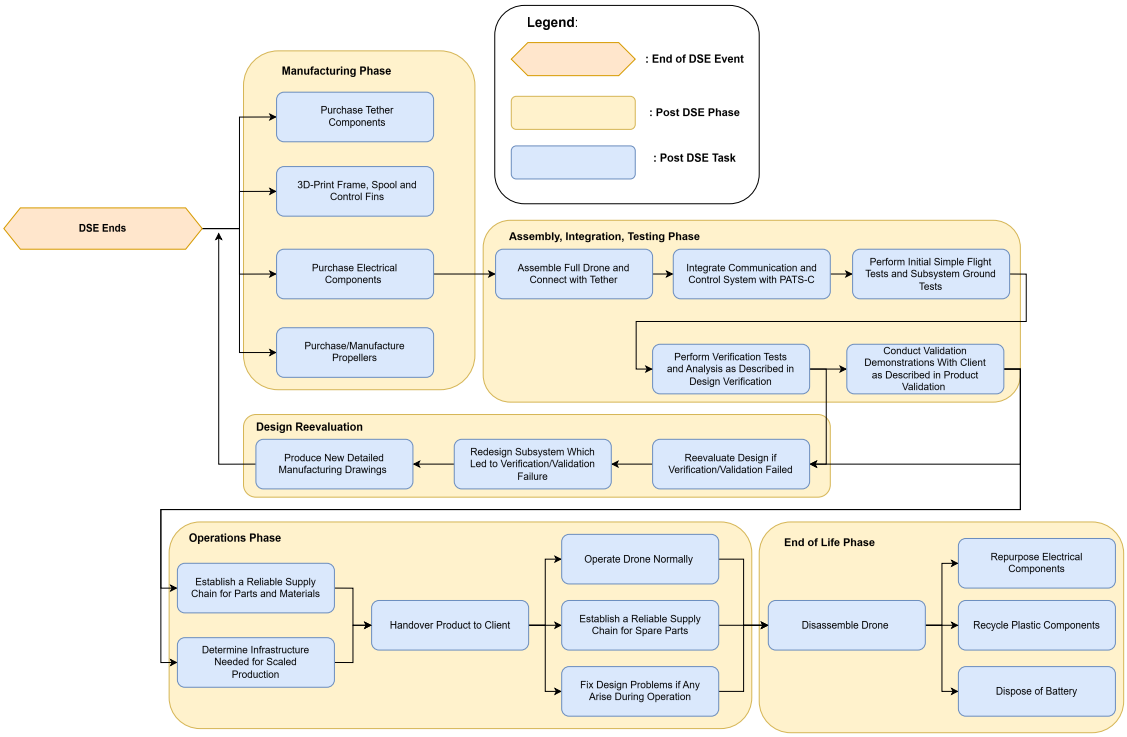

Figure 15.1: Project Design and Development Logic showing post-DSE activities.

15.2. Manufacturing, Assembly & Integration Plan

The Manufacturing, Assembly & Integration Plan (MAI Plan) outlines the activities required for series production of the proposed design. This includes manufacturing instructions for the custom 3D printed components and assembly instructions for the final product. This is summarised in the flow diagram presented below in Figure 15.2.

Custom parts

As per the requirement SYS-32 and Guideline (SDP-1), the drone must be made fully from off-the-shelf parts or parts made via additive manufacturing (3d printing). This requirement has been followed with two exceptions, namely component *D 1mm Shaft 25mm* and the *Custom Propeller(s)* from the bill of materials, presented in Appendix D. *D 1mm Shaft 25mm* is an off-the-shelf part that requires an extra cutting modifi-

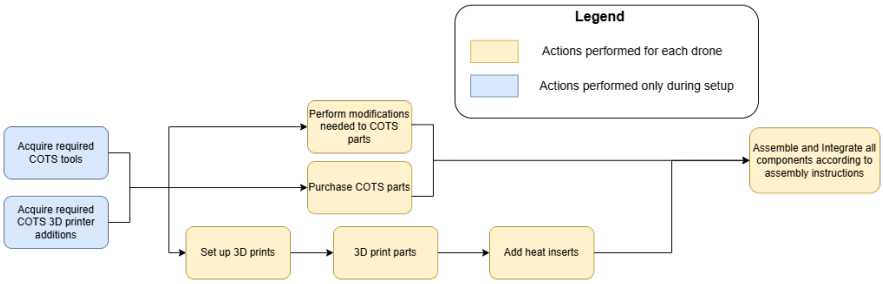

Figure 15.2: Manufacturing, Assembly & Integration Plan Outline

cation. Since this is a simple operation requiring only a ruler and cutting pliers, which are both cheap and readily available tools, it was concluded that this exception would not violate the requirement. The second exception is the custom propeller. As mentioned in Section 6.3, the counter counterrotating propeller setup at this scale would require a custom set of propellers. As a very precise shape and fine surface finish are needed, they can't be manufactured via 3d printing, thus violating the requirement. They will be manufactured via injection moulding. For this, a custom mould is needed, which can be made from the negative of the propeller geometry described in Chapter 6. As this is a specialised process, the design and fabrication of this mould need to be outsourced to a specialist tooling manufacturer. Once the mould has been produced, the propellers can be mass-manufactured by an injection moulding company. The associated costs are discussed in Section 6.3.

Additionally, it's planned that some of the 3d printed parts will be further modified with the addition of off-the-shelf brass heat inserts for plastic, such that parts can be joined together with standard metric fasteners. This is done for ease of assembly and with modularity in mind (SDP-6). The heat inserts can be added with the help of an inexpensive soldering iron and a small enough soldering tip, or a special tip which comes with some heat inserts.

For a detailed list of all parts and associated weights, the reader is referred to the Bill of Materials in Appendix D.

Required tooling

As mentioned above, some simple additional tooling will be needed for the manufacturing process. Overall, the goal for the design has been to minimise its cost, while not harming the durability and modularity of the final design. The needed manual tools include soldering irons with changeable tips, for installing heat inserts, rulers, regular and cutting pliers, and hex keys (Allen keys).

The many parts of the design are fastened together. Thus for the assembly process, hex keys for ISO and DIN standard metric fasteners are needed. The sizes are M1.4 and M2 on the drone, and M3, M5 and M6 for the spooling station (that will reel back the drone). Specifically, with reference to the different length fasteners of these thread sizes, listed in the BOM (Appendix D), the required fastener hex key sizes are:

- *M2x8 DIN912* - 1.5mm Hex Key (Allen)[1]
- *M2x5 ISO 10642* and *M2x8 ISO 10642* - 1.3mm Hex Key (Allen)[2]
- *M1.4x4 DIN912* - 1.3mm Hex key (Allen)[3]
- *M6x12 DIN912* and *M6x16 DIN912* - 5mm Hex key (Allen)[4]

[1] `https://stainlesssteelbolts.co.uk/products/m1-4-x-3-socket-cap-screw-a2-stainless-steel-din-912` - Accessed 17.06.2026

[2] `https://monsterbolts.com/pages/metric-socket-screw-drive-sizes` - Accessed 17.06.2026

[3] `https://stainlesssteelbolts.co.uk/products/m1-4-x-3-socket-cap-screw-a2-stainless-steel-din-912` - Accessed 17.06.2026

[4] `https://stainlesssteelbolts.co.uk/products/m1-4-x-3-socket-cap-screw-a2-stainless-steel-din-912` - Accessed 17.06.2026

- *M3x8 DIN912* - 2.5mm Hex key (Allen)[5]
- *M5x16 DIN912* - 4mm Hex key (Allen)[6]

Additionally, some further machine tooling is required. Currently, the client uses Bambu Labs P1S 3d printers [61]. This machine ships with 0.4mm diameter printing nozzle installed by default[7]. However, as is detailed later in this chapter, some of the smaller parts with finer details will need a smaller hotend nozzle. Hence, some of the machines will need to be equipped with such nozzles. They can be purchased from Bambu's official store[8] for 16.99€ per hotend nozzle assembly (one per machine). This new nozzle can be straightforwardly installed on the P1S according to Bambu's maintenance manual[9].

According to SYS-31, the projected production rate is 1000 units per year. For this production rate, the amount of each required tool has been estimated in Table 15.1. They can be purchased if not already available. Additionally, if the production rate grows to more than 1000 units, the number of these tools should be scaled linearly. Furthermore, more 3d printers will need to be procured than the current ≈ 10 PATS operates [61].

Table 15.1: Required Additional Tooling

Tool	Description	Quantity Required
Soldering Iron (with changeable tips)	For installing heat inserts	2
Ruler	For manual measurement	1
Cutting Pliers	For manual finishing	1
0.2mm Hardened Steel Nozzle Bambu Hotend - P1 Series	Replacement nozzle for finer detail parts on Bambu P1S	3
Pliers	For assembly	2
1.5mm Hex Key (Allen)	For *M2x8 DIN912* fasteners	3
1.3mm Hex Key (Allen)	For *M2x5 ISO 10642*, *M2x8 ISO 10642*, and *M1.4x4 DIN912* fasteners	3
5mm Hex Key (Allen)	For *M6x12 DIN912* and *M6x16 DIN912* fasteners	3
2.5mm Hex Key (Allen)	For *M3x8 DIN912* fasteners	3
4mm Hex Key (Allen)	For *M5x16 DIN912* fasteners	3

D1mm x 25mm shaft

This part is made by modifying an existing off-the-shelf product. The original product is a stainless steel shaft made for RC toy cars. It comes in standard lengths of 100, 300mm or others, and can easily be cut to length for the desired application. The one selected in the BOM is of 300mm length, hence it can be made into 12 smaller shafts of 25mm via 11 cuts. A ruler with millimetre precision is used to make 11 equidistant marks on the original shaft with a pencil, marker or a metal scriber if available. Cuts are then made at each marking with the help of wire snips or cutting pliers, yielding 12 smaller 25mm shafts.

3D printed parts

All other custom components are made via fused deposition modelling (FDM) additive manufacturing, also known as 3D printing. These parts are the *Fuselage, Top motor mount, Battery cap, Shaft cap, PCB cap, Servo mount, Vane, Spool,* and *Platform* from the bill of materials, which can be found in the Appendix D

[5] `https://stainlesssteelbolts.co.uk/products/m1-4-x-3-socket-cap-screw-a2-stainless-steel-din-912` - Accessed 17.06.2026

[6] `https://stainlesssteelbolts.co.uk/products/m1-4-x-3-socket-cap-screw-a2-stainless-steel-din-912` - Accessed 17.06.2026

[7] `https://eu.store.bambulab.com/nl/products/P1S` - Accessed 15.06.2026

[8] `https://eu.store.bambulab.com/nl/products/P1S` - Accessed 15.06.2026

[9] `https://wiki.bambulab.com/en/p1/maintenance/complete-hot-end-assembly` - Accessed 15.06.2026

The instructions on how to manufacture the 3D printed parts required can be found in Appendix E

Heat inserts

Some of the custom 3d printed parts also need to have brass heated inserts added to them. This is done such that parts can later be joined with metric fasteners for ease of assembly and disassembly (This is in accordance with requirement SDP-5, which states that permanent joints shall be avoided if possible).

For installation the following two guides can be used[10] [11]. They have been reviewed and found sufficiently detailed. For installation into polycarbonate, a soldering iron temperature of 220-240°C should be used [12]. The number and type of heat inserts can be found below in Table 15.3.

Table 15.3: Heat Insert Specifications

Component	Insert Type	Quantity
Fuselage	M2×4 brass	4
	M1.4×2.5 brass	2
PCB cap	M1.4×2.5 brass	1
Servo mount	M1.4×2.5 brass	8

Assembly Instructions

After all of the parts from the Bill of Materials (Appendix D) are either manufactured or procured, they need to be assembled. In this section, the main focus falls on the drone part of the system as it's the more complicated assembly and also the main focus of this report. The assembly instructions for it are presented through 12 exploded view sketches of the different steps of the assembly process. As an additional visual aid, an assembly animation is also available via the QR code shown in Figure 15.9a.

The first three steps focus on securing the motors to the drone's frame, also referred to as the Fuselage. In step one (Figure 15.3a), the bottom motor is attached to the drone frame with 4 countersunk M2x8 fasteners. They thread into existing M2 threads on the frame of the motor. Then in the second step (Figure 15.3b), the top motor is similarly fastened to the *Top motor mount* via 4 countersunk M2x5 fasteners forming the top motor subassembly.

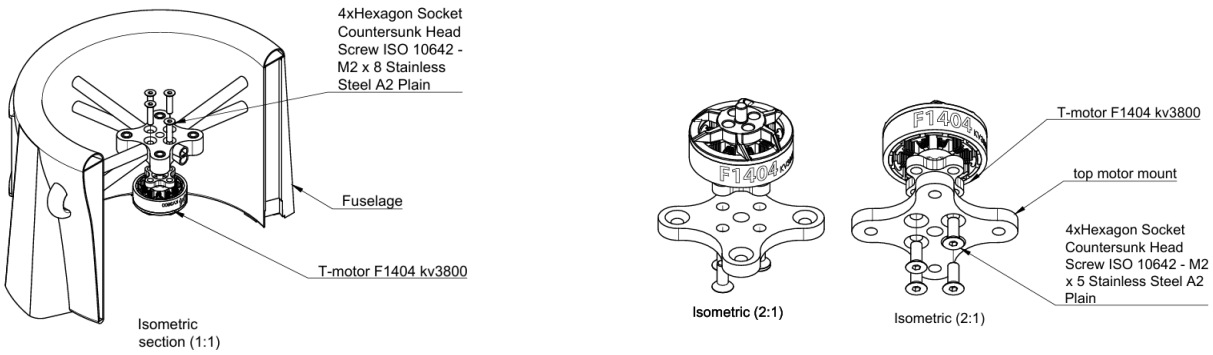

(a) Assembly step 1

(b) Assembly step 2

Figure 15.3: Assembly steps 1 and 2

Next, in step 3 (Figure 15.4a), the top motor subassembly is united with the fuselage through four additional

[10] `https://www.printables.com/article/heat-inserts-and-3d-printing-a-guide-W5ob2VN` – Accessed: 16.05.2026

[11] `https://www.padtinc.com/2019/08/06/adding-inserts-to-3d-printed-parts-hardware-tips-plus-one-click-design-in-grabcad-print-advanced-fdm/` – Accessed: 16.05.2026

[12] `https://rivetfix.com/blog/how-to-choose-threaded-inserts-for-plastics/` – Accessed: 16.05.2026

countersunk M2x8 fasteners. They screw into heat inserts embedded within the top part of the fuselage's mount. The top motor subassembly sits flush on top of the fuselage's mount due to the use of countersunk fasteners. Afterwards, in step 4 (Figure 15.4b), the propellers are attached to the drone. After aligning each propeller with the threaded holes on the motor's rotor, each propeller is slid onto the motor shaft. It's then secured with the help of two M2x8 hex socket bolts.

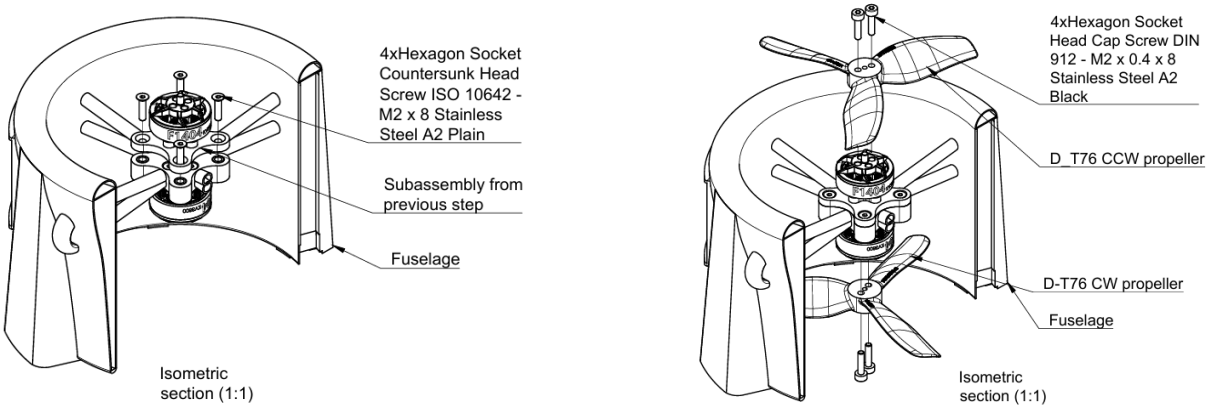

(a) Assembly step 3

(b) Assembly step 4

Figure 15.4: Assembly steps 3 and 4

Assembly step 5 (Figure 15.5a) covers the direction control sub-assembly, which is comprised of the *Servo mount*, 4 *micro servos* and 4 *Vanes*. First, a servo is secured to the Servo mount with two M1.4x4 fasteners. They screw into the corresponding heat inserts in the Servo mount. Then the airfoil vane is attached to the servo's gear via its matching cutout. This is designed as a plastic-on-plastic press-fit that can be done and undone with moderate force by hand. Note that there is a hole both in the servo's gear and through the vane. A friction-fit metal shaft will later pass through them. In step 6 (Figure 15.5b), this process is repeated 3 more times

Mind that there is a small cutout on one side of the Servo mount to pass the servo's cable through. Once all servos are installed, the cables can be routed along the protrusion on the Servo mount with a zip tie, which will route them to the outside of the drone's shell.

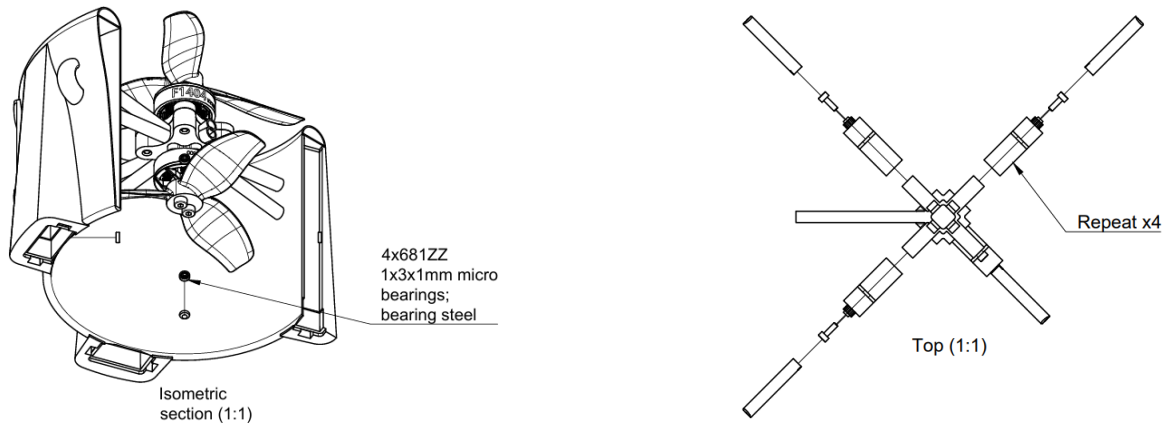

(a) Assembly step 5

(b) Assembly step 6

Figure 15.5: Assembly steps 5 and 6

In assembly step 7 (Figure 15.6a), 4 681ZZ micro bearings are added to the fuselage. These are designed to

be press-fit into place, into the plastic fuselage, by hand or with the help of the tip of a pair of pliers. If a bearing ever needs to be removed, this can be done by pushing through a small screwdriver from the opposite side. Then in step 8 (Figure 15.6b), the servo direction control assembly is inserted into the fuselage from below. The holes in the direction control vanes are aligned with the bearings. There are 4 small holes on the outside of the fuselage, where each bearing is located. By looking through them from the outside, they can be used as a visual guide for the alignment.

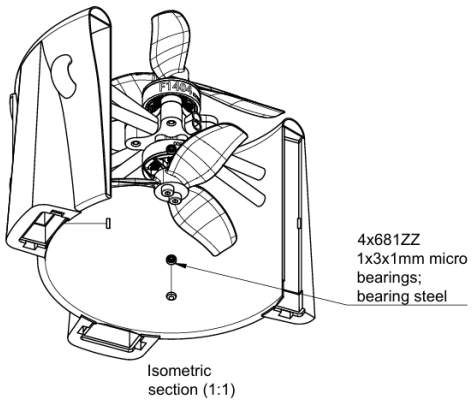

(a) Assembly step 7

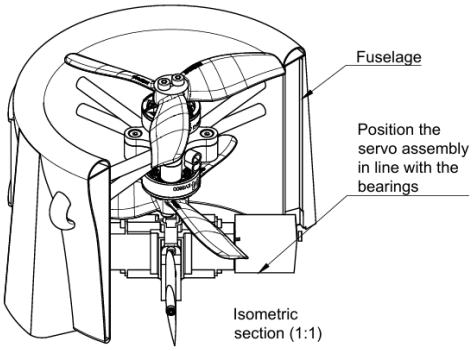

(b) Assembly step 8

Figure 15.6: Assembly steps 7 and 8

In step 9 (Figure 15.7a), four shafts (*D 1mm Shaft 25mm*) are introduced through the aforementioned four small holes on the outside of the fuselage. These stainless steel shafts go all the way through the bearing, control vane and end up in the servo's gear, giving the whole subassembly a lot of strength. This is a friction fit, which can be done by grabbing one end of the shaft with pliers and pushing it in all the way through. The shaft is designed such that it sticks out 3-4mm and can thus be taken out for disassembly with the use of pliers (in accordance with requirement SDP-5 that states permanent joining of parts shall be avoided). After the shafts are put in, a small plastic cap (*Shaft cap*) is used to cover the sharp edges of the shaft that stick out.

In step 10 (Figure 15.7b), the flight controller is installed. It is mounted with two M1.4x4 Hex socket head fasteners that screw into corresponding heat inserts in the Fuselage. Wiring to the flight controller is routed through the holes in the flight controller casing to the outside of the drone. Then the cover cap (*PCB cap*) is installed. The cover cap has two pins at the top, which, when introduced at a slight angle, slide into corresponding cutouts on the frame.

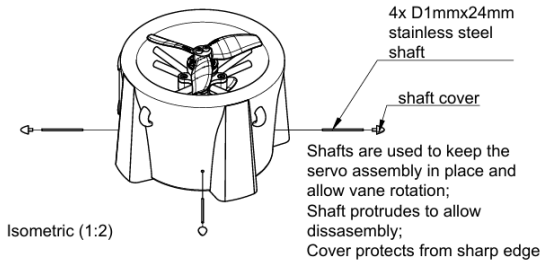

(a) Assembly step 9

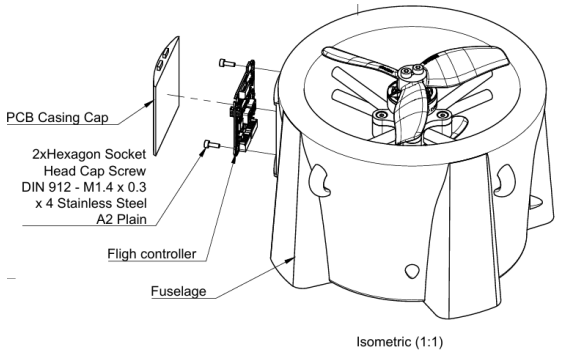

(b) Assembly step 10

Figure 15.7: Assembly steps 9 and 10

In the penultimate step 11 (Figure 15.8a), the aforementioned cover cap (*PCB cap*) is secured in place with another M1.4x4 Hex socket head fastener. It screws into a heat insert inside the cap. Finally, in step 12

(Figure 15.8b), the four batteries are put in. Each one is secured with a snap-on cap with a latch that is pressed into place until it snaps in, similarly to the battery caps on some (older) remote controls.

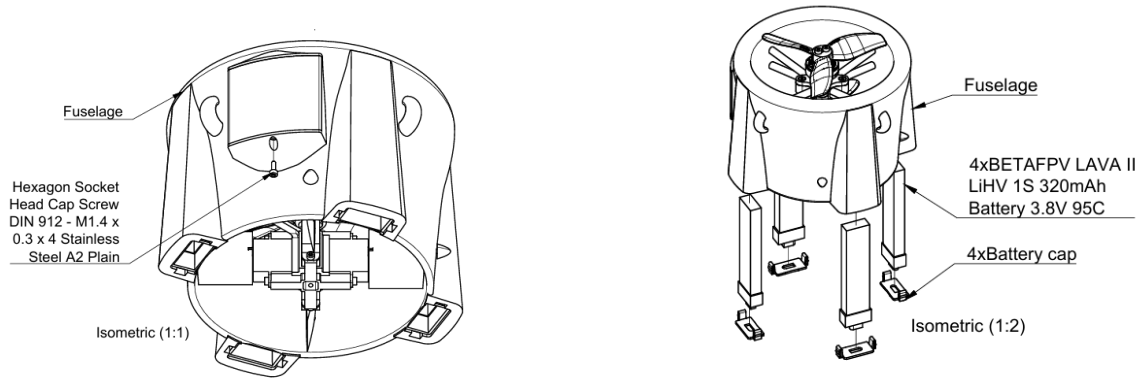

(a) Assembly step 11

(b) Assembly step 12

Figure 15.8: Assembly steps 11 and 12

Lastly, as previously mentioned, a 3D animation of the above assembly steps has been made in case the reader finds something unclear. The fastener sizes specified in the drawings above should be used. The animation is intended to illustrate how the parts go together better. It can be accessed via the QR code presented below in Figure 15.9a for readers of the paper format or with the associated alternate link for readers of the digital format of this report.

(a) Animation on how to assemble the drone
Equivalent link: `https://youtu.be/3DxaxD4CUzU`
Alternative link: `https://doi.org/10.5281/zenodo.20814282`

(b) Animation on how to assemble the spooling station
Alternative link: `https://youtu.be/K96fUnHi-mQ`
Alternative link: `https://doi.org/10.5281/zenodo.20814282`

Figure 15.9: Assembly videos

The assembly for the spooling station is a simpler procedure. For this reason, no detailed instructions were made. Only an animation illustrating the procedure was prepared. It can similarly be accessed via Figure 15.9b

15.3. Configuration and layout of the design

Readers are strongly encouraged to review the previous subsection on assembly before proceeding, in case they skipped it. Through reading the assembly instructions and with the help of Figure 15.3a through Figure 15.8b, the reader should be able to gain a clear understanding of the drone's layout and the placement of its internal components. Thus, to avoid repetition, this chapter will focus on why certain layout and design choices were made. Furthermore, renders showcasing the internal and external appearance of the design will be presented.

As a whole, DFMA (Design for Manufacturing and Assembly) principles and established design conventions were incorporated throughout the design process, and particularly in the layout of the drone. This was also demonstrated in the previous assembly subsection. Although the system is relatively complex for a birotor platform, it remains straightforward to assemble and disassemble. In line with the theme of modularity and repairability, any permanent joints were avoided as dictated by SDP-5.

The first big design challenge that had to be overcome was mounting two counterrotating motors with concen-

tric shafts. Each motor must be secured using bolts inserted from the rear. However, there is another motor in the way. Off-the-shelf solutions exist with conjoined stators and a different mounting option, but they do not fall within the size and power requirements, as they are much bigger than what is employed here. Hence, a custom solution was developed. Each motor is attached to a separate mount using countersunk fasteners. The two parts can then sit flush on top of each other as shown in Figure 15.10. The two parts (*Fuselage* and *Top motor mount*) are then fastened together at a position where the motor does not obstruct the bolt path, as shown in Figure 15.16.

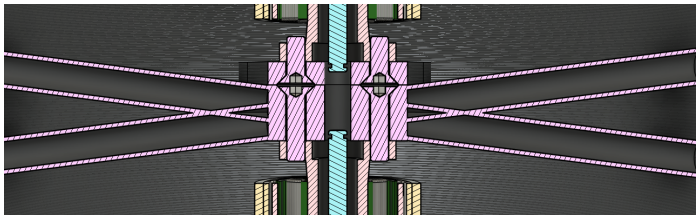

Figure 15.10: Section through the centre of the motor mounting solution

Since the servo direction control mechanism is the most fragile part of the design, it was integrated deep inside the drone. Additionally, the direction control vanes need to catch the airflow created by the propellers. It should also be noted that the vane geometry is designed such that there is enough clearance for the vanes to rotate, but there isn't enough free space for the bearing to fall out or for the vane to detach from the servo's gear unless the whole sub-assembly moves down and out of the fuselage. For this to happen, all 4 shafts would have to be fully removed at least up to the bearing. This can be seen in the cross-section, presented below in Figure 15.11

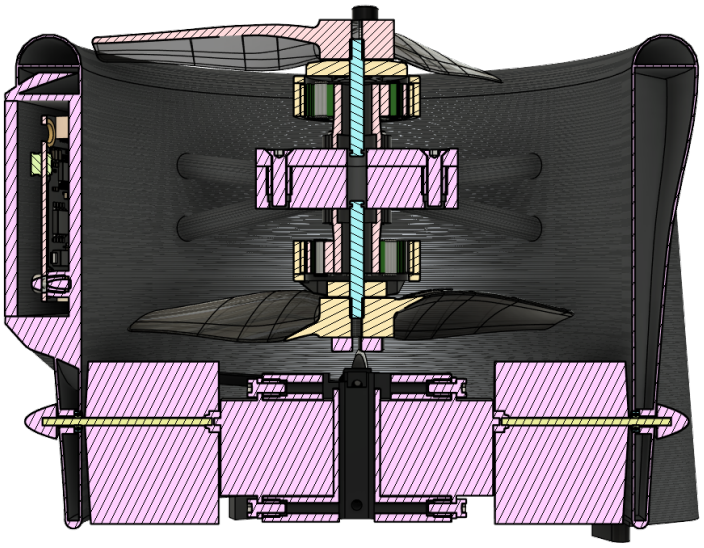

Figure 15.11: Section view through the whole drone design

Furthermore, it's important to point out that, besides allowing the vanes to rotate, these shafts also locate the Servo mount and servos. As the vane, shaft, and the servos' gear rotate in one direction, a counter torque is generated on the servo and thus the rest of the subassembly. Once the servo holds its position, the aerodynamic forces on the vane also create a torque that gets transferred from the vane through the shaft into the servo and servo sub-assembly. The rotation of the servo subassembly due to this torque is constrained by the two shafts perpendicular to the one considered. This generates a force normal to the cylindrical surface of the bearing's inner ring. For this reason, actual bearings with ball bearings were used instead of the cheaper and simpler

plain bearings. They are much more resistant to wear and will ensure free rotation of the shafts even with this applied load.

Since there is no space left on the inside for the other bulkier components like the batteries and the flight controller, they were integrated inside the body with the use of aerodynamic fairings, as is shown in Figure 15.12. Because the batteries pose a severe risk, much effort was put into protecting them. They are embedded deep inside the structure, as can be seen in Figure 15.12. Additionally, the infill on the inside of the structure, between the two solid walls, should act as a crumple zone and absorb and dissipate energy in case of a direct crash against one of the battery casings, as shown in Figure 15.13. Figure Figure 15.12a showcases that a similar crumple zone was also left in front of the battery in case of a head-on collision.

Lastly, during the breaking manoeuvre, the inertia of the batteries will carry them forward into the structure. For this reason, they are put in from behind. This way, they won't apply a large force on the cap, keeping them inside the drone during breaking. As the cap won't experience big forces, it was designed as a snap fit to facilitate easy replacement of the batteries, as they are considered the most likely component to need replacement.

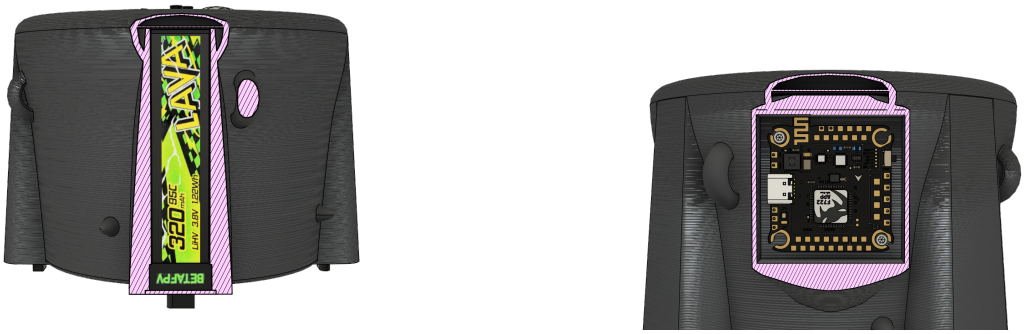

(a) Section view revealing one of the batteries

(b) Section view revealing an example flight controller

Figure 15.12: Battery and flight controller integration inside aerodynamic fairings

(a) Section view revealing how the batteries integrate into the structure

(b) Equivalent view of how this will look in the 3d printed structure

Figure 15.13: Integration of the batteries and steps taken to protect them

A render of the internal layout of the drone is presented in Figure 15.14. Some further visuals of the design in flight can be found in Figure 15.15

Figure 15.14: Render of the internal appearance of the 3d printed design

(a) External appearance of the design. Side view render

(b) External appearance of the design. Front view render

Figure 15.15: Renders of the external appearance of the 3d printed design

For the 3d model and renders of *the Chameleon*, some existing models were used to illustrate the design. These are a mockup of the motor[13] and a flight controller[14]. All other components are modelled according to the dimensions found online.

Finally, the layout of the spooling system, which is less size-constrained, is primarily determined by the spool shaft. All rotating components are in line with this shaft. Because the brake and motor activate in separate flight phases, each is placed on one side of the spool. Due to RPM considerations, the motor is connected to the main shaft via a one-way bearing so as not to overspeed the motor during the interception phase. Because the one-way bearing does not match the shaft diameter that the brake supports, another coupling is used. The general bearings next to the spool are used for support. This linear layout is well visualised in Figure 15.16. Originally, a gimbal system was designed to aim the drone before launch, since this greatly increased complexity, another alternative was designed. A simple passive yaw swivel that uses

[13] `https://grabcad.com/library/t-motor-f1404-3800kv-1` – Accessed 19.06.2026
[14] `https://grabcad.com/library/flight-controller-diatone-mamba-mk4-f722-app-1` – Accessed 19.06.2026

an off-the-shelf ball bearing lets the spool turn in the correct direction (see Figure 15.16b. In future design iterations, the gimbal could be reconsidered.

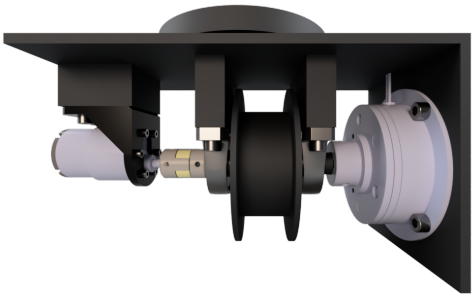

(a) Front view of the spooling platform. On the right, the brake is visible, on the left, the reelback motor. Between the motor and spool, a spider coupling is coupled to the spool shaft and the one-way bearing (not visible, located inside the spider coupling).

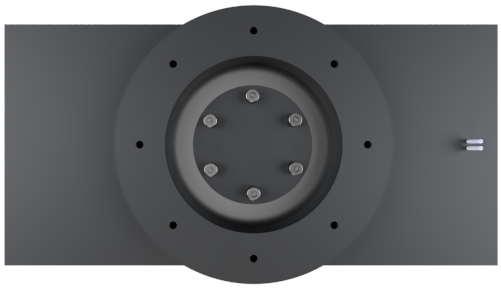

(b) Top view of the spooling platform, the yaw swivel, including the metal ball bearing, is clearly visible. On the right, a cable duct is visible.

Figure 15.16: Renders of the spooling platform.

15.4. Gantt Chart for post-DSE operations

The activities displayed in Figure 15.1 have been put in a timeline and have been assigned a responsible person. The timeline is shown in Figure 15.17, and it shows that the first full operation cycle is completed at the start of the fourth quarter of 2027, by estimate. The activities are labelled with the corresponding phase and the responsible function. Refer to the figure caption for an explanation. Except for this timeline, two other timelines, optimistic and pessimistic, were developed. These are located in Appendix B, along with an explanation.

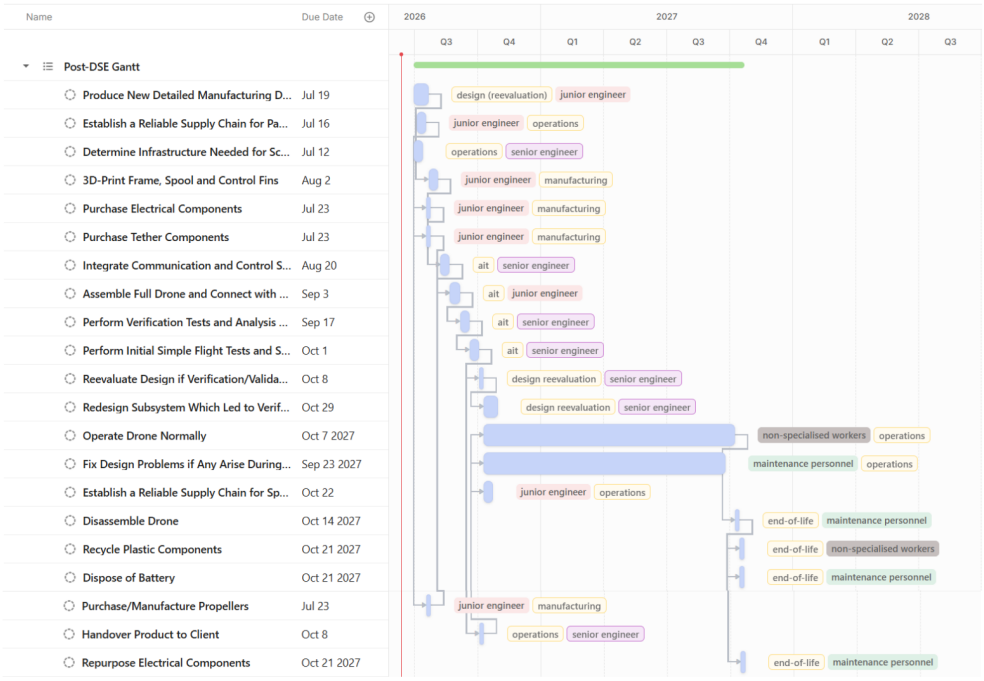

Figure 15.17: Post-DSE activities timeline (nominal), with phases indicated in the yellow tags (where 'ait' stands for 'assembly, integration and testing') and the assignee indicated by the red, violet, grey, and green colored tags (junior engineer, senior engineer, non-specialised workers and maintenance personnel, respectively).

16
Finances

In this chapter, the economic viability of the project is evaluated. System costs are estimated using a bottom-up Cost Breakdown Structure. Furthermore, using the target system cost and expected market penetration from Chapter 3, the Net Present Value (NPV) and the Return on Investment (ROI) are established to quantify the long-term financial feasibility.

16.1. Cost Breakdown

Methodology

Cost estimation for *the Chameleon* was conducted utilising a bottom-up methodology, baselined to Fiscal Year 2026 (FY2026). System-level costs were determined by aggregating the lowest-level elements of the Cost Breakdown Structure (CBS) (see Figure 16.1. Recurring hardware expenses were sourced from Commercial Off-The-Shelf (COTS) vendor quotes or marketplace listings (as of June 2026). Labour costs for engineering, manufacturing, assembly, integration, and testing were calculated by multiplying estimated task man-hours (from Section 15.4) by standardised local (Dutch) wage rates. To accurately reflect actual employer costs, these base wages are multiplied by a fully burdened wrap rate. This rate accounts for standard fringe benefits, overhead, General and Administrative (G&A), and the commercial margins associated with hiring short-term external project engineers. The exact derivation of these hourly tariffs per technical role is given in Appendix C. The development budget does not take into account the standard costs of the engineering work performed during the DSE.

Asset depreciation assumes a standard five-year hardware replacement cycle for the 3D-printer farm. Finally, projected end-of-life sustainability liabilities (as detailed in Chapter 2) are captured in the annual costs.

Contingency Development Budget

To address the technical risks identified in Chapter 14, a development contingency budget is established. Rather than applying an arbitrary percentage margin, this budget is derived using a scenario-based estimation methodology, linked to the project scheduling variances outlined in Section 15.4. Three development timelines were mapped in the post-DSE Gantt chart: optimistic, nominal, and pessimistic. The pessimistic scenario models a complete system verification and validation failure. This scenario captures the necessary senior engineering labour hours required for a five-week design re-evaluation and subsystem redesign, alongside the costs of repeating integration, supply chain re-establishment, and assembly line setup.

The contingency budget represents the financial delta between the nominal and pessimistic development scenarios. Based on this calculated delta, the final development contingency budget is allocated at EUR 109k. The detailed cost breakdown of this scenario-based analysis is located in Appendix C.

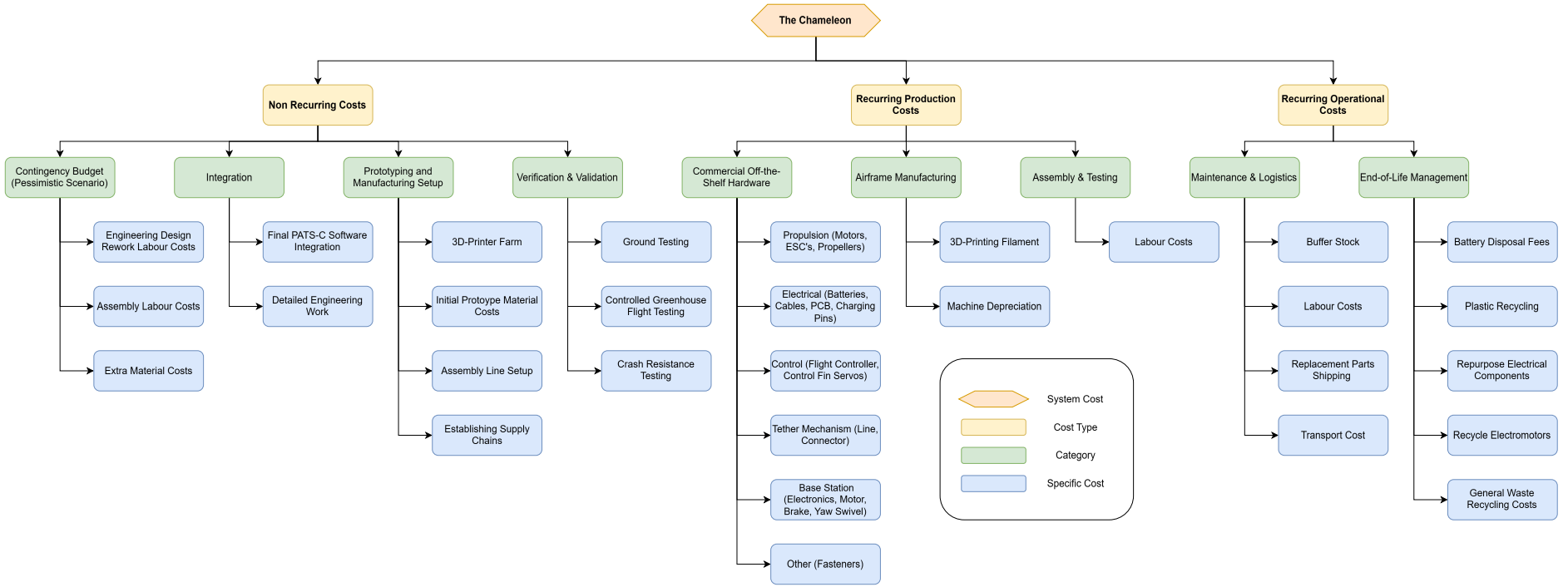

Figure 16.1: Cost Breakdown Structure

Cost Summary

The total system cost is segmented into three primary categories: Non-Recurring Costs for initial development, recurring unit production costs, and recurring operational and maintenance expenses. The costs for the system are summarised as follows:

- Development Cost: EUR 103k nominal scenario, EUR 212k pessimistic scenario
- Unit Cost: EUR 239
- Annual Recurring Costs (Year 1): EUR 561k

This breakdown reveals distinct cost drivers across the categories. The Non-Recurring Cost is dominated by engineering labour hours required for system integration, verification, and validation (by over 85%). Because development expenses are primarily driven by labour rather than hardware, this phase is highly sensitive to schedule overruns, thereby validating the schedule-based contingency approach. Conversely, the Unit Production Cost is driven almost entirely by hardware costs (by over 90%).

These estimates are evaluated against the initial engineering requirements. The unit manufacturing cost of EUR 239 complies with the EUR 250 limit specified by requirement SYS-29. For the development budget, the nominal projection is EUR 103k. This exceeds the EUR 100k budget established by requirement SYS-30. Rather than reducing the project's scope to ensure compliance with this requirement, this cost overrun is accepted. As demonstrated in Section 16.2, the model is resilient to non-recurring cost overruns; even in the pessimistic scenario where development costs double, both the NPV and the ROI remain high.

16.2. Net Present Value and ROI

To evaluate the commercial viability of *the Chameleon*, a five-year Discounted Cash Flow model is established. Future cash flows are discounted at a conservative rate of 35% to account for early-stage risks associated with start-ups [119]. This sits well above the standard 7% to 10% discount rates of typical aerospace companies [120, 121, 122, 123]. Market deployment is capped at 1,000 units annually for market adaptation and to resolve early teething issues. Annual is assumed to scale by a flat 30% every year, which captures the compounding maintenance and logistics of supporting an expanding active fleet.

Utilising a unit production cost of EUR 239 yields a net annual cash flow that grows from EUR 49.9k in Year 1 to EUR 1,640k in Year 5. The net present value is calculated using the nominal development cost of EUR 103k:

$$\text{NPV} = \sum_{t=1}^{5} \frac{CF_t}{(1+r)^t} - C_0$$

This yields a strongly positive NPV of EUR 1,546k (IRR: 250%). A sensitivity analysis confirming positive returns across a wider range of discount rates, alongside the NPV calculation for the pessimistic scenario, is tabulated in Appendix C.

Because the NPV confirms that the project is worthwhile, the ROI is established: $\text{ROI} = \frac{\text{Profit}}{\text{Investment}}$ To reflect capital requirements, the denominator includes the annual costs from Year 1, alongside the development budget, meaning the total initial investment is EUR 664k. The resulting nominal ROI is 739%. The detailed calculations and the ROI for the pessimistic scenario (635%) are located in Appendix C.

It must be emphasised, however, that these projections only capture operational economics and are therefore heavily optimistic. Actual profit margins will be significantly lower when corporate income taxes (about 25%[1]) and customer acquisition costs are factored in. In this limited financial estimation, the latter costs are out of scope, and corporate income tax is only applied after all costs are accounted for, hence the omission. Additionally, due to the volatility of marketplace listings, it is recommended that in future phases, prices be sourced from bulk vendors.

[1] `https://www.belastingdienst.nl/wps/wcm/connect/bldcontentnl/belastingdienst/zakelijk/winst/vennootschapsbelasting/tarieven_vennootschapsbelasting` – Accessed: 20-6-2026

17
Requirements Compliance

In this chapter, the compliance of the final design with the requirements is evaluated. Furthermore, the verification and validation methods of these requirements is presented

17.1. Verification & Validation of Requirements

The following section describes the various verification and validation procedures which should be used in the future throughout the different stages of the project. A breakdown of the verification and validation that should be performed throughout the project is given below.

1. Verification of the final design. This refers to confirming through various means (e.g., analysis, testing, etc.) that the final product meets all derived system requirements established throughout the design process.
2. Validation of the final product. This refers to assessing whether the final product fulfils the intended operational objectives and stakeholder requirements under representative mission conditions using system-level analysis and testing where possible.

Verification of Final Design

While several requirements can be verified through analysis and simulation during the DSE, others require physical testing or demonstrations, which fall outside the scope of the present project. Consequently, these verification activities are not performed within the DSE itself, but a verification plan for future implementation is provided. All relevant information regarding the proposed verification methods and estimated costs is presented in Table 17.1. It should be noted that, for most of the requirements, no special facilities are required, and thus no such column is added. The exception to this, is the verification of SYS-23 and SYS-24. For these two, a small chamber in which humidity and temperature can be regulated would be needed.

Validation of Final Design

All requirements relevant for the product validation, as well as their validation method and estimated cost, can be seen in Table 17.2. No special facilities will be needed to perform the validation. The only requirement is that the demonstrations are performed in conditions resembling operational conditions, which can be achieved by conducting them in any greenhouse environment.

17.2. Compliance and Feasibility

At the end of Table 17.1 and Table 17.2, two additional columns are provided. The first indicates whether the final design is compliant with the requirement, while the second presents the attained value or provides further explanation. These values are primarily based on analysis. For some requirements, analysis alone is sufficient to verify or validate compliance, whereas others require testing or demonstration. Thus the symbols which can be seen in the matrix together with their meaning are the following: ✓- requirement is considered fully met, ✓* - analysis shows requirement is met, but further testing is needed for full confirmation, FT - future testing is required to see if requirement is met, TBS - to be shown in the future (regards requirements which should be confirmed in the future by means other than testing), x - requirement is not met.

Table 17.1: Final Design Verification of Requirements

ID	Requirement	Method*	Test / Procedure	Est. Cost (€)	Compliance	Attained Value
SYS-01	The drone shall achieve a stopping distance $\leq$ 0.8 m from 5 m/s	T	Final verification should be conducted experimentally by measuring the stopping distance of the drone during a braking manoeuvre from an initial velocity of 5 m/s.	$\leq$ Cost of 10 drones	✓	0.4 m from 9.6 m/s
SYS-02	The drone shall absorb an impact energy of $\geq$ 2.806 J	T	Final verification should be conducted experimentally through controlled impact testing in which the absorbed impact energy is measured	$\leq$ Cost of 10 drones	FT	Simulation shows it does for a solid body, 3D model has to be tested.
SYS-03	The drone shall withstand loads from maximum acceleration and deceleration	A	Structural analysis of inertial load cases verifying stress	≈ 0	✓	6 x Deceleration loads measured
SYS-04	The drone's natural frequencies shall be outside the range of the propeller and motor excitation frequencies by a margin of 10%	A	Modal analysis to verify 10% separation between natural and excitation frequencies	≈ 0	FT	Accurate eigenmodes cannot be found for 3D-printed structures
SYS-05	The drone shall deform $\leq$ 10% of the larger side of the frame under mission loads	A	Static structural analysis to verify maximum deformation under mission loads	≈ 0	✓	7%
SYS-07	The drone shall have a turnaround time of $\leq$ 5 min	A	Availability estimation using probabilistic modelling	≈ 0	✓	4 min 16 sec maximum
SYS-08	The drone shall have a spool-up time of $\leq$ 1 s	T	System response time tested by measuring time between pest detection and lift-off of drone in normal operating conditions environment	$\leq$ Cost of 10 drones	FT	N/A
SYS-09	The drone shall have a recharge time to 30%-70% capacity $\leq$ 5 min	T	Test in which battery is charged with the charging method which will be used in operation and charge time is measured	$\leq$ Cost of 10 batteries	x	12 min, however turnaround time $\leq$ 5 min
SYS-12	The drone shall have a position accuracy of at least one propeller diameter	T	Test in which the drone flies to a specific point and the distance between the point and the actual final location of the drone is measured	$\leq$ Cost of 10 drones	FT	N/A
SYS-16	The drone shall achieve a T/W $\geq$ 5	T	Test in which a weight is attached to the drone that makes the total weight equal to 5 times the drone weight, and it is seen whether the drone can take off	$\leq$ Cost of 10 drones	✓*	5.3
SYS-18	The drone shall have VTOL capabilities	D	Demonstration in which the drone takes off vertically	$\leq$ Cost of 10 drones	✓*	N/A
SYS-19	The drone's energy capacity shall be $\geq$ 600 (Cl. 1) / 250 (Cl. 2) mAh	A	Determined by looking at the specifications of the battery placed in the drone	≈ 0	x	320 mAh, however sufficient for required flight time
SYS-22	The total mass shall be below 200 grams	I	Measure the drone's weight with a scale	≈ 0	✓*	143.4 g
SYS-23	The drone shall be able to operate at relative humidity of 85 %	T	Test in which the drone is placed in such an environment, and it is checked whether it can operate normally	$\leq$ Cost of 10 drones	✓*	N/A

Continued on next page

ID	Requirement	Method*	Test / Procedure	Est. Cost (€)	Compliance	Attained Value
SYS-24	The drone shall be able to operate in a temperature range of 10-35 °C	T	Test, which is conducted at different temperatures in the stated range, and it is checked whether the drone operates normally	$\leq$ Cost of 10 drones	✓*	N/A
SYS-27	The drone shall have a minimum of 1000 mission cycles	A	Simulations using known probability of failure of components	≈ 0	✓	Yes if batteries are replaced, fatigue tests for frame performed
SYS-28	Drone shall consist of modular parts	I	It is inspected whether the drone parts can be disassembled and assembled again	≈ 0	✓*	Designed to meet req.
SYS-29	The cost per drone shall be below 250 euros	A	Price of all parts the drone consists of is obtained and added together	≈ 0	✓	EUR 239
SYS-30	Development cost shall be below 100 000 euros	A	Price of all parts the drone development consists of is calculated and added together	≈ 0	x	Budget overrun in both pessimistic (EUR 212k) and nominal scenario (EUR 103k), this is accepted since ROI remains high.
SYS-31	Production rate shall be 1000 units per year	A	Time to produce drone and obtain off-the-shelf components is estimated based on 3D printing simulations and market data	≈ 0	✓	> 1500
SYS-32	Drone shall be made fully of off-the-shelf or 3D-printed components	I	All drone components are checked, and it is determined whether they can be bought off the shelf or 3D printed	≈ 0	✓	Designed to meet req.
SYS-33	Braking system control shall be integrable with the existing control system	A	Analysis of current control system and control software needed for correct operation of braking system	≈ 0	x	New system needs to be designed but it is included in development cost
SYS-34	The communication system shall interface with the existing external moth tracking system	A	Analysis of operating frequencies and conditions of existing tracking system and drone communication system	≈ 0	✓	COTS receiver is used
SYS-36	The communication system shall meet the required range ≥ 9 m	T	Test in which the drone is placed 9m away, and it is tested whether it can still send and receive communication	$\leq$ Cost of 10 drones	FT	N/A
SYS-38	The drone shall dock autonomously	D	Demonstration in which the drone docks autonomously	$\leq$ Cost of 10 drones	✓*	Autonomously reeled by tether
SYS-39	The drone shall achieve docking accuracy ≤ 1 cm	T	Test in which the drone has a target point on which it needs to land and it is observed whether it lands less than 1cm away from the point	$\leq$ Cost of 10 drones	✓*	Drone is reeled by tether
SYS-40	The drone shall not ingest the tether during flight	D	Demonstration in which the drone performs a flight without ingesting the tether	$\leq$ Cost of 10 drones	FT	N/A
SYS-44	The drone system shall be priced at EUR 10,000/ha/year	I	Inspection of the price of the drone system	≈ 0	TBS	N/A

*A = Analysis, T = Test, I = Inspection, D = Demonstration

Table 17.2: Final Design Validation of Stakeholder and Mission Requirements

ID	Requirement	Method*	Validation Procedure	Est. Cost (€)	Compliance	Attained Value
STK-01	The drone shall not sustain damage during the mission	D	Perform repeated mission demonstrations under operating conditions to assess whether the drone completes missions without sustaining damage	$\leq$ Cost of 10 drones	TBS	N/A
STK-02	The drone shall intercept moths	D	Perform repeated demonstrations in which the drone attempts moth interception under operating conditions to assess mission success	$\leq$ Cost of 10 drones	TBS	N/A
STK-03	The drone shall operate safely within the greenhouse environment	D	Perform operational demonstrations and safety testing within greenhouse environments	$\leq$ Cost of 10 drones	TBS	N/A
STK-05	The drone shall be sustainable	A	Do a lifecycle and environmental impact assessment, considering materials, recyclability and operations	≈ 0	✓	Drone eliminates the need for pesticides
STK-06	The drone shall be commercially viable	A	Perform economic feasibility assessment considering manufacturing, operational, and maintenance costs	≈ 0	✓	ROI is 739% after five years, product is EUR 5,000 per year cheaper than pesticides.
STK-07	The drone shall be able to be integrated with current PATS infrastructure	D	Perform integrated operation demonstrations with existing PATS systems and infrastructure	$\leq$ Cost of 10 drones	x	New docking system needed, included in development cost
MIS-04	The drone shall intercept moths with its propeller	D	Perform operational demonstrations in which the drone intercepts moths using its propellers	$\leq$ Cost of 10 drones	TBS	N/A
MIS-05	The drone shall have 80 sorties per day	D	Estimate achievable sortie rate analytically through component-wise statistical calculations and demonstrate repeated mission execution	$\leq$ Cost of 10 drones	✓*	≥ 200
MIS-06	The drone shall fly to the moth	D	Perform demonstrations in which the drone autonomously flies toward a detected moth target	$\leq$ Cost of 10 drones	TBS	N/A
MIS-07	The drone shall sustain a mission duration of $\geq$ 30 s	D	Perform demonstrations in operating conditions while measuring mission duration	$\leq$ Cost of 10 drones	✓*	$\geq$ 40 s
MIS-09	The drone shall not damage crops or humans	D	Perform operational safety demonstrations in greenhouse conditions	$\leq$ Cost of 10 drones	TBS	N/A
MIS-10	The drone shall be able to operate in greenhouse conditions	D	Perform operational demonstrations under representative greenhouse temperature and humidity conditions	$\leq$ Cost of 10 drones	TBS	N/A
MIS-11	The drone shall minimise environmental impact	A	Perform environmental impact assessment considering operational and material-related impacts	≈ 0	✓	>99% lower environmental impact than pesticides (using the eco-cost framework)
MIS-12	The drone shall be commercially viable	A	Perform cost and production feasibility assessment	≈ 0	✓	ROI is 739% after five years, product is EUR 5,000 per year cheaper than pesticides.

Continued on next page

ID	Requirement	Method*	Validation Procedure	Est. Cost (€)	Compliance	Attained Value
MIS-13	The drone shall be controlled by PATS existing system	D	Perform integrated demonstrations with the existing PATS control system	$\leq$ Cost of 10 drones	TBS	N/A
MIS-14	The drone shall communicate with the PATS-C camera system	D	Perform communication demonstrations between the drone and the PATS-C system under representative conditions	$\leq$ Cost of 10 drones	✓*	COTS communication components used
MIS-15	The drone shall dock on existing PATS docking infrastructure	D	Perform docking demonstrations using existing PATS docking infrastructure	$\leq$ Cost of 10 drones	x	New docking system design included in the development cost

*A = Analysis, T = Test, I = Inspection, D = Demonstration

17.3. Sensitivity Study

The final design presented in Chapter 12 converges on a 75mm propeller (Table 1). The purpose of this section is to verify that this diameter constitutes an optimum rather than an arbitrary choice, by probing the design space on either side of it. Both a larger (90mm) and a smaller (60mm) variant are evaluated using the same optimisation framework introduced in Chapter 5 (Chapter 6), in particular the first iteration loop (IL-1) used to size the motor, battery, and structure. Reusing this framework ensures that the snowball estimates presented here are consistent with the loops that produced the baseline design, rather than ad-hoc calculations. As shown below, enlarging the propeller to 90mm violates the weight and cost budgets, while shrinking it to 60mm lowers the T/W ratio. Since neither going bigger nor going smaller yields a better system, the 75mm diameter is confirmed to be optimal.

The design is built upon maximising the propeller diameter within the set weight constraint. Additionally, the mission profile inherently benefits from a higher T/W ratio, making a lighter configuration potentially more attractive. Therefore, two variants are considered in this sensitivity study: a 90mm and a 60mm propeller *Chameleon*. The following hypotheses are evaluated:

1. *The 90mm version will not fit within the weight and/or cost budgets.*
2. *The 60mm version will not yield a sufficiently higher T/W ratio to constitute a better system iteration.*

90mm Version

To test hypothesis 1, a conservative snowball estimate is performed, comparing the mass and cost of the motors, batteries, and dry structural mass between the 75mm and 90mm variants. The permissible increases in mass and cost are derived from the SYS-22 & SYS-29 (Table 17.1) requirements and the final design weight and cost of 143.4g and EUR 239, respectively. Subtracting these values from the respective budgets yields the available margins:

$$200\text{g} - 143.4\text{g} = 56.6\text{g} \qquad €250 - €239 = €11 \tag{17.1}$$

The baseline propeller[1] is scaled to a 90mm diameter while preserving its chord and twist distributions. Evaluating this geometry through the initial stage of IL-1 (motor-matching) produces the heat map shown in Figure 17.1.

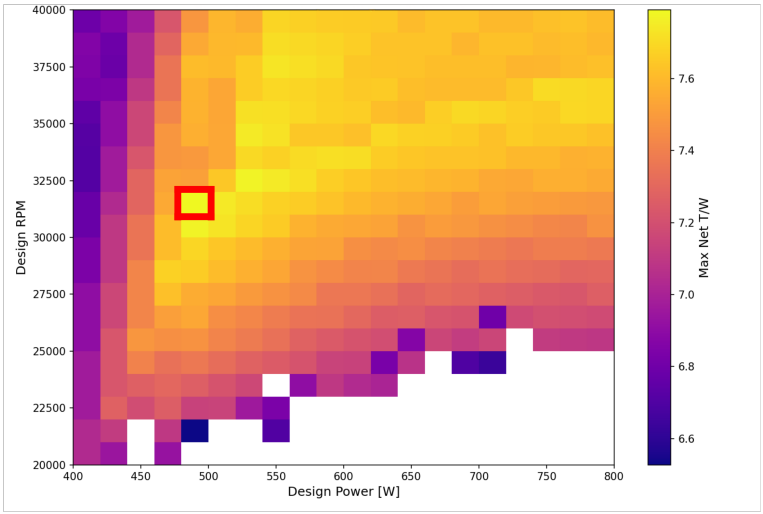

Figure 17.1: Net T/W heat map of the 90mm propeller–motor matching, based on a 130g motorless weight. The x-axis denotes design power and the y-axis design RPM.

The T/W values in Figure 17.1 are computed from a motorless weight of 130g and twice the matched motor

[1] `https://droneshop.nl/hqprop-t76mmx3-v2-propellers-cinewhoop` – Accessed: 16.06.2026

mass. For this configuration, the matched motor has a mass of 12g[2], yielding a total system mass basis of 154g. The red box in Figure 17.1 indicates the selected design point. Following the IL-1 sequence, the updated parameters dictate the battery sizing.. Although the 580mAh battery is capable of delivering the required peak power, its predicted cycle life follows $N(42.97, 12.15)$, which is considered insufficient. The 680mAh battery is therefore required, yielding a cycle life prediction of $N(323.04, 849)$, comparable to that of the 75mm design[3]. To estimate the structural mass and cost increase, the duct is scaled proportionally to the propeller diameter. This estimate accounts solely for the dry structural mass and assumes all remaining components, including vanes, screws, and wires, are unchanged, making it an optimistic upper bound on the savings. The mass and cost differences per component are presented in Table 17.3. Both the mass and cost

Table 17.3: Weight and Cost Summary by Component

Component	$\Delta_{\textbf{weight}}$ **[g]**	$\Delta_{\textbf{cost}}$ **[€]**
Motor	8	5.00
Batteries	36	7.50
Structure	15	0.69
Total	**59**	**13.19**

increments exceed their respective budgets, confirming hypothesis 1. Although the margins are small, the estimate is deliberately optimistic. The true mass and cost penalties are expected to be larger upon detailed design. Given that the 200g and EUR 250 requirements are hard operational limits, the 90mm configuration is infeasible. In the present design, only commercially available propeller sizes are considered; however, since a custom propeller is developed, future iterations could explore intermediate diameter increments. This is left as a recommendation for future work.

60mm Version

Reducing the propeller to 60mm scales the interception area with the square of the diameter, to approximately $(60/75)^2 \approx 64\%$ of the 75mm baseline. To justify this smaller interception area, the reduction in size would need to be compensated by a meaningful increase in the T/W ratio. Given that the design is already compact and components such as the servos cannot be scaled down further, it is unlikely that the achievable mass reduction is sufficient to produce such a gain. To test hypothesis 2, a conservative T/W estimate is performed, accounting for changes in motor mass, battery mass, and dry structural mass while holding all other components constant. The analysis begins by identifying the appropriate design point for the 60mm propeller. As before, the T/W values in Figure 17.2 are computed from a motorless weight of 130g and twice the matched motor mass. The selected design point is indicated by the red box, and its parameters are evaluated through the remainder of IL-1 (updating the battery and structure). The dry structural mass is scaled proportionally to the propeller diameter. The resulting component mass changes are summarised in Table 17.4. The 60mm

Table 17.4: Weight Summary by Component

Component	$\Delta_{\textbf{weight}}$ **[g]**
Motor	0
Batteries	-5.6[4]
Structure	-6.5
Total	**-12.1**

design point is matched to the same motor as the 75mm design, resulting in no change in motor mass. Ap-

[2] `https://www.drone-fpv-racer.com/en/gts-v3-1804-2450kv-brushless-motor-by-rcinpower-10697.html` – Accessed: 16.06.2026

[3] `https://betafpv.com/collections/batteries/products/lava-ii-1s-battery?variant=42566849331334` – Accessed: 15.06.2026

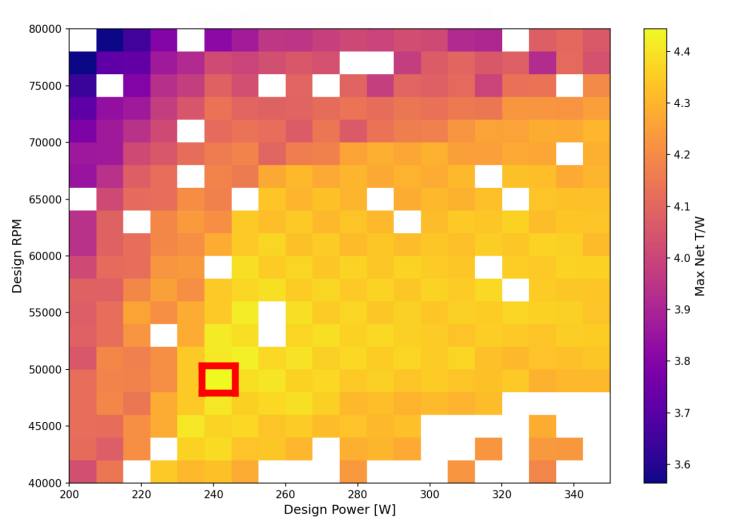

Figure 17.2: Net T/W heat map of the 60mm propeller–motor matching, based on a 130g motorless weight. The x-axis denotes design power and the y-axis design RPM.

plying the total estimated mass reduction of 12.1g to the baseline design mass (Table 1) yields an updated system mass of:

$$143.4\text{g} - 12.1\text{g} = 131.27\text{g} \tag{17.2}$$

Since the motor mass is 8.7g, the net T/W from Figure 17.2 corresponds to a total mass of 147.4g, consistent with a 130g motorless weight and two motors. Correcting for the estimated design mass gives:

$$\frac{4.4 \times 147.4}{131.4} = 4.9 \tag{17.3}$$

This represents a decrease of 7.5% relative to the 75mm design T/W of 5.3 (Table 1). A reduction in T/W is undesirable and confirms hypothesis 2. This concludes the sensitivity study and quantitatively supports the 75mm design presented in Chapter 12.

18

Conclusion & Recommendations

This report documents the detailed design and performance analysis of *the Chameleon*, an autonomous drone platform engineered to intercept moths in greenhouse environments. Through the application of a concurrent engineering framework, the highly coupled design parameters were successfully converged to meet all critical user requirements set by PATS Drones. By merging the aerodynamic efficiency of a flying duct enclosure with the rapid deceleration capability of a mechanical tether, the system presents a highly effective mechanical alternative that replaces harmful chemical pesticides. Consequently, this design proves that high-tech indoor agriculture can transition towards ecological sustainability without compromising efficacy.

The rapid interception capabilities are validated by the system's propulsion performance. The drone achieves a thrust-to-weight ratio of 5, which provides the necessary excess thrust to execute an aggressive, sub-2-second nominal mission profile. Within this envelope, the drone completes the interception phase in 0.267 s, which limits moth movement. Throughout these flight phases, attitude stability and trajectory tracking are maintained by the LQR controller.

The multibody dynamics simulations confirm the operational safety of the tethered braking system. During the peak deceleration phase, the experienced g-loads and tether tension remain safely below the structural limits of the custom 3D printed polycarbonate fuselage and the nylon fishing wire tether. Furthermore, the tether restricts the braking distance within safe margins. To safely mitigate the primary operational risk of pendulum-like ground strikes following the braking phase, the operational coverage has been constrained to a 6 m x 6 m area.

Restricting the operational coverage area requires a higher drone density per hectare, a strategy that is supported by the platform's financial and operational scalability. The cost of deploying additional units is easily absorbed by the low cost per drone of EUR 239. Furthermore, high system availability is maintained by rapid recharge times, which facilitate up to 80 sorties per drone daily. As a result, the EUR 10,000.00 per hectare subscription model yields a strongly positive NPV and high ROI, while undercutting the expenses growers currently allocate to chemical pesticides. Ultimately, *the Chameleon* demonstrates that high-tech indoor agriculture can be implemented in a manner that is technically compliant, financially viable, and environmentally sustainable.

To facilitate the transition from the detailed design phase to prototyping and deployment, the following recommendations are prioritised:

1. For further development of the control system, curved trajectories could be considered, along with larger control surfaces. In addition, higher fidelity software for deriving the derivatives is advised.
2. It is imperative that the docking hardware is fully integrated with the new system to ensure reliable, automated recharging after the drone is reeled back.
3. While finite element analysis confirms that the structure can withstand the maximum simulated g-loads with a large safety margin, the material properties of thin-walled 3D-printed polycarbonate parts remain highly anisotropic. Rigorous flight and crash testing is recommended to validate these simulation results before full-scale deployment. In case of a structural failure, it can be considered to print the fuselage at an angle instead of in plane.

Bibliography

[1] Kadoić Balaško, M., Bažok, R., Mikac, K. M., Lemic, D., and Pajač Živković, I., "Pest Management Challenges and Control Practices in Codling Moth: A Review," *Insects*, Vol. 11, No. 1, 2020, p. 38. doi:10.3390/insects11010038.

[2] Ahmad, M. F., Ahmad, F. A., Alsayegh, A. A., Zeyaullah, M., AlShahrani, A. M., Muzammil, K., Saati, A. A., Wahab, S., Elbendary, E. Y., Kambal, N., Abdelrahman, M. H., and Hussain, S., "Pesticides impacts on human health and the environment with their mechanisms of action and possible countermeasures," *Heliyon*, Vol. 10, No. 7, 2024, p. e29128. doi:10.1016/j.heliyon.2024.e29128.

[3] University of Kentucky, "Pesticides and Their Application," , 1995. PAT-4 publication.

[4] European Environment Agency, "How Pesticides Impact Human Health and Ecosystems in Europe," , 2023.

[5] Albaseer, S. S., Jaspers, V. L. B., Orsini, L., Vlahos, P., Al-Hazmi, H. E., and Hollert, H., "Beyond the field: How pesticide drift endangers biodiversity," *Environmental Challenges*, 2024. doi:10.1016/j.envpol.2024.125526.

[6] Food and Agriculture Organization of the United Nations, "Pesticide Application Techniques in Crop Protection," , n.d. FAO Plant Production and Protection Paper.

[7] PAN Europe, "Report: Water Sampling Confirms "Closed" Greenhouses Leak Alarming Number of Pesticides," , Dec. 2023.

[8] Roseth, R., and Haarstad, K., "Pesticide runoff from greenhouse production," *Water Science and Technology*, Vol. 61, No. 6, 2010, pp. 1373–1381. doi:10.2166/wst.2010.040.

[9] Damalas, C. A., and Koutroubas, S. D., "Pesticides and Respiratory Health," *European Respiratory Review*, Vol. 24, No. 136, 2015, pp. 306–319.

[10] Kim, K.-H., Kabir, E., and Jahan, S. A., "Human Health Effects of Pesticides: Current Issues in the Context of Residential Greenhouse Exposure," *International Journal of Environmental Research and Public Health*, Vol. 17, No. 11, 2020.

[11] Papadakis, E. N., Vryzas, Z., Kotopoulou, A., Kintzikoglou, K., and Papadopoulou-Mourkidou, E., "Occurrence and Environmental Risk Assessment of Pesticides in Greenhouse Wastewaters," *Global NEST Journal*, Vol. 26, No. 10, 2024.

[12] Pizzol, M., Sacchi, R., Köhler, S., and Anderson Erjavec, A., "Non-linearity in the Life Cycle Assessment of Scalable and Emerging Technologies," *Frontiers in Sustainability*, Vol. 1, 2021, p. 611593. doi:10.3389/frsus.2020.611593.

[13] Jung, S. Y., et al., "Is Additive Manufacturing an Environmentally and Socially Sustainable Manufacturing Approach?" *ACS Omega*, Vol. 8, No. 17, 2023, pp. 15057–15073. doi:10.1021/acsomega.2c08127.

[14] Noma, T., Colunga-Garcia, M., Brewer, M., Landis, J., and Gooch, A., "Golden twin spot Chrysodeixis chalcites," Tech. rep., Michigan State University Extension, Feb. 2010. MSU IPM Program.

[15] Sullivan, M., and Molet, T., "CPHST Pest Datasheet for Chrysodeixis chalcites," Tech. rep., USDA-APHIS-PPQ-CPHST, 2014. Revised January 2014.

[16] European Commission, "Farm to Fork Strategy: Action Plan," Policy document, European Commission, Brussels, 2020.

[17] Nitzko, S., "Consumer Evaluation of Food from Pesticide-Free Agriculture in Relation to Conventional and Organic Products," *Farming System*, Vol. 2, No. 4, 2024, p. 100112. doi:10.1016/j.farsys.2024.100112.

[18] Zhou, W., Li, M., and Achal, V., "A comprehensive review on environmental and human health impacts of chemical pesticide usage," *Emerging Contaminants*, Vol. 11, No. 1, 2025, p. 100410. doi:10.1016/j.emcon.2024.100410.

[19] Alavanja, M. C., "Pesticides Use and Exposure Extensive Worldwide," *Reviews on Environmental Health*, Vol. 24, No. 4, 2009, pp. 303–309. doi:10.1515/reveh.2009.24.4.303.

[20] Tudi, M., Daniel Ruan, H., Wang, L., Lyu, J., Sadler, R., Connell, D., Chu, C., and Phung, D. T., "Agriculture Development, Pesticide Application and Its Impact on the Environment," *International Journal of Environmental Research and Public Health*, Vol. 18, No. 3, 2021, p. 1112. doi:10.3390/ijerph18031112.

[21] van Lenteren, J., "Biological Pest Control in Greenhouses: An Overview," *Arab Journal of Plant Protection*, Vol. 10, No. 1, 1992, pp. 35–43.

[22] Sanders, J., and Strijbis, P., "Bestrijding van Turkse mot (Chrysodeixis chalcites) met diverse spuittechnieken in Gerbera," Tech. Rep. Proefnummer 210436, Vertify, 2021.

[23] Grosman, A., and Bloemhard, C., "Nieuwe sluipwespen tegen turkse mot, Chrysodeixis chalcites, in paprika: Opsporen en toetsen," Tech. Rep. Rapport GTB-1306 (PT 14167), Wageningen UR Glastuinbouw, 2013.

[24] del Pino, M., Cabello, T., and Hernández-Suárez,

E., "Biological Control Options for the Golden Twin-Spot Moth, Chrysodeixis chalcites (Esper) (Lepidoptera: Noctuidae) in Banana Crops of the Canary Islands," *Insects*, Vol. 13, No. 6, 2022, p. 516.
doi:10.3390/insects13060516.

[25] Leman, A., Voorburg, C., Le Hesran, S., Heijkoop, M., van der Heide, H., Bloemhard, C., Sewkaransing, D., Campacci, F., Ros, V., and Kruidhof, M., "Factsheet afronding Masterplan Rups," Glastuinbouw Nederland / Wageningen University & Research, 2025. Behorend bij project P22004: Masterplan rupsen in de glastuinbouw.

[26] Smit, A. B., Jager, J. H., Manshanden, M., and Bremmer, J., "Cost of crop protection measures: A follow-up to the study 'The future of crop protection in Europe' (2021)," Tech. Rep. PE 690.043, European Parliamentary Research Service (EPRS), Scientific Foresight Unit (STOA), sep 2021.
doi:10.2861/67868.

[27] Fuentes, E. G., Hernández-Suárez, E., Simón, O., Williams, T., and Caballero, P., "Chrysodeixis chalcites, a pest of banana crops on the Canary Islands: Incidence, economic losses and current control measures," *Crop Protection*, Vol. 108, 2018, pp. 137–145.
doi:10.1016/j.cropro.2018.02.020.

[28] European Parliament and Council of the European Union, "Regulation (EC) No 1107/2009 of the European Parliament and of the Council of 21 October 2009 concerning the placing of plant protection products on the market and repealing Council Directives 79/117/EEC and 91/414/EEC," *Official Journal of the European Union*, Vol. L 309, 2009, pp. 1–50.

[29] RaboResearch Food & Agribusiness, "Global Greenhouse Update 2025," Industry update, Rabobank, Utrecht, Netherlands, March 2025. Published via Topsector Tuinbouw & Uitgangsmaterialen.

[30] Mordor Intelligence, "Netherlands Commercial Greenhouse Market - Size, Share & Industry Analysis," Market Research Report MI475, Mordor Intelligence, 2026. Forecast Period: 2026–2031.

[31] Bergmann, O., Götten, F., Braun, C., and Janser, F., "Comparison and Evaluation of Blade Element Methods Against RANS Simulations and Test Data," *CEAS Aeronautical Journal*, Vol. 13, No. 2, 2022, pp. 535–557.
doi:10.1007/s13272-022-00579-1.

[32] Goldstein, S., and John, S., "On the Vortex Theory of Screw Propellers," *Proceedings of the Royal Society of London. Series A, Containing Papers of a Mathematical and Physical Character*, Vol. 123, No. 792, 1929, pp. 440–465.
doi:10.1098/RSPA.1929.0078.

[33] Betz, A., "Airscrews with Minimum Energy Loss," Tech. rep., Kaiser Wilhelm Institute for Flow Research, Göttingen, Germany, 1919. Original German title: Schraubenpropeller mit geringstem Energieverlust.

[34] Theodorsen, T., *Theory of Propellers*, McGraw-Hill, New York, 1948.

[35] Larrabee, E. E., and French, S. E., "Minimum Induced Loss Windmills and Propellers," *Journal of Wind Engineering and Industrial Aerodynamics*, Vol. 15, 1983, pp. 317–327.

[36] Drela, M., *QPROP – Theory*, Massachusetts Institute of Technology, 2007.

[37] McLain, T., "Small Unmanned Aircraft: Theory and Practice," *Small Unmanned Aircraft: Theory and Practice*, 2012.
doi:10.1515/9781400840601.

[38] Jr., J. D. A., *Fundamentals of Aerodynamics*, 6th ed., McGraw-Hill Education, New York, 2017.

[39] Ryu, M., Cho, L., and Cho, J., "The Effect of Tip Clearance on Performance of a Counter-Rotating Ducted Fan in a VTOL UAV," *TRANSACTIONS OF THE JAPAN SOCIETY FOR AERONAUTICAL AND SPACE SCIENCES*, Vol. 60, 2017, pp. 1–9.
doi:10.2322/tjsass.60.1.

[40] Jiang, Y., Zhang, L., Offer, G., and Wang, H., "A User-Friendly Lithium Battery Simulator Based on Open-Source CFD," *Digital Chemical Engineering*, 2022, p. 100055.
doi:10.1016/j.dche.2022.100055.

[41] Gotti, D., Prodanovic, M., Pinilla, S., Muñoz-Torrero, D., García-Quismondo, E., and Palma, J., "A Novel Doyle-Fuller-Newman Battery Model Formulation for Online Parameter Estimation," *Journal of Energy Storage*, 2025, p. 119115.
doi:10.1016/j.est.2025.119115.

[42] Galeotti, M., Cinà, L., Giammanco, C., Di Carlo, A., Santoni, F., De Angelis, A., Moschitta, A., and Carbone, P., "LiPo Batteries Dataset: Capacity, Electrochemical Impedance Spectra, and Fit of Equivalent Circuit Model at Various States-of-Charge and States-of-Health," *Data in Brief*, Vol. 50, 2023, p. 109561.
doi:10.1016/j.dib.2023.109561.

[43] Lu, J., Xiong, R., Tian, J., Wang, C., Hsu, C.-W., Tsou, N.-T., Sun, F., and Li, J., "Battery Degradation Prediction Against Uncertain Future Conditions with Recurrent Neural Network Enabled Deep Learning," *Energy Storage Materials*, 2022, p. 105007.
doi:10.1016/j.ensm.2022.05.007.

[44] "Shape Optimization of Porous Electrode Batteries," *AIAA SCITECH 2025 Forum*, 2025.
doi:10.2514/6.2025-1747.

[45] Sulzer, V., Marquis, S. G., Timms, R., Robinson,

M., and Chapman, S. J., "Python Battery Mathematical Modelling (PyBaMM)," *Journal of Open Research Software*, Vol. 9, No. 1, 2021, p. 14. doi:10.5334/jors.309.

[46] Chen, C.-H., Brosa Planella, F., O'Regan, K., Gastol, D., Widanage, W. D., and Kendrick, E., "Development of Experimental Techniques for Parameterization of Multi-scale Lithium-ion Battery Models," *Journal of The Electrochemical Society*, Vol. 167, No. 8, 2020, p. 080534. doi:10.1149/1945-7111/ab9050.

[47] Hoque, M. A., Nurmi, P., Kumar, A., Varjonen, S., Song, J., Pecht, M. G., and Tarkoma, S., "Data Driven Analysis of Lithium-Ion Battery Internal Resistance Towards Reliable State of Health Prediction," *Journal of Energy Storage*, Vol. 41, 2021, p. 102902. doi:10.1016/j.est.2021.102902.

[48] "Temperature, Overcharge and Short-Circuit Studies of Batteries Used in Electric Vehicles," *Przegląd Elektrotechniczny*, Vol. 93, No. 5, 2017. doi:10.15199/48.2017.05.13.

[49] Green, C. R., and McDonald, R. A., "Modeling and Test of the Efficiency of Electronic Speed Controllers for Brushless DC Motors," *AIAA Propulsion and Energy Forum*, 2015. doi:10.2514/6.2015-3191.

[50] Granitzki, R. F., and Barton, A., "High-G Verification of Lithium-Polymer (Li-Po) Pouch Cells," Tech. Rep. ARMET-TR-15067, U.S. Army Armament Research, Development and Engineering Center (ARDEC), Munitions Engineering Technology Center, Picatinny Arsenal, NJ, May 2016. Approved for public release; distribution is unlimited.

[51] Autodesk, Inc., *Autodesk Explicit 2022 User's Manual*, Autodesk, Inc., 2022. Accessed: 2026-06-17.

[52] Song, P., Trivedi, A. R., and Siviour, C. R., "Mechanical response of four polycarbonates at a wide range of strain rates and temperatures," *Polymer Testing*, Vol. 121, 2023, p. 107986. doi:10.1016/j.polymertesting.2023.107986.

[53] Rubin, A., Gauthier, C., and Schirrer, R., "The friction coefficient on polycarbonate as a function of the contact pressure and nanoscale roughness," *Journal of Polymer Science Part B: Polymer Physics*, Vol. 50, No. 8, 2012, pp. 580–588. doi:10.1002/polb.23046.

[54] Naeim, F., "Dynamics of Structures, Theory and Applications in Earthquake Engineering, 2nd Edition Chopra, Anil K., 2001, Upper Saddle River, NJ: Prentice Hall, 844 pp." *Earthquake Spectra*, Vol. 17, No. 3, 2001, pp. 549–550. doi:10.1193/1.1586188.

[55] Zhang, C., Hong, H., Bi, K., and Xueyuan, Y., "Dynamic amplification factors for a system with multiple-degrees-of-freedom," *Earthquake Engineering and Engineering Vibration*, Vol. 19, 2020, pp. 363–375. doi:10.1007/s11803-020-0567-9.

[56] Mozos, C. M., and Aparicio, A. C., "Static Strain Energy and Dynamic Amplification Factor on Multiple Degree of Freedom Systems," *Engineering Structures*, Vol. 31, No. 11, 2009, pp. 2756–2765. doi:10.1016/j.engstruct.2009.07.003.

[57] De Vries, H., Engelen, R., and Janssen, E., "Impact strength of 3D-printed polycarbonate," *Facta universitatis - series: Electronics and Energetics*, Vol. 33, 2020, pp. 105–117. doi:10.2298/FUEE2001105V.

[58] Ailon, Herting, D., Johnson, S. E., and Pauley, K. E., "NASTRAN User's Guide – Level 15," Tech. Rep. NASA CR-2504, Universal Analytics, Inc., Los Angeles, CA, Apr. 1975.

[59] MSC Software Corporation, *MSC Nastran 2021.2 Verification Guide*, 2021st ed., 2021. Accessed: 2026-06-22.

[60] Juračka, D., Bujdoš, D., and Lehner, P., "Numerical and experimental analysis of mechanical and fatigue properties of special shaped 3D printed sample," *Fracture and Structural Integrity*, Vol. 19, 2025, pp. 415–421. doi:10.3221/IGF-ESIS.74.25.

[61] PATS Drones, "Project meeting with client representatives," , May 2026. Meeting held in Delft, The Netherlands, 11 May 2026.

[62] McCormick, B. W., *Aerodynamics of V/STOL Flight*, Dover Publications, Mineola, NY, USA, 1999.

[63] Sheridan, C. N. D., Pham, D. D. V., and Whiteside, S. K. S., "Evaluation of VSPAERO Analysis Capabilities for Conceptual Design of Aircraft with Propeller-Blown Wings," *Proceedings of the AIAA AVIATION Forum 2021*, American Institute of Aeronautics and Astronautics, Virtual, United States, 2021. NASA Document ID 20210017397.

[64] Mariën, F., "Software Testing: VSPAERO," Master's thesis, Hamburg University of Applied Sciences, Hamburg, Germany, 2021. doi:10.15488/11559.

[65] Alvarez, E. J., and Ning, A., "Meshless Large-Eddy Simulation of Propeller–Wing Interactions with Reformulated Vortex Particle Method," *Journal of Aircraft*, Vol. 61, No. 3, 2024, pp. 811–827. doi:10.2514/1.C037279.

[66] Gonçalves, L. E., and da Silva, R. G. A., "Parametric Study of Propeller-Wing Aerodynamic Interaction Using VSPAERO for Conceptual Aircraft Design," *AIAA AVIATION Forum*, American Institute of Aeronautics and Astronautics, 2025. doi:10.2514/6.2025-3290, aIAA Paper 2025-3290.

[67] Fernández, M. B., "CFD Tool VSPAERO: Actu-

ator Disk and Flow Visualization," Master thesis, Hamburg University of Applied Sciences, Hamburg, Germany, Oct. 2023.

[68] Leishman, J. G., "Airfoil Geometries," *Introduction to Aerospace Flight Vehicles*, Embry-Riddle Aeronautical University, 2026, Chap. 32.

[69] Yacoubi, M., Jlassi, A., Karoun, J., Ben Kirane, T., Bekkali, L., Jhabli, H., and Hendrick, P., "Design and Optimization of a Ducted Fan VTOL MAV Controlled by Electric Ducted Fans," *Proceedings of the 8th European Conference for Aeronautics and Space Sciences (EUCASS)*, 2019. doi:10.13009/EUCASS2019-108.

[70] Rugh, W. J., and Shamma, J. S., "Research on gain scheduling," *Automatica*, Vol. 36, No. 10, 2000, pp. 1401–1425. doi:10.1016/S0005-1098(00)00058-3.

[71] Leith, D. J., and Leithead, W. E., "Survey of gain-scheduling analysis and design," *International Journal of Control*, Vol. 73, No. 11, 2000, pp. 1001–1025. doi:10.1080/002071700411304.

[72] Franklin, G. F., Powell, J. D., and Workman, M. L., *Digital Control of Dynamic Systems*, 3rd ed., Addison-Wesley, Menlo Park, CA, 1998.

[73] Etkin, B., and Reid, L. D., *Dynamics of Flight: Stability and Control*, 3rd ed., John Wiley & Sons, New York, 1996.

[74] Caughey, D. A., "Introduction to Aircraft Stability and Control," Course Notes for M&AE 5070, Sibley School of Mechanical and Aerospace Engineering, Cornell University, 2011.

[75] Theodoulis, S., Gassmann, V., Brunner, T., and Wernert, P., "Fixed Structure Robust Control Design for the 155mm Canard-Guided Projectile Roll-Channel Autopilot," *Proceedings of the 21st Mediterranean Conference on Control and Automation (MED)*, IEEE, 2013. doi:10.1109/MED.2013.6608714.

[76] Waymeyer, W. K., and Banach, T. P., "Roll Damper for Thrust Vector Controlled Missile," , Nov. 1993.

[77] Cole, D. E., "Rolling Airframe Autopilot," , Oct. 1977.

[78] Awad, A., "Integrated Roll-Pitch-Yaw Autopilot via Equivalent Based Sliding Mode Control for Uncertain Nonlinear Time-Varying Missile," *International Journal of Aeronautical and Space Sciences*, Vol. 18, No. 4, 2017, pp. 688–696. doi:10.5139/IJASS.2017.18.4.688.

[79] Ali, K. M., Abozied, M., Arafa, I., and Elhalwagy, Y. Z., "Design of a Roll Autopilot for a Skid-to-Turn Guided Missile," *IOP Conference Series: Materials Science and Engineering*, Vol. 610, IOP Publishing, 2019, p. 012017. doi:10.1088/1757-899X/610/1/012017, 18th International Conference on Aerospace Sciences & Aviation Technology, Military Technical College, Cairo, Egypt, 9–11 April 2019.

[80] Dobrokhodov, V., "Kinematics and Dynamics of Fixed-Wing UAVs," *Handbook of Unmanned Aerial Vehicles*, edited by K. P. Valavanis and G. J. Vachtsevanos, Springer, Dordrecht, 2015, pp. 243–277. doi:10.1007/978-90-481-9707-1_53.

[81] Goldstein, H., Poole, C. P., and Safko, J. L., *Classical Mechanics*, 3rd ed., Addison-Wesley, San Francisco, 2002, Chap. 4, pp. 134–183. Chapter 4: The Kinematics of Rigid Body Motion.

[82] Diebel, J., "Representing Attitude: Euler Angles, Unit Quaternions, and Rotation Vectors," , 2006.

[83] Goldstein, H., Poole, C. P., and Safko, J. L., *Classical Mechanics*, 3rd ed., Addison-Wesley, San Francisco, 2002, Chap. 5, pp. 184–237. Chapter 5: The Rigid Body Equations of Motion.

[84] Stevens, B. L., Lewis, F. L., and Johnson, E. N., *Aircraft Control and Simulation: Dynamics, Controls Design, and Autonomous Systems*, 3rd ed., John Wiley & Sons, Hoboken, NJ, 2015.

[85] Litherland, B., "OpenVSP VSPAERO Basics," NASA OpenVSP Ground School, Sep. 2025. Updated September 30, 2025.

[86] Pimentel-Garcia, J. C., "The Full Multi-wake Vortex Lattice Method: A Detached Flow Model Based on Potential Flow Theory," *Advances in Aerodynamics*, Vol. 5, 2023. doi:10.1186/s42774-023-00153-1.

[87] Ding, Y., Pandala, A., Li, C., Shin, Y.-H., and Park, H.-W., "Representation-Free Model Predictive Control for Dynamic Motions in Quadrupeds," *IEEE Transactions on Robotics*, Vol. 37, No. 4, 2021, pp. 1154–1171. doi:10.1109/TRO.2020.3046415.

[88] Åström, K. J., and Murray, R. M., *Feedback Systems: An Introduction for Scientists and Engineers*, Princeton University Press, Princeton, NJ, 2008.

[89] Narkhede, P., Poddar, S., Walambe, R., Ghinea, G., and Kotecha, K., "Cascaded Complementary Filter Architecture for Sensor Fusion in Attitude Estimation," *Sensors*, Vol. 21, No. 6, 2021, p. 1937. doi:10.3390/s21061937.

[90] The MathWorks, Inc., "interpn: Interpolation for 1-D, 2-D, 3-D, and N-D Gridded Data in ndgrid Format," MATLAB Documentation, MATLAB Help Center, 2026. Accessed: 2026-06-15.

[91] The MathWorks, Inc., "lqr: Linear-Quadratic Regulator (LQR) Design," MATLAB Control System Toolbox Documentation, 2026. Accessed: 2026-06-15.

[92] Srivastava, A., Sharma, R., and Indu, S., "Design and Flight Testing of LQRi Attitude Control for

Quadcopter UAV," , 2024.

[93] Treiber, M., and Kanagaraj, V., "Comparing Numerical Integration Schemes for Time-Continuous Car-Following Models," *Physica A: Statistical Mechanics and its Applications*, Vol. 419, 2015, pp. 183–195. doi:10.1016/j.physa.2014.09.061.

[94] LeVeque, R. J., *Finite Difference Methods for Ordinary and Partial Differential Equations: Steady-State and Time-Dependent Problems*, Society for Industrial and Applied Mathematics (SIAM), Philadelphia, PA, 2007.

[95] Mysore, S., Mabsout, B., Saenko, K., and Mancuso, R., "How to Train Your Quadrotor: A Framework for Consistently Smooth and Responsive Flight Control via Reinforcement Learning," *ACM Transactions on Cyber-Physical Systems*, Vol. 5, No. 4, 2021, pp. 1–24. doi:10.1145/3466618.

[96] Folk, S., Paulos, J., and Kumar, V., "RotorPy: A Python-based Multirotor Simulator with Aerodynamics for Education and Research," *The Role of Robotics Simulators for Unmanned Aerial Vehicles Workshop, IEEE International Conference on Robotics and Automation (ICRA)*, 2023. doi:10.48550/arXiv.2306.04485.

[97] Li, S., Öztürk, E., De Wagter, C., de Croon, G. C. H. E., and Izzo, D., "Aggressive Online Control of a Quadrotor via Deep Network Representations of Optimality Principles," *2020 IEEE International Conference on Robotics and Automation (ICRA)*, IEEE, 2020, pp. 6282–6287. doi:10.1109/ICRA40945.2020.9197443.

[98] Shampine, L. F., Gladwell, I., and Thompson, S., *Solving ODEs with MATLAB*, Cambridge University Press, Cambridge, 2003.

[99] ExpressLRS, "The ExpressLRS Lua Script: Packet Rate and Telemetry Ratio," , 2026. Accessed: 2026-06-16.

[100] International Organization for Standardization, "Mechanical vibration — Rotor balancing — Part 11: Procedures and tolerances for rotors with rigid behaviour," Standard ISO 21940-11:2016, International Organization for Standardization, Geneva, Switzerland, 2016.

[101] Rao, S. S., *Mechanical Vibrations*, 6th ed., Pearson, Hoboken, NJ, 2017.

[102] Todorov, E., Erez, T., and Tassa, Y., "MuJoCo: A physics engine for model-based control," *2012 IEEE/RSJ International Conference on Intelligent Robots and Systems*, IEEE, 2012, pp. 5026–5033. doi:10.1109/IROS.2012.6386109.

[103] Erez, T., Tassa, Y., and Todorov, E., "Simulation tools for model-based robotics: Comparison of Bullet, Havok, MuJoCo, ODE and PhysX," *2015 IEEE International Conference on Robotics and Automation (ICRA)*, 2015, pp. 4397–4404. doi:10.1109/ICRA.2015.7139807.

[104] Google DeepMind, *MuJoCo Documentation: Fluid Dynamics (Version 3.2.1)*, Google DeepMind, . Software Documentation.

[105] Ongun, R., and Saruhan, H., "Experimental Investigation of Suspension Cord Material Influence on Modal Parameters in Free-Free Boundary Conditions," *Duzce University Journal of Science and Technology*, Vol. 13, No. 4, 2025, pp. 1592–1600. doi:10.29130/dubited.1709900.

[106] Agricultural Machinery Testing and Evaluation Center (AMTEC), "PAES 415:2001 Agricultural Structures - Greenhouses," Philippine agricultural engineering standard, University of the Philippines Los Baños, 2001.

[107] MatWeb, "Nylon 6, Unreinforced - Material Property Data," , 2026.

[108] Interroll, *DM Electromagnetic Brakes Product Data*, Interroll Group, 2024.

[109] Saravanan, J., and Sridhar, M., "Life cycle assessment of alternative building materials using idematlightlca mobile app," *Materials Today: Proceedings*, Vol. 65, No. 2, 2022, pp. 1243–1249. doi:10.1016/j.matpr.2022.04.184.

[110] Guillén Sanches, L. F., Botelho Junior, A. B., and Espinosa, D. C. R., "Physical Process for Li-Ion Battery Recycling from Electric Vehicles," *Industrial & Engineering Chemistry Research*, Vol. 63, No. 45, 2024, pp. 19788–19803. doi:10.1021/acs.iecr.4c03271.

[111] Degen, F., Winter, M., Bendig, D., and Tübke, J., "Energy Consumption of Current and Future Production of Lithium-Ion and Post Lithium-Ion Battery Cells," *Nature Energy*, Vol. 8, No. 11, 2023, pp. 1284–1295. doi:10.1038/s41560-023-01355-z.

[112] Ashby, M. F., "Chapter 6: Eco-data: Values, Sources, Precision," *Materials and the Environment*, Butterworth-Heinemann, Oxford, 2013, 2nd ed., pp. 119–174.

[113] Hopkins, N., Jiang, L., and Brooks, H., "Energy Consumption of Common Desktop Additive Manufacturing Technologies," *Cleaner Engineering and Technology*, Vol. 2, 2021, p. 100068. doi:10.1016/j.clet.2021.100068.

[114] Homologa, "Deltamethrin Product Information and Application Guidelines," , Mar. 2022. Technical document on deltamethrin application prior to flowering.

[115] Carl Roth GmbH + Co. KG, "Safety Data Sheet: Deltamethrin ROTICHROM® Pestilyse® HPLC (Article number: 22T8)," , 2025. According to Regulation (EC) No. 1907/2006 (REACH), amended by

2020/878/EU.

[116] Zaliskyi, M., Odarchenko, R., Askerov, T., Shcherbyna, O., and Petrova, Y., "Reliability Synthesis for UAV Flight Control System," *Proceedings of the 6th International Conference "Telecommunications, Electronics and Informatics" (ICTEI 2017)*, Vol. 1844, CEUR-WS.org, 2017, pp. 569–573.

[117] Petritoli, E., Leccese, F., and Ciani, L., "Reliability and Maintenance Analysis of Unmanned Aerial Vehicles," *Sensors*, Vol. 18, No. 9, 2018, p. 3171. doi:10.3390/s18093171.

[118] Kambushev, K. M., "Analysis of the Reliability of DC Brushless Electric Motors with Power up to 200W Used in MAVs," *Machines. Technologies. Materials.*, Vol. 13, No. 6, 2019, pp. 257–258.

[119] Foster, L., "Maximizing Value when Calculating a Startup's Valuation," , May 2026. Accessed: June 9, 2026.

[120] Finbox, "Dassault Aviation SA (ENXTPA:AM) WACC," , 2026. Accessed: June 9, 2026.

[121] ValueInvesting.io, "Northrop Grumman Corp. (NOC) WACC," , . Accessed: June 9, 2026.

[122] ValueInvesting.io, "Boeing Co. (BA) WACC," , 2026. Accessed: June 9, 2026.

[123] AlphaSpread, "Airbus SE (AIR) Discount Rate," , . Accessed: June 9, 2026.

[124] Chattot, J.-J., "Actuator Disk Theory: Steady and Unsteady Models," *Journal of Solar Energy Engineering*, Vol. 136, No. 3, 2014. doi:10.1115/1.4026947.

[125] Muehlebach, M., and D'Andrea, R., "The Flying Platform – A Testbed for Ducted Fan Actuation and Control Design," *Mechatronics*, Vol. 42, 2017, pp. 77–91. doi:10.1016/j.mechatronics.2017.01.001.

[126] Union Internationale des Associations d'Alpinisme (UIAA), "Pictorial Representation of EN 892 and UIAA 101: Dynamic Mountaineering Ropes," Tech. rep., UIAA, 2020. Designed by Georg Sojer. A simplified pictorial presentation of standards EN 892: 2012 + A1: 2016 and UIAA 101: 2018.

[127] Leuthäusser, U., "Physics of Climbing Ropes - Part 3: Viscous and Dry Friction Combined, Rope Control and Experiments," Tech. rep., Leuthäusser Systemanalysen, Jul. 2012. English Version 1 (July 2, 2012).

[128] The MathWorks, Inc., "Control System Toolbox," MathWorks, 2026. Accessed: 23.06.2026.

[129] Van Loan, C. F., "Computing Integrals Involving the Matrix Exponential," *IEEE Transactions on Automatic Control*, Vol. 23, No. 3, 1978, pp. 395–404. doi:10.1109/TAC.1978.1101743.

[130] dos Santos, P., and Oliveira, P., "Thrust vector control and state estimation architecture for low-cost small-scale launchers," , 03 2023. doi:10.48550/arXiv.2303.16983.

[131] Hibbeler, R. C., *Mechanics of Materials*, 10th ed., Pearson, 2023.

[132] van Drooge, H. L., Groeneveld, C. N., and Schipper, H. J., "Data on application frequency of pesticide for risk assessment purposes," *Annals of Occupational Hygiene*, Vol. 45, No. Suppl 1, 2001, pp. S95–S101. doi:10.1016/s0003-4878(00)00112-5.

A

Verification & Validation

Aerodynamics

Assumptions

Vortex Lattice Method

The following assumptions are made in VLM:

1. Inviscous flow
2. Irrotational flow
3. Incompressible flow
4. A velocity potential ϕ exists such that $\mathbf{V} = \nabla\phi$ and $\nabla^2\phi = 0$

As a result, relevant flow phenomena like separation and skin friction drag are not taken into account. The velocities at points along the surface are computed by placing horseshoe vortices at defined grid points and using Biot-Savart's law with the boundary condition that the sum of induced normal velocities is zero. The vortex is placed at $\frac{1}{4}c$ and the control point at $\frac{3}{4}c$. The grid of horseshoe vortices is superimposed, and by summing contributions for all control points on the wing, a linear algebraic system for the strength of each horseshoe vortex is constructed. The vortex strength and velocity are calculated, resulting in a pressure distribution that is integrated to obtain total forces and moments. By modelling lifting surfaces as infinitely thin sheets of discrete vortices, computational time is reduced, but surfaces cannot be taken into account. For this reason, the duct is modelled using the panel method. Modelling the duct using VLM gives very inaccurate results because it is represented by a cylinder with a flat ring around it. The mathematics behind the VLM method is explained in more detail in [38] and the application procedure in [64].

Panel Methods

Similar to VLM, the Panel Method uses a velocity potential to generate a system of linear algebraic equations that is solved to determine the strength of the sources, doublets and vortices that are placed on the surface grid. The difference is that boundary conditions are applied on the actual surface in panel methods. By using sources, doublets and vortices and applying these boundary conditions on the surface, the thickness of the lifting surface is taken into account. In contrast to the thin control surfaces, this is necessary to do for the duct, as its thickness has a non-negligible effect on the pressure distribution. Although the panel method is more accurate, computational effort increases, resulting in the choice to use VLM for all components besides the duct.

Actuator Disk Theory

Actuator disk theory relies on the following assumptions[124]:

1. Steady flow
2. Inviscid flow
3. Axisymmetric flow
4. Incompressible flow

The propeller is modelled by an infinitely thin disk that creates a pressure jump resulting in a thrust. The mathematics and details behind actuator disk theory are explained in [67].

Verification

OpenVSP is an established open-source parametric aircraft geometry tool developed by NASA for more than 10 years and is therefore considered verified[1].

Validation

This section focuses on validation of the aerodynamic characteristics results from the VSPAERO analysis. First, the accuracy of force and moment calculations is validated, followed by validation of the estimated thrust vectoring performance. While the configurations analysed differ from the configuration of the final design, the validation serves to demonstrate the ability of the software to accurately model downstream wake interactions between propellers and aerodynamic surfaces.

Numerical results comparison

To assess the accuracy of VSPAERO simulations using actuator disk theory, its results are compared to results obtained using other simulation software in Figure A.1a. This figure from a study by Sheridan et al. (2021)[63] shows the total forces and moments based on four simulation softwares for alpha ranging from $-5°$ to $20°$. The simulation is performed for the propeller wing configuration shown in Figure A.1b. The configuration resembles the propeller control surface configuration in *the Chameleon* design and can therefore be used to validate results. The red line in Figure A.1a shows the results for a VLM with actuator disk

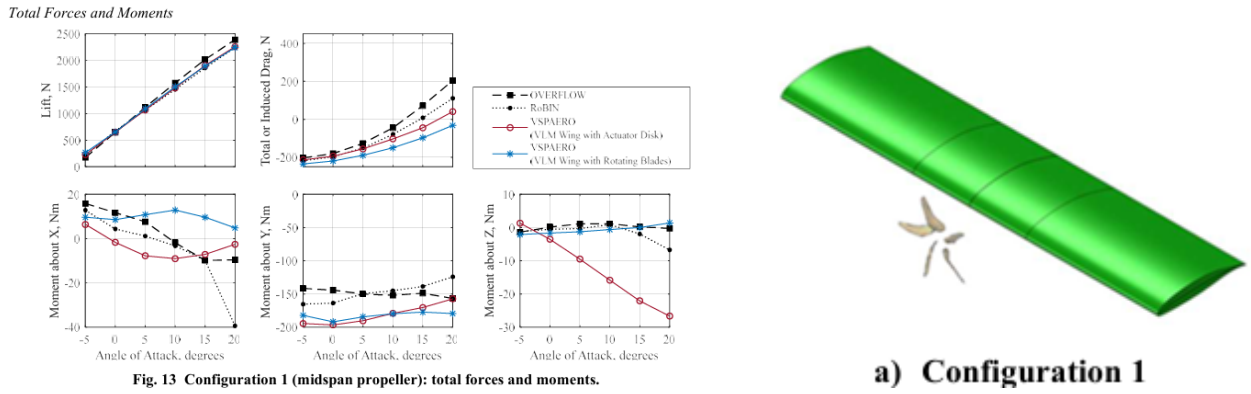

(a) Simulated total forces and moments acting on a wing.

(b) Propeller over wing

Figure A.1: Comparison of the validation results and simulation configuration.

simulation, which will be compared with the results from the OVERFLOW software shown in the line with black squares. OVERFLOW is a Navier-Stokes CFD solver developed by NASA[63]. This computationally expensive high-fidelity software is considered to correspond with reality and is used as a baseline. Comparing results at $\alpha = 0°$, the angle at which aerodynamic characteristics will be obtained, the actuator disk overpredicts lift only 1.1 % compared to the OVERFLOW prediction[63]. Although exact values are not provided, the upper right graph shows drag is slightly overestimated. The difference is marginal, however, leading to the conclusion that the drag results are sufficiently valid at this stage of the design. It can be seen from the lower three graphs that there are quite some discrepancies between moments simulated by VSPAERO and OVERFLOW. According to Sheridan et al. (2021), VSPAERO is not very useful for determining precise control dynamics but generally predicts moments within the expected range of values by 15%-20%. Considering the computing time of unsteady VSPAERO (at least 370 minutes) and OVERFLOW simulations(at least multiple days) and resources at this stage of the design, these results are sufficiently accurate.

Thrust vectoring validation

In order to increase the chance of catching a moth, the thrust vectoring system should function properly. This

[1] `https://mcdonaldaerospace.com/projects/openvsp/` - Accessed: 12.06.2026

important aspect of the design will therefore be validated to ensure sufficient control. In [125], the horizontal thrust generated by a control flap of a similar design is analysed. The thrust vectoring system of *the Chameleon* and flying duct design from Muehlebach and D'Andrea (2017) are shown in Figure A.2. Both designs consist of two contra-rotating propellers driven by an electric motor in a duct and a thrust vectoring system based on control flaps driven by servos. As these designs are very similar, the ratio between vertical and horizontal

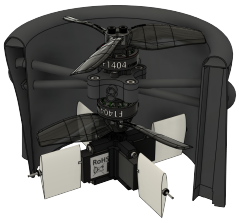

(a) *Chameleon* internal cross-section showing the control flaps

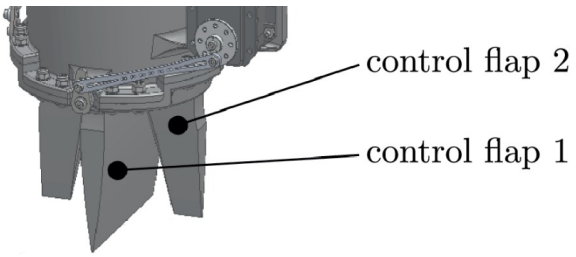

(b) Thrust vectoring system of the flying duct design by Muehlebach and D'Andrea (2017).

Figure A.2: *Chameleon* and flying duct design[125] showing a similar control system configuration.

thrust is expected to be approximately the same magnitude. This ratio is used as a thrust vectoring performance metric and can thus validate if thrust vectoring estimations from OpenVSP are reasonable. The ratios for both designs are shown in Table A.1. Values presented in Table A.1 are estimated from the horizontal and vertical

Table A.1: Comparison of thrust vectoring capabilities of the *Chameleon* and Flying duct design at 18° control flap deflection.

	Vert. Thrust [N]	**Horiz. Thrust [N]**	**TV Ratio**
Flying Duct			
Reference Case	24.8	1.5	16.5
Chameleon			
6 m/s	7.4	0.534	13.9
12 m/s	6.4	0.415	15.7

thrust graphs for an 18 ° deflection of the small flap of the flying duct[125]. The small flap can deflect at most 18 ° and was selected based on Figure A.2 because small control flap 2 shown in Figure A.2b is most similar to the control flaps of *the Chameleon*. Vertical and horizontal thrust values are computed using CFytot from VSPAERO. The ratio's are calculated using flap reference area, and a deflection angle of 18 ° for operating point velocities and maximum velocity. The results presented in Table A.1 show similar ratio's between vertical and horizontal thrust ($< 20\%$ difference) for a significant part of the operating range. The horizontal force estimation from OpenVSP is therefore considered sufficiently accurate at this stage of the design, and can be used for control system simulation.

Simulation output example

Table A.2: OpenVSP simulation conditions.

Parameter	Value
Reference area, S_{ref} [m^2]	0.0040
Reference chord, c_{ref} [m]	0.0700
Reference span, b_{ref} [m]	0.0700
Centre of gravity, x_{cg} [m]	0.0000
Centre of gravity, y_{cg} [m]	0.000015
Centre of gravity, z_{cg} [m]	-0.000042
Density, ρ [kg/m^3]	1.225
Freestream velocity, V_∞ [m/s]	12.0
Mach number	0.0
Angle of attack [deg]	0.0
Sideslip angle [deg]	0.0

Table A.3: Base aerodynamic coefficients at $V = 12\frac{m}{s}$ and $n = 40419$ RPM.

Coefficient	Value
C_{Fx} ($= C_D$ because $\alpha = 0$)	0.17079
C_{Fy}	0.02927
C_{Fz}	-0.00015
C_{Mx}	-0.01528
C_{My}	0.00172
C_{Mz}	0.01802

Table A.4: Aerodynamic stability and control derivatives obtained from OpenVSP at $V = 12\frac{m}{s}$ and $n = 40419$ RPM.

Coefficient	α	β	q	ConGrp 1	ConGrp 2	ConGrp 4
C_{Fx}	-0.0351	-0.0410	-0.1697	-0.0062	-0.0015	-0.0043
C_{Fy}	2.7053	-10.3079	-4.2577	-0.0807	-1.3703	-0.0483
C_{Fz}	12.5726	3.3146	29.3229	1.6172	0.0967	1.8227
C_{My}	-1.0000	-0.6522	-10.4939	-1.1617	-0.1328	-1.2598
C_{Mz}	0.3366	0.0467	1.9904	0.0503	-1.0934	-0.0037

Power and Electronics

Verification

The battery simulation tool is a Python script which was fully constructed from scratch. As previously explained, the model encompasses several physical equations combined together with several regression models trained on LiPo experimental data. Due to the large number of interacting equations, lookup functions and degradation models included in the simulation, performing a complete hand calculation for the entire model is impractical. Because of this, two steps are performed in order to verify the model.

Firstly, a list of unit tests is created. Those unit tests test the implementation of the equations and the general workings of the model. Those include tests in which separate functions and equations are extracted from the model, and their output is compared to hand calculations, as well as logical tests like whether SOC is a monotonically decreasing function during a single flight. A summary with all unit tests is given in Table A.5

Table A.5: Unit tests for LiPo battery simulation

Description	Input	Expected Output
Circuit Model Mathematics		
Power extracted from battery is equal to the power delivered plus loss factors	$V_{\text{ocv}} = 15.5\,\text{V}$ $R = 0.04\,\Omega$ $P = 200\,\text{W}$	$V_{\text{ocv}} \cdot I - V_{\text{term}} \cdot I = I^2 R$
Discriminant of Current equation is 0 at max theoretical power	$V_{\text{ocv}} = 16\,\text{V}$ $R = 0.05\,\Omega$ $P_{\text{max}} = V^2/4R = 1280\,\text{W}$	Discriminant $= V^2 - 4RP_{\text{max}} = 0$

Table A.5: Unit tests for LiPo battery simulation (continued)

Description	Input	Expected Output
Quadratic equation for I correctly implemented	$V_{\text{ocv}} = 16.8\,\text{V}$ $R = 0.045\,\Omega$ $P = 250\,\text{W}$	$I = 15.527\,\text{A}$ and $V_{\text{term}} = 16.101\,\text{V}$ (hand calc: disc $= 237.24$, $\sqrt{\text{disc}} = 15.403$)
Zero power gives zero current and full open-circuit voltage	$V_{\text{ocv}} = 16\,\text{V}$ $R = 0.05\,\Omega$ $P = 0\,\text{W}$	$I = 0\,\text{A}$ and $V_{\text{term}} = V_{\text{ocv}} = 16\,\text{V}$ (hand calc: disc $= V^2$, $I = 0$)
I $\approx P/V_{\text{ocv}}$ for small loads	$V_{\text{ocv}} = 16\,\text{V}$ $R = 0.04\,\Omega$ $P = 1\,\text{W}$	$I \approx P/V_{\text{ocv}} = 0.0625\,\text{A}$ (hand calc: disc $= 255.84$, $\sqrt{\text{disc}} = 15.9950$, $I = 0.005/0.08 = 0.0625\,\text{A}$)
Kirchhoff's Voltage Law: terminal voltage drop equals $I \cdot R_{\text{i}}$	$V_{\text{ocv}} = 15.5\,\text{V}$ $R = 0.04\,\Omega$ $P = 200\,\text{W}$	$V_{\text{ocv}} - V_{\text{term}} = I \cdot R$ (hand calc: $I = 13.364\,\text{A}$, drop $= 0.535\,\text{V}$ $= 13.364 \times 0.04$)
Degradation Physics		
OCV monotonically decreases with falling state of charge	SOC $\in \{0.9, 0.5, 0.1\}$ applied to `Vocv_poly`	$V_{\text{ocv}}(0.9) > V_{\text{ocv}}(0.5) > V_{\text{ocv}}(0.1)$, consistent with LiPo electrochemistry
Full Simulation Physical Constraints		
SOC is non-increasing throughout discharge: battery cannot spontaneously charge	Full simulation run ($P_{\text{max}} = 320\,\text{W}$, $P_{\text{avg}} = 130\,\text{W}$, $t = 10\,\text{s}$)	$\Delta\text{SOC}(t) \leq 10^{-9}$ for all consecutive timesteps
Terminal pack voltage remains within physical 4S LiPo boundaries	Full simulation voltage time-series	$10\,\text{V} \leq V_{\text{pack}}(t) \leq 17\,\text{V}$ for all t
Current and C-rate are non-negative	Full simulation current and C-rate time-series	$I(t) \geq -10^{-6}\,\text{A}$ and $\dot{C}(t) \geq -10^{-6}$ for all t
Recharge time is physically consistent with a 2C charge rate	Depth of discharge from simulation, $C_{\text{charge}} = 2$	$0 < t_{\text{recharge}} < 1800\,\text{s}$ (upper bound from a full 100 % DoD at 2C)

After it has been verified that the equations are correctly implemented in the model, a higher-level system verification test can be performed to ensure that all components are integrated correctly. For this purpose, the experimental data from the LiPo battery tests is used [42]. Since the objective of this test is verification rather than validation, the same battery that was used to derive the regression models is intentionally employed. The purpose is not to assess the model's ability to generalise to unseen batteries, but rather to verify that the regression models, SOC calculations and voltage calculations have been implemented correctly and interact as intended within the integrated simulation framework.

As explained previously, the regression models were developed to capture the variation of V_{ocv} and R_i with SOC, as well as the increase in R_i due to cycle degradation. The experimental dataset contains measurements from a constant-current discharge test, where the terminal voltage is recorded throughout the discharge. To reproduce this experiment, the battery simulation tool was slightly reorganised to accommodate a constant-current load rather than the constant-power load used for the mission simulations. The governing physical equations, however, remained unchanged.

Although the regression models were derived from this battery dataset, reproducing the measured discharge curve still requires the correct implementation and integration of all governing equations within the simulation. The simulated voltage therefore provides a useful verification of the software implementation. As shown in Figure A.3, the simulated and measured terminal voltages match closely throughout the discharge, while the predicted discharge duration also agrees well with the experimental results. The maximum observed difference between the measured and simulated voltage is 1.4 %.

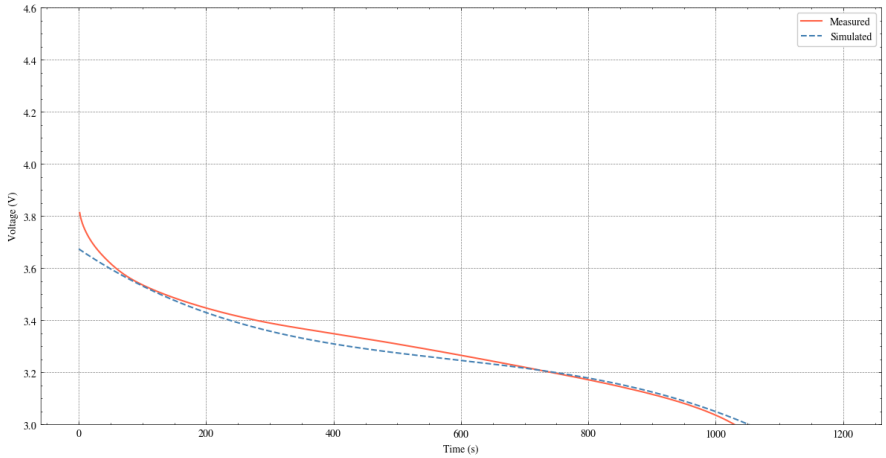

Figure A.3: Measured and simulated terminal voltage during a constant-current discharge test.

Considering that all unit tests were successfully passed and that the integrated simulation reproduces the experimental discharge behaviour with a maximum voltage deviation of only 1.4 %, sufficient evidence was obtained that the battery model has been implemented correctly and is suitable for use in the subsequent design analyses.

Validation

Unfortunately, no independent dataset containing raw measurement data from a separate LiPo battery experiment could be identified to perform a fully quantitative validation of the model. However, the battery manufacturer BetaFPV provides discharge curves for its batteries on its website[2]. These graphs show the terminal voltage of batteries discharged at a constant current under controlled conditions.

Although the underlying measurement data is not publicly available, a qualitative validation can be performed by comparing the manufacturer's published discharge curve with the discharge curve predicted by the battery simulation tool for the same battery and operating conditions. To do this, a simulation was performed for a 320 mAh LiPo battery discharging at a constant current of 18 A, matching the conditions reported by BetaFPV.

As shown in Figure A.4, the overall discharge behaviour predicted by the model closely resembles the behaviour observed in the manufacturer's measurements. In particular, the gradual voltage decay throughout most of the discharge and the rapid voltage drop near the end of discharge are both captured by the simulation. Furthermore, the predicted discharge duration closely matches the duration observed in the published measurements. Some discrepancies are visible during the initial stage of the discharge; however, the overall shape and characteristic features of the discharge curve remain consistent with the measured behaviour.

[2] `https://betafpv.com/collections/batteries/products/lava-ii-1s-battery?variant=42566848839814`. Accessed: 10.06.2026

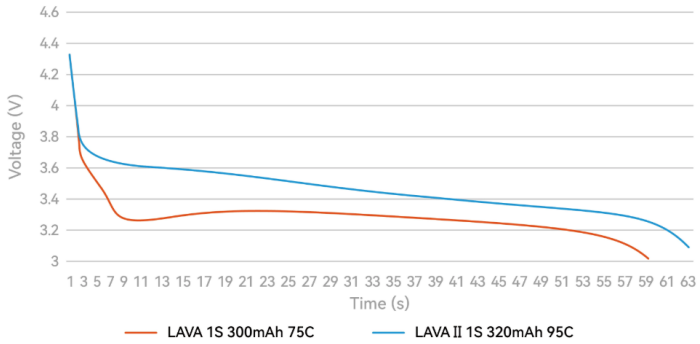

(a) Measured terminal voltage for a 320 mAh LiPo battery (blue line) discharging at a constant current of 18 A. Source: BetaFPV.

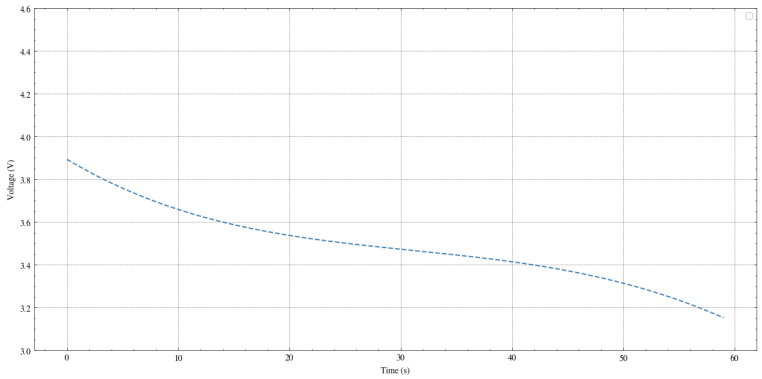

(b) Simulated terminal voltage for a 320 mAh LiPo battery discharging at a constant current of 18 A using the battery simulation tool.

Figure A.4: Qualitative comparison between manufacturer's measurements and simulated terminal voltage for a 320 mAh LiPo battery.

While the absence of raw measurement data prevents a rigorous quantitative validation, the close agreement in discharge profile shape and discharge duration provides confidence that the model captures the general physical behaviour of the battery. Combined with the verification activities presented previously, this qualitative validation indicates that the model is sufficiently representative for the preliminary design of the power system.

Tether

Assumptions

- The tether is only modelled geometrically. It neglects cable sag and aerodynamic drag.
- The tether stiffness ($k = AE/L$) assumes elastic behaviour up until the break strain.
- Structural damping is simplified to a constant damping ratio ($\zeta = 0.02$).
- Drag is calculated using a quadratic drag model, where C_D is interpolated linearly for different pitch angles.
- The model assumes free-stream airflow at all times, rotor wash and wind are neglected
- The brake engages as soon as the brake-phase is triggered, no communication latency between the camera system and the brakes is assumed.
- The simulation assumes that the propellers instantly operate at full thrust.

Verification

The tether simulation is a Python script that is built on the MuJoCo physics engine. MuJoCo is expended opon by three extra models for aerodynamic drag (`aero.py`), moth trajectory playback (`moth.py`) and custom

tether physics (`main.py`). The simulation is explained in Chapter 11. These modules interact continuously with the MuJoCo solver during the simulation, this makes a complete verification of the simulation impractical. Verification will therefore be done by completed in two steps, namely: Unit tests, Physics consistency.

For the unit tests, a single equation is isolated from the code and evaluated for a concrete set of input values. The output is than compared to an independent hand calculation. These calculations are shown in Table A.6. Secondly, the physics consistency is checked with the energy method and energy conservation method. These results are also shown in Table A.6

Table A.6: Unit tests for the flight performance simulation

Description	**Input**	**Expected Output**
Propulsion & Mass Budget		
Maximum thrust equals mass × thrust-to-weight ratio × g	$m = 0.150\,\text{kg}$ $\text{TW} = 4$ $g = 9.81\,m/s^2$	$F_{\text{max}} = m \cdot \text{TW} \cdot g = 5.886\,\text{N}$ **Result: 5.886 N**
Drone weight	$m = 0.150\,\text{kg}$, $g = 9.81\,m/s^2$	$W = mg = 1.472\,\text{N}$ **Result: 1.472 N**
Net upward acceleration at full thrust	$F_{\text{max}} = 5.886\,\text{N}$ $W = 1.472\,\text{N}$ $m = 0.150\,\text{kg}$	$a = (5.886 - 1.472)/0.150 =$ $29.43\,\text{m/s}^2 = 3.00\,g$ (exactly $(\text{TW} - 1)\,g$, mass-independent) **Result: 29.43** m/s^2
Aerodynamic Drag Model		
Drag formula $D = \frac{1}{2}\rho S_{\text{ref}} C_d V^2$ reproduces all 19 tabulated values	$\rho = 1.225\,\text{kg m}^{-3}$ $S_{\text{ref}} = 0.001\,\text{m}^2$ $V = 5\,m/s$ angles 0°–90°	$D_{hand} = D_{sim}$ at every angle **Result: all 19 pass**
Drag at $V = 5\,m/s$, 0°	$C_d(0°) = 1.248$ $\rho = 1.225\,\text{kg m}^{-3}$	$D(S_{\text{ref}} = 0.001) = 0.01911\,\text{N}$ **Result: 0.01911 N**
Tether Mechanics		
Wire cross-sectional area $A = \pi(D/2)^2$	$D = 0.5\,\text{mm}$	$A = \pi \times (2.5 \times 10^{-4})^2 = 1.9635 \times 10^{-7}\,\text{m}^2$ **Result: 1.9635×10^{-7} m^2**
Tether axial stiffness $k = AE/L$ at four deployed lengths	$A = 1.9635 \times 10^{-7}\,\text{m}^2$ $E = 2 \times 10^9\,\text{Pa}$ L at 0.5, 1.0, 2.0, 3.0 m	$k(0.5) = 785.4\,N/m$ $k(1.0) = 392.7\,N/m$ $k(2.0) = 196.4\,N/m$ $k(3.0) = 130.9\,N/m$ **Result: all match**
Intercept Performance (Energy Method)		
Peak intercept speed (without drag) going straight down $v = \sqrt{2(\text{TW}+1)g\,d}$	d at 1, 2, 2.5 m $\text{TW} = 4$ $g = 9.81\,m/s^2$	$v(1\,\text{m}) = 9.90\,m/s$ $v(2\,\text{m}) = 14.00\,m/s$ $v(2.5\,\text{m}) = 15.66\,m/s$ **Result: matches numerical integration**
Drag slows the drone down	$d = 2\,\text{m}$ $m = 0.150\,\text{kg}$	$v_{\text{drag}} \approx 12.96\,m/s$ vs $v_{\text{ideal}} = 14.00\,m/s$ **Result:**
Braking & Structural Loads (Energy Conservation)		
Maximum tether stretch $\Delta x_{\text{max}} = v\sqrt{m/k}$ (spool locked, linear spring)	$v = 6\,m/s$ $k = 392.7\,N/m$ ($L = 1\,\text{m}$) $m = 0.150\,\text{kg}$	$\Delta x = 6\sqrt{0.150/392.7} = 0.117\,\text{m}$ **Result: 0.117 m**
Peak tether force during braking $F_{\text{max}} = k\,\Delta x_{\text{max}}$	$v = 6\,m/s$ $L = 1\,\text{m}$ $k = 392.7\,N/m$	$F_{\text{max}} = 392.7 \times 0.117 = 46.0\,\text{N}$ Peak deceleration $= 46.0/0.150 = 307\,\text{m/s}^2 = 31.3\,g$ **Result: formula consistent**

Validation

To ensure the tether forces exerted on *the Chameleon* platform are physically accurate, the MuJoCo tether simulation (including the aerodynamic model) was validated against the UIAA 101 standard drop test [126]. A simulated 80 kg cylindrical mass was dropped 4.8 meters on a 2.8 meter tether, to validate the empirical peak impact forces (7.8-9.9 kN) and dynamic elongations (29%-33%) of standard polyamide climbing ropes (Mammut[3], Petzl[4], Edelrid[5]).

Tether Dynamics: Initial Approach, Discrepancies, and Simulation Improvements

Initially, the simulation attempted to derive the damping coefficient from the absolute volumetric viscosity ($\eta = 0.1$ GPa·s [127]) and $C = \frac{\eta A}{L}$. However, this method yielded extreme validation errors: over 100% too high peak forces and less than a third of the elongation measured for the climbing ropes.

Further analysis showed that this method yielded an effective damping ratio of 1.29, which is an overdamped system. This is inconsistent with existing literature, typical nylon ropes and wires are heavily underdamped and have damping ratios of about 0.02 [105]. Therefore, the choice was made to change the model, and to let the tether have a constant damping coefficient that aligns with literature ($\zeta = 0.02$ [105]). This damping coefficient is utilised for both the nylon climbing ropes and the nylon fishing wire (both for validation and simulation).

With this ζ, the damping coefficient is calculated using $C = 2\zeta\sqrt{km}$, where k is calculated using $k = \frac{EA}{L}$, using a Young's modulus of 0.42 GPa for the climbing ropes [127]. This logic update resolved the high validation errors. The revised simulation yielded an average impact force error of 8.5%, and an average elongation error of 7.2%. The small discrepancies ($< 10\%$) can be attributed to the constant, and possibly slightly inaccurate ζ, and the zero tether mass assumption; however, since the errors are relatively low, confidence in the simulation remains high. While the simulation has a slight bias towards overestimating the elongation, this conservative margin ensures that the actual braking distance remains within the constraints and minimises the risk of possible crashes during deployment. The force model also seems to be quite accurate, especially considering the zero tether weight assumption of MuJoCo. This assumption will hold up better for a lightweight fishing wire than a heavier climbing rope.

Table A.7: UIAA 101 Validation Results for Tether Dynamics

Metric	Mammut Alpine	Petzl Volta	Edelrid Swift
Diameter [mm]	8.7	9.2	8.9
Impact Force [kN]	7.8	8.6	9.9
Sim. Impact Force [kN]	8.29	9.16	8.63
Abs. Force Error [%]	6.28	6.51	12.8
Elongation [%]	31.0	33.0	29.0
Sim. Dyn. Elongation [%]	33.18	32.78	33.02
Abs. Elongation Error [%]	7.03	0.67	13.9

Braking System

For the braking system, as mentioned, a brake force of 140 N was necessary. The electromagnetic brake system can provide 5 Nm of torque according to the manufacturer[6]. The tether is wound around a 7 cm diameter spool, and the 140 N braking force can therefore be met. The brake ramp-up time can be validated by looking at the latencies of similar electromagnetic brakes, which show similar ramp-up times of about

[3] `https://www.mammut.com/nl/en/products/2010-06570-2285/8-7-alpine-sender-dry-rope-40m` – Accessed: 12-6-2026

[4] `https://www.petzl.com/INT/en/Sport/Ropes/VOLTA-9-2-mm` – Accessed: 12-6-2026

[5] `https://edelrid.com/eu-en/sport/ropes/swift-protect-pro-dry-8-9mm?variant=911224` – Accessed: 12-6-2026

[6] `https://www.aliexpress.com/p/tesla-landing/index.html?scenario=c_ppc_item_bridge&productId=1005009302086016` – Accessed: 14-6-2026

0.03 s [108]. In conclusion, the successful validation of the tether dynamics against the UIAA 101 standard, combined with the large torque margin of the spool brake, confirms that the MuJoCo simulation can reliably estimate the braking performance of *the Chameleon*.

Control and Integration

To verify the code, state space matrices A and B are constructed at $V = 9$ m/s, RPM = 36000 using two different methods and compared. Method one uses simulated aerodynamic coefficients and the second method interpolates between A, B matrices at the operating points (all combinations of V=[1,6,12] and RPM= [30000, 41807]). The results for method 1 (real model) and method 2 (interpolated model) are shown in Table A.8 and Table A.9. These tables show the entries and error between those entries in percentage. Calculating error between interpolated state-space matrices and simulated state-space matrices shows an average error of 30% with an outlier of 178.14 %, indicating incorrect aerodynamic coefficients or a mistake in the code.

Plotting aerodynamic coefficients at the operating points to check their behaviour results in the plots shown in Figure A.5.

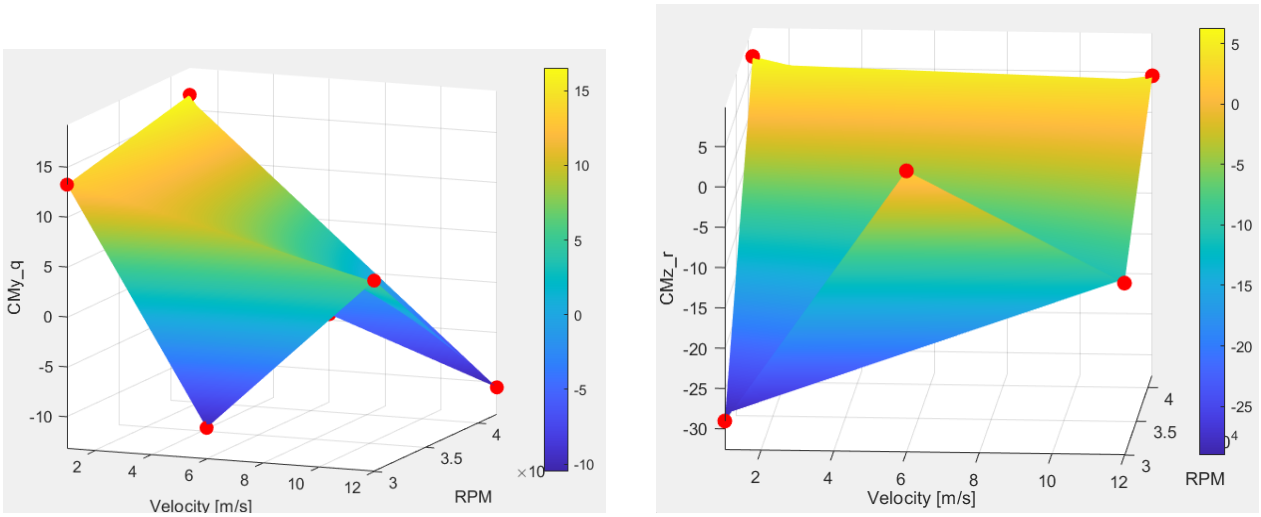

(a) Plot of Cmy_q at operating velocities and RPM

(b) Plot of Cmz_r at operating velocities and RPM

Figure A.5: Example of poor behaviour shown by multiple aerodynamic coefficients.

The aerodynamic coefficients are expected to follow either an increasing or decreasing trend with increasing velocity or RPM (e.g linear, quadratic or logarithmic). Figure A.5 shows that some stability derivatives alternate in sign and differ in magnitude without following a trend. This indicates the error found when comparing the eigenmatrices is at least partially caused by incorrect aerodynamic coefficients. Incorrect aerodynamic coefficients could be a result of the following two reasons:

- Grid too coarse, causing it to miss important highly non-linear behaviour of the model
- Fidelity of VSPAERO simulations is too low to give useful results

As mentioned in the validation of Aerodynamics, OpenVSP estimates moments with an error up to 20%. The error in these coefficients, in combination with the coarse grid, could be the cause of a big part of the error encountered when comparing the state space matrices. Due to the limited resources and scope of the project, the code cannot be further verified. Instead, the following recommendations are presented to verify the code in a further stage of the design:

1. Increase grid size significantly. Evaluating the aerodynamic coefficients at a 10x10 grid will increase required computational effort but also improve the model's ability to capture non-linear behaviour due to smaller step sizes.
2. Eliminate outliers found in the dataset generated by OpenVSP. By identifying and removing outliers

from the dataset, the interpolation becomes more reliable as extreme values are not used.

3. Apply regression to the OpenVSP dataset to identify trends and filter out oscillating values between data points.
4. Manually set terms that are small and oscillating around zero to zero.

These measures allow for a more reliable aerodynamic dataset. As a result, errors in the code and OpenVSP results can be analysed separately. The previously presented verification method can then be used to verify the code used for determining controllability.

Table A.8: Comparison of non-zero and non-unity entries of state space matrix A at the $V = 9$ m/s, RPM = 36000.

Entry	Real model	Interpolated model	Error [%]
$A_{4,4}$	-0.0518	-0.0625	20.79
$A_{5,5}$	0.6081	1.6913	178.14
$A_{6,6}$	-3.0304	-2.0239	33.21
$A_{4,7}$	-8.4957	-8.4957	0.00
$A_{6,7}$	4.9050	4.9050	0.00
$A_{5,10}$	-9.0000	-9.0000	0.00
$A_{6,9}$	9.0000	9.0000	0.00
$A_{9,6}$	-34.9621	-1.9275	94.49
$A_{10,5}$	-25.3573	-16.0222	36.81
$A_{9,9}$	-2078.6421	-1023.0932	50.78
$A_{10,10}$	-394.4709	-878.5719	122.72
$A_{11,11}$	-8.3333	-8.3333	0.00
$A_{12,12}$	-8.3333	-8.3333	0.00
		Mean element-wise error	**29.83**

Table A.9: Comparison of non-zero entries of the input matrix at $V = 9$ m/s, RPM = 36000.

Entry	Real model	Interpolated model	Error [%]
$B_{4,1}$	0.0018	0.0018	0.25
$B_{5,3}$	2.8169	3.6162	28.37
$B_{6,2}$	4.3499	3.9332	9.58
$B_{9,2}$	243.5827	206.9106	15.06
$B_{10,3}$	-201.5027	-232.4803	15.37
$B_{11,2}$	8.3333	8.3333	0.00
$B_{12,3}$	8.3333	8.3333	0.00
		Mean element-wise error	**9.80**

The `lqr()` function in MATLAB is part of the control toolbox, and is a widely used commercially maintained implementation of the LQR algorithm. Therefore, it will be viewed as a trusted tool and will not be verified in this report [128, 91]. The Runge-Kutta iteration step is verified by confirming the error is in $\mathcal{O}(h^4)$. Simulations without forcing term (making the system Linear Time-Invariant) using time step $dt = 1e^{-4}, 5e^{-5}$ and $2.5e^{-5}$ were compared against an exact solution calculated from the frozen state-space model. This is calculated using a method analogous to the one described by van Loan [129]. Then error size was confirmed using $\frac{f(4h)-f(2h)}{f(2h)-f(h)} \approx 16$, confirming that RK4 has been implemented correctly.

Validation

Due to time limitations, difficulties in finding comparable validation data and improvements that are expected to be implemented, validation has not been done for the controller. After improvements are implemented,

the poles and zeros of the interpolated state-space system could be compared to those of a launch vehicle simulation described by dos Santos et all [130].

Structures

FEM simulations in Autodesk Fusion Verification

Static stress simulations are used for quantifying the structures' strength during breaking. To verify the correct use of the FEM tool, a simple load case of a cantilever beam is simulated and compared with analytical results computed with a Python program. The force is applied at one end of the beam while the other is rigidly supported. The force is defined by a magnitude, positive being tensile, and two angles ψ and χ, as seen in Figure A.6a. From the internal loads, the normal and shear stresses can be found using the equations below [131] [7]. Additionally, from the normal and shear stresses, the von Mises stress can be found[8], where in this case $\sigma_{xx} = 0, \sigma_{zz} = 0, \tau_{xz} = 0$. The coordinate system and dimensions used are as defined in Figure A.6b.

$$\sigma_{yy} = \frac{F_y}{A} + \frac{M_x z}{I_{xx}} + \frac{M_z x}{I_{zz}} \qquad \tau_{yz} = \frac{F_z Q_{xx}}{I_{xx} w} = \left(\frac{F_z}{I_{xx}}\right) \frac{1}{2} \left(\frac{t^2}{4} - z^2\right)$$

$$\tau_{yx} = \frac{F_x Q_{zz}}{I_{zz} t} = \left(\frac{F_x}{I_{zz}}\right) \frac{1}{2} \left(\frac{w^2}{4} - x^2\right) \qquad \sigma_{\text{von Mises}} = \sqrt{\sigma_{yy}^2 + 3\tau_{yx}^2 + 3\tau_{yz}^2}$$

(a) Coordinate system for the angles

(b) Coordinate system for the beam cross-section.

Figure A.6: Coordinate system

For the FEM study, a beam of length l=150mm, width w=30mm and height t=10mm was used, with a force of F=100N, applied at $\psi = 40°$ and $\chi = 20°$. Additionally, a mesh size of 5% of the feature length was used. Then the stresses at a cross-section 100mm from the rigid end are inspected. The results for the total von Mises stress and the normal stress due to bending, which is the leading component, are presented below in Table A.10. Overall, the difference is very small except at the centre of the cross-section, where the stress values are small. This can be explained by the discretisation of the beam into elements of distinct size. Even the difference is always less than 15% and in most cases less than 2%, which leads to the conclusion that the FEM simulation is correctly set up and representative of what can be expected in real life.

Table A.10: FEM Validation: Cantilever Beam Stress Comparison

Location	Qty	Ana.	FEM	Diff	Location	Qty	Ana.	FEM	Diff
Center	σ_{yy}	0.17 MPa	0.148 MPa	-12.9%	Bot-left	σ_{yy}	2.52 MPa	2.517 MPa	-0.1%
	σ_{VM}	0.69 MPa	0.788 MPa	$+14.2\%$		σ_{VM}	2.52 MPa	2.557 MPa	$+1.5\%$
Top-center	σ_{yy}	-4.06 MPa	-3.991 MPa	-1.7%	Bot-right	σ_{yy}	6.40 MPa	6.405 MPa	$+0.1\%$
	σ_{VM}	4.09 MPa	4.046 MPa	-1.1%		σ_{VM}	6.40 MPa	6.403 MPa	$+0.0\%$

[7] `https://oit.tudelft.nl/CEG-mechanics-BSc/stresses_displacements/solve_bending/shear.html` – Accessed 19.05.2026

[8] `https://www.continuummechanics.org/vonmisesstress.html` – Accessed 19.05.2026

B

Post DSE Gantt Chart for different development timelines

In this appendix, the Gantt charts for the three different timeline scenarios are presented: optimistic, nominal, and pessimistic. These are visualised in Figure B.1, Figure B.2, and Figure B.3, respectively. The optimistic timeline assumes all testing is performed without issue, leading to a shorter development time. To be conservative throughout the report, this timeline is generally disregarded. The pessimistic timeline assumes a failure of the verification and validation, leading to a redesign and significant extra development time. This timeline is used to establish the contingency budget in Chapter 16.

Figure B.1: Post DSE Gantt Chart, optimistic scenario.

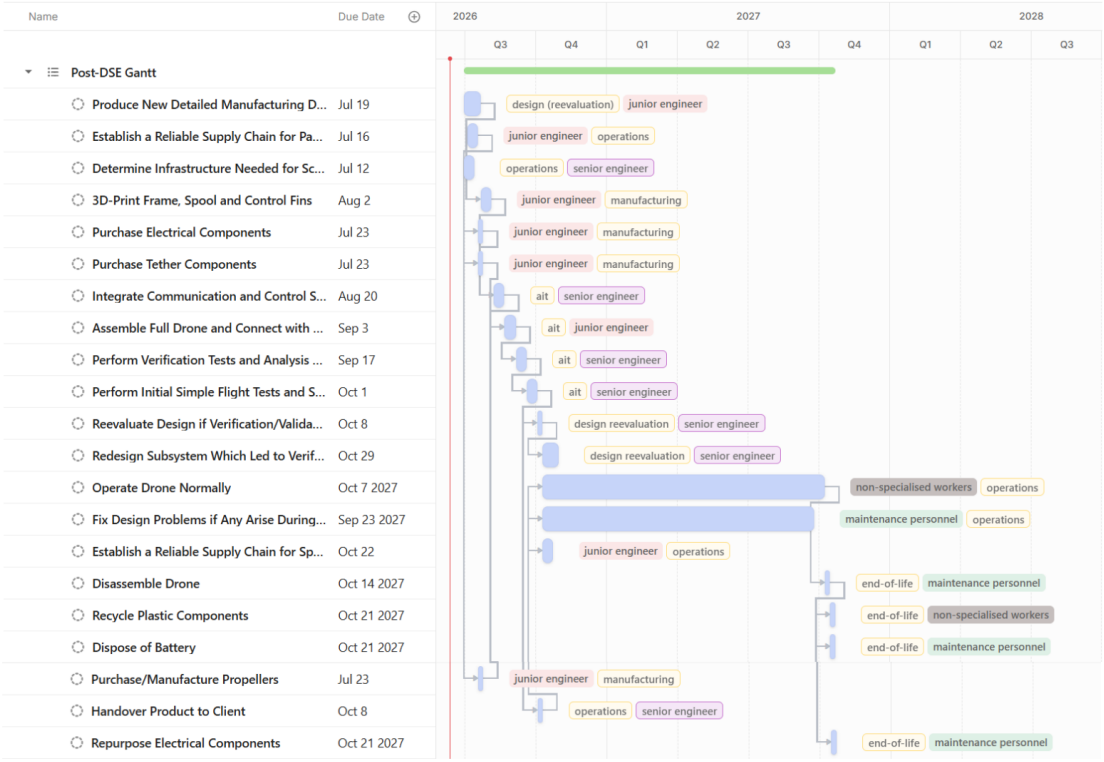

Figure B.2: Post DSE Gantt Chart, nominal scenario.

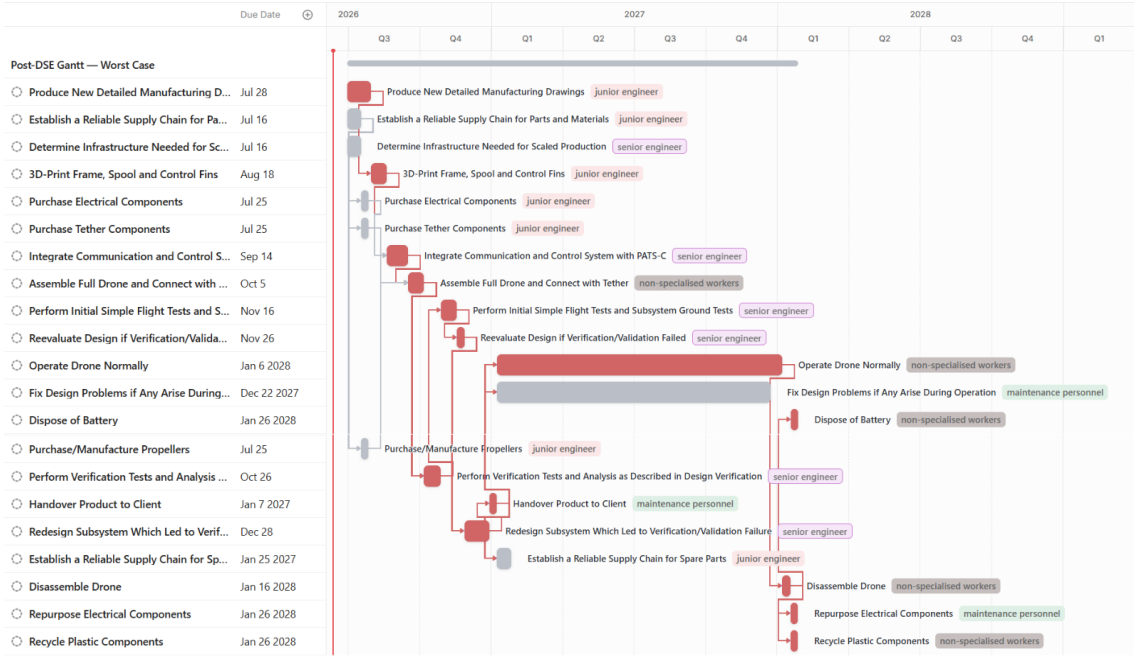

Figure B.3: Post DSE Gantt Chart, pessimistic scenario.

C

Extended Financial Breakdowns

Current Spending on Chemical Pest Control

Spending on chemical pest control varies widely depending on factors such as the greenhouse situation, the type of pest, and the crop. Contact with PATS revealed that greenhouse growers approximately spend EUR 1.5/m^2 per year on pest control. Additional costs for growers stem from the labour costs of applying pesticides (approximately EUR 40 per hour, 8 hours per hectare). Some savings for growers can be made by installing only PATS-C systems, which saves approximately EUR 0.10/m^2. The final cost estimate and justification can be found in Table C.1.

Table C.1: Pest control costs and justification

Type	Cost/ha/year (EUR)	Justification
General Pest Control	15,000	Included in cost estimation
Application Fees	2,240	Most pesticides are sprayed for a maximum of seven times per year, but use varies widely [132]. Neglected in pesticide cost estimation to keep a conservative estimate
Savings by PATS-C	-1,000	Not included in pesticide cost estimation to keep comparison with the drone system fair.

Market Penetration

General methodology

This section details the projected active fleet coverage (in hectares) and total market penetration (percentage of the 4500 ha Westland market) at year 5. The model uses the following constant parameters:

- Initial production rate: 1,000 units/year
- Deployment density: 10 drones/hectare
- Serviceable Addressable Market: 4,500 ha (Westland)

With these parameters, the active fleet and covered area are calculated iteratively for each year using the following equations (in Excel):

$$P_t = P_0(1+g)^{t-1}, \quad A_{new,t} = \frac{P_t - (F_{t-1} \times R_{fail})}{D}$$

Where $A_{new,t}$ is the new area covered in year t (hectares), P_t is the total production in year t (units), P_0 is the initial base production capacity (1,000 units/year), g is the annual production growth rate, F_{t-1} is the active fleet at the end of the previous year (units), R_{fail} is the hardware failure rate, and D is the deployment density (10 drones/hectare).

Sensitivity study

Various combinations of production growth and failure rates are tested in the model and tabulated in Table C.2. It should be noted that the failure rate strictly represents total loss incidents; repairable damage is accounted for in the maintenance budget and does not affect the fleet size.

Table C.2: Sensitivity Analysis of Year 5 Market Penetration (Hectares / % of Westland)

Failure Rate	Production Growth Rate				
	0%	**5%**	**10%**	**15%**	**20%**
1%	490 (10.89%)	542 (12.04%)	599 (13.31%)	663 (14.73%)	732 (16.27%)
5%	452 (10.04%)	503 (11.18%)	558 (12.40%)	619 (13.76%)	686 (15.24%)
10%	410 (9.11%)	457 (10.16%)	510 (11.33%)	568 (12.62%)	634 (14.09%)
20%	336 (7.47%)	379 (8.42%)	428 (9.51%)	481 (10.69%)	540 (12.00%)
30%	277 (6.16%)	317 (7.04%)	361 (8.02%)	410 (9.11%)	464 (10.31%)

Estimated Wages and Employer Cost

Labour costs are calculated using fully burdened hourly tariffs to capture employer liabilities. Four personnel roles are defined for this project. Non-specialised production workers assemble the hardware, and maintenance personnel conduct deliveries and field repairs. Engineering roles are split into junior engineers (detailed design, supply chain setups) and senior engineers (integration, verification and validation).

To determine the final employer cost, base hourly wages. To determine the final employer cost, base hourly wages[1,2,3] are multiplied by a wrap rate. Two different wrap rates are applied depending on the employment structure of the role[4,5]:

- Internal Personnel (Wrap Rate: 2.1): Production and maintenance staff are considered as full-time employees. This wrap rate accounts for fringe benefits (approximately 35%, comparatively high to attract personnel), overhead (45%, also comparatively high because of manufacturing and testing space, and software licenses), and G&A expenses (9%, average for engineering)
- External Personnel (Wrap Rate: 2.5): Because the hardware development phase is short-term, junior and senior engineers are modelled as external hires instead of permanent staff. This higher wrap rate includes the standard fringe, overhead and G&A burdens, alongside a commercial agency profit margin (about 15%) that does not apply to internal personnel.

It is important to note that the sources for the rates are American, meaning there is a geographical mismatch with the European rates, where, specifically, employee benefits (fringe) are typically higher. Since European rates are not as publicly available, the decision is made to use the upper limits of American rates for fringe and overhead. The hourly wages, applied wrap rates, and resulting employer costs per role are tabulated in Table C.3.

Table C.3: Base wages, wrap rates, and fully burdened employer costs per personnel category.

Role	Base Hourly Wage [EUR]	Wrap Rate	Employer Cost [EUR]
Non-Specialised Production Worker	16.00	2.1	33.60
Maintenance Personnel	20.00	2.1	42.00
Junior Engineer	40.00	2.5	100.00
Senior Engineer	60.00	2.5	150.00

[1] `https://www.nationaleberoepengids.nl/salaris/reparatie-en-onderhoudsmonteur` – Accessed: 15.06.2026
[2] `https://nextleveljobs.eu/blog/software-engineer-salary/netherlands` – Accessed: 15.06.2026
[3] `https://www.werkzoeken.nl/salaris/productiemedewerker/` – Accessed: 15.06.2026
[4] `https://www.govdash.com/blog/wrap-rate-government-contracting-guide` – Accessed: 20-06-2026
[5] `https://cabrilloclub.com/insights/federal-contract-wrap-rate-calculator` – Accessed: 20-06-2026

Detailed Cost Breakdown

In this section, the detailed cost breakdown is presented. The split-up into unit, annual, and development costs, including justifications, is tabulated in Table C.4. The costs for Off-the-Shelf components are tabulated in Table C.5. In both tables, sites were accessed as sources for the pricing. For readability, these website sources were referenced as [S...]. At the end of this appendix, in Table C.12, the full website links are located.

Table C.5: Off-the-shelf components cost breakdown.

Component	Cost [EUR]	Ref.	Component	Cost [EUR]	Ref.
Propulsion	**37.86**		**Base Station**	**45.49**	
Motors	34.60	[S10]	Ball Bearing Swivel	3.10	[S29]
Propellers	3.26	Quote	One-way bearing	1.00	[S17]
Electrical	**22.60**		Brake	16.00	[S18]
Batteries (including 4 backups)	17.60	[S11]	Coupling	2.00	[S19]
Cables	4.00	[S12]	Bearing	3.25	[S20]
Charging Pins	1.00	[S13]	Motor	11.69	[S21]
Control	**98.00**		Controller	1.00	[S22]
Flight Controller	54.00	[S14]	Electro-controller	2.00	[S23]
Servos	44.00	[S15]	Adapter	4.30	[S24]
Tether	**1.70**		Step Down Converter	0.50	[S25]
Wire	1.00	[S16]	Connector	0.50	[S26]
Connection	0.70	[S27]	Diodes	0.15	[S28]
Other Components	**10.86**				
Fasteners	10.86	BOM			

Net Present Value and Sensitivity to discount rates

The NPV is calculated for each year to determine the discounted cash flow. It is important to note that the annual operational costs scale by 30% each year, which reflects the compounding logistical and maintenance costs related to the expanding drone fleet.

The NPV calculation used the input parameters tabulated in Table C.6, and was calculated for both the nominal and pessimistic scenarios. It is assumed that only 85% of the drones are sold, 10% is kept for replacement, and 5% extra is kept as buffer. The resulting annual cash flows and NPV totals are detailed in Table C.7 for the nominal scenario and Table C.8 for the pessimistic scenario. To test the limits of the nominal business case, a sensitivity analysis showing the project's NPV across various discount rates is provided in Table C.9.

The sensitivity analysis shows that the nominal model achieves an IRR of 250%. The project's profitability is mainly sensitive to annual costs; however, the strongly positive NPV, even in very conservative discounting scenarios, shows that the project is worthwhile from a business perspective.

Table C.6: Inputs for NPV

Parameter	Value
Production Rate	1,000 units/year
Grower Price per Hectare	EUR 10,000.00
Initial Investment (Nominal Baseline)	EUR 102,893.15
Initial Investment (Pessimistic Baseline)	EUR 211,779.45
Operational Cost (Year 1)	EUR 560,739.64
Production Cost (Annual)	EUR 239,314.92
Discount Rate	35.0%
Total Backup Fleet (10% replacements, 5% Buffer)	15%

Table C.4: Cost estimates for unit, development, and annual costs

Item	Cost [EUR]	Justification
Unit Costs (per Drone)	**239.31**	
Propulsion	37.86	See Table C.5
Electrical	22.60	See Table C.5
Control	98.00	See Table C.5
Tether	1.70	See Table C.5
Base Station	45.49	See Table C.5
Other	10.86	See Table C.5
3D Filament	6.00	EUR 45 per kg Polycarbonate [S1]
Assembly Labour	16.80	Non Specialised Production worker (30 minutes)
Development Costs (Nominal)	**102,893**	
PATS-C integration	12,000	Senior Engineer (Man-hours: 80 h)
Detailed Engineering Work	24,000	Junior Engineer (Detailed Engineering Drawings, Docking Station Redesign, Man-hours: 120 h), Senior Engineer (Determining Necessary Production Scaling Infrastructure, Man-hours: 80 h)
3D printer farm	2,500	5 professional Polycarbonate printers [S2], includes extra nozzles (Section 15.2)
Prototype Material Costs	8,393	EUR 6,000 for two propeller moulds and costs for 10 prototypes
Supply Chain setup	12,000	Junior Engineer (Man-hours: 120 h)
Assembly Line Setup	8,000	Junior Engineer (Man-hours: 80 h)
Ground Testing	12,000	Senior Engineer (Man-hours: 80 h)
Flight Testing	12,000	Senior Engineer (Man-hours: 80 h)
Crash Testing	12,000	Senior Engineer (Man-hours: 80 h)
Development Costs (Contingency)	**108,886**	
Design Reevaluation (Labour)	75,600	Redesign (Senior Engineer (Man-hours: 200 h), V&V and integration redone (Same costs as above)
Assembly Line (Prototyping)	30,893	Full assembly line redone (Same costs as above)
Extra Material	2,393	Budget for 10 full new drones
Annual Costs	**560,740**	
Machine Depreciation	500	Assumption: Printer lifetime of 5 years
Buffer Stock	11,966	Keep 5% of Drones as buffer
Labour Costs	518,246	3 Non Specialised Production Workers (241 Working Days), 4 Maintenance Employees (241 Working Days)
Delivery Van Costs	6,000	1 Company van (EUR 500 per month [S3])
Replacement Stock	23,931	Assumption: 10% of drones need to be replaced yearly
Battery Disposal (SDP-6)	46	EUR 0.046 per battery [S4]
Electric Repurposing (SDP-6)	0	Leads to cheaper production costs
Plastic Recycling Labour (SDP-6)	50	EUR 500 per tonne [S5]
Extra Recycling Costs (SDP-6)	20	50 employees [S6], 2 kg waste per person [S7], EUR 0.20 per kg waste [S8]
Motor Recycling (SDP-6)	10	EUR 0.45 per kg [S9]

Table C.7: Net Present Value (NPV) cash flow tabulation over 5 years (Nominal Scenario).

Metric [EUR]	Year 1	Year 2	Year 3	Year 4	Year 5
Income from Sales	850,000.00	1,615,000.00	2,303,500.00	2,923,150.00	3,480,835.00
Operational Cost	560,739.64	728,961.53	947,649.99	1,231,944.99	1,601,528.48
Production Cost	239,314.92	239,314.92	239,314.92	239,314.92	239,314.92
Cash Flow (CF)	49,945.44	646,723.55	1,116,535.09	1,451,890.09	1,639,991.59
Discounted CF	36,996.62	354,855.17	453,806.87	437,117.98	365,740.27
Net Present Value (NPV)					**1,545,623.76**

Table C.8: Net Present Value (NPV) cash flow tabulation over 5 years (Pessimistic Scenario).

Metric [EUR]	Year 1	Year 2	Year 3	Year 4	Year 5
Income from Sales	850,000.00	1,615,000.00	2,303,500.00	2,923,150.00	3,480,835.00
Operational Cost	560,739.64	728,961.53	947,649.99	1,231,944.99	1,601,528.48
Production Cost	239,314.92	239,314.92	239,314.92	239,314.92	239,314.92
Cash Flow (CF)	49,945.44	646,723.55	1,116,535.09	1,451,890.09	1,639,991.59
Discounted CF	36,996.62	354,855.17	453,806.87	437,117.98	365,740.27
Net Present Value (NPV)					**1,436,737.46**

Table C.9: Sensitivity Study of the NPV with different discount rates, including the calculation of the Internal Rate of Return (Nominal Scenario).

Discount Rate	NPV [EUR]	Discount Rate	NPV [EUR]
10.0%	3,325,829.62	45.0%	1,189,695.41
20.0%	2,393,238.93	50.0%	1,051,420.78
25.0%	2,054,718.86	60.0%	831,483.34
30.0%	1,776,456.53	80.0%	541,008.86
35.0%	1,545,623.76	100.0%	365,320.21
40.0%	1,352,513.51	150.0%	145,980.94
IRR: 250.0%	**0.00**		

ROI Calculation

To establish the ROI, which, unlike the NPV, does not take into account the time value of money, the cumulative profit is divided by the project's total initial investment. This initial investment includes the annual costs of the first year. Since PATS must secure sufficient capital to survive its first year of commercial operations before self-sustaining cash flows are established. The calculations for the ROI are detailed in Figure C.10 and Figure C.11.

Table C.10: Cumulative Operational Profit and RoI (Nominal).

Year	Profit [EUR]	RoI
1	49,945.44	7.53%
2	696,668.98	104.98%
3	1,813,204.07	273.22%
4	3,265,094.16	492.00%
5	4,905,085.76	739.13%

Table C.11: Cumulative Operational Profit and RoI (Pessimistic).

Year	Profit [EUR]	RoI
1	49,945.44	6.47%
2	696,668.98	90.18%
3	1,813,204.07	234.71%
4	3,265,094.16	422.66%
5	4,905,085.76	634.95%

Financial Appendix: Component Sources

Table C.12: Component and cost sources for the financial appendix. All URLs accessed 15.06.2026.

Ref.	Description	URL
[S1]	3D Filament (PC)	https://eu.store.bambulab.com/nl/products/pc-filament
[S2]	PC 3D Printers	https://eu.store.bambulab.com/nl/products/p1s?srsltid=AfmBOorqt78RwSwCsz1QCesCjMNIL_vihXM3E8MuMJmdFMh02HFr6bdt
[S3]	Van running costs	https://www.loadsofvans.com/blog/unveiling-van-running-costs
[S4]	Battery disposal cost	https://share.google/mQxnJuCkp5ArzPFMV
[S5]	Plastic recycling economics	https://thundersaidenergy.com/downloads/plastic-recycling-the-economics/
[S6]	PATS employee count	https://www.zoominfo.com/c/pats/478620003
[S7]	Office waste per person	https://www.businesswaste.co.uk/waste-facts/office-waste-facts/
[S8]	Waste disposal rate	https://www.verpact.nl/en/rates
[S9]	Motor scrap price	https://www.kh-metals.nl/nl/schrootprijzen/
[S10]	Motors (Axisflying C145)	https://www.rotorama.com/product/axisflying-c145-1404-5-4500kv
[S11]	Batteries (LAVA II 1S)	https://www.aliexpress.com/item/1005010442637715.html
[S12]	Cables	https://www.aliexpress.com/item/1005008423959416.html
[S13]	Charging Pins (Pogo-pin)	https://www.amazon.com/Golden-Plating-Copper-Replacement-POGOPIN/dp/B0C7GKJRG3/
[S14]	Flight Controller	https://www.hobbydrone.cz/fc-pilotix-f405-v3-icm42688/
[S15]	Servos	https://www.sol-expert-group.de/1-87-modelbouw/Micro-servos/Set-van-5-stuks-S18JST-1-8-gram::891.html
[S16]	Monofilament Wire	https://www.amazon.nl/monofilament-transparant-visdraad-snoekbaars-decoraties/dp/B0BG2P8C16/
[S17]	One-way Bearing	https://www.amazon.nl/-/en/Needle-Bearing-6%C3%9710%C3%978mm-Precision-Instruments/dp/B083QK7X7H
[S18]	Brake	https://www.aliexpress.com/item/1005009302086016.html
[S19]	Coupling	https://nl.aliexpress.com/item/1005002950147081.html
[S20]	Bearing	https://nl.aliexpress.com/item/1005009676464871.html
[S21]	Braking Motor	https://nl.aliexpress.com/item/1005008869525638.html
[S22]	Controller	https://nl.aliexpress.com/item/1005004305055818.html
[S23]	Electro-controller	https://nl.aliexpress.com/item/1005010696158261.html
[S24]	Adapter	https://nl.aliexpress.com/item/1005009551534120.html
[S25]	Step Down Module	https://nl.aliexpress.com/item/1005005567940260.html
[S26]	Connectors	https://nl.aliexpress.com/item/1005005909840125.html
[S27]	Tether Connection Ring	https://www.pescareinliberta.it/it/cultiva-p19-micro-solid-ring
[S28]	Diodes	https://nl.aliexpress.com/item/1005012179615414.html
[S29]	Ball Bearing Swivel	https://www.lagerkoning.nl/ibb-axiale-naaldkrans-axk-5070.html

D

Bill of Materials

In this appendix, the Bill of Materials is presented. Hyperlinks to websites for most components were already tabulated in Appendix C. Therefore, these links will not be shown again. Only the fasteners will have a website link, as these were not detailed per fastener type in the previous chapter. This appendix contains four tables. Table D.1 contains the Bill of Materials for the drone, Table D.2 outlines all the fasteners, bearings, and shafts for the drone, Table D.3 details the parts used for the spooling platform, and finally, Table D.4 presents the fasteners for the spooling platform, along with a passive yaw swivel. All presented links were accessed on 16.06.2026.

Table D.1: Bill of Materials: Drone (Fasteners detailed in Table D.2)

Part	**Quantity**	**Total Weight [g]**
Axisflying C145 1404.5 4500 Kv	2	17.4
Custom Propeller	2	3.3
LAVA II 1S 320 mAh	4	32.8
AWG 14 Wiring	15 cm	5.2
Pogo-pin contacts	7	2.1
Safety capacitor: 35V, 470 μF	1	1.8
AIO flight controller	1	7.0
S18JST Microservo	4	7.2
0.5 mm Nylon Monofilament Fishing Wire	15 m	2
4.5 mm C'ultiva P-19 Micro Solid Ring	1	0.07
Fuselage (custom PC FR 3d print)	1	48.06
Top motor mount (custom PC FR 3d print)	1	0.89
Battery cap (custom PC FR 3d print)	4	0.96
Shaft cap (custom PC FR 3d print)	4	0.27
PCB cap (custom PC FR 3d print)	1	1.42
Servo mount (custom PC FR 3d print)	1	1.99
Vane (custom PC FR 3d print)	4	3.64
Total Weight	-	136.10

Table D.2: Bill of Materials: Fasteners, Bearings and Shafts for the Drone

Part	**Quantity**	**Total Weight [g]**	**Ref.**
Micro Bearings 1x3x1 IDxODxh	4	0.12	[S1]
D 1mm Shaft 25mm	4	0.6	[S2]

Continued on next page

Table D.2 – continued from previous page

Part	Quantity	Total Weight [g]	Ref.
M2x8 DIN912/ISO4762 Hex Black	4	0.824	[S3]
M2x5 ISO 10642 Countersunk Hex	4	0.544	[S4]
M2x8 ISO 10642 Countersunk Hex	8	1.648	[S5]
M2 Brass Heat Insert Long	4	0.88	[S6]
M1.4 Brass Heat Insert	11	0.77	[S7]
M1.4x4 DIN912 Hex	11	1.067	[S8]
M1.2x3 DIN965A Screw	2	0.048	[S9]
Total Weight Fasteners	-	7.271	-
Total Weight Full Drone	-	143.4	-

Table D.3: Bill of Materials: Spool Platform (Fasteners in Table D.4)

Part	Quantity	Total Weight [g]
Spool (custom PC FR 3d print)	1	213.1
Platform (custom PC FR 3d print)	1	475.48
Coupling 10-15 mm	1	150
DZD5-5A Electromagnetic Brake	1	320
HF0608 One way Bearing	1	2.2
JGB37-528	1	160
KP002 Bearing	2	133
Arduino Nano 3.0 Atmega328	1	7
MOSFET Trigger Switch Drive Module DC 5V-36V	2	7
DC 24V 2A Power Supply Adaptor	1	120
LM2596 DC-DC Step-down Power Supply Module	1	11
Female Jack Sockets	1	4
Diode	1	≈ 0
AXK5070 Ball Bearing	1	20
Total Weight	-	1491.1

Table D.4: Bill of Materials: Fasteners for the Platform

Part	Quantity	Total Weight [g]	Ref.
M 6 x 1 DIN 934 Nut	4	10	[S10]
M 6 x 16 DIN 912	4	13	[S11]
M 6 x 12 DIN 912	4	12	[S12]
M 3 x 8 DIN 912	6	10.2	[S13]
M 5 x 16 DIN 912	6	21	[S14]
Total Weight	-	276.2	-

Bill of Materials: Component Sources

Table D.5: Component sources for the Bill of Materials appendix. All URLs accessed 16.06.2026.

Ref.	Description	URL
[S1]	Micro Bearings 1x3x1	https://www.amazon.com/CBRIGHT-1x3x1mm-Miniature-Bearings-Bearing/dp/B0FY5V8X4B/
[S2]	D 1mm Shaft 25mm	https://www.amazon.nl/QUARKZMAN-Stainless-Projects-Helicopter-Airplane/dp/B0D1FYJSCR/
[S3]	M2x8 DIN912 Hex Black	https://www.amazon.nl/-/en/PDKKFF/dp/B0GRHHJWSH/
[S4]	M2x5 ISO 10642 Countersunk	https://www.amazon.nl/-/en/Pack-Stainless-Steel-Screws-Countersunk/dp/B0FNXBH91M/
[S5]	M2x8 ISO 10642 Countersunk	https://www.amazon.nl/-/en/Pack-Stainless-Steel-Screws-Countersunk/dp/B0FNX72RYX/
[S6]	M2 Brass Heat Insert Long	https://www.amazon.nl/-/en/ruthex-Threaded-Bushing-Plug-ultrasound/dp/B088QJG676/
[S7]	M1.4 Brass Heat Insert	https://www.amazon.nl/-/en/HANGLIFE-Threaded-Plastic-Printing-Components/dp/B0D4DRZ5B9
[S8]	M1.4x4 DIN912 Hex	https://www.amazon.nl/Sourcingmap-Threaded-Stainless-Socket-DIN912/dp/B01MG0RFMP/
[S9]	M1.2x3 DIN965A Screw	https://www.screwsandmore.de/nl/50-stuks-verzonkenkopschroeven-din-965-a2-m1-2x3/9652123-15528
[S10]	M6x1 DIN 934 Nut	https://ttohandel.nl/zeskantmoer-m6-rvs-a2/
[S11]	M6x16 DIN 912	https://de.screwerk.com/nl/shop/detail/stm/STM410600160S.html
[S12]	M6x12 DIN 912	https://schroevengroothandel.nl/inbusbouten-cilinderkop-m6-x-12mm-verzinkt-din912-100-stuks
[S13]	M3x8 DIN 912	https://www.rvspaleis.nl/bouten/binnenzeskant/din-912/din-912-[-]-a2/din-912-[-]-a2-[-]-m3/912-2-3x8_100
[S14]	M5x16 DIN 912	https://rvsland.nl/inbusbout-m5x16-rvs-din912-50stuks

E

3D Print Instructions

Instructions on how to make these parts within the Bambu lab[1] ecosystem of 3d printers, materials and software will be provided below. Currently, the client operates such machines and uses filament sourced from this manufacturer [61], so this was found most prudent. However, with sufficient knowledge of 3D printing fundamentals, these parts should also be manufacturable on other systems and software from the provided files. In fact, test prints of the fuselage in a different material were made within the Prusa Research[2] ecosystem. All files necessary for the manufacturing of the 3d printed components can be found at the end of this section in Figure E.11.

The instructions below briefly cover the settings required to manufacture the parts using the Bambu Studio slicer and a Bambu lab P1S 3d printer, which is what the client primarily operates at present [61]. These instructions assume little to no 3d printing experience. Each file is named after its corresponding part according to the BOM's naming convention (Appendix D). All files are provided in the STEP (Standard for the Exchange of Product Data) CAD file format ".step".

The very first step is getting the slicer software that generates the machine code to run the 3d printer from the provided files. The download for Bambu's slicer software, called Bambu Studio, can be found on their website[3]. From now on, Bambu Studio may also be referred to simply as the slicer. This guide was made for the latest version of this software (v 2.7.1.57) as of 15.06.2026. The installation guide and setup guide upon launch can be followed.

Next, the print settings need to be set up. First, the steps applicable to all parts are covered. As covered in Figure 8.3, the polycarbonate (PC) filament from Bambu's ecosystem will be used. Thus, Bambu's optimised settings for it will be used as the starting point. In some versions, not all materials come installed with the software by default, so the PC filament preset may first need to be imported. This is done by following the steps described in Figure E.1.

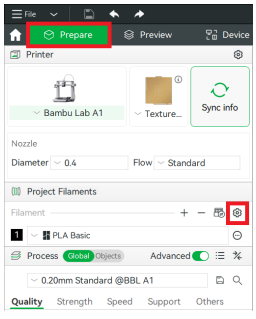

(a) Under the prepare tab, navigate to filament and then the gear icon

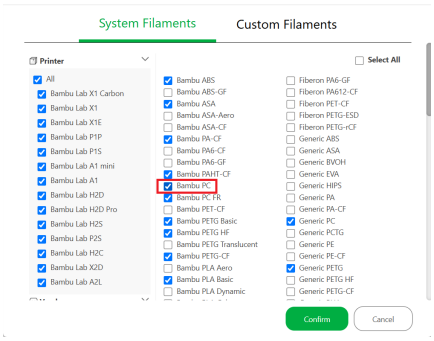

(b) In the menu that shows up, tick Bambu PC and proceed with confirm

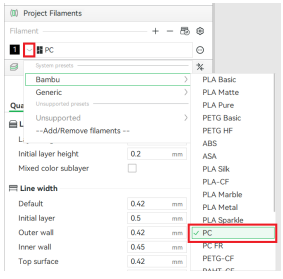

(c) Lastly, under the filament tab, select Bambu and then PC in the next dropdown menu

Figure E.1: Step 1 (a)-(c): Configuring the correct filament in Bambu studio

[1] `https://bambulab.com/en-eu` - Accessed 15.06.2026
[2] `https://www.prusa3d.com/` - Accessed 15.06.2026
[3] `https://bambulab.com/en-eu/download/studio` - Accessed 15.06.2026

Following this, the correct printer needs to be selected, such that the system's presets for build volume, speed, etc., are correct. This is important if more than one printer was connected during the initial setup. This step is again done in the prepare tab as detailed in Figure E.2a. Additionally, the advanced settings should be toggled on as shown in Figure E.2b. Afterwards, a lot more settings should become available in the Quality, Strength, Speed, and Support process tabs.

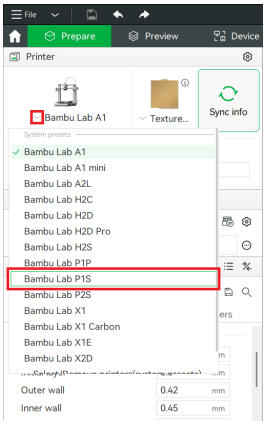

(a) Under the printer tab, select the correct printer preset, in this case the P1S

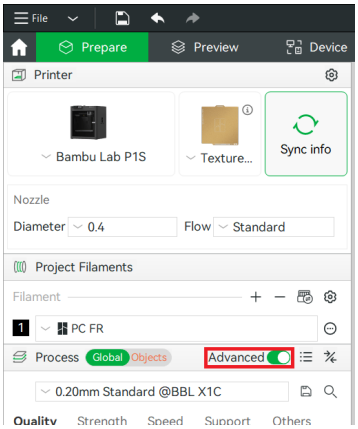

(b) Turn on the advanced settings under the Process tab

Figure E.2: Step 2: Configuring printer and accessing the advanced settings

Now, some global settings that will be used for all models can be set, as shown below in Figure E.6. The Arachne wall generator must be selected so that extra-thin walls still get printed. Furthermore, Gyroid infill is selected as it has "near-isotropic characteristics" and "excellent strength-to-weight ratio"[4]. This means that it exhibits similar strength in all planes and directions, which is important for impact resistance. Most importantly, however, it gives the structure increased strength for the same infill mass.

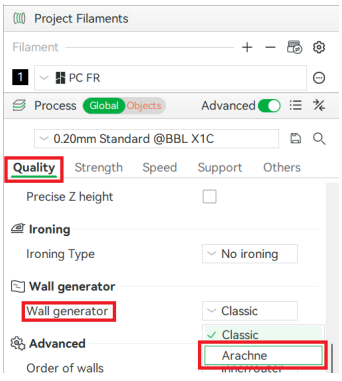

(a) Under the quality tab, go down to the wall generator setting that is now available under the advanced settings mode. Select Arachne as the wall generator.

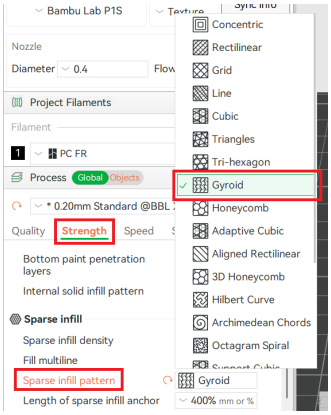

(b) Next, under the Strength tab, change the sparse infill pattern to Gyroid

Figure E.3: Step 3 (a) and (b): Selecting the correct wall generator and Gyroid infill

Next, support settings for parts of the 3d print that would normally start in the air must be configured as shown in Figure E.4. Once the print is finished, the supports will have to be removed by hand or with the help of (needle-nose) pliers. Tree supports are used as they are easier to remove than normal supports and leave a better surface finish. Additionally, they create less waste material than normal supports, since the support material is scrapped after the print. For example, for the largest custom part, the *Fuselage*, normal supports would take 22.95g of material, while tree supports take 10.7g

[4] `https://www.wevolver.com/article/gyroid-infill` - Accessed 16.06.2026

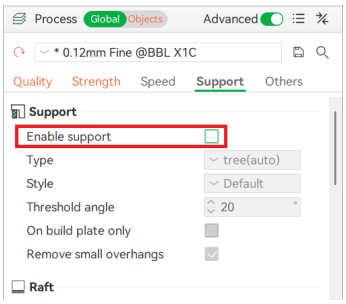

(a) Under the support tab, go down to enable support and tick the box

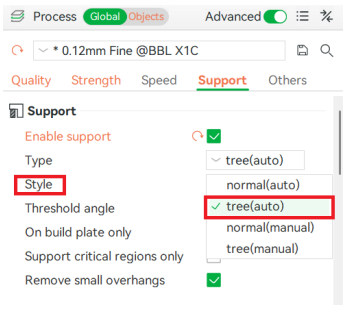

(b) The support type should be tree(auto) by default. In case it is not, select it.

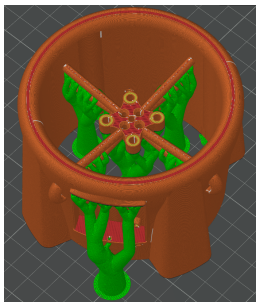

(c) Tree supports that are generated after slicing the design (generating machine code) as described in Figure E.9

Figure E.4: Step 4 (a) and (b): Configuring the support settings for parts of the 3d print that start in the air. (c): Resuling supports

What setting to use for what part is given at the end of this section in Table E.1. Where to find each setting is explained below. First, the nozzle size and layer height are shown in Figure E.5. Keep in mind that the nozzle size is a physical property of the 3d printer. To print with a different nozzle size, the nozzle on the printer also has to be changed.

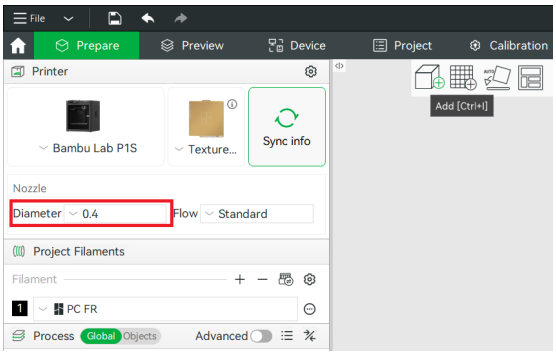

(a) The nozzle diameter setting can be found below the printer. This must correspond to what is physically installed on the machine.

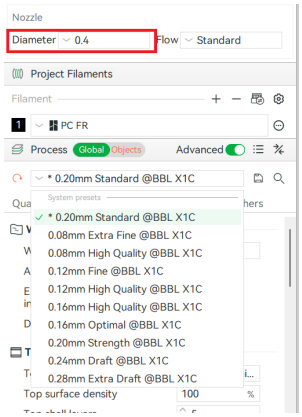

(b) Layer height presets available for a 0.4mm nozzle

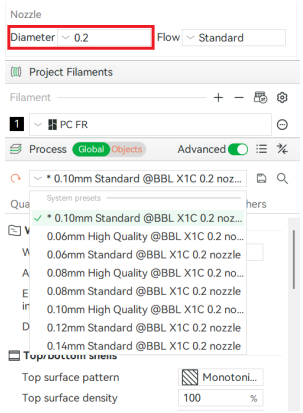

(c) Layer height presets available for a 0.4mm nozzle

Figure E.5: Step 4 (a): Configuring what nozzle size the printer has; (b)-(c): Different layer height presets available for the different nozzle sizes

After that, the number of walls the 3d print has, called wall loops, and the percentage of the inside that's filled in, called infill, can be set straightforwardly as depicted in Figure E.6.

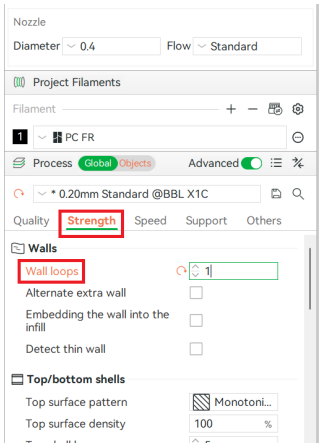

(a) Wall loops can be set under the Strength tab in the walls subsection

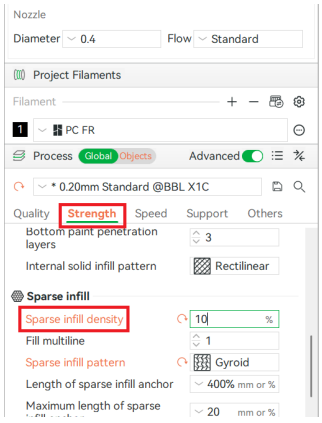

(b) Infill percentage can be set as sparse infill density again under the Strength tab in the sparse infill subsection

Figure E.6: Step 5 (a) and (b): Setting wall loops and infil density

Finally, it is shown how to add modifiers to objects in Figure E.8. To do this, the ".step" file itself must come with the required additional geometry. Modifiers are used to make a 3d printed object denser and hence stronger via extra infill and wall loops only in specific locations, which are expected to get highly stressed. Thus, a lot of structural performance can be gained with only a marginal increase in weight. The effect on the structure can be seen below in Figure E.7. Additionally, the additional wall loops are necessary for adding heat inserts. To have optimal strength and catch properly, heat inserts need at least 3-4 wall loops[5] (this also depends on nozzle size).

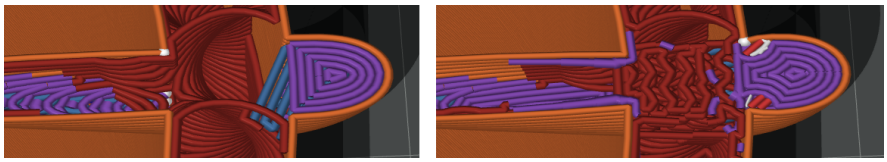

Figure E.7: Results on the internal structure from a correctly applied modifier on the right. No modifier present on the left.

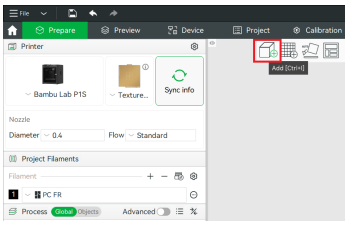

(a) Import the ".step" file with the modifier bodies via the add button.

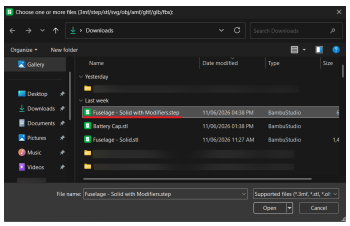

(b) Select the correct file

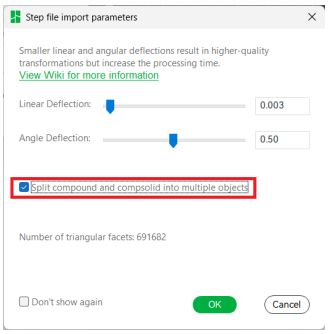

(c) When importing, tick the "Split compound and compsolid into multiple objects", the rest can be left default

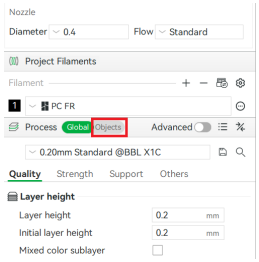

(d) In the process tab, switch over to objects. The individual objects inside the file can now be adjusted separately.

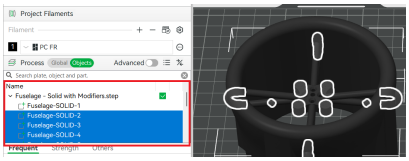

(e) Select all bodies, except the biggest one, which is also usually first. Use Ctrl or click the first one, then Shift and then the last one.

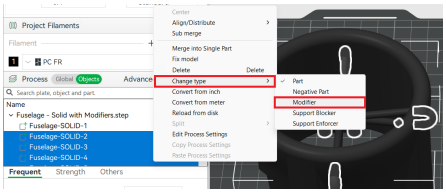

(f) Right click on the selection and go down to the Change type option in the dropdown menu. Select Modifier

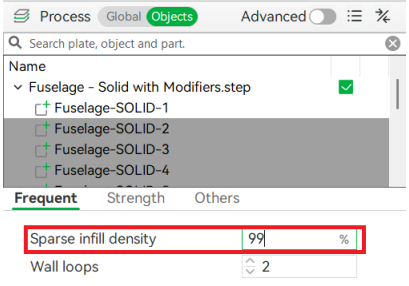

(g) While the selection is active, the infill density of the modifiers can be adjusted

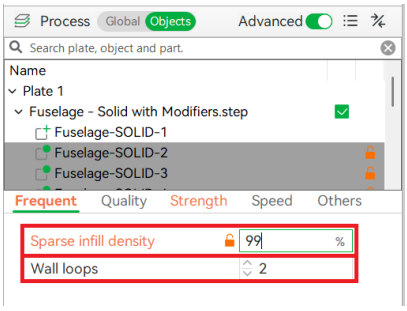

(h) While the selection is active, the wall loop count of the modifiers can be adjusted

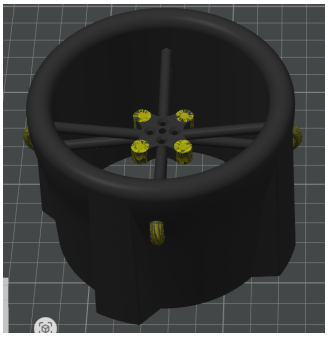

(i) Go back to the Global tab under process. If everything was done correctly, the modifiers should be shown in yellow

Figure E.8: Step 6: How to add a modifier, substeps (a)-(i)

[5] `https://medesignlab.me.wisc.edu/3d-printing/heat-set-inserts/#slicer-settings` – Accessed 16.06.2026

Finally to print the design the machine tool path code (GCODE) must first be generated and then it must be sent to the printing utility. This is detailed below in Figure E.9

(a) To generate the machine toolpath code (".gcode") press slice plate at the top right corner

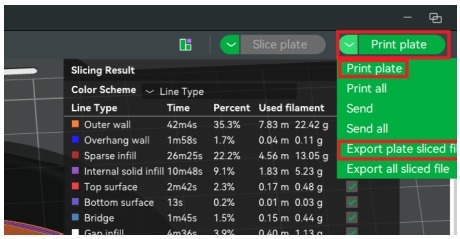

(b) Once the toolpath code (".gcode") has been generated, the design can finally be printed. If a printer was connected during the setup the print plate can be used directly. Othewise the toolpath code can be exported to a SD card (P1S does not come with USB option) which can be plugged into the 3d printer to print the part

Figure E.9: Step 7 (a) and (b): Machine code generation and printing

Additionally, after generating the machine code (slicing), the design that the 3d printer will print, or at least attempt to, can be inspected layer by layer, as shown in Figure E.10.

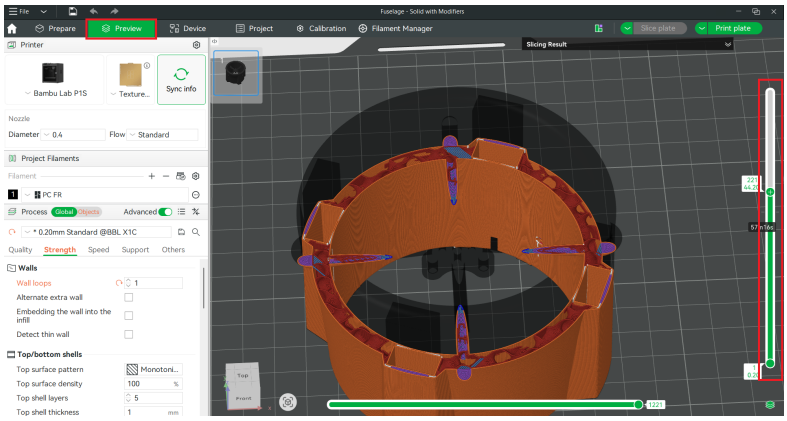

Figure E.10: After slicing (generating machine code), under the preview tab the design that is to be 3d printed can be inspected layer by layer with the slider to the right

The appropriate values for each of the settings that vary by part can be found below in Table E.1. As discussed in Chapter 8, to minimise the possibility of delamination of the 3d printed layers, low layer heights are used. This means that the individual layers are squished together better and thus joined more strongly. Additionally, with low layer heights, as one layer is printed, the material in the previous layer locally gets heated more and melts more. This again leads to a stronger bond between layers. More wall loops and infill are used for parts that need to be strong and or rigid. For parts of *the Chameleon*, the weight is also minimised as much as possible, as it's critical. For parts of the Spooling Station, strength and print.

Table E.1: 3D Printing Settings for Custom Parts

Part Name	Nozzle Diameter (mm)	Layer Height Preset	Wall Loops	Infill Density (%)	Modifiers (Y/N)	Modifier Infill Density (%)	Modifier Wall Loops	Batch Qty	Batch Weight Estimate (g)	Print Time Estimate	Filament Weight (g)
Fuselage	0.4	0.12mm High Quality	1	10	Y	50	3	1	48.06	4h25m	58.76

Part Name	Nozzle Diameter [mm]	Layer Height Preset	Wall Loops	Infill Density [%]	Modifiers (Y/N)	Modifier Infill Density [%]	Modifier Wall Loops	Batch Qty	Part Weight Estimate [g]	Print Time Estimate	Filament Weight [g]
Top Motor Mount	0.4	0.12mm High Quality	3	50	N	-	-	1	0.89	12m26s	0.89
Battery Cap	0.2	0.08mm High Quality	3	50	N	-	-	4	0.96	38m42s	1.13
Shaft Cap	0.2	0.08mm High Quality	2	10	N	-	-	4	0.27	16m45s	0.27
PCB Cap	0.4	0.12mm High Quality	1	10	Y	50	3	1	1.42	29m42s	1.70
Servo mount	0.4	0.12mm High Quality	3	10	Y	50	3	1	1.99	43m32s	2.74
Vane	0.2	0.08mm High Quality	2	10	N	-	-	4	3.54	1h29m	3.64
Spool	0.4	0.20mm Standard	6	20	N	-	-	1	83.22	5h56m	127.99
Platform	0.4	0.20mm Standard	4	20	N	-	-	1	82.18	5h29m	123.09
Total Filament Used (g)											**320.21**
Total Print Time — 0.4 mm nozzle										**17h 15m 40s**	
Total Print Time — 0.2 mm nozzle										**2h 24m 27s**	

Figure E.11: Files used for manufacturing the custom 3d printed components
Equivalent link: `https://doi.org/10.5281/zenodo.20813981`